6-2022

Development Of Flexible Hybrid Electronics For Sterilization And Structural Health Monitoring Applications

Arnesh Kumar Bose
Western Michigan University

DEVELOPMENT OF FLEXIBLE HYBRID ELECTRONICS FOR STERILIZATION AND STRUCTURAL HEALTH MONITORING APPLICATIONS

Arnesh Bose, Ph.D.

Western Michigan University, 2022

Traditional MicroElectroMechanical systems (MEMS) devices are fabricated utilizing Integrated Circuit (IC) based batch processing techniques. These systems are capable of sensing, controlling, and actuating on the micro scale and function/operate individually or in arrays. However, such devices typically utilize rigid substrates and are therefore not flexible. The upfront cost of research and development phase, investment for cleanroom and foundry facilities, testing and quality equipment is very expensive. Flexible Hybrid Electronics (FHE) refers to devices and systems that are fabricated utilizing an amalgamation of functional materials, films, membranes and integrated with functional electronic components that are mechanically flexible and stretchable. FHE combines the flexibility and low cost of printed functional inks on plastic film substrates with the performance of semiconductor devices to create a new category of electronics.

Microplasma discharge devices have been fabricated using MEMS processes. One application of microplasma is for sterilization of pathogenic microorganisms. Sterilization using microplasma has been of great interest in research as it provides a low-cost, safe, clean and more effective alternative to traditional methods. Among the various electrode design configurations available for microplasma discharge, planar dielectric barrier discharge (DBD) configuration was identified as the most suitable for a microplasma device where FHE fabrication method such as laser ablation can be utilized. The cross-section of a microplasma discharge device (MDD) consisting of a polyimide-based dielectric sandwiched between two copper electrodes was used for modelling the microplasma discharge characteristics in an argon environment. The sterilization

efficacy of the fabricated comb and honeycomb patterned electrode configurations was investigated. It was inferred that the honeycomb structured MDD was more effective in inactivating bacteria. The effectiveness of the honeycomb MDD for inactivating bacterial cells in liquid media was also demonstrated. The honeycomb MDD was then further characterized to calculate the power density of the discharge, optical spectra of the microplasma radiation and surface temperature of the MDD.

In structural health monitoring (SHM) applications, one of the most common sensors utilized for monitoring the health of load bearing components are strain gauges. Conventional strain gauges are typically manufactured using MEMS based technology. The traditional additive printing process of screen printing is more advantageous since it involves fewer manufacturing steps, roll-to-roll (R2R) fabrication capabilities and low operating temperatures during fabrication. A silver ink was blended with a carbon ink to achieve a silver-carbon (Ag/C) composite ink. The composite ink was then screen printed on a polyimide substrate in a meandering pattern to achieve a desired gauge resistance of ~350 Ω. The printed strain gauge was bonded to a flat aluminum beam and the capability of the printed strain gauge to detect linear and transverse strain were investigated by applying varying tensile and compressive loads on the aluminum beam, to simulate micro strain. Corresponding linear and transverse gauge factors for tensile and compressive loads were calculated and compared to a commercial strain gauge of similar gauge resistance. The temperature coefficient resistance of the Ag/C ink was calculated and its invariance to humidity was also investigated.

DEVELOPMENT OF FLEXIBLE HYBRID ELECTRONICS FOR STERILIZATION AND STRUCTURAL HEALTH MONITORING APPLICATIONS

by

Arnesh Bose

A dissertation submitted to the Graduate College
in partial fulfillment of the requirements
for the degree of Doctor of Philosophy
Electrical and Computer Engineering
Western Michigan University
June 2022

Doctoral Committee:

Massood Z. Atashbar, Ph.D., Chair
Silvia Rossbach, Ph.D.
Dinesh Maddipatla, Ph.D.
Bradley J. Bazuin, Ph.D.

ACKNOWLEDGMENTS

I would like to first express my sincere thanks and extend my deepest gratitude to my committee chair and advisor Prof. Massood Z. Atashbar for his guidance, and for providing me with the opportunity to pursue my doctoral studies. His valuable feedback helped me to stay on the right course for my research and drove me to accomplish more as an engineer. I will always be grateful to my committee member, Dr. Silvia Rossbach's support, insight and knowledge in subject matter which allowed me to successfully complete my project. I am also grateful to my committee member, Dr Bradley Bazuin for taking his valuable time in encouraging and supporting my dissertation and providing perceptive suggestions. I would like to express my deepest appreciation to committee member, Dr Dinesh Maddipatla for his support, constant help and invaluable time spent during the course of my graduate studies.

Special thanks to Carol Beaver for her unwavering support and collaborative effort which was key to successful completion of my dissertation. Many thanks to my fellow lab members, Xingzhe Zhang, Simin Masihi, Masoud Panahi, Anthony Hanson, Valliammai Palaniappan and Sajjad Hajian for their continuous support at the Center for Advanced Smart Sensors and Structures (CASSS) and the Sensors Technology Lab (STL). I would also like to thank the School of Engineering, and the Biological Sciences department and all staff members especially David Florida and Matthew Stoops for the considerate guidance throughout the course of my PhD program. A special thank you to the Electrical and Computer Science Department for providing financial assistance through Teaching Assistantship.

I am beyond grateful to my parents who have sacrificed a lot for me and provided all the financial support throughout my undergraduate and master's degree. My parents, along with my sister have always encouraged me to fulfil my dreams. I am also indebted to my late maternal grandparents and my late cousin, for believing in me and have inspired me to achieve my goals. Last but not the least, I am forever grateful for the love and support of my wife and for her patience throughout my doctorate program.

Arnesh Bose

TABLE OF CONTENTS

Table of Contents—continued

Table of Contents—continued

CHAPTER

Table of Contents—continued

CHAPTER

LIST OF TABLES

LIST OF FIGURES

CHAPTER I

INTRODUCTION

1.1 Background

Traditional MicroElectroMechanical systems (MEMS) devices are fabricated utilizing Integrated Circuit (IC) based batch processing techniques [1-3]. MEMS are integrated micro devices, sensors or systems with electrical and mechanical components, ranging in size from micrometers to millimeters [4-10]. These systems are capable to sense, control and actuate on the micro scale and operate individually or in arrays [11-13]. From the beginning of mid-1970, MEMS have emerged as the most widely used technology for creating devices used in actuators, physical, chemical, and biological sensors applications [14-37]. However, such devices typically utilize predominantly silicon based rigid substrates and are therefore not flexible. Moreover, MEMS devices are very costly during the research and development phase. The upfront costs of investment for cleanroom and foundry facilities, testing and quality equipment are very high [38]. MEMS are not always suitable for niche applications as the price associated with the fabrication and assembly of such MEMS devices are very high for low quantities.

Flexible Hybrid Electronics (FHE) refers to devices and systems that are fabricated utilizing an amalgamation of functional materials, films, membranes and integrated with electronic components that are mechanically flexible and stretchable [39-53]. FHE combines the flexibility and low cost of printed functional inks on plastic film substrates with the performance of semiconductor devices to create a new category of electronics [54-60]. In other words, FHE combines traditional electronics with new fabrication methods including additive (printed electronics (PE)) and subtractive manufacturing processes. Utilizing such materials can provide

devices that are flexible, stretchable and conformal, improving its mechanical reliability and reduction in weight, unlike traditional devices that manufactured on rigid substrates [61-64]. Such advantages of FHE have resulted in new applications in many fields including healthcare and medicine, structural health monitoring applications, consumer goods, wearable applications, and smart packaging [65-67]. The advancement of flexible device manufacturing has tremendous market potential in the years ahead [68-70]. With the advent of the Internet of Things (IoT), FHE will provide massive opportunities to develop and integrate low-cost smart systems and devices for use in healthcare, aerospace, automotive industries [71, 72]. According to Mordor Intelligence, the FHE market was valued at around $108 million in 2020 and is expected to reach around $264 million by 2026, registering a CAGR of 16.2% over the forecast period (2021-2026) [73]. North America has the largest market, and Asia Pacific has the fastest growing market. Similarly, according to IDtechEX, FHE market can exceed $3 billion by 2030 with health care and smart packaging being the dominant application area [74].

Fabrication of FHE devices is based on subtractive and additive print manufacturing processes [75-84]. Subtractive manufacturing process includes laser ablation/cutting is also commonly known as laser digital patterning (LDP) [85-88]. LDP is a photolithography free electrode fabrication and patterning method controlled by digitized parameters and uses a computer-aided design (CAD) image [89]. In order words, LDP utilizes a CAD image for patterning instead of a physical patterning mask. A laser emits a collimated light of single wavelength. The laser beam is focused on a very small surface which produces localized heating and incineration of the material. As laser source can produce rapid heating, it can increase the temperature of the surface faster than conventional heating systems. To mitigate thermal damage of the laser on the substrate, the beam diameter, laser pulse duration, laser power, and distance to

the target object can be optimized [90, 91]. This makes LDP a viable and effective tool for cutting and patterning thin film heat sensitive materials.

On the other hand, additive print manufacturing processes include screen, inkjet, flexography, gravure and 3D printing [92-94]. Screen printing is a technique in which paste-like material (ink) will be transferred onto the substrate by pushing the ink through a screen mesh by a squeegee [95-99]. A section in the screen consists of the design of the desired print and the ink is allowed to pass through it to create the desired design on the substrate [100]. Inkjet printing is a mask-less fabrication method and uses a digital image signal to print the design by propelling ink droplets onto the substrate instead of using any physical image carriers [101-104]. A continuous flow of ink droplets is controlled electronically by a voltage source [105]. Flexographic printing utilizes a steel cylindrical roller, that has finely engraved cells on its surface which collects the specific amount of ink from the ink reservoir [95, 106, 107]. The collected ink is transferred onto the elevated structures of the printing plate and is subsequently transferred on to the substrate [108]. Gravure printing uses low viscosity inks where the entire gravure cylinder is flooded by ink from the ink reservoir and the extra ink is wiped off from the cylinder with the doctor blade prior to printing [109-112]. The ink is transferred onto the substrate from the gravure cylinder with high pressures and the substrate movement is controlled by the impression cylinder [113]. Another form of additive manufacturing process such as three-dimensional (3D) printing has got a lot of attention in recent years for its ability to convert 3D CAD drawings into a physical object [114, 115]. 3D printing allows for fabricating of complex geometrical shapes by depositing materials in a layer-by-layer process [116, 117]. Among traditional additive print manufacturing methods, screen-printing is one of the simplest and cost-effective printing methods that enables mass production [118-120]. In this screen printing, different inks can be used to work with different material

surfaces such as fabrics, metals, plastics, wood, glass, ceramics, as well as paper, and such printing methods lowers tooling, setup costs and also accommodate different image sizes. Parameters such as screen mesh, ink, squeegee pressure and speed can be optimized for precision printing [121, 122]. Screen printing has been extensively utilized to fabricate sensors [123-127], transistors [128], solar cells [129], organic light emitting diodes [130] and printed circuit boards [131]. In this dissertation, LDP and screen-printing processes were employed as examples of subtractive and additive manufacturing process to develop FHE in sterilization and structural health monitoring applications, respectively.

Sterilization using microplasma has been of great interest in research as it provides a low-cost, safe, clean and more effective alternative to traditional sterilization methods. Microplasma, which is a non-thermal plasma (NTP) treatment of microorganisms at room temperature and atmospheric pressure, has shown to reduce growth of microorganisms such as bacteria on different surfaces like metals and fabric [132, 133]. The time required for sterilization is in the order of seconds [134-136], a considerable reduction when compared with traditional sterilization methods. The time reduction, and the capability of sterilization at ambient temperatures and pressures, has made microplasma discharge, a prospective technology for the future. The operating principle of plasma discharge is based on Paschen's Law, which states that the breakdown voltage is a function of the environmental pressure and the gap distance between electrodes [137, 138]. Hence, electrode design is a crucial parameter for efficient microplasma discharge. Among the various electrode design configurations available, the planar dielectric barrier discharge (DBD) configuration was identified as the most suitable configuration for a microplasma device where FHE fabrication methods can be utilized [138-141]. Also, DBD devices have multiple design configurations for volumetric and surface plasma discharges that can operate at atmospheric

pressure and temperature with variable voltage and frequency applications [142-144]. The choice of the DBD configuration is based on its ease of scalability as well as geometrical and mechanical flexibility for microplasma discharge applications [142]. Traditional plasma discharge devices have been fabricated using MEMS processes [145-148]. These devices are fabricated on rigid substrates which do not have the mechanical flexibility and conformability [149-151]. To address this, in this work, laser ablation was employed to pattern the electrodes on metallic tapes and are attached to flexible platforms such as plastic films [152-155]. The development of novel and flexible microplasma discharge devices (MDD) using laser ablation will advance the field of plasma science and medicine for applications in surface sterilization.

In structural health monitoring (SHM) applications, one of the most common sensors utilized for monitoring the health of load bearing components are strain gauges [156-158]. A strain gauge is a piezoresistive, active, analog sensor that has been used in a variety of applications [159]. Conventional strain gauges are typically manufactured using MEMS based technology [160-162], involving manufacturing processes, that have slow developmental cycles, multiple fabrication platforms and high cost of research and development. Commercially available strain gauges have been fabricated on flexible polyimide or glass-fiber reinforced epoxy-phenolic substrates using lithography-based fabrication process [163, 164]. Typical sensing layers are Constantan (Copper-Nickel) and Karma alloy (Nickel-Chromium) lithographically fabricated with metallic foils in a meandering pattern [163, 164]. Such fabrication processes also require controlled environments, thus significantly increasing the complexity of fabrication, costs of manufacturing, thereby potentially increasing the cost of the device. PE has emerged as one of the forms of manufacturing methods that can alleviate the limitations associated with conventional MEMS based fabrications methods [123, 165]. In this work, screen printing has been utilized to fabricate strain sensors by

directly depositing conductive composites on thin films, since it involves less manufacturing steps, roll-to-roll (R2R) fabrication capabilities and low operating temperatures during fabrication. This significantly improves production throughput and thus lowers the cost of fabrication [166-168].

1.2 Author's Contributions

The author's research work has resulted in 10 high quality refereed journal articles and 27 peer-reviewed conference proceedings. The list of publications is provided in Appendix A. The author is the recipient of the Graduate Student Research Grant from Western Michigan University.

1.3 Organization of the Dissertation

In this dissertation, the author describes in detail the research he performed during the doctoral studies. This includes two-dimensional modelling and finite element analysis of the effect of varying parameters such as varying input voltage, electrode and dielectric thickness on electron temperature and electron density for optimizing design parameters. A flexible comb structured microplasma discharge device (MDD) was fabricated using LDP for inactivation of gram-negative bacteria such as *Escherichia coli* (*E. coli*) and *Pseudomonas aeruginosa* (*P. aeruginosa*), using ambient air as the sterilizing agent for surface sterilization applications. In addition, a honey-comb structured MDD was successfully developed for inactivating multi-drug resistant Gram-negative (*E. coli*, *P. aeruginosa*) and Gram-positive (*Staphylococcus aureus*, *Bacillus subtilis*) bacteria suspended in liquid media, under ambient operating conditions. Lastly, a printed strain gauge based on metal/non-metal composite was successfully fabricated and tested for micro-strain ($\mu\varepsilon$) detection applications. In the above three projects, subtractive and additive fabrication methods such as laser ablation and screen printing were utilized, respectively.

The dissertation consists of seven chapters. The first chapter provides the introduction to the contents presented in this dissertation. In Chapter 2, a comprehensive literature review of the types of disinfection and sterilization methods used has been provided. Then a short overview of microplasma and the various configurations of microplasma based sterilization devices has also been provided. Mechanisms of microbial inactivation due to plasma activated agents such as reactive species and ultraviolet radiation has been provided as well.

In Chapter 3, the voltage distribution and surface DBD of an MDD were studied and modelled in two-dimensional domain using FEA. Initially, the voltage distribution across comb, H-tree and honeycomb structured MDD were analyzed. Then, the cross-section of an MDD consisting of a polyimide-based dielectric sandwiched between two copper electrodes was used for modelling the microplasma discharge characteristics in an argon environment. The spatial distribution of electron temperature across the electrodes for varying input voltages was simulated to demonstrate the importance of breakdown voltage. A detailed analysis on the effect of varying electrode and dielectric barrier thicknesses on the electron density and electron temperature was also performed to realize the importance of optimizing device configurations for microplasma discharge for a better understanding of the plasma discharge parameters. This may enable us to optimize design parameters for fabricating MDDs and the operating conditions for effective sterilization applications.

In Chapter 4, flexible MDDs were successfully developed for inactivation of Gram-negative bacteria such as *E. coli* and *P. aeruginosa*, using ambient air as the sterilizing agent. The design of the electrodes influences the voltage distribution across the device and is an important contributor to the overall sterilization efficacy. Therefore, the voltage distribution across the top electrode of two different MDDs (designed in comb and honeycomb patterns) was analyzed

initially using COMSOL Multiphysics® simulation software. The fabrication of MDD was realized using a flexible copper tape and polyethylene terephthalate (PET) film. Top electrodes of comb and honeycomb design were patterned using a laser ablation process. Similarly, rectangular and circular shaped bottom electrodes were laser ablated for the comb and honeycomb structured MDDs, respectively. PET was used as the dielectric layer, sandwiched between top and bottom layers of flexible copper tape. The efficacy of the MDDs was analyzed by varying parameters such as gap distance between MDD surface and bacteria (1 mm to 9 mm), treatment time (10 seconds to 300 seconds), input DC voltage (4 V to 8 V) and bacterial concentrations. Bacterial viability against varying parameters using comb and honeycomb patterned MDDs was analyzed in this project.

In Chapter 5, a flexible honeycomb patterned MDD was successfully developed for inactivating multi-drug resistant Gram-negative (*E. coli*, *P. aeruginosa*) and Gram-positive (*S. aureus*, *B. subtilis*) bacteria, under ambient operating conditions. The MDD was fabricated similarly as described in the previous chapter. The efficacy of the MDD to inactivate bacterial cells in phosphate buffer saline (PBS) was investigated by testing the effect of varying treatment times and input voltages, ranging from 1 to 10 minutes and 6 to 10 V, respectively. The flexibility of the device was also tested by bending the MDD on surfaces with a radius of curvature of 25 mm and 50 mm and calculating its power density for each bent condition. The optical spectra of the microplasma radiation and surface temperature profile of the MDD were also characterized and reported in this project.

In Chapter 6, a printed strain gauge based on metal/non-metal composite was successfully fabricated and tested for micro-strain ($\mu\varepsilon$) detection. A silver ink was blended with a carbon ink to formulate a silver-carbon (Ag/C) composite ink. The composite ink was then screen printed on a

polyimide substrate in a meandering pattern to achieve a desired resistance of ~350 Ω. The printed strain gauge was bonded on to a flat aluminum beam. The capability of the printed strain gauge to detect linear strain was investigated by applying varying tensile and compressive loads on the aluminum beam, to simulate με. Corresponding linear gauge factors for tensile and compressive loads were calculated and in addition transverse gauge factors for tensile and compressive loads were also calculated. The screen-printed Ag/C composite strain gauge was also compared to a commercial strain gauge of similar gauge resistance. The electromechanical response of the fabricated strain gauge as a function of resistance was investigated and included in Chapter 6. Finally, the conclusion for these projects along with suggestions for future work is provided in Chapter 7.

CHAPTER II

A REVIEW OF MICROPLASMA BASED DISINFECTION AND STERILIZATION: AN EFFECTIVE ALTERNATIVE TO CONVENTIONAL DECONTAMINATING METHODS

2.1 Introduction

Bacterial wound infections are a particularly significant problem for civil and military personnel due to the long delay between the injury and treatment at a hospital or clinic. Bacteria such as *Enterococcus faecium, Staphylococcus aureus, Klebsiella pneumoniae, Acinetobacter baumannii, Pseudomonas aeruginosa*, and *Enterobacter* species termed as ESKAPE pathogens, are the leading cause of health-care associated (nosocomial) infections throughout the world [169-171]. These infections can easily lead to chronic wounds and according to the National Institutes of Health, currently, there are 6.5 million people in U.S. suffering from chronic wounds resulting in additional costs of $3.5-10 billion a year [170]. The majority of hospital-associated infections (surgical site wound infections, urinary tract infections, bacteremia, respiratory pneumonia, gastrointestinal and skin infections) are currently being treated using antimicrobial agents called antibiotics [172].

Antibiotics, either used single or in combination, have been effective in treating wound infections. However, the pathogens are increasingly escaping the biocidal action of antibiotics by acquiring new resistance mechanisms and becoming non-responsive, thus making infections difficult to treat and increasing the risk of disease transmission, illness and death [173]. In other words, these bacteria evolve multi-drug resistance (MDR) and are tough to treat. For example, infections caused by *E. coli* (which, together with *Klebsiella* and *Enterobacter*, belongs to the bacterial family *Enterobacteriaceae*) were treated with fluoroquinolone antibiotics,

but *E. coli* acquired complete resistance against them [173, 174]. Later, the antibiotic ciprofloxacin was developed and used for treatment against *E. coli*. However, many countries reported to the Global Antimicrobial Resistance and Use Surveillance System (GLASS) that *E. coli*'s rate of resistance to ciprofloxacin increased to 92.9% [173]. Currently, colistin, which has severe side effects and has been banned in many countries, is the only antibiotic authorized to be used as a last resort treatment for life-threating infections caused by *E. coli* [173]. Nevertheless, a few countries recently reported that they detected an increased rate of resistance towards colistin as well, which is terrifying. A similar multi-drug resistance phenomenon was observed for all ESKAPE pathogens [173, 175]. The clinical pipeline for the development of novel antibiotics is alarmingly low, increasing the risk of recovery failures and deaths during any post-surgery recoveries [174, 175, 176, 177, 178]. The World Health Organization (WHO) declared the antimicrobial resistance (AMR) problem as a global health threat in October 2020 and called for an urgent multisectoral action [173]. This created a significant health requirement for novel technologies that facilitate effective treatment against ESKAPE pathogens and aid in wound healing.

Various technologies such as photodynamic therapy (PDT) and UV-plasma were explored to address MDR pathogens [179, 180]. A photosensitizer (PS), oxygen, and light are the three main components of PDT. The PS such as porphyrin, chlorin, porfimer sodium, and 5-aminolevulinicacid are activated by light of a specific wavelength in the presence of oxygen leading to the generation of reactive oxygen species (ROS) [180]. ROS are the key factor that results in localized cell death. In theory, a light-excited PS can directly react with an unsaturated lipid, a protein or nucleic acids to produce unstable radicals such as a hydroxyl radical or hydrogen peroxide, a superoxide anion radical, and convert molecular oxygen to singlet oxygen via energy transfer. In PDT, singlet oxygen is a major cytotoxin that causes cell damage and cell death via

necrosis, apoptosis, necroptosis, or autophagy. PDT causes these different types of cell death depending on the cell type, PS type or concentration, light dose, intracellular localization, and oxygen partial pressure. Although PDT is effective at inhibiting bacterial growth, it has certain limitations which constrains its use in the real world. The limitations include photobleaching of photosensitizers, limited light dose delivery, protracted activation time (approximately 20 minutes), toxicity and bio-incompatibility [180, 181]. In addition, the PS is meant for single use and should be disposed right after the usage. Furthermore, ROS generation and distribution in a closed space can result in heterogeneous accumulation of PS in the wound regions, making it difficult to determine the light dose required to induce photodynamic effects and avoid photobleaching reactions [180].

An alternate method, UV radiation, has been gaining attention for disinfecting applications and has several advantages when compared to other aforementioned methods [179, 182]. UV-based disinfection devices operate in ambient conditions and utilize no chemicals. Research has shown that disinfection efficacy against various bacteria is dependent on the wavelength of the UV light source [183]. Commercial based UV lamps operate at a single wavelength, thereby limiting its sterilization efficacy [184]. Microplasma, which provides a wide range of UV wavelengths along with ROS as well as reactive nitrogen species (RNS), is an emerging field of non-thermal plasma technology that can alleviate the disadvantages and shortcomings of various methods currently in use [184-187]. Therefore, a flexible and portable microplasma discharge device (MDD) that can be potentially applied as a bandage over a wound and can generate UV light, ROS and RNS, is envisioned as a promising alternate technological solution to inactivate and destroy ESKAPE pathogens.

Microplasma-based UV radiation is a non-thermal plasma (NTP) device technology that can expand our arsenal in fighting infections caused by antibiotic resistant pathogens. The key advantage of MDD's is the generation of UV radiation through microplasma discharge in ambient air and *in-situ* production of reactive oxygen and nitrogen species. The UV radiation causes lethal damage to DNA by the process of thymine-dimerization [188]. In addition, reactive species of oxygen and nitrogen, such as atomic oxygen, hydroxyl radicals ($OH*$), hydroperoxyls ($HOO*$), superoxides ($O_2^{-}*$) and nitric oxide (NO), can rapidly oxidize various macromolecules, including membrane lipids [189, 190]. Once the lipid membrane is compromised, the reactive substances provoke damage inside the cells to proteins, nucleic acids and carbohydrates leading to cell death. Therefore, the exposure of bacteria to the microplasma causes fatal damage to the bacteria due to UV light, ROS and RNS.

The MDD technology is envisioned to control the infection of wounds effectively without the need of any special equipment. FHE is an emerging field that combines the flexibility of plastic and metallic film substrates with the performance of traditional semiconductor-based devices [67, 191-202]. FHE based devices can conform to three dimensional surfaces. Laser ablation is a form of subtractive manufacturing process that involves focusing high power lasers through optical lenses to the surface of a specific area to remove material with a high level of precision [203-210]. This process does not involve toxic chemical solvents and does not leave any toxic waste. This process is cost effective, enables rapid prototyping, has minimal heat transfer and has been utilized in cutting a wide range of materials, which is a major advantage when compared to existing methods and practices in use.

2.2 Short History on Microbial Decontamination Methods

Various methods have been used to disinfect surfaces throughout history. Tar, sulphur, vinegar, and copper were among the early disinfecting and preserving substances used [211-214]. Mercury was first used in the 4th century, and later mercury chloride was implemented by physicians as an antiseptic [215-217]. Copper sulphate, zinc chloride and sodium permanganate were used during the 18th and 19th centuries as disinfectants. In 1744, chlorine was discovered and used mainly as a bleaching agent in the textile industry. By 1823, hypochlorite was used to disinfect wounds and deodorize exhumed corpses. Phenol, along with formaldehyde, was used during the late 19th century as an antiseptic and disinfectant in hospitals and for surgical instruments [215-217].

Dry heat, pressurized steam-based methods were also discovered and developed as an alternative chemical-based processes for disinfection and sterilization. In the 1830s, a physician named William Henry discovered that treating articles of clothing from infected individuals with a steam-heated hot-air vessel was an effective way of neutralizing microorganisms. Autoclaves using both dry heat and steam sterilization were studied and found to demonstrate that moist heat was more effective than dry heat [215-217]. In 1680 a French physicist, Denis Papin invented a pressure cooker which was found to sterilize objects by trapped boiling water which was then converted to steam [215-217]. The pressure cooker enabled boiling water to be maintained above 100°C in the pressurized metal container. Louis Pasteur and Charles Chamberland, his collaborator, developed the first pressure steam sterilizer now known as the autoclave in 1876. They discovered that exposing items with steam under pressure at 110 - 120°C for 30 minutes was as effective as exposure to dry heat at 130 - 150°C for 1 hour [215-217].

Gas phase disinfection using ethylene oxide, formaldehyde, and chlorine has been used since the mid-20th century and continues to be used in present times. The effects of natural light began to be studied in the late 19th century. It was discovered that certain bacterial cultures exposed to light would not grow [217]. The effects of varying wavelengths as a biocide were studied by Ward in 1892. He discovered that blue light was more toxic than red. Later, in 1903, Barnard and Morgan found that blue light had a maximum bactericidal effect in the wavelength range of 226 - 328 nm [217]. This discovery led to implementing ultra-violet light for air and water sterilization applications. Other research by Mink in 1896, and Pancinotti and Porcelli in 1898 proved that radioactive rays in the form of gamma and X-rays had anti-microbial properties which are still used in industrial sterilization processes to this day [217]. The newest form of sterilization is a cold plasma process developed and patented by Steris in 1987. The first hydrogen peroxide gas plasma system was field tested for sterilizing medical surgical devices in the 1980s and 1990s. This method has remained on the market since 1993 [218, 219]. In the modern age, there are different disinfection and sterilization practices (thermal, filtration, chemical, ultrasonic, microwave, radiation, ultraviolet and plasma) used in medical and industrial facilities [220-222]. There are certain advantages and disadvantages with all forms of disinfection and sterilization techniques. Some of the methods are best suited depending on factors such as the type of material to be treated, use for surface treatment or treating densely packaged items, resistance to heat or chemicals, biofilms or dense biomatter and disinfecting agent being environmentally friendly. A brief introduction to all the different types of disinfection and sterilization processes used are provided in this chapter to understand the advantages and disadvantages that the plasma-based sterilization offers.

2.3 Different Types of Disinfection and Sterilization Methods

2.3.1 Thermal Sterilization

One of the earliest and most widely used forms of sterilization techniques is thermal sterilization which has been used for centuries [223]. The two main types of thermal sterilization are dry and steam based. Dry thermal sterilization utilizes high heat (176 ºC - 232ºC) in either a temporarily closed or sealed chamber which is at ambient pressure conditions [224]. This process involves inactivation of the microorganisms via oxidation of the cellular components using pyrolysis [225]. However, dry thermal sterilization is not appropriate for sterilizing thermosensitive materials, dense biomatter, or objects with complex surfaces [226]. Thermal sterilization using steam-based sterilization in a pressurized chamber known as an autoclave, exposes objects to pressurized steam at temperatures ranging from 120ºC - 129ºC [224]. The hydrolysis of the cellular components of microorganisms renders them inactive by caveating the outer cell membrane [227]. Steam sterilization is more effective for sterilizing complex surfaces, dense biomatter and penetrating dense biomatrices. The steam-based method is not suited to thermosensitive instruments and materials prone to corrosion [228].

2.3.2 Filtration

The simplest and the most commonly used separation process is filtration. It is ubiquitous in the drinking water purification, food manufacturing, and oil producing industries [229, 230]. There are several different kinds of filtration methods used for filtering solid particles including microorganisms. These techniques include filtration from fluid using gravity, vacuum, centrifugal, cold and heat, and multilayer filtrations [229-232]. The type of filter media and filter porosity determine the capability and effectiveness of the various types of filtrations [232, 233]. Pore size

of the filter media is important as pores that are too small can affect the flow of fluid and become clogged with organic matter. Multilayer filtration combines various layers of filter material with increasing fineness directionally with filtration [234, 235]. Sterilizing the fluid media by passage through sterile bacteria retaining filters such as plastic, cellulose fibers, suitable sintered glass filters, porous ceramic, or a combination can be used. Cellulose based gravity filters are the most common method for filtering microorganisms such as bacteria and viruses. All filtration methods, however, pose a risk of contamination due to bacterial and viral particle size being smaller than the pore size or if there is a defect in the surface or depth of the filter being used.

2.3.3 Chemical Sterilization

Chemically based disinfection and sterilization techniques are the most common methods found in hospitals, commercial, and household environments. Chemical disinfecting and sterilizing substances are widely available and used on surfaces, and for sterilizing medical equipment and instruments. This type of sterilization is quite useful for thermosensitive materials that can be damaged by radiation sterilizing methods [236]. The most frequently used types of chemicals include isopropyl alcohol, ethyl alcohol, hydrogen peroxide, chlorine compounds, phenolics, formaldehyde, glutaraldehyde, peracetic acid, ethylene oxide and ozone [237]. The chemical agents can cause inactivation in a number of ways including inhibition of protein synthesis, oxidation of amino acids and membrane lipids, and oxidation of cellular components with depression of DNA synthesis [238]. As with other methods, there are certain disadvantages of chemical-based sterilization. Skin and eye irritation can occur and if ingested may cause gastric burns. High chemical concentrations can also cause metal corrosion [239]. Other chemicals such as aqueous formaldehyde, glutaraldehyde and ethylene oxide gas are also carcinogenic to humans and can cause neurological dysfunction [238, 239]. Alcohol based sterilizing agents have varying

efficacy dependent on the concentration and volume of chemical agent used. Surfaces containing dense biomatter, or thick biomatrices may require longer exposure time or higher concentrations of chemicals for disinfection or sterilization to have any germicidal effect [240].

2.3.4 Ultrasonics

Ultrasonication based sterilization is a decontamination technique used as an alternative to manual scrubbing found in commercial and healthcare facilities for cleaning contaminated surgical and dental instruments. This can help to standardize the ineffective mechanical scrubbing process by cleaning the inaccessible areas of the instruments [241, 242]. The ultra-sonification process uses an ultrasonic transducer mounted outside a steel basin to generate ultrasonic waves in the frequency ranging from 20 to 120 kHz [241, 242]. Effectiveness can be enhanced by adding chemical solutions in the processing basin. Another important parameter is temperature inside the basin as it increases the chemical solution's vapor pressure for the cavitation process [243, 244]. Pressure from the ultrasonic waves creates sufficient impact to rupture the cell membrane causing leakage of intracellular components such as nucleic acids, including DNA through the cavity formed on the cell membrane. This irreversible cellular damage inactivates the microorganism [244-246]. The negative effect of the ultrasonic sterilization process is that it can corrode plastics and steel after long-term use. The chemical detergents used in conjunction can also be harmful to the operators and is not environmentally friendly [247]. Another issue is that the process is time intensive and can also be ineffective on surfaces with dense biomatter or, thick biomatrices.

2.3.5 Radiation

Radiation based sterilization techniques have been used extensively in industrial and biomedical commercial packaging. It is of high interest as it can be used to sterilize samples at room temperature and provides the highest penetrability among the varying sterilizing methods [248]. Three different types of radiation based sterilizing methods include gamma rays, electron beams, and X-rays [249]. Gamma rays emitted by ^{60}Co have been used to rapidly sterilize large quantities of densely packaged materials [250]. Electron beams and X-rays are high energy electrons and photons, respectively [249, 251]. X-rays have higher penetrability than electron beams but lower penetrability than gamma radiation. They also reduce material degradation and provide flexibility to mix different products with different dose requirements in the same irradiation cycle [249, 251]. Radiation causes ionization of key cellular components, especially nucleic acids, resulting in the death of the microorganisms [252, 253]. Radiation induced oxidoreduction reactions due to water radiolysis into H^+ and OH^- radicals also alter DNA [254]. The increase in charged ions increases the electrostatic force on the cell membrane causing rupture and thus exposure of the cellular components to oxidation. This type of damage to the DNA of the cell has been proven to have excellent microbicidal effects [254]. Although radiation sterilization techniques are useful in large-scale industrial environments for sterilizing highly dense packaging, they require a controlled environment with highly skilled workers and are an expensive option. Not all materials and apparatuses are compatible with these techniques [252, 255].

2.3.6 Microwave

Microwave based sterilization is the most common process used in the food industry for sterilizing packaged and pre-cooked food [256]. It utilizes electromagnetic energy to generate dry heat which can inactivate pathogenic microorganisms. The US Federal Communication

Commission (FCC) allocates 915 MHz and 2450 MHz bands for industrial and domestic microwave heating applications [257]. The food industry sterilizes at 915 MHz and 2450 MHz frequency with heating capacities ranging from 10 to 200 kW [258]. The microwave-based method has the advantage of not involving any combustion of materials used to generate the heat with cycle times being quite reduced compared to that of thermal based sterilization. As it does not incinerate the food upon exposure to microwaves and helps retain nutrients during the heat generation, this method is of high importance in the food industry for thermally processed foods [256]. The microwaves generate ionized water molecules which in turn generate hydroxyl ions. These are essential for rupturing the cell wall due to electrostatic force generated outside the cell membrane [259, 260]. Drawbacks of microwave-based sterilization include unsuitability for metallic objects and surfaces. The packaging density and thickness of the object to be sterilized are also dependent on the electromagnetic radiation penetrability [256, 261]. This method is also bulky and requires high power units to operate, increasing operating costs due to increased electricity consumption. It is also prone to heating non-uniformly which can affect sterilization efficacy [256, 261].

2.3.7 Ultraviolet Radiation

Ultraviolet radiation is a form of electromagnetic radiation with wavelengths from 10 nm to 400 nm [262]. UV radiation has been used for decades by hospitals for disinfecting indoor air, surfaces and instruments in laboratories, and hospital and drinking water treatment facilities [262-264]. It is one of the most cost-effective methods used for disinfection of drinking water and the surfaces of objects. UV based disinfection devices utilize no chemicals, have no discharge byproducts (DBPs), and operates in ambient conditions [265]. The most sensitive targets of microorganisms during UV exposure are the nuclei acids of bacteria and viruses. This exposure

causes photochemical reactions not only in nucleic acids, but also in proteins such as enzymes and damages other intercellular and viral components [183, 184, 266]. Mercury-vapor lamps have traditionally been used for UV radiation and are widely used in biosafety cabinets and hand-held UV-lamps. Unfortunately, mercury vapors are extremely toxic when inhaled or not contained from environmental leakage [267]. More recently, LED based UV radiation lamps have been implemented to alleviate this issue. They are safer and more easily adjusted for tuning the UV radiation for specific wavelengths [268]. Research has proven that disinfection efficacy against various bacteria is wavelength dependent [269, 270]. As similar to other methods of sterilization, there are certain disadvantages with the use of UV radiation. It provides limited use for surfaces with dense biomatter and thick biomatrices. Disinfection of liquids is largely dependent on the presence of miniature solid particles that can block the penetration of UV radiation through the liquid media and on turbidity of the liquid media [271, 272].

2.3.8 Plasma

Plasma based sterilization involves highly excited gas, where the plasmas are generated in an enclosed chamber, utilizing high frequency and voltage to excite the gas molecules and produce charged particles, many of which are in the form of free radicals [273]. A free radical is an atom with an unpaired electron and is a highly reactive species. The action mechanism of this device is the production of free radicals within a plasma field that are capable of interacting with essential cell components (e.g., enzymes, nucleic acids) and thereby disrupt the metabolism of microorganisms [274, 275]. The discharge medium, type of excited gas, electrode configuration and treatment time are the most important variables that can determine the effectiveness of this process [276-278]. Ethylene oxide (EO) and vaporized hydrogen peroxide (VHP) are the two most common types of gases that are being commercially used in hospitals for generation of plasma

[279]. However, EO is a carcinogen and a major occupational health hazard for the workers. Therefore, VHP are commonly used for sterilization of medical devices and instruments. Moreover, the byproduct of the VHP during sterilization is water and oxygen [280]. The oxygen radicals are crucial for killing the microbial pathogens. This method of sterilization is therefore relatively safe and does not produce any toxic chemical byproduct after the sterilization process. However, since hydrogen peroxide is an oxidizer, it reacts with various surfaces and can also be an occupational hazard for the operator. Hydrogen peroxide can cause eyes and skin irritation and if exposed by inhalation can result in lung irritation as well [280]. It can also cause permanent eye damage, DNA damage and mutations. The American International Agency on Cancer Research (IARC) has categorized hydrogen peroxide as a carcinogen and according to the Environmental Protection Agency (EPA), it has been registered as a pesticide [281, 282]. Also, commercially available VHP systems are bulky, require high sterilization time ranging from 15-60 minutes and have a very high-power consumption in the order of kW [283, 284]. Research is being done to use sterilizing agents that are non-toxic and inert. Uses of inert gases is a major advantage as it does not react with materials [187, 285]. Ambient air as a sterilizing agent is a prospective new field of sterilization. Ambient air as a sterilizing agent is a prospective new field of sterilization. Ambient air is abundant in nature and use of it will not only reduce costs but will make the sterilization system less bulky. As compared to thermal and microwave sterilization, plasma-based sterilization is operated under ambient temperature and can also be operated in ambient pressure conditions. The use of toxic chemicals can be reduced if the sterilizing agent is inert or ambient air and does not involve any harmful radioactive exposure. Unlike ultrasonics- based sterilization, which can only sterilize hard metallic and polymer surfaces, plasma sterilization can be utilized to sterilize pathogens on a variety of materials (metals, polymers, ceramics, textile etc.). The key advantage

of ambient air based microplasma discharge for disinfection applications, is its ability to generate UV radiation and *in situ* production of reactive oxygen and nitrogen species [276, 278]. It is hypothesized that UV radiation causes lethal damage to the DNA strand by the process of photodesorption [286, 287]. Reactive oxygen and nitrogen species also cause oxidation of the cytoplasmic membrane causing it to rupture because of electrostatic force due to accumulation of the charged particles [288, 289]. This synergic effect of UV photons and reactive species makes ambient air microplasma discharge a prospective disinfection and sterilization method.

A summary of all types of sterilization methods and their corresponding advantages as well as disadvantages is shown in Table 2.1. In addition, the key information of each sterilization method such as sterilizing media, variable parameters, sterilizing agents and the mechanisms of sterilization is summarized in Table 2.2.

Table 2.1: Advantages and disadvantages of various sterilization and disinfection methods

	Method	Advantages	Disadvantages
1.	**Thermal**	• Widely used method and involves no pyrolysis • Relatively inexpensive • Does not pollute or cause toxic fumes	• Requires specialized chamber for operation • Slow cycle time • Not suitable for thermosensitive objects
2.	**Filtration**	• Least expensive method • Works well for thermosensitive fluids • Large volumes of fluids can be filtered relatively faster	• Can only be used for liquids and gases. • Will not filter microorganisms that are smaller than the pore size of the filter membrane
3.	**Chemical**	• Relatively rapid cycle time • Used in ambient to low temperature • Most popular method used in medical and hospital environment	• Not suitable for objects sensitive to chemicals • High risk of pollution and health-risk for workers • Chemicals must be safely stored and have short shelf-life
4.	**Ultrasonics**	• Provides alternative method to manual scrubbing improving reliability and effectiveness • Removes pathogens from less accessible surfaces	• Requires specialized electronic wet bath and multi-step processing • Cannot be used for materials sensitive to corrosion caused due to ultrasonic waves • Can only be used on solid objects
5.	**Microwave**	• Relatively rapid cycle time • Does not require any chemicals and involves no gas or combustion	• Cannot be used for sterilizing metal surfaces or instruments • Requires specialized and enclosed chamber for operation • Heat sensitive materials are prone to convection in the chamber
6.	**Radiation**	• Very rapid cycle time and high cell penetration of the radiation • Effective in ambient and sub-zero temperature environments • Products can be processed in final packaging format and leaves no residue	• Special chamber and equipment required for storing, handling and operating of radioactive isotopes and system • Radioactive isotopes are highly toxic for the environment • Plastics are sensitive to radiation
7.	**Ultraviolet Radiation**	• Non-toxic and no formation of hazardous by-products • Inexpensive and can be portable • The most user-friendly method	• Loses effectiveness in turbid fluid environment • Discharge wavelength dependent on the type of lamp and operates at single wavelength
8.	**Plasma**	• Rapid cycle time and high rate of efficacy • Relatively inexpensive when ambient air is used as the sterilizing agent • Along with reactive species, it also radiates UV that adds to it sterilizing capability	• Low penetrability of the reactive species and UV radiation on thick bio-matter • Complexity of operation increases if used in enclosed chamber and use of special gases such as Ar, Xe, N_2 etc.

Table 2.2: Sterilization and disinfection methods

	Method	Sterilizing Media	Varying Parameters	Sterilizing or Disinfecting Agent	Cause of Sterilizing or Disinfection
1.	**Thermal**	Solid surfaces, Liquids	Ambient temperature and pressure	Hight heat	Leads to hydrolysis, coagulation and oxidation of cellular proteins
2.	**Filtration**	Liquid, Gases	Pore size, granule size and ambient pressure	Perforated cellulose, ceramic or metallic membrane	Pore size small enough to block bacteria and most viruses
3.	**Chemical**	Solid surfaces, Liquids	Chemical concentration and exposure time	Alcohols, Aldehydes, Halogens, etc.	Denaturation of proteins
4.	**Ultrasonics**	Solid surfaces	Ultrasonic frequency and basin temperature	Ultrasonic shock waves	Formation of cavitation on the cell membrane due to ultrasonic waves
5.	**Microwave**	Solid surfaces, Liquids	Microwave frequency, exposure time	Electromagnetic radiation	Degradation of the cells due to convection of heat
6.	**Radiation**	Solid surfaces, Liquids, Gases	Energy density and exposure time	Radioactive isotopes, X-rays, Electron beam	Rupturing of cell membrane due to exposure of highly charged particles
7.	**Ultraviolet Radiation**	Solid surfaces, Liquids, Gases	Intensity of UV light and exposure time	Photons	Degradation of the cell DNA due to UV rays
8.	**Plasma**	Solid surfaces, Liquids, Gases	Electrode design, exposure time, discharge medium	Reactive species, UV radiation	Degradation of the cell DNA due to UV rays, electroporation of cell membrane due to electrostatic force

2.4 Plasma and Microplasma Fundamentals

2.4.1 Plasma Background and Theory

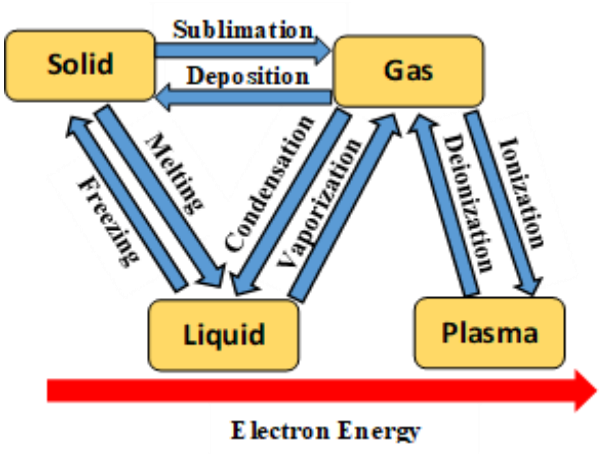

Figure 2.1: States of matter.

Plasma is an excited gas sustained in special environments and conditions. It is a collection of charged particles (electrons and ions) and excited elements collectively termed plasma that is sustained in a neutral background of gas [273]. Plasma can be defined as a physical state with very high conductivity due to the presence of free ions and radicals. Plasma is initiated when the electrons are accelerated between a cathode and anode electrode in a gaseous environment [290]. When the appropriate plasma discharge conditions such as high electric field, high electron energy and ambient conditions (temperature and pressure) are no longer applied to the plasma, electrons recombine with ions, returning the gas to its natural state. In Fig. 2.1 is a description of the states of matter and the process required to convert from one state to another. The direction of increasing electron energy is also indicated. These states of matter occur as the substance acquires more or less electron energy, to an electron temperature above or below the bonding energy corresponding to a particular state, respectively. This causes the phase transition which transforms the substance to the next state of matter [291]. Almost all matter in the universe is in the state of plasma, such as the sun, stars, interstellar matter, planetary atmospheres and terrestrial ionosphere. Plasmas that occur naturally on earth are very rare and can be seen in the form of lightning. Artificially induced plasma is generated for applications in surface sterilization, manufacturing microelectronic devices, environmental remediation, arc welding, plasma torches, high pressure fluorescent lamps,

the ignition spark in an internal combustion engines and space thruster for propulsion [292-297]. One of the most promising applications of microplasma discharge is surface sterilization from microbial contamination for food processing and alleviating skin infection of surgical, burn wounds and cancer treatment on human skin [298-303].

In 1889, Friedrich Paschen published a manuscript on the breakdown voltage of plasma which is now commonly known as Paschen's Law. The breakdown voltage (V_B) of microplasma NTPs is a function of the product of the pressure and the electrode gap distance. The V_B is mathematically written as Eq. (1) [304-307]:

$$V_B = \frac{Bpd}{\ln(Apd) - \ln\left[\ln\left(1+\frac{1}{\gamma_{se}}\right)\right]} \quad \text{Eq. (1)}$$

where, A is the ionization saturation, B is the excitation & ionization energies, p is the pressure (Pa), d is the gap distance (m), and γ_{se} is the secondary electron coefficient. A, B and γ_{se} are constants. Constants A and B depend upon the composition of the gas, and they are mathematically defined as [306]:

$$A \equiv \frac{\sigma}{k_B T} \quad \text{Eq. (2)}$$

$$B \equiv \frac{V_i \sigma}{k_B T} \quad \text{Eq. (3)}$$

where σ is the collision cross-section, V_i is the ionizing potential, k_B is Boltzmann's constant and T is the temperature of the neutral atoms. Hence, constants A and B can be correlated as $B = V_i A$. Differentiating Eq. (1) with respect to the product of the pressure and distance (pd) and setting the derivative to zero, the minimum voltage, or breakdown voltage can be written as

$$V_{B|\mathbf{min}} = \frac{Bln\left(1+\frac{1}{\gamma}\right)}{\mathrm{A}} e \quad \text{Eq. (4)}$$

Also, the minimum pressure and distance product can be given by Eq. (5):

$$pd|\min = \frac{\exp(1)\ln\left(\frac{1}{\gamma}\right)}{A} \qquad \text{Eq. (5)}$$

Paschen's curve is obtained from Eq. (6) and by differentiating Eq. (1) with respect to *pd* and setting the derivative to zero:

$$pd = e^{1-B} \qquad \text{Eq. (6)}$$

It has been observed that as the size of the gas/atom increases, σ also increases due to more frequent collisions, lowering V_B for low *pd* but increasing V_B when *pd* is higher [307]. From experiments, it has been demonstrated that a higher γ_{se} has a very small effect in the higher *pd* region [307]. The plasma discharge environment and the choice of electrodes and dielectric material are some of the most crucial parameters that must be considered when designing the microplasma NTP device. Operating conditions such as ambient pressure, the type of discharge medium is crucial in characterizing the "Paschen's curve" and every discharge medium or gas (argon, helium, air etc.) has its own characteristic curve [304-307]. An example of the Paschen's curve in air, in relation to the breakdown voltage (V_B) vs the pressure electrode distance (*pd*) are given in Fig. 2.2. The pressure is kept constant at 1 atm and the electrode gap distance is varied. It was observed that as the electrode gap distance increases, the breakdown voltage also increases. At 0.1 mm, 0.5 mm, 5 mm and

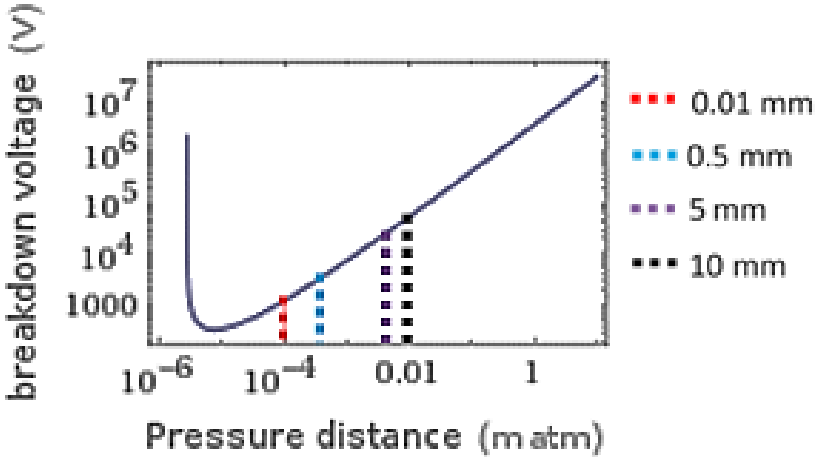

Figure 2.2: Paschen's curve for air at varying electrode gap distances.

10 mm electrode spacing, the breakdown voltages are calculated as 1.2 kV, 4.2 kV, 29.1 kV and 53.2 kV, respectively, using constant values of A = 4.36×10^{7} V/(m atm) and B = 362,000 m^{-1} atm^{-1}. The curve was obtained using the WolframAlpha breakdown voltage model [308].

2.4.2 Thermal vs Non-thermal Plasma

A plasma is ignited between or around two electrodes of opposite polarity in a gaseous medium, where the gas is dissociated into free electrons, radicals, ions, and excited molecules. The electrons accelerate towards the anode, colliding with the gaseous elements, thereby creating a chain reaction, that excites neutral atoms and molecules in the discharge medium [291]. These reactions can cause complete or partial ionization of the electrons energy which is denoted as electron temperature (T_e) [309, 310]. These additional electrons freed from the atoms are then accelerated towards the anode, causing more collisions and ionizations. When the frequency of collisions between the electrons, radicals, ions, neutral and excited molecules increases, the transfer of kinetic energy of the particles increases, which causes an increase in the gas temperature (T_g) [310]. Such conditions can be achieved if the plasma is generated under high pressure discharge or very high ambient pressure conditions while sustaining high voltage difference between the anode and cathode.

Plasma can be generally categorized as thermal and non-thermal plasma depending on its electron temperature and gas temperature [311-313]. When the gas particles attain the same energy as the electrons, it reaches a state of equilibrium. This state of plasma is referred to as thermal equilibrium, where the electron and gas temperature are the same [309]. Traditional plasma discharges tend to exist in thermal equilibrium in the bulk plasma, where energy distributions for electrons, ions, and neutral particles are assumed to be Maxwellian everywhere, and electrons and

ions have the same temperature [314]. The electron and gas temperature ranges from 10^3 to 10^4 K. Electron density for thermal plasma ranges between 10^{21}-10^{26} m^{-3} and electrode gap distance is much greater than 1 mm [309]. Typical examples of thermal plasma are DC transferred arcs, plasma torches and RF inductively coupled discharges. Thermal plasmas are used in industrial welding and cutting applications, processing wastewater, synthesis of nano powders and plasma based vapor deposition processes [309, 314]. NTP discharges are those in which, ions, electrons and neutral particles cannot be described by a single temperature. Rather, electrons ($T_e>>T_g$) are at significantly higher temperatures than heavy particles (ions and neutral species) [309, 313]. Thus, electrons drive gas phase reactions while little energy is spent on heating heavy species. This type of plasma is referred to as non-equilibrium, non-thermal or cold plasma and NTP is generated at vacuum low pressure conditions or ambient pressure conditions [309, 313]. The gas temperature is under 400 K and electron temperature ranges from 10^4 to 10^6 K. Electron density for NTP ranges between 10^{13}-10^{20} m^{-3} and the electrode gap distance is smaller than 1 mm. NTP's are used in a variety of applications such as sterilization, surface property modification, etching processes,

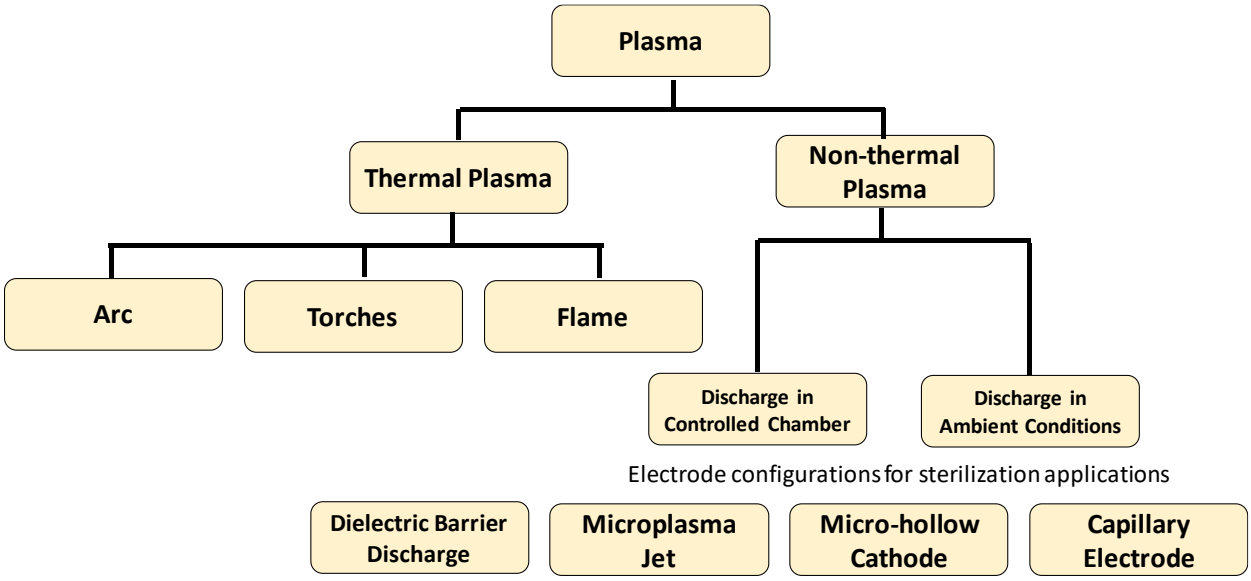

Figure 2.3: Types of thermal and non-thermal plasmas.

elemental analysis and micro propulsion technologies [314-320]. Figure 2.3 provides a detail depiction of the different types of plasma and the type of discharge in various conditions.

2.4.3 Microplasma

Microplasmas are stable glow discharge NTPs generated over a pressure range from 0.1 to 1.5 atm [316]. Electron temperatures range from 10,000 K to 100,000 K while ion and neutral particle temperatures remain at ambient levels, preventing the destruction of temperature-sensitive materials [321]. They are created by spatially confining the energy discharge to micro-cavities with dimensions less than 1000 μm [322]. Microplasmas are gaining interest and have been a major focus of research in biomedical, food, and environmental industries [323-325]. The major advantage of microplasma devices lies in the ease of fabrication with various miniaturized configurations, thereby enabling portability and increasing cost efficiency. The small sizes of these devices allows for applications focused on trace detection of various elements with sample volumes in the nanoliter range [326, 327]. A decadal survey by the National Research Council, Physics 2020/Plasma Science Committee states that the expanding scope of plasma research is creating significant interest and scientific opportunities in NTPs within the fields of chemistry, biology, physics, and materials science and engineering [328]. Emerging and exciting areas of plasma research focus on developing novel applications for NTPs, including surface sterilization, cancer treatment, water purification, and surface etching. In Fig. 2.4, the relation between pressure and plasma discharge size is

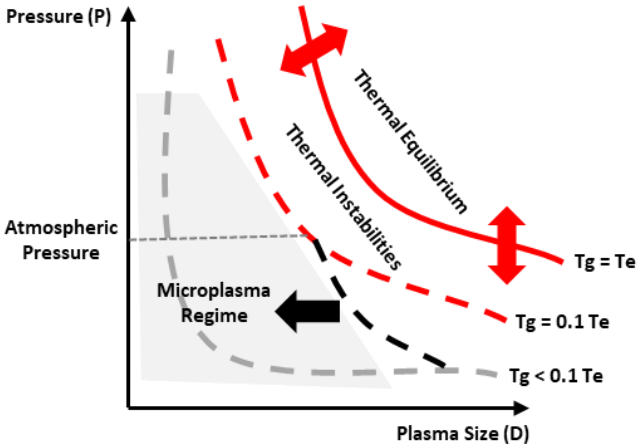

Figure 2.4: Graphical representation of Equilibrium & Non-Equilibrium Plasma.

compared. Also shown are the plasma operation regimes in relation to the ratio of bulk gas temperature to electron temperature. Hence, at atmospheric pressure or below, with smaller plasma size, an NTP can be generated where the gas temperature is significantly lower than the electron temperature [323-325].There are several factors that contribute to a stable microplasma in the discharge medium. One stabilizing factor can be explained in terms of "*pd* scaling", where "*p*" is the ambient pressure in the discharge medium and "*d*" is the distance between the cathode and anode [326]. The voltage required to generate a plasma discharge, is called the breakdown voltage, which depends on the product of pressure "*p*" and electrode separation "*d*" as shown schematically in Fig. 2.2 (Paschen's curve) [329]. If the separation between the two electrodes are kept constant and the ambient pressure increases the required breakdown voltage for microplasma discharge increases [330]. At atmospheric conditions and electrode separations in the range of centimeters to tens of centimeters, breakdown voltages at several kV range are required to ignite the microplasma discharge. The high breakdown voltage leads to a high current density after the discharge is ignited, particularly in the cathode fall of the discharge [331]. The high current density is the source of discharge instabilities in the cathode fall region, which quickly leads to the formation of an undesirable arc. This also results in gas dynamics of heating and momentum transfer from the electrons to the gas molecule, due to thermionic emission [332]. From "*pd* scaling," the breakdown voltage can be kept low if the electrode separation "*d*" is reduced when the pressure "*p*" is increased. At atmospheric pressure, electrode separation below 1 mm are required to be near the minimum in the Paschen's curve for essentially all discharge medium gases [333]. Another factor, that at least in part contributes to the stability of high-pressure microplasmas are the high losses of charge carriers to the surrounding walls [334]. The typical operating parameters of microplasmas corresponding to "*pd*" values are between 1 and 10 Torr-cm, with

pressures exceeding 1 atm (760 Torr) and electrode separation dimensions below 1 mm [321]. These "*pd*" values are similar to those for large volume, low-pressure plasmas, although the current and the energy densities in microplasmas are much higher [321].

2.5 Microplasma Discharge Device Configurations for Sterilization Applications

The breakdown voltage is a function of the environmental pressure and the gap distance between electrodes, therefore the electrode design is a crucial design parameter for efficient microplasma discharge. There are various electrode configurations such as dielectric-barrier discharge (DBD), atmospheric pressure plasma jet (APPJ), micro-hollow cathode discharge (MHCD), cathode boundary layer (CBL), capillary plasma electrode discharge (CPED), inverted square pyramidal (ISP) and square cross-sectional cavities (SCSC) [138]. Operation at high frequencies offers some advantages: gas breakdown in high frequency fields requires lower voltages than in DC fields, and the potential across the sheaths decreases [335]. As a result, high frequency operation results in less energy being transferred to the ions (which in atmospheric pressure plasmas ends up mostly heating the background gas), more efficient plasma generation, and a longer device lifetime [336, 337]. A schematic drawing of the different types of microplasma discharge configurations is provided in Fig. 2.5. Description of each of these in the rest of this section.

2.5.1 Dielectric Barrier Discharge

Dielectric barrier discharge (DBD) is a type of plasma actuation discharge configuration. The microplasma is formed between two parallel conducting electrodes separated by an insulated dielectric material and/or discharge medium [338]. The dielectric layer can be monolithically attached between two electrodes or cover one or both electrodes. This layer limits charge transfer

by forming a barrier preventing spark or arc discharges in the conduction path [339]. As the dielectric material properties such as operating temperature, insulation strength, dielectric constant, and mechanical properties determine the stability of the DBD and most discharge parameter, material choice is important [340]. As the dielectric barrier alters the gap field strength, it must be higher than average field strength. The constant of the dielectric barrier layer must be higher than that of the dielectric constant of air or other gases. Commonly used materials for the dielectric layer are quartz, glass, ceramics, and polymer layers. Thickness of this layer and the electrode gap are directly proportional to the breakdown voltage [338, 340]. A thicker dielectric layer can deliver adequate breakdown strength and reliable insulation from discharge current to prevent spark discharge. However, thicker layers require a higher applied voltage. As such, a balance between dielectric thickness, electrode gap, and applied voltage must be obtained for optimum microplasma discharge [341-343].

DBDs can function under a wide range of gas pressures (normally 0.01 to 10 MPa) and are driven by a pulsed voltage and by AC voltage with a broad frequency band (50 Hz–1 MHz) [143, 344]. Some specific layouts with special dielectric material arrangements can be driven by a DC voltage [345, 346]. One end is comprised of a grounded electrode (ground electrode) while a sinusoidal voltage is applied to the other electrode (terminal electrode). At atmospheric pressure, the breakdown of the gap in the DBD is generally streamer breakdown [347]. The applied voltage should be sufficiently high enough to cause ionization of the discharge media. The discharge medium can be in a controlled chamber in an environment with inert gases (He, Ar, Xe, or a mixture) and elemental gases (N_2, O_2, or mixture of the gases) or can be discharged in environmental ambient air which primarily consists of N_2, O_2, CO_2 and water vapors (H_2O) [344].

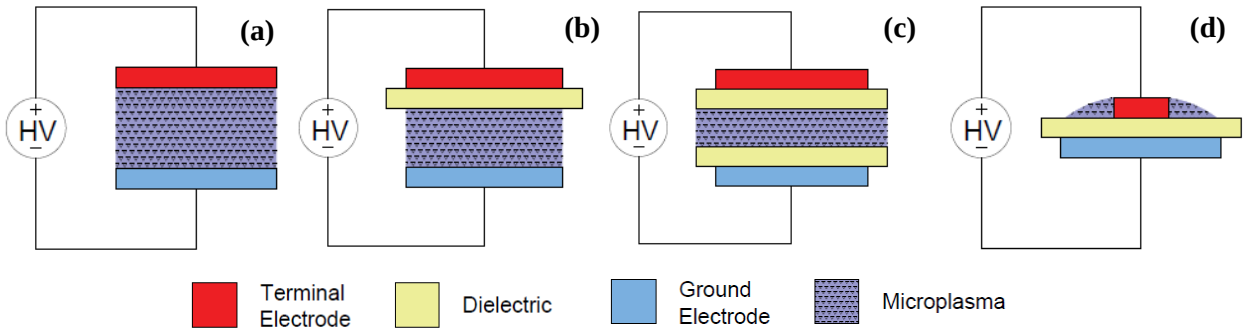

Figure 2.5: Various DBD configurations for microplasma discharge.

The discharge medium between the electrodes reaches a higher state of electron energy as the high sinusoidal voltage is applied. Once the applied voltage is high enough, the electrons dissociate from the atoms, and form free electrons and ions [143, 344]. A cascading effect is achieved as the free electrons in the discharge gap accelerate and acquire higher potential, increasing the number of free electrons. These free electrons and ionized charges move across the discharge gap to the opposite electrode potential [143, 344]. As the charge accumulation process is temporary, once the electric field potential is reversed the entire process flips in the opposite direction and repeats as long as the sinusoidal voltage is applied. The primary DBD configurations are illustrated in Fig. 2.5 (a,b,c). Typical gap distance and dielectric thickness in DBDs vary from 0.1 mm to several centimeters. The discharge gap and dielectric thickness should be kept small depending on the application and power usage to lower the breakdown voltage and gas temperature. In Fig. 2.5(a), the high-voltage electrode is covered by a dielectric layer. The thermal heat generated with extended operation can be dissipated through the metallic electrode although it then becomes exposed to erosion. In Fig. 2.5(b) both electrodes are covered by the dielectric layer. Electrode erosion can be avoided using this configuration which improves longevity of the device. Using the configuration Fig. 2.5(c), the two electrodes can be monolithically attached together without requiring any discharge gap. The breakdown gap for the plasma discharge is

based on the thickness of the dielectric layer. This enables thin DBD configurations to be quite flexible. These basic configurations can be planar, coaxial, surface, or other novel combinations.

2.5.2 Atmospheric Microplasma Jets

The plasma jet is a broad concept covering different electrode configurations in electrical operating modes of gaseous discharge. Key parameters for the projection of the discharged plasma species into an open environment include enclosed electrode arrangement and the type of gas used for plasma discharge [348-351]. Traditional plasma jet devices are usually operated as a thermal arc jet and used in applications such as welding, cutting, and other material techniques. The discharge is ignited and operated on a feed stock gas with application of radio frequency (RF) power. It flows between an outer grounded electrode and a central electrode producing a high velocity effluent stream of highly reactive chemical species [352]. The high flow of a carrier or working gas is often the cause of plasma expansion but electrical field geometry can also be a determinant. RF power drives the central electrode causing acceleration of free electrons. In-elastic collisions between the free electrons and freed gas cause the production of excited state molecules, atoms, free radicals and additional ion-electron pairs [353-355]. Rapid recombination of the ions and electrons causes many to be lost once the gas exits the discharge volume, but neutral metastable species and radicals are still contained in the fast-flowing effluent [356, 357]. A distinctive feature of the plasma jet configuration is the ability to launch the stable plasma species into a separate environment containing a significantly lower electric field. Thus, allowing the treated target to be no longer confined to the close proximity of the plasma source. Microplasma jets can operate with a kHz AC power supply, RF, microwave, or pulsed DC supply [358-362]. Atmospheric pressure microplasma jets can be driven by a DC power source with varied current in some electrode configurations [362]. Orientation of the electric field with respect to the direction

of gas flow varies depending on microplasma jet configuration. Research for biomedical applications and surface modifications has been focused on generating laminar longitudinal flow of gases through the tube to generate longer afterglow [363, 364]. Higher discharge gas temperatures can be reduced by using noble gases such as argon and helium [365]. Although there is a similar flow rate through the capillary, when utilizing inert noble gases as feed gases it becomes relatively expensive to operate and provides a shorter plasma afterglow when compared to feed gas of oxygen, nitrogen and ambient air [366]. Inert feed gases such as argon and helium also create a less reactive plasma afterglow which does not generate the reactive species useful for sterilization and biomedical applications [190]. However, significantly less expensive, nitrogen, oxygen and ambient air generate filamentary microplasma discharges which produce a high current arc. The plasma discharge can become highly unstable leading to higher gas temperature [367]. Reducing the capillary (dielectric tube) diameter can reduce the radial size of the plasma jet to micrometer ranges. Jets can be moved across the object surface or operated in an array mode for applications requiring a large area or bulk treatment [368, 369]. Parallel operation of multiple jets requires uniformity and stability, which is dependent on balancing voltage and current of the driving circuit [369, 370]. Microplasma jets not only improve the discharge and treatment area but can also provide a different diameter of the electrode and tune the reactive species composition using different feeding gas mixtures to each jet. The primary configurations for producing

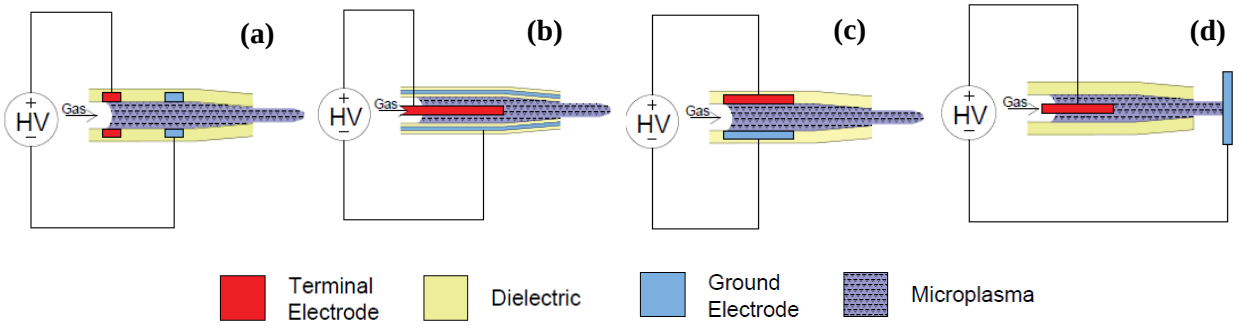

Figure 2.6: Various jet configurations for microplasma discharge.

microplasma jet is given in Fig. 2.6 (a,b,c). Coaxial electrode, DBD based and floating electrode DBD are typically used for generating microplasma jets. Configuration of the electrodes can be altered based on application and power usage. In Fig. 2.6 (a,b), a coaxial arrangement of the electrodes is shown used for generating microplasma jet. Feed gas is passed through the capillary tube which is surrounded by coaxial rings of the terminal and ground electrodes. The third geometry shown in Fig. 2.6 (c), is also suitable for generating microplasma jets and the operation is similar to DBD based devices. The dielectric separating of the two electrodes on adjacent sides is the thickness of the capillary tube and the outer diameter. Feed gas passes through the tube generating reactive species in between the electrodes. These three geometries have been extensively utilized for biomedical and sterilization applications. The fourth geometry is typically used for applications in plasma torches and generated high gas temperature. This design generates arc jets and is un-suitable for applications involving thermolabile materials.

2.5.3 Micro-hollow Cathode

A type of plasma discharge, where microplasma is generated in microcavities of electrode-dielectric-electrode sandwich structures, is known as micro hollow cathode discharges (MHCD's) [371, 372]. The phrase "hollow cathode" has historically referred to a specific mode of plasma discharge operation where the current increases, as the operating voltage drops. Current research, however, uses a different method without the hollow cathode mode using stable glow discharges [371, 372]. Because of this modern shift, several research groups refer to such microplasma discharges as "microdischarges" or "micro-structured electrode arrays". MHCD allows for higher pressure operation when the perforated electrode hole diameter is decreased [373, 374]. A hole diameter less than 1000 μm for a high feed gas rate allows for lower gas temperature at ambient conditions. A non-equilibrium microplasma having a density above 10^{14} cm^{-3} can easily be

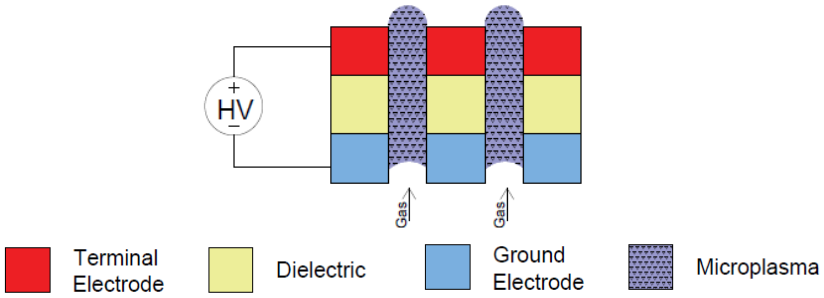

Figure 2.7: MHCD configuration for microplasma discharge.

achieved in an MHCD [375]. Use of MHCD for surface modification, treatment of wastewater, and use in micro-thrusters for guiding microsatellites is a growing area of interest aside from the use in sterilization applications [376-380]. The primary configuration for producing micro hollow cathode jet is given in Fig. 2.7. The geometry consists of thin dielectric layer sandwiched between a cathode and anode. The thickness can be changed along with the hole diameter. The type and rate of feed gas can also be altered and optimized based on the application. The standard low-pressure discharge with a hollow cathode effect typically has the advantage of higher concentrations of electrons and ions with lower breakdown and operating voltages as compared to traditional normal glow discharges. Two dimensional arrays of individual MHCDs can be operated in parallel without individual ballast resistors if the current voltage curve has a positive slope. However, a current voltage curve with a negative slope MHCD array can be generated by using a distributed resistive ballast or multilayered structure where each micro-discharge is individually ballasted.

2.5.4 Capillary Plasma Electrode Discharge

The capillary plasma electrode discharge (CPED) configuration is one of several actuations of discharge concepts which generate and sustain high electron density stable glow discharges with

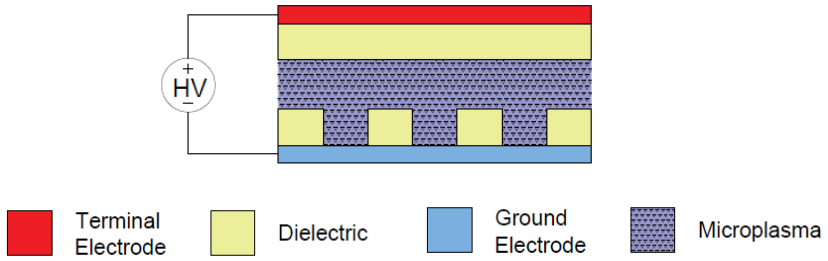

Figure 2.8: CPED configuration for microplasma discharge.

self-current limiting [381, 382]. The basis of the CPED is suppression of the glow-to-arc transition instability by stabilizing the cathode fall region of the discharge [381, 382]. A narrow channel is provided by a micro-hole in the perforated dielectric layer limiting discharge current. This uses a novel design where dielectric capillaries cover one or both electrodes of a discharge device (Fig. 2.8). Many details of the CPED look similar to conventional dielectric barrier discharge (DBD) but CPED exhibits a mode of operation called "capillary jet mode" which is not seen with DBDs [383]. Capillaries with diameters ranging from 0.01 to 1 mm and length-to-diameter (L/D) ratios from 10:1 to 1:1, serve as plasma sources and produce jets of high-intensity plasma at high pressure. These jets emerge from the end of the capillary forming a "plasma electrode" [384]. When excited by pulsed DC or AC, CPED displays two distinct modes of operation. When the applied voltage pulse frequency is increased above a few kHz, initially a diffuse mode similar to the DBD's diffused glow can be observed as described by Okazaki et al. [385]. Once the frequency reaches a critical value (depending on the L/D value and the feed gas), the capillaries "turn on" and bright, intense plasma jets emerge. When many capillaries are in close proximity to each other, the emerging plasma jets overlap, and the discharge appears uniform [321]. The preferred mode of operation of the CPED is the "capillary" mode. It has been characterized for multiple laboratory-scale research discharge devices in terms of its electrical and plasma properties [386-388].

2.6 Gram-positive and Gram-negative Bacteria

The bacterial cell envelope is a multilayered and complex structure encasing the cytoplasm serving to protect the organism and internal contents from the surrounding environment. In 1884, Christian Gram developed a staining method allowing him to classify most bacteria into two broad categories, ‘Gram-positive’ and ‘Gram-negative’. The Gram-negative and Gram-positive cell wall structure is show in Fig. 2.9. The envelopes of Gram-negative bacteria are composed of three principal layers; the outer membrane, the peptidoglycan cell wall, and the cytoplasmic or inner membrane [389]. Gram-positive bacteria lack the outer lipid membrane. This unique outer membrane is a lipid bilayer containing phospholipids which are confined to the inner leaflet of the membrane [390]. The outer leaflet of the outer membrane is composed of glycolipids, principally lipopolysaccharide. Both Gram-positive and Gram-negative bacteria have a peptidoglycan layer surrounding the entire cell which is a heteropolymer of glycan chains crosslinked by amino acids. The covalently bonded peptidoglycan layer varies in thickness between the two types with Gram-positive bacteria having a thicker peptidoglycan layer (20-80 nm) and Gram-negative bacteria a thinner one (<10 nm) [391]. The cytoplasmic or inner membrane is composed of a layer of proteins and phospholipids with some proteins interspersed. It encloses the internal contents of the bacterium regulating flow of materials in and out the cell. The cytoplasm, or protoplasm, of

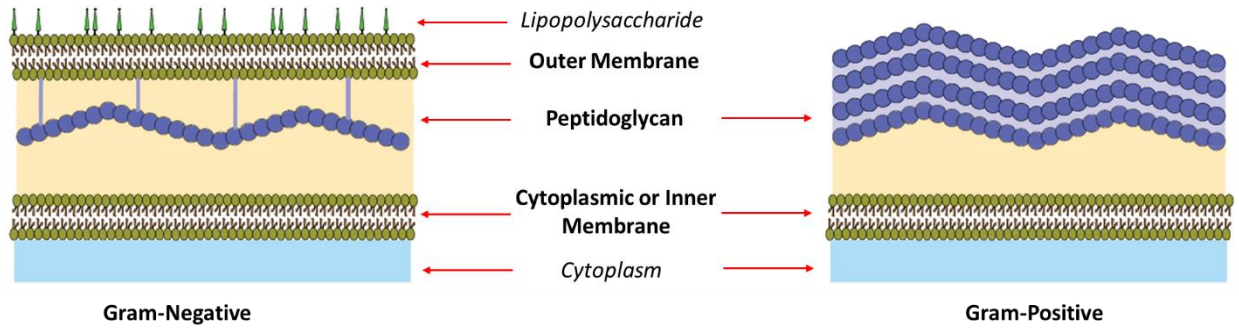

Figure 2.9: Gram-negative and Gram-positive cell wall structure.

bacterial cells is where the metabolic reactions and the replication of nucleic acids occur, allowing bacterial growth and multiplication [389, 392].

2.7 Plasma Actuated Agents for Sterilization and Disinfection

The complex chemical composition of microplasma is comprised of different reactive agents (electrons and positive and negative ions, free radicals, excited atoms and molecules) and UV radiation. A key advantage of microplasma discharge for disinfection and sterilization applications under ambient conditions is the ability to generate UV radiation and *in situ* production of reactive agents [393, 394]. UV radiation is known to cause lethal damage to the DNA strand by the process of photo-desorption [395]. ROS and RNS accumulate creating an electrostatic force causing lipid and protein oxidation and eventually rupturing of the cytoplasmic membrane which leads to the exposure of the intracellular matter of the cell to the environmental elements [274]. Due to the synergistic effect of reactive species and UV photons, this makes microplasma discharge a potential disinfection and sterilizing method for neutralizing pathogenic microorganisms [396]. The microbicidal effects of reactive species, and ultraviolet radiation (Fig. 2.10) will be discussed in the following section.

2.7.1 Reactive Species

Research has shown that reactive nitrogen species (RNS) and reactive oxygen species (ROS) generated from microplasma (particularly plasma energy particles such as electrons and excited atoms) can cause mechanical erosion or oxidative damage (lesions) to cellular envelopes [188-401]. Accumulation of charges (electrons, excited atoms, RNS and ROS) on cellular envelopes can lead to permeabilization through the formation of pores, in a phenomenon known as electroporation [398, 402]. A schematic representation of the effects of microplasma on bacteria

is shown in Fig. 2.10. At the intracellular level, reactive species of oxygen and nitrogen, such as atomic oxygen, hydroxyl radicals (OH∗), hydroperoxyls (HOO∗), superoxides (O2-∗) and nitric oxide (NO), can rapidly diffuse into the cells and oxidize various macromolecules [398, 402]. Once inside the cell, reactive substances provoke damage not only on lipids, but also on proteins, nucleic acids and carbohydrates. Reactive species also initiate lipid peroxidation phenomena, chain reactions that begin with the attack of unsaturated fatty acids by the oxygen species and can compromise cell viability by modifying membrane properties, decreasing permeability and even its integrity [190, 402]. Compromising the cellular membrane facilitates the release of important

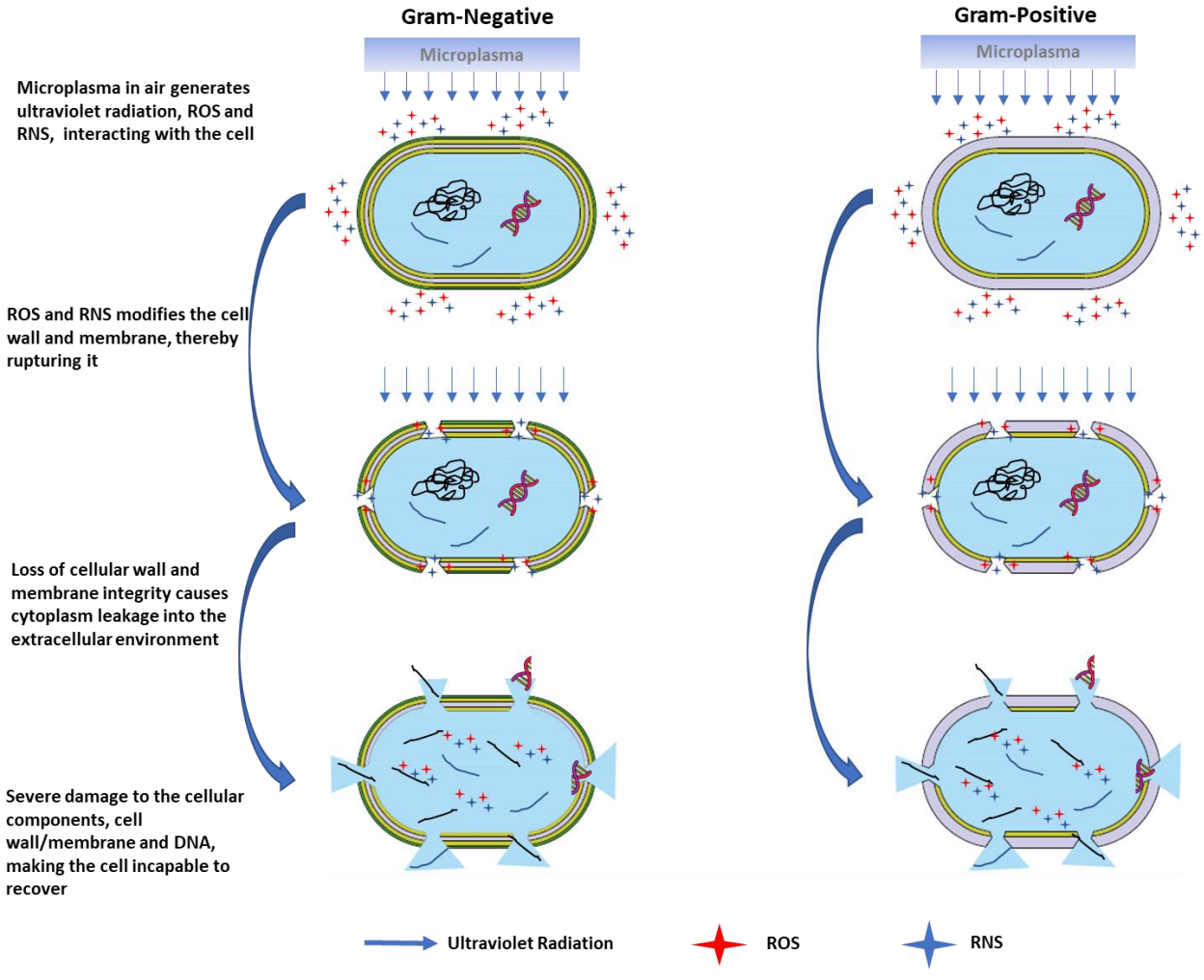

Figure 2.10: Schematic representation of the effect of microplasma on bacteria.

intracellular components to the external environment thus accelerating the inactivation process. Therefore, the exposure of bacteria to the microplasma causes an uncontrolled damage to the bacteria.

2.7.2 Ultraviolet Radiation

UV radiation is a form of electromagnetic radiation that covers the wavelengths in the range from 100 to 400 nm. The UV spectrum can be categorized as UVA (400–315 nm), UVB (315–280 nm), UVC (280–200 nm), and vacuum-UV (VUV, 200-100 nm) subdivisions. The UVC band is divided into near-UVC (280–240 nm) and far-UVC (240–200 nm) [403]. Microbial growth inhibition by induction of DNA thymine dimers is widely known to occur with exposure to UV radiation wavelengths in the 220–280 nm range [404]. Intercellular components of living cells; e.g. nucleic acids, such as ribonucleic acid (RNA) and deoxyribonucleic acid (DNA), and proteins; can absorb UVC with different sensitivities. As these UVC photons have the highest absorption rate by microbial pathogens, these wavelengths are also referred as germicidal UV wavelengths. The microorganism is inactivated by UV radiation and prevents from reproducing, but does not destroy microorganisms [401, 405, 406]. The most sensitive targets during UVC exposure are the DNA of bacteria, the DNA and RNA of viruses [183, 407, 408, 409] and damages the nucleic acid, cyclobutane pyrimidine dimers, (6–4) photoproducts, and protein-nucleic acid cross-links [188, 410]. UVC radiation damages biological molecules with unsaturated bonds like coenzymes, hormones, and electron carriers as well as other intracellular and viral components by causing photochemical reactions in proteins and enzymes [188, 411]. However, different proteins have different wavelength-sensitivity patterns of UVC absorption than nucleotides [412]. Peak UVC absorption is reached near the range around 265 nm, whereas the protein UVC absorption starts increasing below 240 nm wavelengths (far-UVC) and even surpasses DNA absorption at around

225 nm [412]. Effects of UV radiation can completely halt cell reproduction due to DNA mutation [411].

2.8 Summary

Microplasma based UV radiation is an emerging field of low temperature, non-thermal plasma device technology that can alleviate the disadvantages and shortcomings of current disinfection methods currently in use [184, 185, 187, 413, 414]. Microplasma NTP treatment of microorganisms at room temperature and atmospheric pressure has been shown to reduce growth of microorganisms such as bacteria on different surfaces like cloth, metal and laboratory-based growth media. Although there are other disinfection and sterilization methods, those methods utilize special chambers and chemicals which makes them non-portable, or can be harmful for the operator due to the use of toxic chemicals, toxic discharge byproducts, high operating temperature and pressure. However, microplasma based sterilization considerably reduces the time required for sterilization into the order of seconds (depending on the device configuration and its operating voltage), which is a considerable time reduction when compared with traditional sterilization methods.

The key advantage of ambient air based microplasma discharge for disinfection applications, is its ability to generate UV radiation and in situ production of reactive oxygen and nitrogen species [415-418]. The synergic effect of UV photons and reactive species makes ambient air microplasma discharge a prospective disinfection method to kill harmful pathogens that cause diseases. Therefore, there is immense potential in flexible microplasma based devices for application in textile, wound surfaces and polymeric surfaces and there is a need to perform more research to develop such low cost and low power flexible devices that will be accessible to the public in future years and provide a safe and low cost alternative to existing disinfection and sterilization methods.

CHAPTER III

2D FINITE ELEMENT MODELING OF SURFACE DIELECTRIC BARRIER PLASMA DISCHARGE DEVICES TO UNDERSTAND THE INFLUENCE OF DESIGN PARAMETERS ON STERILIZATION APPLICATIONS

3.1 Introduction

Traditional thermal and non-thermal plasma require very high voltage of operation and often operated in special chambers where the ambient conditions such as temperature and pressure are continuously monitored and controlled [419, 420]. The major advantage of microplasma discharge device (MDD) lies in the ease of fabrication with various miniaturized configurations, which reduces the breakdown voltage for igniting plasma, requiring relatively smaller transformer and power supply. This increases the possibility to design and fabricate portable MDDs, thus leading to cost efficiency. The performance of MDDs are dependent on a stable and uniform microplasma discharge. MDD parameters such as electrode gap distance (dielectric thickness), electrode thickness and the applied voltage will affect microplasma discharge characteristics such as electron density (n_e) and electron temperature (T_e) [421]. Moreover, the change in ambient conditions such as temperature and pressure will affect the net n_e of the microplasma discharge due to the change in electron mobility (μ_e) [422]. Understanding the effect of such variable parameters including electrode and dielectric thickness, applied voltage, and changing ambient conditions will enable us to design effective MDDs based on their operating conditions.

The generation of uniform and effective plasma in MDDs depends on electrode configurations and designs [182, 423-430]. It is hypothesized that uniform voltage distribution across the electrodes will result in the generation of uniform n_e and T_e, which will lead to uniform, stable and steady microplasma discharge across the electrode. DBD is the most suitable

configuration for fabricating a surface plasma based MDDs due to its ease of scalability and geometrical flexibility (planar geometry) unlike other configurations [142, 431, 432]. These devices can operate at atmospheric pressure and temperature with variable input voltage and frequency. Recently, new geometries such as micro hollow cathode geometries and plasma pencil geometries have been used to generate microplasma for medical and sterilization purposes [431, 432]. While MDDs utilizing such geometries operate at ambient pressure and temperature, the effective treatment area for each device is very small and not scalable unlike for MDDs that can be made of DBD configuration. Various DBD based electrode designs including comb, H-tree and honeycomb were chosen to simulate and study its voltage distribution effect on the microplasma discharge of MDDs. Typically, comb structure is selected due to its simplicity [433], and H-tree design is a very common design feature utilized in the electronics industry to keep the clock frequency and voltage uniform across the printed circuit board [434]. Honeycomb pattern has high surface area, provides uniform voltage and is highly scalable in size and area as compared to the other designs [435]. Moreover, the hexagon pattern has proven to divide surfaces into regions of equal area with the most highest density [436, 437].

Microplasma based finite element analysis (FEA) simulations have been performed to study the electron and ion kinetics and breakdown voltages in coplanar electrode based microplasma devices [438-442]. Some application specific FEA simulations [443-450], were utilized to study microplasma discharges including plasma thruster [451, 452], material deposition [453], etching processes [454], pollution degradation devices [455] and analytical spectroscopy [456]. Deconinck et. al. and Shimizu et. al. performed simulations on microplasma jet-based propulsion device to study the variations in plasma kinetics for various applied voltages and the flow velocity in microcavities, respectively [451, 457]. Seo et. al. performed simulations of AC

driven DBD microplasma in circular microcavities to understand the effect of the cavity diameter on n_e under various ambient pressure conditions [458]. Simulations for microplasma used for additive (printing) and subtractive (etching) manufacturing processes have also been performed by Sawant et. al. and Dai et. al. respectively, to study the effects of dimensional properties on material deposition and n_e [453, 454]. As microplasma based sterilization is of growing interest, there is a need to investigate the effect of dielectric and electrode parameters for microplasma discharge. To the best of the authors' knowledge, there is no literature available on two-dimensional FEA simulations focusing on the effects of electrode and dielectric dimensional parameters on the surface DBD based microplasma discharges for sterilization applications. Therefore, in this work, the effect of different electrode designs on voltage distribution were investigated. Effect of varying applied voltages, electrode, and dielectric thickness on the n_e and T_e were also analyzed across the electrodes using COMSOL Multiphysics® simulation software.

3.2 Simulation Model

Dielectric barrier discharge (DBD) are plasma discharges characterized by formation of electrical discharges between two conducting electrodes, separated by an insulating material [341]. A sinusoidal voltage is applied to one of the electrodes (terminal electrode) and the other electrode is grounded. Depending on the thickness of the dielectric and/or discharge gap and the discharge medium the amplitude of the sinusoidal voltage will vary [143]. A schematic drawing of the

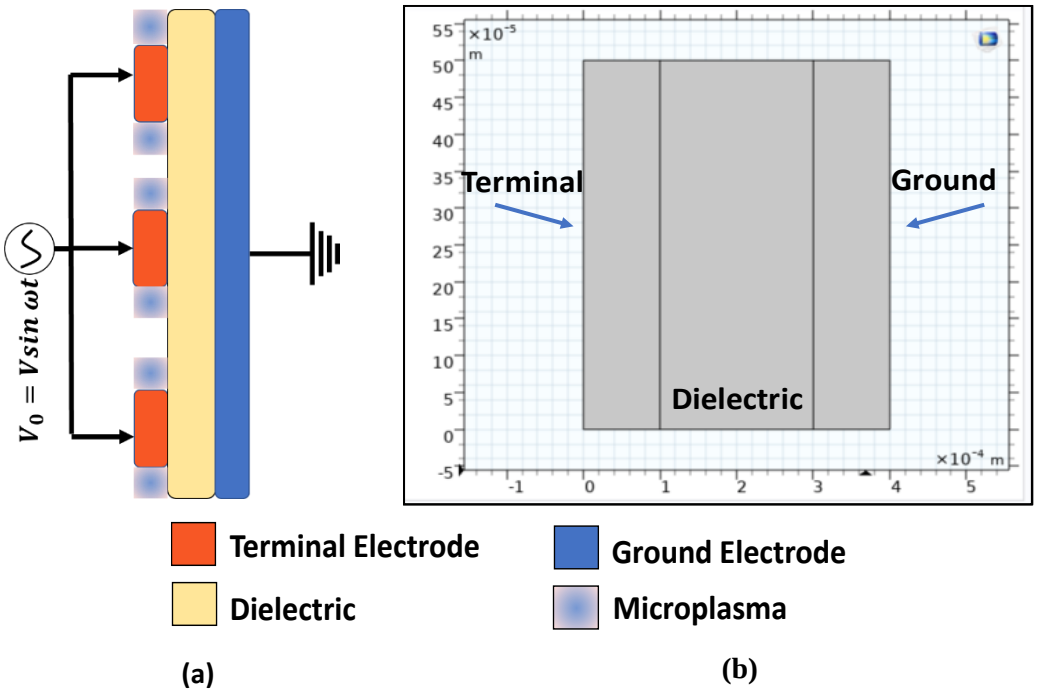

Figure 3.1: (a) Schematic of the simplified surface DBD and (b) cross-sectional view of DBD model in COMSOL simulation software.

simplified DBD based microplasma discharge (side-view) and its two-dimensional model (cross-sectional view) created in COMSOL Multiphysics® software along with their different layers is shown in Fig. 3.1(a) and (b), respectively. Simulation were performed utilizing the Plasma (plas) module in COMSOL Multiphysics®. This program couples the drift diffusion, heavy species transport, and electrostatics interfaces into an integrated multiphysics interface to model plasma discharges. The model consists of two copper electrodes (ground and terminal electrode) and a polyimide based dielectric medium. In a surface based DBD, the thickness of the dielectric between the two electrodes is also referred as the gap distance [459, 460]. The electrodes were separated from each other with a gap distance comprised of a dielectric such as polyimide and a sinusoidal voltage was applied to the terminal electrode [459]. The applied voltage should be high enough to cause ionization of the discharge medium of argon (Ar). Argon gas was chosen as the

discharge medium for its smaller reaction model and slower gas phase chemistry. This enables faster computational times, thereby allowing vast parametric studies [461]. The free electrons across the electrodes accelerate and acquire higher potential which leads to an electron avalanche, increasing the number of free electrons. The free electrons and the ionized charge species move across the electrode gap to the opposite electrode potential [447]. This process of charge accumulation is temporary and when the electric field potential is reversed, the process reverses in the opposite direction and repeats as long as the sinusoidal voltage is applied.

The operating principle of microplasma is based on Paschen's Law which states that the breakdown voltage (V_B) of an MDD is a function of the ambient pressure (p) (Pa) and electrode gap distance (d) [307, 462]. The relation between V_B and p is given by Eq. (1) [307, 462].

$$V_B = \frac{Bpd}{\ln(Apd) - \ln\left[\ln\left(1+\frac{1}{\gamma_{se}}\right)\right]} \tag{1}$$

where A is the ionization saturation constant, B is the excitation and ionization energy constant, and γ_{se} is the coefficient of secondary electronic emission. Using Paschen's Law, the breakdown voltage for microplasma discharge can be calculated. The breakdown voltage and electrode gap distance are some of the most important parameters for an optimized electrode configuration. For high pd values the applied V_B is directly proportional to d [463]. Therefore, if d increases, the V_B required to dissociate the electrons of the ambient gas (in this work, Ar gas) also increases. A surface based DBD can also be related to a parallel electrode configuration. From the fundamental laws of electromagnetics, the relation between electric field and electrode gap distance is given by [464]:

$$E = \frac{V}{d} \tag{2}$$

where, E is the electric field and V is the potential difference between the parallel conductive plates. When the applied voltage (V) at the terminal electrode is kept constant, it can be derived that E is inversely potential to d. Therefore, if the electrode gap distance increases, the electric field across the two parallel plates will decrease and vice versa. This will affect the electron drift velocity (v_d) and from the fundamental laws for μ_e in electric field [464]:

$$v_d = \mu_e E \tag{3}$$

where, μ_e is the electron mobility. Therefore, v_d is directly proportional to E. According to kinetic theory of gases, the relationship between the v_d and electron temperature T_e is given by [465]:

$$v_d = \left(\frac{8k_b T_e}{\pi m_e}\right)^{\frac{1}{2}} \tag{4}$$

where, k_b is the Boltzmann constant and me is the electron mass. According to Maxwellian electron energy distribution function the effect of T_e on the electron density (n_e) and electron energy density ($n_\mathcal{E}$) is given by [466]:

$$T_e = \frac{2}{3}\left(\frac{n_\varepsilon}{n_e}\right) \tag{5}$$

therefore, n_e is inversely proportional to T_e and $n_\mathcal{E}$ is directly proportional to T_e. The T_e must be several orders of magnitude greater than the gas temperature in the discharge medium to be classified as non-equilibrium plasma discharge to maintain lower surface temperature [321]. Therefore, n_e is inversely proportional to T_e if $n_\mathcal{E}$ is constant. It can also be inferred that for a constant applied voltage, T_e is inversely proportional to the electrode gap distance (d) (distance between the terminal and ground electrode). This reduction in T_e will inhibit the microplasma discharge of the device. Similarly, the electrode thickness is also an important design parameter

for microplasma discharge. The relation between T_e and electrode layer thickness (d_s) is given by [467]:

$$T_e = C_1 v_d p d_s \tag{6}$$

Therefore, the electrode layer thickness (d_s) is directly proportional to T_e. The gap distance between the two electrodes and electrode thickness should be optimized for a lower breakdown voltage allowing for greater operating range of the MDD. If the electrode gap distance is not optimized, it would result in low T_e, rendering the MDD ineffective.

Constituent equations from the Drift Diffusion Model (DDM) in COMSOL Multiphysics® used for determining the n_e for microplasma discharge is mathematically calculated using Eq. (7) [468].

$$\frac{\partial}{\partial t}(n_e) + \nabla \cdot \Gamma_e = R_e \tag{7}$$

where,

$$\Gamma_e = -(\mu_e \bullet E) n_e - \nabla D_e n_e \tag{8}$$

and, n_e denotes the n_e ($1/m^3$), R_e is the electron rate expression ($1/(m^3 \cdot s)$), μ_e is the electron mobility which is either a scalar or tensor ($m^2/(V \cdot s)$), E is the electric field (V/m), D_e is the electron diffusivity coefficient (m^2/s), and $-(\mu_e \bullet \vec{E})$ ne and $-\nabla \vec{D}_e$ ne represents the effect of electric field on electron drift and electron diffusion between high to low n_e , respectively. The effect of n_e and the electric field, for varying input voltages across the two electrodes were simulated and investigated. The electric field across the MDD is also a crucial parameter for uniform microplasma discharge. The generation of the reactive species is dependent on n_e and μ_e. Non-uniform electric fields across

the MDD will result in inconsistent generation of the reactive species across the electrode, compromising the optimum performance of the MDD.

Similarly, the $n_\mathcal{E}$ was determined using Eq. (9) [468].

$$\frac{\partial}{\partial t}(n_\varepsilon) + \nabla \cdot \Gamma_\varepsilon + \vec{E}.\Gamma_e = R_\varepsilon \tag{9}$$

where,

$$\Gamma_\varepsilon = -(\mu_\varepsilon \bullet E)n_\varepsilon - \nabla D_\varepsilon n_\varepsilon \tag{10}$$

and, n_ε denotes the $n_\mathcal{E}$ (V/m^3), $R\varepsilon$ is the energy gain/loss (V/(m^3·s)), μ_ε is the electron energy mobility which is either a scalar or tensor (m^2/(V·s)), E is the electric field (V/m), and D_ε is the electron energy diffusivity (m^2/s), -(μ_ε•$\vec{E}$) nε and - ∇ $\vec{D}_\varepsilon$ n_ε represents the effect of electric energy on electron drift and electron diffusion between high to low electron energy density, respectively and $\vec{E}.\Gamma_e$ represents the effect of external electric field on heating of electrons, where the heating can be a form of source or sink. Electrons are lost to the dielectric wall due to random motion within a few mean free paths of the wall, and are gained later due to secondary emission effects, resulting in the following boundary condition for the electron flux [468]:

$$n.\Gamma_e = \left(\frac{1}{2}v_e, n_e\right) - \sum_p \gamma_p(\Gamma_p.n) \tag{11}$$

and the electron energy flux is given as [468]:

$$n.\Gamma_\varepsilon = \left(\frac{5}{6}v_e, n_\varepsilon\right) - \sum_p \varepsilon_p\gamma_p(\Gamma_p.n) \tag{12}$$

The second term on the right side of Eq. 11 is the gain of electrons due to secondary emission effects where γ_p is the secondary emission coefficient. The second term in Eq. 12 is the secondary emission energy flux, where ε_p is the mean energy of the secondary electrons.

Table 3.1. The reactions of electron impact with active species of argon.

Reaction	Formula	Type	ΔE (eV)
R1	$e^- + Ar \rightarrow e^- + Ar$	Elastic Scattering	m/M = 0.136e-4
R2	$e^- + Ar \rightarrow e^- + Ar^*$	Excitation	11.50
R3	$e^- + Ar \rightarrow e^- + Ar^*$	Superelastic	-11.50
R4	$e^- + Ar \rightarrow 2e^- + Ar^+$	Ionization	15.80
R5	$e^- + Ar^* \rightarrow 2e^- + Ar^+$	Ionization	4.27

Table 3.2. Reactions between the atoms and molecules with its reaction rates.

Reaction	Formula	Rate (m^3/s.mol)
R6	$Ar^* + Ar^* \rightarrow e^- + Ar + Ar^+$	3.3734e8
R7	$Ar^* + Ar \rightarrow Ar + Ar$	1807

Using the classical kinetic theory, μ_e is dependent on the change in ambient temperature (T_a) and is mathematically given by Eq. (13) [469].

$$\mu_e N = \frac{4}{3} \frac{e}{(2\pi m)^{\frac{1}{2}} (k_B T_a)^{\frac{5}{2}}} \int_0^{\infty} \left(\frac{\varepsilon}{\sigma_{mt}(\varepsilon)} \right) e^{-\left(\frac{\varepsilon}{k_B T_a}\right)} d\,\varepsilon \tag{13}$$

where, N is the gas density, σ_{mt} is the electron-atom momentum transfer scattering cross section, m and e are the electron mass and charge respectively, k_B is the Boltzmann's constant. Also, as per the ideal gas law [470], since T_a and N are dependent on p, it can be inferred that a change in ambient conditions (pressure or temperature) should affect μ_e and n_e.

The reactions due to electron impact inside the gas gap are given in Table 3.1 and Table 3.2. The reactions of electron impact with active species of Ar including: metastable argon (Ars), Ar molecule and singly ionized Ar molecule (Ar^+) are depicted in Table 3.1 [307, 462]. In Table 3.2, the reaction rates for Ar atoms and molecules along with their corresponding two-body reaction are also given [307, 462, 464]. The surface reactions are also given in Table 3.3. The

Table 3.3. Surface reactions.

Reaction	Formula	Sticking Coefficient
R8	$Ar^+ \rightarrow Ar$	1
R9	$Ar^* \rightarrow Ar$	1

initial electron density (ε_0) was considered as 10^6 and the mean electron energy was considered as 4 eV. The ambient temperature and pressure were kept constant at 300 K and 1 atm, respectively: when simulating for voltage distribution, T_e and n_e for varying electrode and dielectric thickness.

3.3 Simulation Results

Surface microplasma discharges produce reactive species of gas molecules, which induce the electroporation effect. This causes DNA mutation, inhibits DNA repair and enzyme activities, resulting in cellular death and is responsible for the pathogenic microbial inactivation [471-479]. To achieve the electroporation effect, the applied voltage to the MDD is an important parameter and the voltage distribution across the device should be uniform for effective destruction of pathogenic microorganisms. To obtain uniform voltage distribution across electrodes, the design

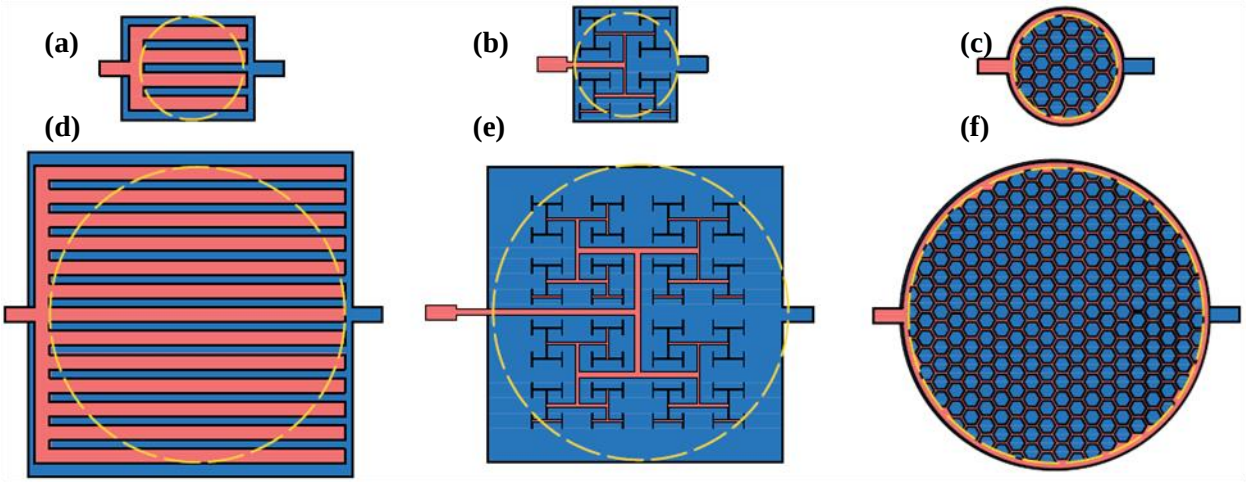

Figure 3.2: Comb (a)(b), H-tree (c)(d), and honeycomb (e)(f) structured microplasma discharge device for 35 mm and 100 mm diameter standard petri dish, respectively. (The doted yellow circle represents the petri dish perimeter and all images are not to scale)

of electrodes is crucial when fabricating the MDD. Non-uniform voltage distribution across the device can result in ineffective sterilization. A case study of three different electrode structures was performed, to investigate the voltage distribution across electrode. A schematic of the comb, H-tree and honeycomb structured MDD for 35 mm and 100 mm diameter petri dish is shown in Fig. 3.2. The red dotted circle indicates the perimeter of the petri dishes, to illustrate the coverage of each designed MDD.

A 2D simulation in FEA software COMSOL Multiphysics®, was performed using the magnetic and electric field modules. An input voltage of 2000 V at 20 kHz was applied to the terminal electrode and the voltage distribution across the different electrode designs to sterilize the surface of 35 mm and 100 mm petri dishes was simulated and is shown in Fig. 3.3. It was observed that, for a comb structured MDD (Fig. 3.3 (a), (b)), the voltage gradually dropped towards the comb tips by ~15%. If the voltage across the comb structured device decreases then it will affect the microplasma discharge leading to non-uniform microplasma discharge. Such non-uniform voltage distribution will ultimately affect the formation of reactive species throughout the surface of the device, causing ineffective sterilization. However, the voltage distribution on the terminal

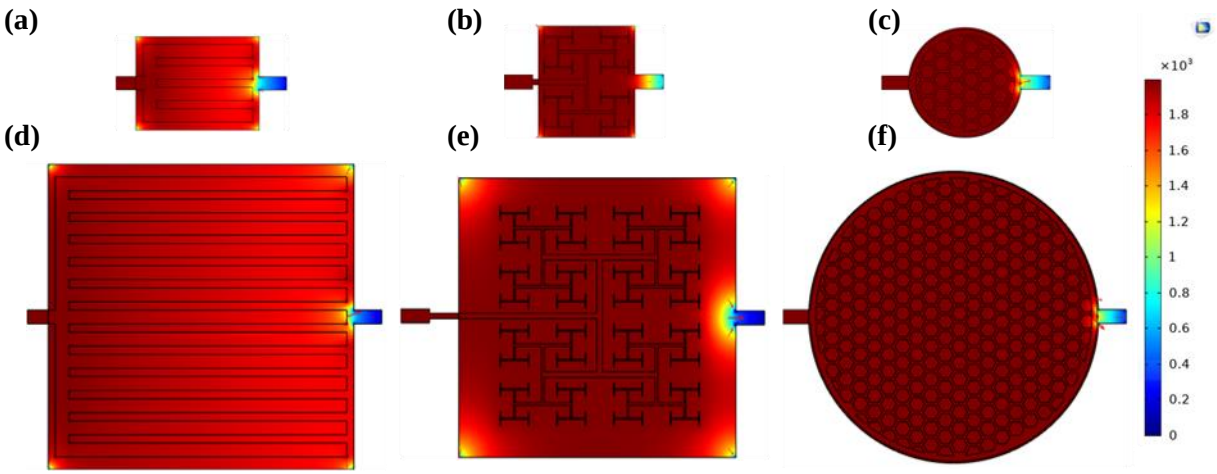

Figure 3.3: Simulated voltage distribution across the comb (a)(b), H-tree (c)(d), and honeycomb structured (e)(f) electrodes for 35 mm and 100 mm diameter petri dish, respectively. (all images are not to scale)

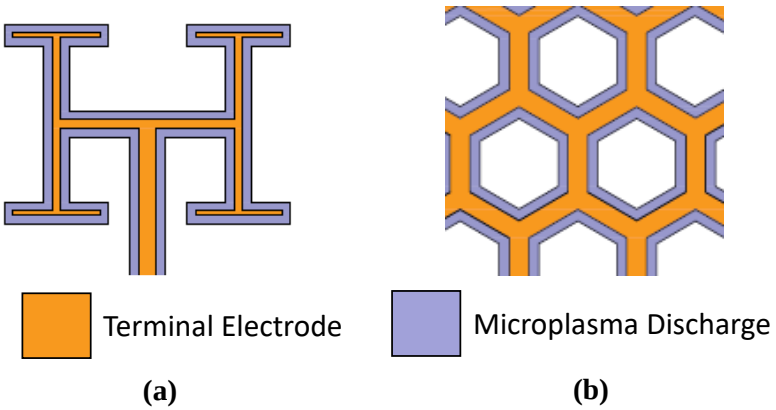

Figure 3.4: Illustration of microplasma discharge coverage for (a) H-tree and (b) Honeycomb structured MDD.

electrode was uniform for the H-tree (Fig. 3.3 (c), (d)) and honeycomb device (Fig. 3.3 (e), (f)), with minimal drop (<0.5%) in voltage towards the ground terminal. This results in uniform electric field distribution and leads to uniform microplasma discharge throughout the surface of the devices. The voltage distribution across the H-tree structured device was very similar to honeycomb, however, the coverage of the microplasma discharge was very different for both the designs. Considering 0.5 mm (Fig. 3.4) thick/wide microplasma spread across the terminal electrode, for 35 mm diameter petri dish, it was calculated that the H-tree structured device has ~12% greater coverage in microplasma discharge as compared to the honeycomb device. However, when the MDD was scaled for 100 mm diameter petri dish, the honeycomb device has ~55% greater coverage of microplasma discharge as compared to the H-tree device. Therefore, the honeycomb structured MDD not only has uniform voltage distribution across the terminal electrode, but it also improves the scalability over the H-tree patterned MDD and provides relatively large microplasma discharge area.

The input sinusoidal voltage at the terminal electrode was varied from 1500 V to 3500 V in steps of 500 V, and its effect on n_e and T_e was investigated. Electric potential distribution across the terminal electrode, dielectric and ground electrode for 1500 V and 3500 V is shown in

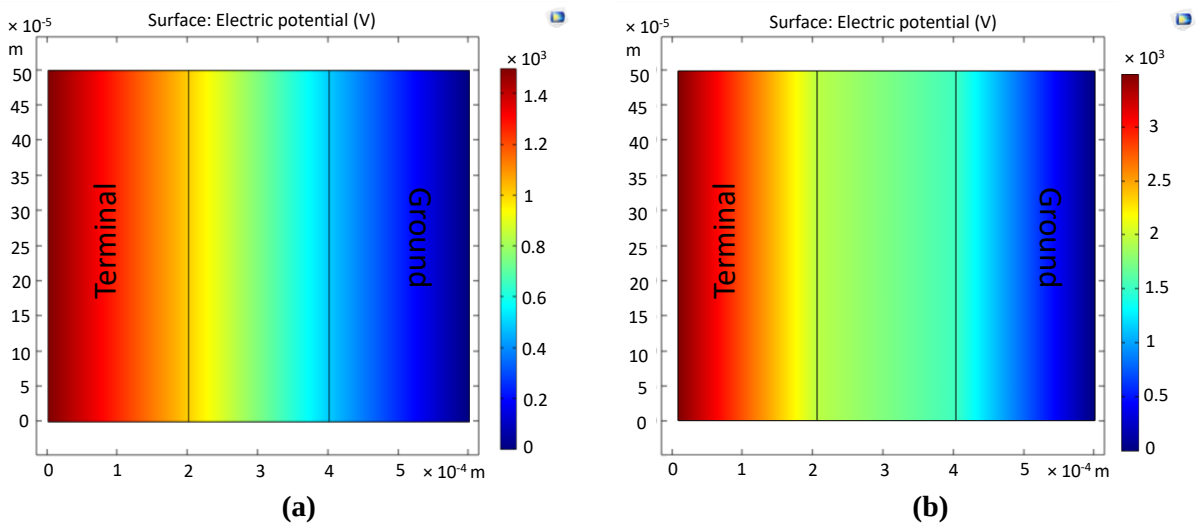

Figure 3.5: The electric voltage distribution across the layers for an input terminal voltage of (a) 1500 V, (b) 3500 V.

Fig. 3.5 (a) and (b) respectively. The thickness of the electrodes and dielectric was considered as 200 µm and the voltage distribution across the electrodes was simulated under ambient atmospheric temperature (300 K) and pressure (1 atm). For varying voltages of 1500 V, 2000 V, 2500 V, 3000 V and 3500 V, the maximum T_e decreased to 4.39 eV, 4.28 eV, 4.20 eV, 4.13 eV and 4.08 eV, respectively. Similarly, the maximum n_e per cubic meter increased to 1.21×10^{13}, 1.05×10^{14}, 1.35×10^{14}, 1.68×10^{14} and 2.01×10^{14} when the input sinusoidal voltage at terminal electrode was varied from 1500 V to 3500 V, respectively. From Fig. 3.6, it was observed that the T_e is inversely proportional to the n_e (also evident from Eq. 5). In addition, the breakdown voltage

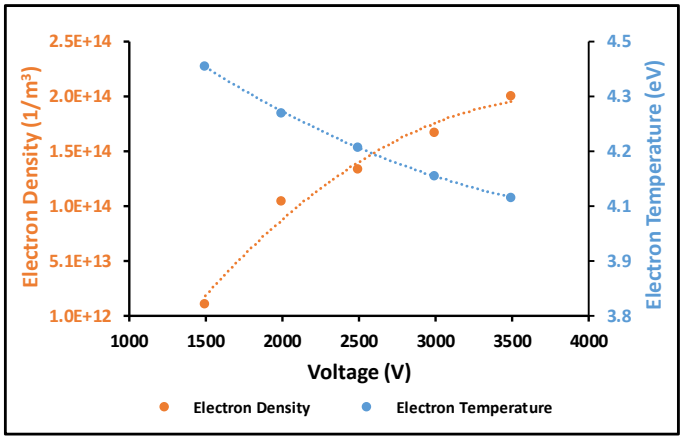

Figure 3.6: Influence of varying input voltage on electron density and temperature.

for 200 µm dielectric was observed at approximately 2000 V. If the voltage distribution across the electrodes is uniform and above the breakdown voltage (2000 V) of the dielectric layer, uniform microplasma can be generated across the surface of MDD.

The effect of varying dielectric thickness on T_e and ne was investigated. The dielectric thickness was varied from 100 µm to 300 µm in steps of 50 µm with an input sinusoidal voltage of 2000 V at the terminal electrode under ambient atmospheric temperature (300 K) and pressure (1 atm). The simulation results of T_e and ne distribution for 100 µm and 300 µm thick dielectric

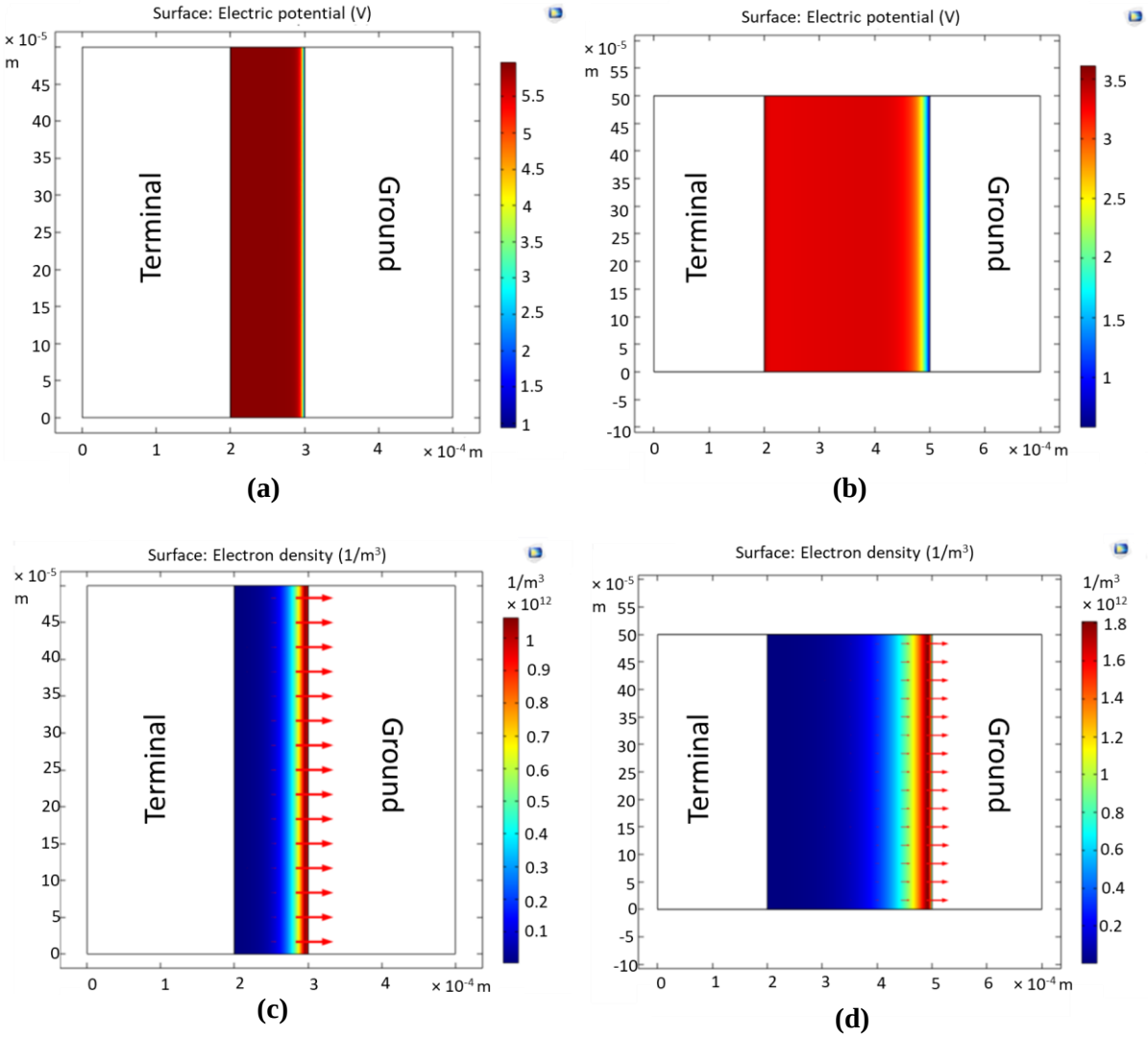

Figure 3.7: The electron temperature and density distribution across (a,b) 100 µm and (c,d) 300 µm thick dielectric where arrows indicates the direction of electron flux towards the ground electrode.

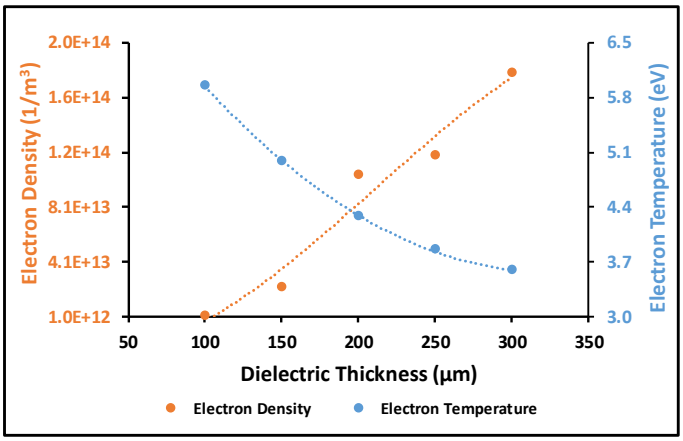

Figure 3.8: Influence of dielectric thickness on electron density and temperature.

along with direction of the electron flux is shown in Fig. 3.7 (a-d), and the results are plotted in Fig. 3.8, respectively. For dielectric thickness of 100 µm, 150 µm, 200 µm, 250 µm and 300 µm, the maximum T_e decreased to 5.95 eV, 4.99 eV, 4.28 eV, 3.86 eV and 3.59 eV, respectively. Similarly, n_e increased to 0.01×10^{14}, 0.22×10^{14}, 1.04×10^{14}, 1.19×10^{14} and 1.79×10^{14} when the dielectric thickness increased from 100 µm to 300 µm, in steps of 50 µm, respectively. From Eq. 2, it is inferred that for a constant voltage at the terminal electrode, the dielectric thickness of a device is inversely proportional to the electric field. The electric field is directly proportional to the drift velocity of the electrons (from Eq. 3). The drift velocity in turn is proportional to the square root of T_e (from Eq. 4). Correlating Eq. 2-5, it can be deduced that the electrode gap distance is inversely proportional to T_e and directly proportional to n_e (from Eq. 5). Therefore, to achieve similar levels of plasma discharge for increased dielectric thickness, a higher voltage needs to be applied at the terminal electrode to increase T_e. However, if the input voltage is kept constant as the dielectric thickness increases, then the voltage at the terminal electrode will not be enough to breakdown and dissociate the discharge media, thereby limiting the generation of microplasma.

Similarly, the effect of varying electrode thickness (increased from 100 µm to 300 µm in steps of 50 µm) on T_e and n_e was investigated with an input sinusoidal voltage of 2000 V at the

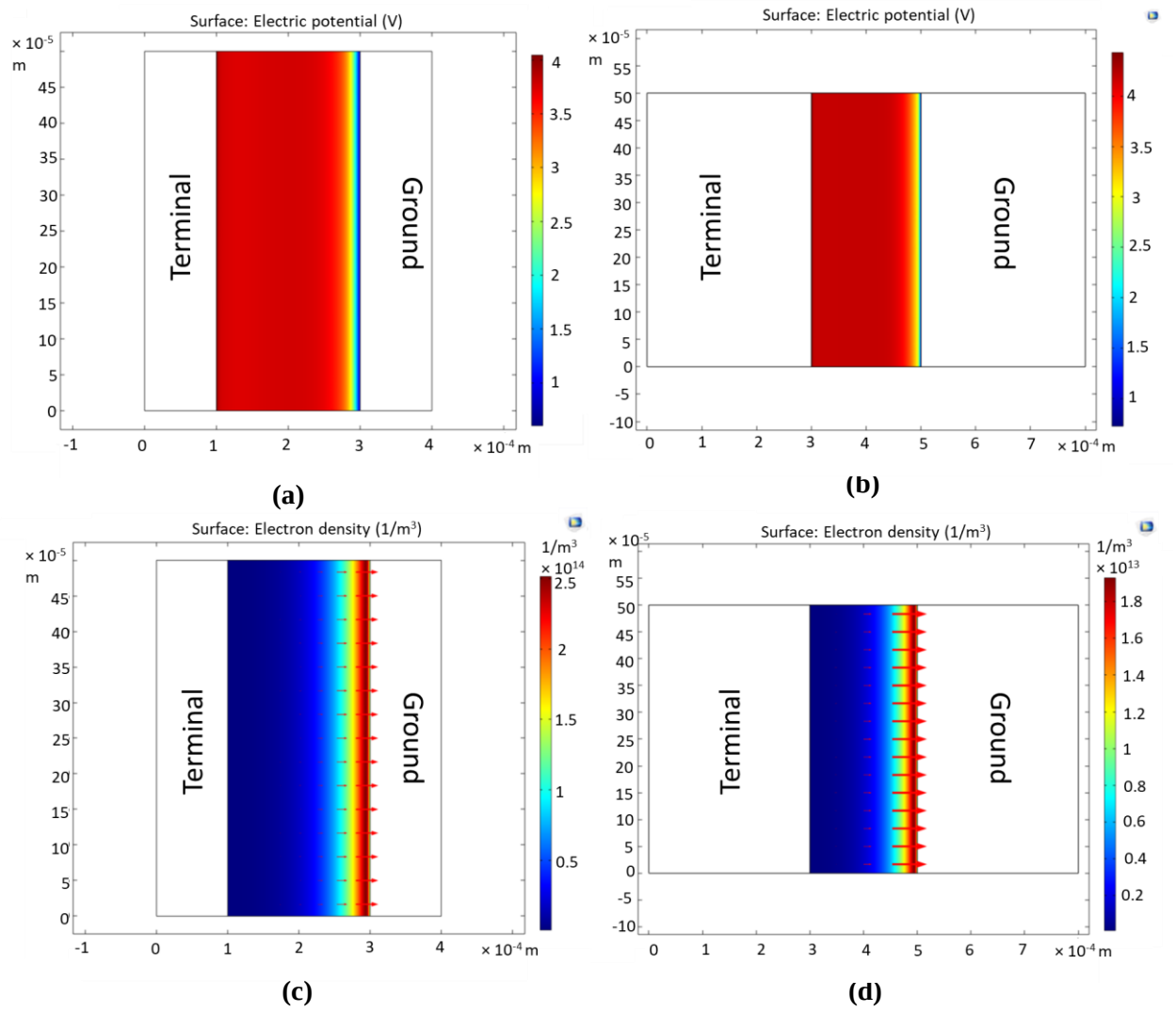

Figure 3.9: The electron temperature and density distribution across (a,b) 100 µm and (c,d) 300 µm thick electrodes where arrows indicates the direction of electron flux towards the ground electrode.

terminal electrode under a temperature of 300 K and a pressure of 1 atm (Fig. 3.9 (a-d)). For increasing electrode thickness of 100 µm, 150 µm, 200 µm, 250 µm and 300 µm, the maximum T_e increased to 4.06 eV, 4.19 eV, 4.28 eV, 4.35 eV and 4.41 eV, respectively. Similarly, n_e increased to $2.28 \times 1014\ m^{-3}$, $1.23 \times 1014\ m^{-3}$, $1.04 \times 1014\ m^{-3}$, $0.74 \times 1014\ m^{-3}$ and $0.11 \times 1014\ m^{-3}$ when the dielectric thickness increased 100 µm to 300 µm. From Eq. 6, and from the results shown in Fig. 3.10 it is inferred that the T_e is directly proportional to the electrode thickness and, n_e is inversely proportional to the electrode thickness. If the electrode is too thick,

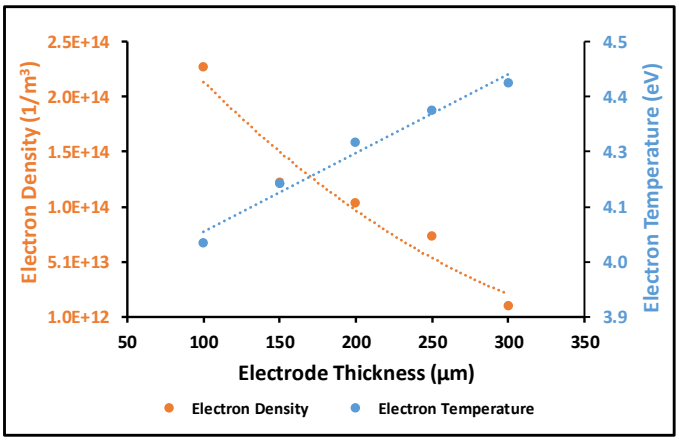

Figure 3.10: Influence of electrode thickness on electron density and temperature.

the voltage drop across the electrode will be higher and this will result in lower input voltages (increasing the breakdown voltage in the discharge medium) across the dielectric. Therefore, the choice of electrode thickness is an important parameter for microplasma discharge.

In Fig. 3.11, the effect of varying ambient temperature on n_e and μ_e is shown. The electrode and dielectric thickness were fixed at 200 µm with an input sinusoidal voltage of 2000 V at the terminal electrode. It was observed that the n_e and μ_e were varied from 2.03×1014 m^{-3} to 4.54×10^{13} m^{-3} and 0.14 [m^2/(V.s)] to 0.19 [m^2/(V.s)], respectively, as the ambient temperature increased from 250 K to 350 K, in steps of 25 K at a constant ambient pressure (1 atm). This corresponds to a 78% and 50% change in the n_e and μ_e, respectively. As the atmospheric

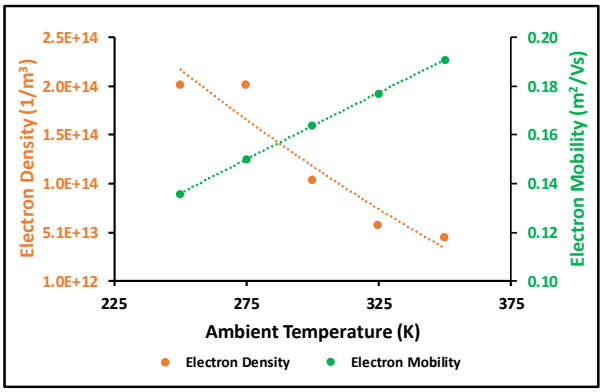

Figure 3.11: Influence of varying ambient temperature on electron mobility and electron temperature

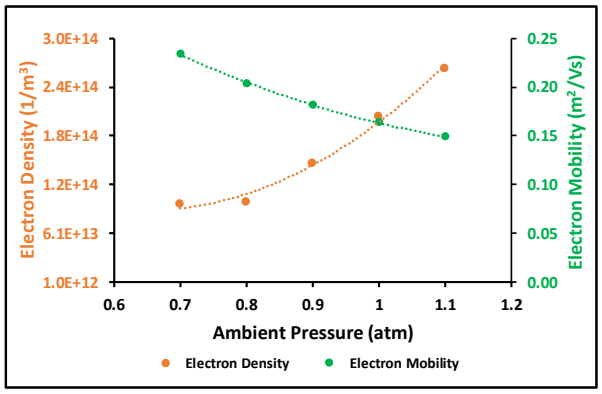

Figure 3.12: Influence of varying ambient pressure on electron mobility and electron temperature

temperature decreases, the μ_e decreases and n_e increases, thereby decreasing the T_e and vice-versa (as per Eq. 5). Therefore, at lower ambient temperature, the input voltage supply must be increased to maintain constant T_e [480]. Similarly, in Fig. 3.12, the effect of varying ambient pressure on n_e and μ_e is shown. The electrode and dielectric thickness were fixed at µm with an input sinusoidal voltage of 2000 V at the terminal electrode. It was observed that the n_e and μ_e varied from 9.64×10^{13} m^{-3} to 2.64×10^{14} m^{-3} and 0.23 [m^2/(V.s)] to 0.15 [m^2/(V.s)], respectively, as the ambient temperature increased from 0.7 atm to 1.1 atm, in steps of 0.1 atm at a constant ambient temperature (300 K). This corresponds to a 174% and 36% change in n_e and μ_e, respectively. The results indicate that the n_e is inversely proportional to the μ_e for varying atmospheric pressure conditions. When the atmospheric pressure increases, the μ_e reduces, thereby reducing the T_e (as per Eq. 3 and 4). To maintain the T_e constant, the input voltage can be increased, which would also increase the collisional energy transfer between electrons and background gas [481, 482]. Therefore, it can be concluded that the change in the n_e and μ_e due to variations in the ambient conditions will have a direct effect on the microplasma discharge, influencing the sterilization efficacy of the MDD towards harmful pathogens.

3.4 Summary

In this work, an MDD was successfully modelled and simulated using FEA in COMSOL Multiphysics® simulation software. Initially, the voltage distribution across comb, H-tree and honeycomb structured MDDs were analyzed to find the optimum design for microplasma discharge. The results indicate that the honeycomb structured MDD provides uniform voltage distribution and relatively larger microplasma coverage as compared to comb and H-tree structured MDDs. The cross-section of a MDD was modelled in an Ar environment with a polyimide dielectric sandwiched between two copper electrodes. Simulations were performed to investigate the n_e and electric field distribution for AC terminal voltages ranging from 1500 V to 3500 V with a constant dielectric and electrode thickness of 200 µm. Then, the effect of varying dielectric and electrode thickness parameters on n_e and temperature was investigated. As the dielectric thickness was increased from 100 to 300 µm the T_e decreased by almost 40%. The results indicate that, it is necessary to have a thinner dielectric between the two copper electrodes for lower breakdown voltage and effective microplasma discharge. The varying electrode thickness from 100 to 300 µm resulted in a 9% increase of T_e. This was because T_e is directly proportional to the electrode thickness. The results from the two-dimensional modelling indicate that electrode configuration is an important parameter to optimize for fabricating MDDs. For light weight and wearable applications, it is essential to have thinner electrode and dielectric such that the device is flexible and conformal enough. Finally, the effect of varying ambient temperature and pressure on n_e and the mobility of the MDD was studied. A variation of 78% and 50% change in n_e and μ_e was obtained as the ambient temperature was increased from 240 K to 360 K at constant ambient pressure (1 atm), respectively. A variation of 174% and 36% change in n_e and μ_e was obtained as the ambient pressure increased from 0.7 atm to 1.1 atm at constant ambient temperature (300 K),

respectively. It was observed that a change in n_e and μ_e will affect the microplasma discharge which in turn can affect the sterilizing efficacy of the MDD. Therefore, further research includes developing an adaptive system such that the input voltage can be changed depending on the varying ambient conditions to generate a consistent microplasma discharge. The system will be developed and tested, to sterilize surfaces from harmful Gram-negative and Gram-positive bacteria such as *Escherichia coli*, *Pseudomonas aeruginosa*, *Staphylococcus aureus* and *Bacillus subtilis*.

CHAPTER IV

IN-VITRO ANALYSIS OF THIN-FILM MICROPLASMA DISCHARGE DEVICES FOR SURFACE STERILIZATION AND INACTIVATING BACTERIA SUSPENDED IN LIQUID MEDIA

4.1 Introduction

Disinfection and sanitization are processes of eliminating pathogenic microorganisms (such as bacteria, viruses, and fungi) on solid surfaces or in fluid media. Surgical site infections (SSI) are most common among all hospital-acquired infections as per World Health Organization (WHO), and many of such SSIs are caused by antibiotic-resistant bacteria [483, 484]. In the United States alone, there are approximately 46.5 million surgical and invasive medical procedures performed every year and almost 300,000 patients are reported to be affected with SSIs, at estimated costs of $3.5-10 billion a year. Health-care facilities must adhere to strict guidelines and protocols to reduce the risk of transmissions of pathogenic microorganisms [221, 485]. There are multiple meta-analysis data available on the SSIs. A meta-analysis published in "New England Journal of Medicine" has concluded that 25% of patients had one or more health care–associated infections (survey includes 183 hospitals and 11,282 patients). Another meta-analysis published in "American Journal of Infection Control" concluded that the SSIs resulted in approximately 1 million additional inpatient-days [486]. Based on the analytical data and the recent increase in pandemic outbreaks, it is clearly evident that there is an urgent need to address the SSIs to improve the health condition of patients and to reduce the burden on the health-care facilities.

According to the World Health Organization (WHO), over 2 billion people consume contaminated drinking water with potentially pathogenic microorganisms, and almost half a

million people die due to various diarrheal diseases each year worldwide [487]. Some of the most common methods for disinfecting drinking water are chemical treatment (adding chemicals such as chlorine, iodine and potassium permanganate), heat treatment and exposing water to ultraviolet (UV) light [488]. Among the chemical treatments, chlorination of drinking water is the most common disinfection method in public facilities [488, 265]. However, excessive addition of chlorine poses a health risk, potentially leading to eye and skin irritation, difficulty in breathing and sore throat [265, 489]. In addition, addition of chlorine adds undesirable bleach taste and odor to the water. The heat treatment or boiling of water to a high temperature of 100 °C is simple and effective for small volumes of water. However, application of heat treatment to large volumes is not effective and economically feasible. An alternate method, UV radiation, has been gaining attention lately for water disinfecting applications and has several advantages when compared to chemical and heat-based disinfection methods [490, 491]. UV-based disinfection devices operate in ambient conditions, utilize no chemicals, and have no discharge byproducts (DBPs) [490]. Research has shown that disinfection efficacy against various bacteria is dependent on the wavelength of the UV light source [183]. Commercial based UV lamps operate at a single wavelength, thereby limiting it efficacy for disinfecting a large variety of bacteria [492]. Microplasma based UV radiation, which provides a wide range of UV wavelengths, is an emerging field of non-thermal plasma technology that can alleviate the disadvantages and shortcomings of water disinfection methods currently in use [184-187, 413].

Escherichia coli and *Pseudomonas aeruginosa* are some of the common bacterial organisms associated with the SSIs [493]. *E. coli* is a Gram-negative bio-safety level 1 bacterium commonly found in the environment, food and lower intestines of humans and animals. Although most strains of *E. coli* are harmless, there are some pathogenic strains that can cause diarrhea,

urinary tract infections, respiratory illnesses and pneumonia [494]. According to the Centers of Disease and Control (CDC), 5-10 % of people diagnosed with severe infections by Shiga-toxin producing *E. coli* can suffer from potentially life-threatening complications [494]. It is important to treat and sterilize surfaces of various materials and textures for better prevention of pathogenic bacterial contamination. *P. aeruginosa* is a Gram-negative ubiquitous, rod-shaped bacterium that can infect patients in hospital environment, especially patients with wounds from surgery or burns [495, 496]. *P. aeruginosa* is classified as a multidrug resistant biosafety level 2 pathogen. According to a report published in 2017 by CDC, there have been around 32,600 cases and 2,700 deaths reported with *P. aeruginosa* related infections in the hospitalized patients, especially those that suffer from weakened immune systems or chronic lung diseases [497, 498]. The transmission of antibiotic resistant pathogens occurs from person-to-person contact via hands, equipment and surface touching or from the patient's own microbiota [497, 498].

S. aureus is a non-spore forming, facultative anaerobic Gram-positive bacterium. It is estimated that 30% of the entire human population are asymptomatic carriers of *S. aureus*, which can be associated with skin infections [499]. Nevertheless, it can be a fatal risk to immune compromised individuals, especially in healthcare settings [499, 500]. *B. subtilis* is a strictly aerobic, spore forming Gram-positive bacterium that is commonly found in soil, air, and water [501]. *B. subtilis* has been extensively used in agriculture for its antibacterial and disease-preventing effects on crops, thereby protecting the plants from pathogenic microorganisms [502, 503]. *B. subtilis* is considered a benign organism as it does not possess any traits that can cause disease [501]. Nevertheless, in a few cases, *B. subtilis* was identified causing infections such as bacteremia, pneumonia, endocarditis, and septicemia in patients with compromised immunity [501]. In this work, *B. subtilis* was also used to demonstrate the capability of MDD towards spore-

Table 4.1: Characteristics of the bacteria used in this research.

Bacteria	Gram Type	Morphology	Growth Condition	Biosafety Level	Transmission and Occurrence	Infection Symptoms
Escherichia coli	Negative	Rod	Facultative anaerobic	1/2	Direct contact, consumption of contaminated food, gastrointestinal tract	Stomach cramps, diarrhea, and vomiting
Pseudomonas aeruginosa	Negative	Rod	Strict aerobic	2	Direct contact, moist environment and healthcare facilities	Pneumonia, ear, eye, wound and urinary tract infections
Staphylococcus aureus	Positive	Spherical	Facultative anaerobic	1/2	Direct contact, person-to-person skin contact	Abscess, cellulitis, bacteremia, pneumonia
Bacillus Subtilis	Positive	Rod	Strict aerobic	1	Direct contact, soil and gastrointestinal tract	Stomach cramps, diarrhea, and vomiting

forming cells such as *B. subtilis*. A summary of the bacteria used in this research and some of its characteristics are provided in Table 4.1. Current methods of inactivating such types of bacteria include thermal and chemical treatments which often require toxic chemicals, involve high temperatures or bulky equipment [504-510]. There is a need to develop MDD's that are flexible and operate at ambient temperatures for inactivating bacteria.

Some of the most common methods for disinfecting drinking water are chemical treatment (adding chemicals such as chlorine, iodine and potassium permanganate), heat treatment and exposing water to UV light [511]. Among the chemical treatments, chlorination of drinking water is the most common disinfection method in public facilities [265, 511]. However, excessive addition of chlorine poses a health risk, potentially leading to eye and skin irritation, difficulty in breathing and sore throat [265, 512]. In addition, addition of chlorine adds undesirable bleach taste and odor to the water. The heat treatment or boiling of water to a high temperature of 100 °C is simple and effective for small volumes of water. However, application of heat treatment to large volumes is not effective and economically feasible. An alternate method, UV radiation, has been gaining attention lately for water disinfecting applications and has several advantages when compared to chemical and heat-based disinfection methods [269, 266]. UV-based disinfection

devices operate in ambient conditions, utilize no chemicals, and have no discharge byproducts [269]. Research has shown that disinfection efficacy against various bacteria is dependent on the wavelength of the UV light source [183]. Commercial based UV lamps operate at a single wavelength, thereby limiting it efficacy for disinfecting a large variety of bacteria [184]. Microplasma based UV radiation, which provides a wide range of UV wavelengths, is an emerging field of NTP technology that can alleviate the disadvantages and shortcomings of water disinfection methods currently in use [184, 187, 413].

There has been an increase in focus of research involving microplasma discharge devices (MDD) for applications in biomedical, food, and environmental industries [513, 514]. Surface sterilization of food processing surfaces and use of microplasma as an antiseptic on human skin are one of the most promising applications of MDDs [515-519]. Although the food industry has been focused on eliminating microbial organisms [518, 519], the biomedical industry has been focused on alleviating healthcare associated infections (HAIs) of surgical and burn wounds [182, 423-425, 520]. However, the current microplasma generation devices are rigid and not conformable which is a crucial factor while decontaminating either wounds or food products.

The generation of uniform microplasma across the surface electrode is dependent on the uniform voltage distribution [427, 428, 429]. To compensate for non-uniform microplasma discharges, high input voltages are applied across the electrodes. This can be avoided by designing and optimizing the electrode design for uniform voltage to generate uniform microplasma discharge. Such optimized electrode design can be utilized to generate the uniform electrons and excited gaseous species required to inactivate the pathogens [274, 415]. There are various electrode configurations such as cathode boundary layer (CBL), dielectric-barrier discharge (DBD), capillary plasma electrode discharge (CPED), micro-hollow cathode discharge (MHCD), inverted

square pyramidal (ISP) and square cross-sectional cavities (SCSC) [138]. DBD based devices were identified as the most suitable configuration for surface microplasma discharge [275, 521, 522]. DBD devices can be made scalable and designed to be geometrically flexible (planar design) unlike other configurations [275, 521, 522]. In this work, comb and honeycomb designed electrodes were employed to study the effect of electrode designs on sterilization efficacy. Comb structured electrodes were selected due to their simplicity, while honeycomb structured electrodes have a high surface area, are expected to provide uniform voltage and are highly scalable in size and area as compared to the other designs [435].

In this chapter, a flexible microplasma discharge device (MDDs) was fabricated to inactivate Gram-negative and Gram-positive bacteria using ambient air as the sterilizing agent, by two different inactivation protocols. In the first protocol, colonies of *E. coli*, *P. aeruginosa* and *B. subtilis* on agar surfaces were exposed to microplasma. The voltage distribution across the comb and honeycomb patterned MDD was simulated and analyzed. The MDDs were then fabricated using a laser ablation process and by attaching flexible copper tape electrodes on two sides of a flexible polyethylene terephthalate (PET) dielectric film. Using laser ablation, the copper tape was patterned in a comb and honeycomb design for the top electrode, and in a rectangular and circular pattern for the bottom electrodes. The sterilizing efficacy of the comb and honeycomb structured MDDs was investigated by exposing pathogenic bacteria such as *E. coli* and *P. aeruginosa* to microplasma discharge from the surface of the MDDs. Since the honeycomb structured MDD was more effective, *B. subtilis* cells were also exposed to microplasma irradiated from the honeycomb device. In the second experimental protocol, Gram-negative (*E. coli*, *P. aeruginosa*) and Gram-positive (*S. aureus*, *B. subtilis*) bacteria were suspended in liquid media and exposed to microplasma. In this experiment, the honeycomb MDD was attached to a custom fabricated

polystyrene platform to irradiate microplasma on the liquid media containing bacterial cultures. The disinfecting capability of the MDD for varying treatment times and input voltages was analyzed by exposing the bacterial cells to the microplasma discharge from the device. The power density of the device was also calculated in its flat state and then compared to power densities in a bent state subjected to a radius of curvature of 25 mm and 50 mm. The optical spectra of the microplasma radiation were captured and analyzed. Finally, the surface temperature of the MDD for varying input voltage was measured. The efficacy of the MDD towards various bacteria was investigated and analyzed in this chapter.

4.2 Protocol 1: *In-Vitro* Analysis of Thin-Film Microplasma Discharge Devices for Surface Sterilization

4.2.1. Theory and Simulation

Atmospheric NTP based medical treatment on biological surfaces such as skin tissue involves a combined effect of ultraviolet and infrared radiation, electric fields and reactive species to induce biochemical processes in the living cells and tissues. The controlled delivery of such reactive species results in altered metabolism of the target cells. Surface microplasma discharges in ambient humid air produce primary reactive species of gas molecules including electric and vibrationally excited N_2 and O_2 molecules, as well as N, O, and H atoms in ground and excited states, OH radicals, positive and negative ions, and electrons [523, 524, 525]. Reactive oxygen- and nitrogen-containing species such as NO, NO_2, O_3, HO_2, HNO_2, HNO_3, H_2O_2, are also generated when the primary species react with the ambient air molecules. The presence of such reactive species of O, N and OH radicals induce the electroporation effect that facilitates the penetration of the target cell membranes. Hence, the applied voltage to the MDD is an important parameter for the electroporation effect and thus the voltage distribution across the device should

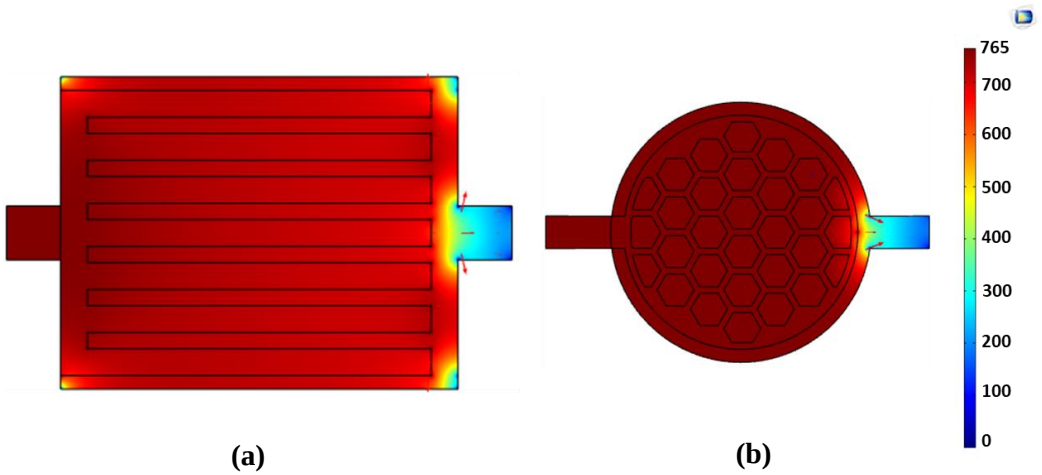

Figure 4.1: Simulated voltage distribution across (a) comb and (b) honeycomb MDD.

be uniform for effective inactivation of pathogenic microorganisms. Moreover, for uniform voltage distribution, design of electrodes is crucial and must be considered when designing the MDD. Non-uniform voltage distribution across the device can result in ineffective sterilization. Therefore, the voltage distribution across the MDD was investigated by simulating the devices shown in Fig. 4.1 in FEA software COMSOL Multiphysics®.

Voltage distribution across the MDD is crucial for uniform microplasma discharge. Therefore, MDDs representing comb and honeycomb configuration were investigated using finite element analysis (FEA) in COMSOL Multiphysics®. The simulated voltage distribution across the device is shown in Fig. 4.1. A two-dimensional (2D) simulation was performed using the magnetic and electric field modules. An AC voltage of 765 V was applied to the terminal electrode for both devices to investigate the voltage distribution across the terminal electrode of the device. The AC voltage of 765 V was chosen because in the experimental study, a maximum of 765 V AC voltage can be applied (this corresponds to 8 VDC which is the input of 5 W DC to AC converter) to the comb MDD as the total power consumption of the MDD reached 5 W. The simulation results are shown in Fig. 4.1. It was observed that, for a comb structure, the voltage gradually dropped

towards the comb tips by ~9 % (See attached supplementary section Fig. 4.15 for simulations with higher input voltages). However, the voltage distribution on the terminal electrode was uniform for the honeycomb device with minimal drop (less than 0.5 %) in voltage towards the ground terminal. Since the electric field distribution was uniform for the honeycomb, it leads to uniform formation of the reactive species throughout the surface of the honeycomb device. This characteristic of the honeycomb device is a major advantage over the comb device for achieving higher sterilizing efficacy. The sterilizing potential of the honeycomb structured electrode when compared to the comb structure MDD was investigated by performing in vitro tests on potentially pathogenic microorganisms such as *E. coli* and *P. aeruginosa*.

4.2.2 Methods

4.2.2.1 Materials

A 50 µm thick transparent PET film from DuPont Teijin Films was used as the substrate. A 4.5" wide and 2 mil thick copper conductive tape (CFT-4.5) from Bertech was utilized to fabricate the top and bottom electrodes of the MDD. A 4" wide and 2 mil thick single-sided Kapton tape (KPT2-4) from Bertech was used as the support/encapsulation layer for PET to avoid short circuit between top and bottom electrodes. High voltage alligator clips (BUU-65-2, Mueller Electric Co.) were used to connect the wires to the MDD.

4.2.2.2 Preparation of Bacteria

A liquid medium of Luria-Bertani (LB) was used to culture *E. coli* (ATCC 35353), *P. aeruginosa* (strain PAO1) and *B. subtilis* (ATCC 6051). The bacterial cultures were incubated at 37 °C for 24 hours. Serial dilutions from 10^{-1} to 10^{-10} were carried out to determine the numbers of colony forming units (CFU). The bacterial colonies were grown on LB agar medium in

petri dishes (diameter 85 mm or 55 mm; height 15 mm). The cultures of *E. coli* and *P. aeruginosa* reached a concentration of 8.85×10^9 CFU/mL cells. The agar plates with the bacteria were placed upside down on the MDDs as per standard aseptic laboratory techniques and the spread plate protocol [475]. A single colony of *B. subtilis* was inoculated into a 50 mL brain heart fusion (BHI) broth batch culture. The cultures were then placed on an orbital shaker and incubated at 28 °C. For vegetative *B. subtilis*, the culture was grown for 24 hours and to induce sporulation in *B. subtilis*, the culture was incubated on the orbital shaker for 7 days. The optical density (OD) of the cultures was then measured using a Pharmacia GeneQuant Pro spectrophotometer at a wavelength of 600 nm. The OD_{600} was adjusted to 0.241±0.006 using BHI broth to achieve cell density in the range of 10^7 cells for the one- and the seven-day old cultures of *B. subtilis*. In this protocol, bacterial cultures were pipetted on top of the agar surface and spread uniformly with a sterile spreader. (The bacteria do not fall onto the device as the bacteria cells attach to the surface of the agar media [524]. The petri dishes containing the agar are often inverted to avoid any external contamination from the ambient environment, and to avoid the falling of water droplets on the media surface during the incubation process [525]). Bacterial cell concentrations of 4.4×10^4 to 10^8 were used in the experiment for varying the input voltage, treatment time and gap distance between the surface of the device and the agar media surface containing the bacteria.

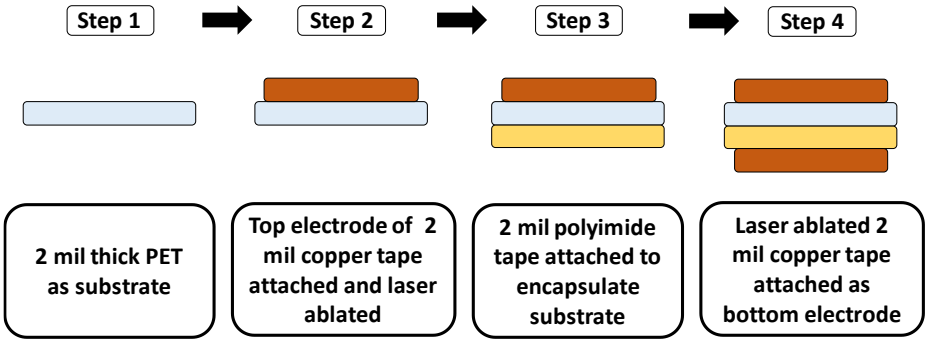

Figure 4.2: Fabrication process of the MDD

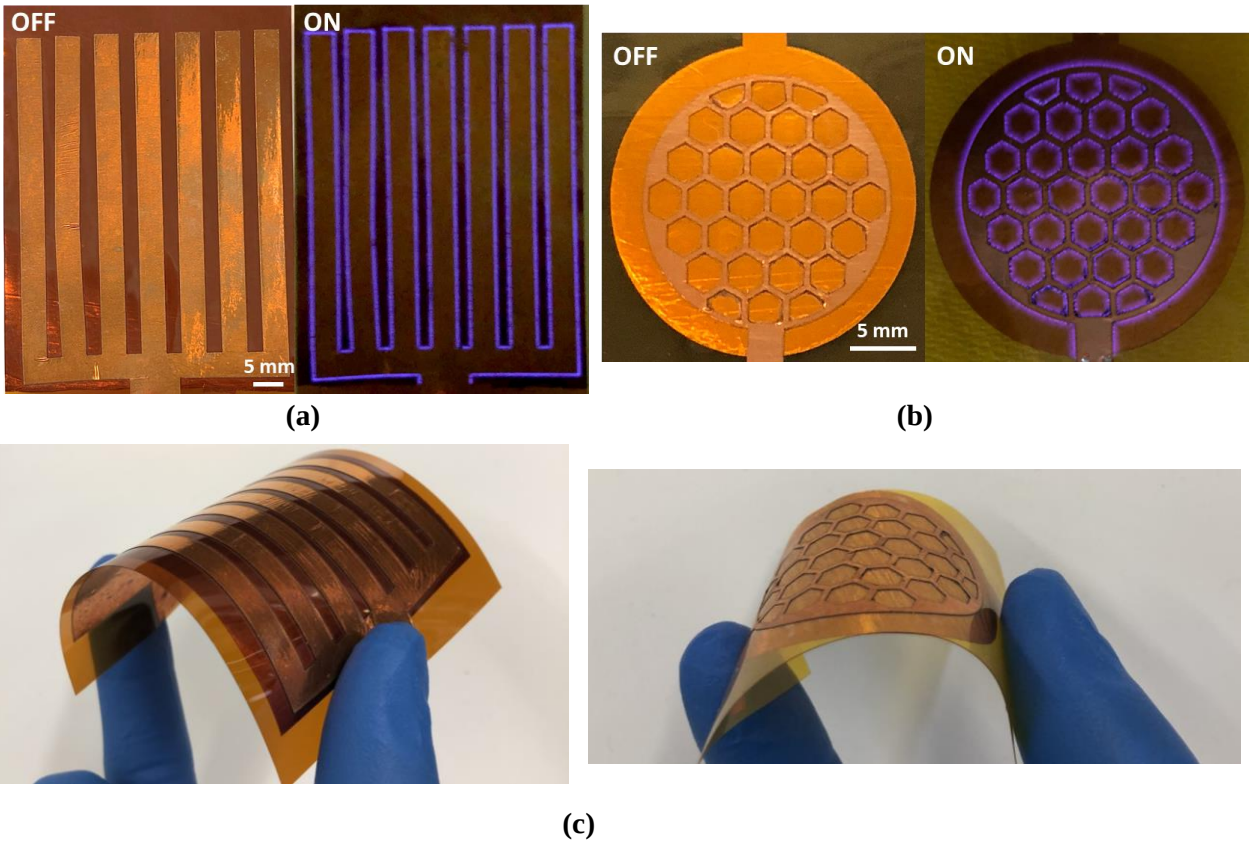

Figure 4.3: Fabricated (a) comb and (b) honeycomb MDDs in the OFF and ON mode (c) Photograph of the flexible MDDs

4.2.2.3 MDD Fabrication

Fabrication steps for assembling the MDDs are shown in Fig. 4.2 and the fabricated comb and honeycomb devices in the OFF and ON modes are shown in Fig. 4.3. First, a flexible PET film of 2-mil thickness was cleaned with isopropyl alcohol (IPA). Then, a copper tape of 2-mil

thickness was attached on one side of the PET film. The copper tape was laser ablated into comb or honeycomb structures as the top electrode. The laser cutter used in this experiment was a Universal Laser System (PLS 6MW). The parameters for the laser to pattern the copper tape using a fiber cartridge were 50% of power, laser cutting speed of 8% and a frequency of 30 kHz using 2.0” lens (focal length 2.0”, spot size 0.005” and depth of focus 0.100”). Only one pass was required to fully cut the ~0.05 mm (2-mil) thick copper tape. The comb structure had an overall dimension of 55 mm×70 mm and the honeycomb structured electrode had an overall diameter of 35 mm. During the laser ablation process, perforations were observed on the PET film. To avoid any short circuit between the top and bottom electrodes, a single sided Kapton tape of 1-mil thickness was attached on the other side of the PET film. Finally, a rectangular electrode with a dimension of 60 mm × 75 mm and a circular ground electrode of 40 mm diameter were laser ablated and attached on the Kapton tape as the ground electrode for comb and honeycomb devices, respectively. The total thickness of the comb and honeycomb MDDs was ~ 8-mil.

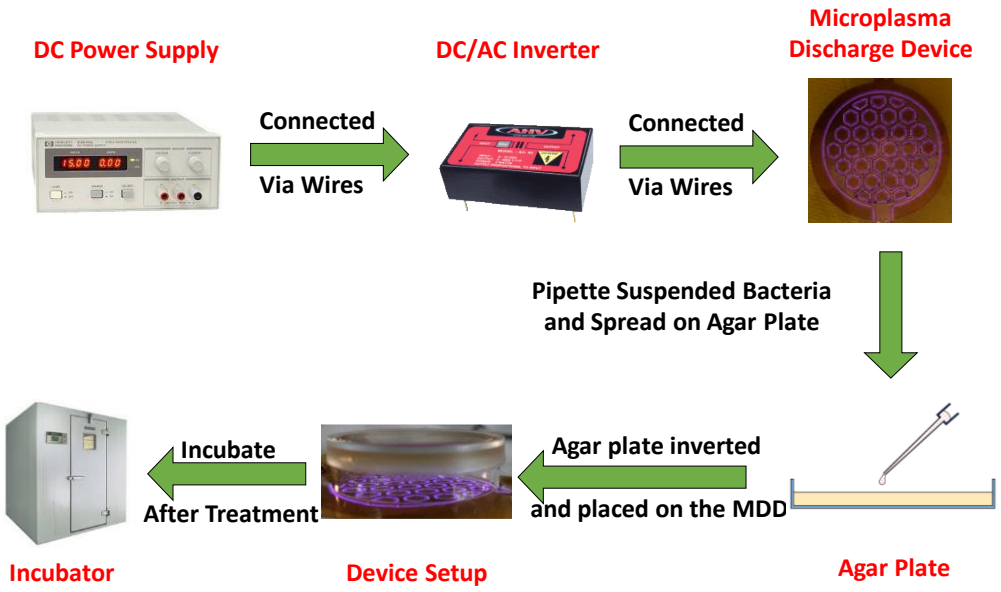

Figure 4.4: Experimental workflow.

4.2.2.4 Experimental Setup

The experimental setup for sterilizing petri dishes containing the *E. coli*, *P. aeruginosa* and *B. subtilis* bacteria is shown in Fig 4.4. A DC power supply of variable input voltage (Agilent E3610A) was connected to a step-up DC/AC inverter (American High Voltage, 5 W) and connected to the MDDs via alligator clips. Bacteria suspended in broth were pipetted on the surface of the agar contained in a petri dish. The bacterial sample was spread on the surface of the agar for uniform distribution and exposure to microplasma discharge. The agar plate containing the target bacteria was inverted and placed on top of the activated MDD. The sterilization efficacy was analyzed by evaluating varying parameters such as gap distance (1 to 9 mm), treatment time (10 to 300 seconds), input DC voltage (4 to 8 V) and higher bacterial cell concentrations. All the experiments for varying parameters were performed three times.

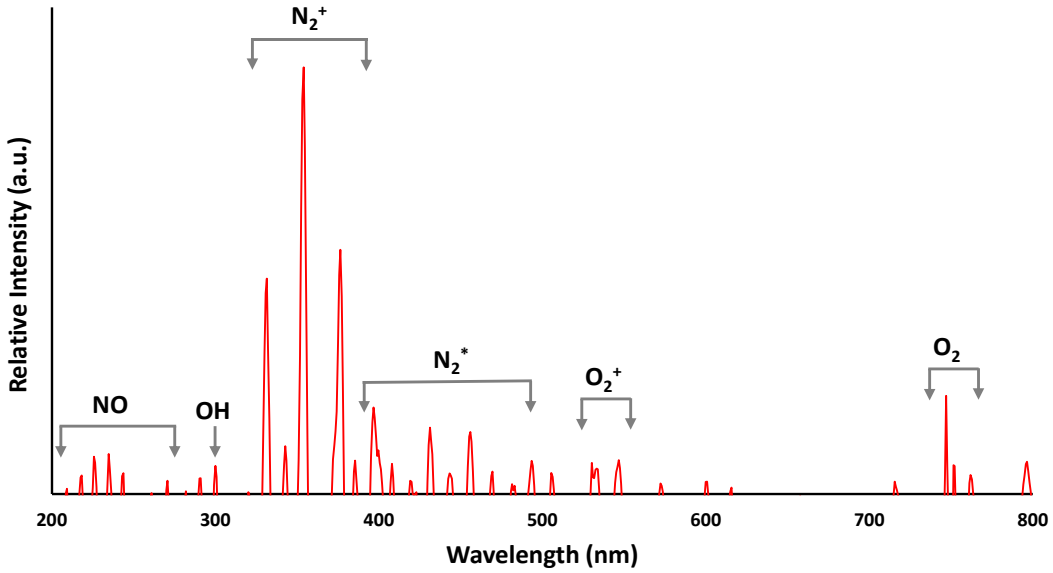

Figure 4.5: Optical spectrum (200 nm – 800 nm) of the microplasma discharge from the honeycomb structured MDD.

4.2.3 Results and Discussion

4.2.3.1 Microplasma Optical Spectroscopy

Ambient air consists of nitrogen, oxygen and water molecules as the primary components along with carbon dioxide, hydrogen and traces of inert elements. The discharge medium of microplasma is critical for generating the reactive species required to inactivate bacteria [418, 475, 477, 526]. The optical spectrum in the range of 200 nm–800 nm of the microplasma discharge from the honeycomb structured MDD is shown in Fig. 4.5. The spectra were obtained using the spectrophotometer SpectraNet Inc. EEP2000 utilizing the F600-UV-VIS-SR probe with a resolution of 0.1 nm. Nitrogen oxide (NO) groups were detected from 200-250 nm [527]. Hydroxyl ions (OH^-) were detected at 309 nm followed by excited nitrogen (N^{2*}) in the range of 350-400 nm [399, 528]. Positively charged species of nitrogen (N^{2+}) were also observed in the range of 400-500 nm along with positively charged species of oxygen (O^{2+}) ranging from 500-550 nm [399, 528]. Atomic oxygen was also detected around 750 nm [399, 528]. It is worth noting that there

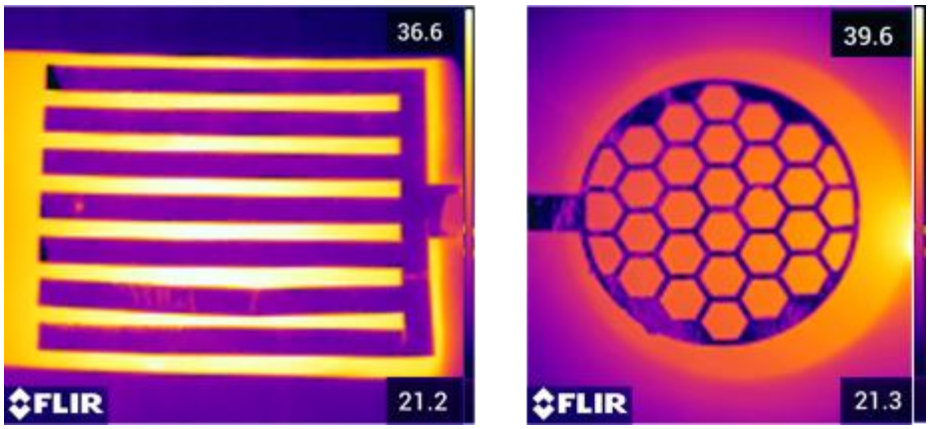

(a) **(b)**

Figure 4.6: Surface temperature profile of (a) comb and (b) honeycomb structured MDD at 8 V of input DC voltage.

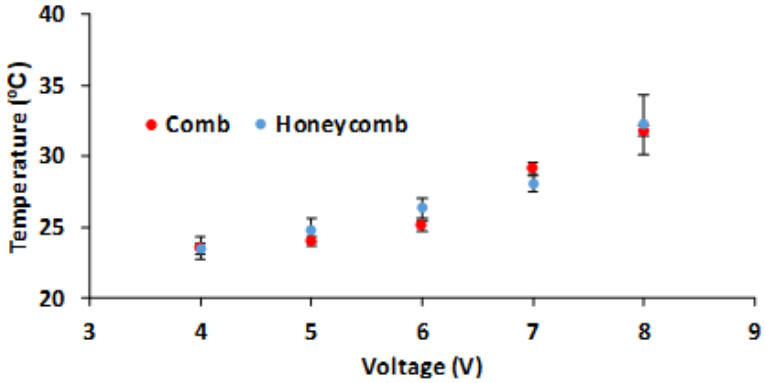

Figure 4.7: Graphical representation across the comb and honeycomb MDD for input voltage varying from 4 V to 8 V.

will be no difference in the types of species created by the comb and honeycomb structured MDDs because species generation is entirely dependent on the discharge media (air in this case). However, due to the difference in surface areas and the total microplasma generated, the concentrations of the species created by the honeycomb structured MDD will be higher than those created by the comb structured MDD.

4.2.3.2 MDD Surface Temperature

The maximum surface temperature generated when the MDDs of honeycomb and comb structured electrode were activated was measured using a thermal camera (FLIR E53). The surface

temperature profile for comb and honeycomb MDD are provided in Fig. 4.6 (a) and Fig. 4.6 (b), respectively. The average temperature for input voltages ranging from 4 to 8 V is graphically presented in Fig. 4.7. It was observed that the temperatures increased from ~23 °C to ~33 °C as the input voltage was increased from 4 V to 8 V, respectively. According to CDC, microorganisms are typically autoclaved at 121 °C for a minimum time of 30 minutes to ensure that all the microorganisms have been destroyed [405]. The average surface temperature of the device is very low as compared to heat-based sterilization. Therefore, it can be concluded that the increase in surface temperature does not play any role in the killing of the bacteria. Moreover, low temperatures are safe to handle during the use of the MDDs and can facilitate the production of wearable MDDs in the near future.

4.2.3.3 Experimental Results for *E. coli* and *P. aeruginosa*

E. coli and *P. aeruginosa* were exposed to the microplasma generated from the surface of the MDDs at a varying distance ranging from 1 to 9 mm, with a step size of 2 mm. This was done by pouring different volumes of LB agar into the petri dishes to create the varying distances. The bacteria were treated for five minutes at a maximum allowable power of 5 W. The number of bacteria treated in this experiment were 4.4×10^4 cells. MDDs of two different top electrode

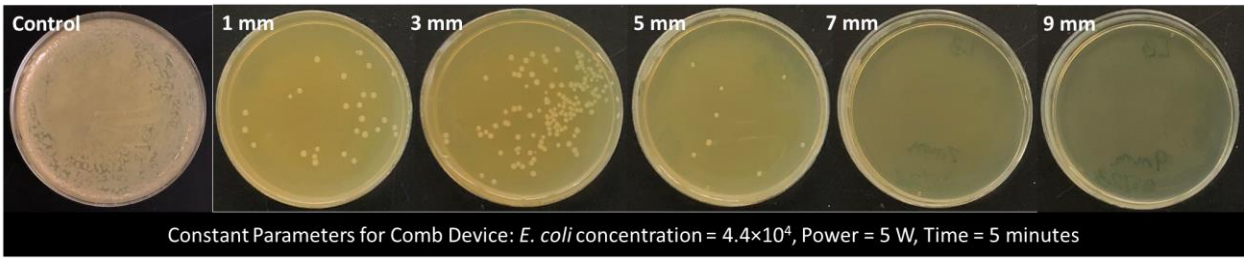

(a)

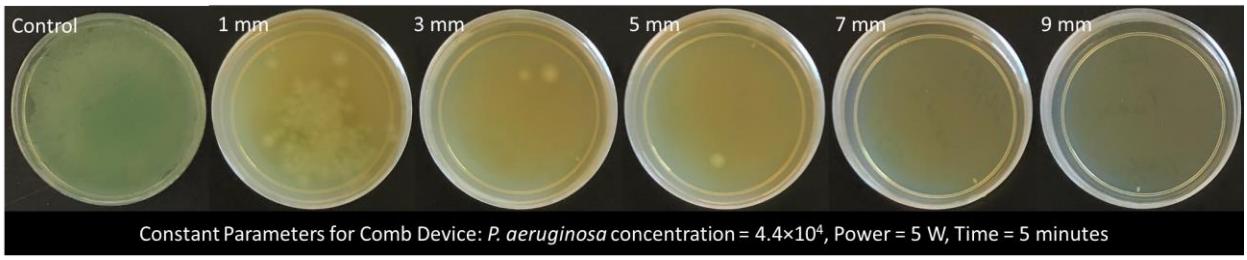

(b)

Figure 4.8: Results for varying gap distance (a) *E. coli* and (b) *P. aeruginosa* on LB solid media for comb device.

structures of comb and honeycomb designs were investigated and the effect of their microplasma discharge on two different bacterial species was observed. After treating the surface of the agar plate, the plates were incubated for 24 hours. Fig. 4.8 and Fig. 4.9 show the effect of the comb and honeycomb structured electrode designs for inactivating *E. coli* and *P. aeruginosa*, respectively.

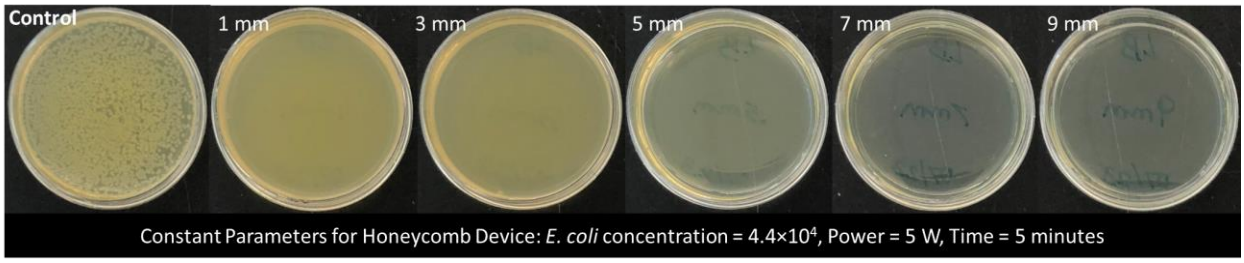

(a)

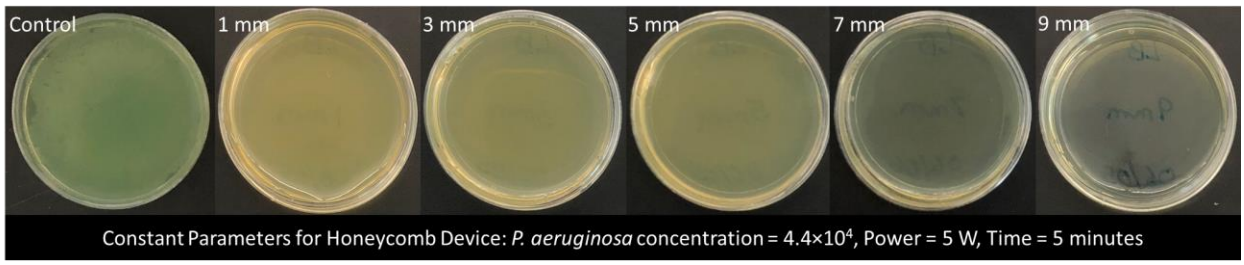

(b)

Figure 4.9: Results for varying gap distance (a) *E. coli* and (b) *P. aeruginosa* on LB solid media for honeycomb device.

For the comb structured MDD, an effective sterilization of 4 $\log_{10}$ reduction was achieved for both *E. coli* and *P. aeruginosa*, with a gap distance of 7 mm and 9 mm while partial inactivation was observed for 1 mm, 3 mm and 5 mm gap distances. This can be attributed to the inefficient voltage distribution on the comb structured MDD and lower volume of ambient air in between the device and the colonies. Larger volume of ambient air results in more availability of the nitrogen, oxygen and hydroxyl groups that are essential for inactivating the bacterial cells. However, for the honeycomb structured MDD, the voltage distribution across the device is uniform, resulting in uniform microplasma discharge and killing of the bacterial cells irrespective of the volume of

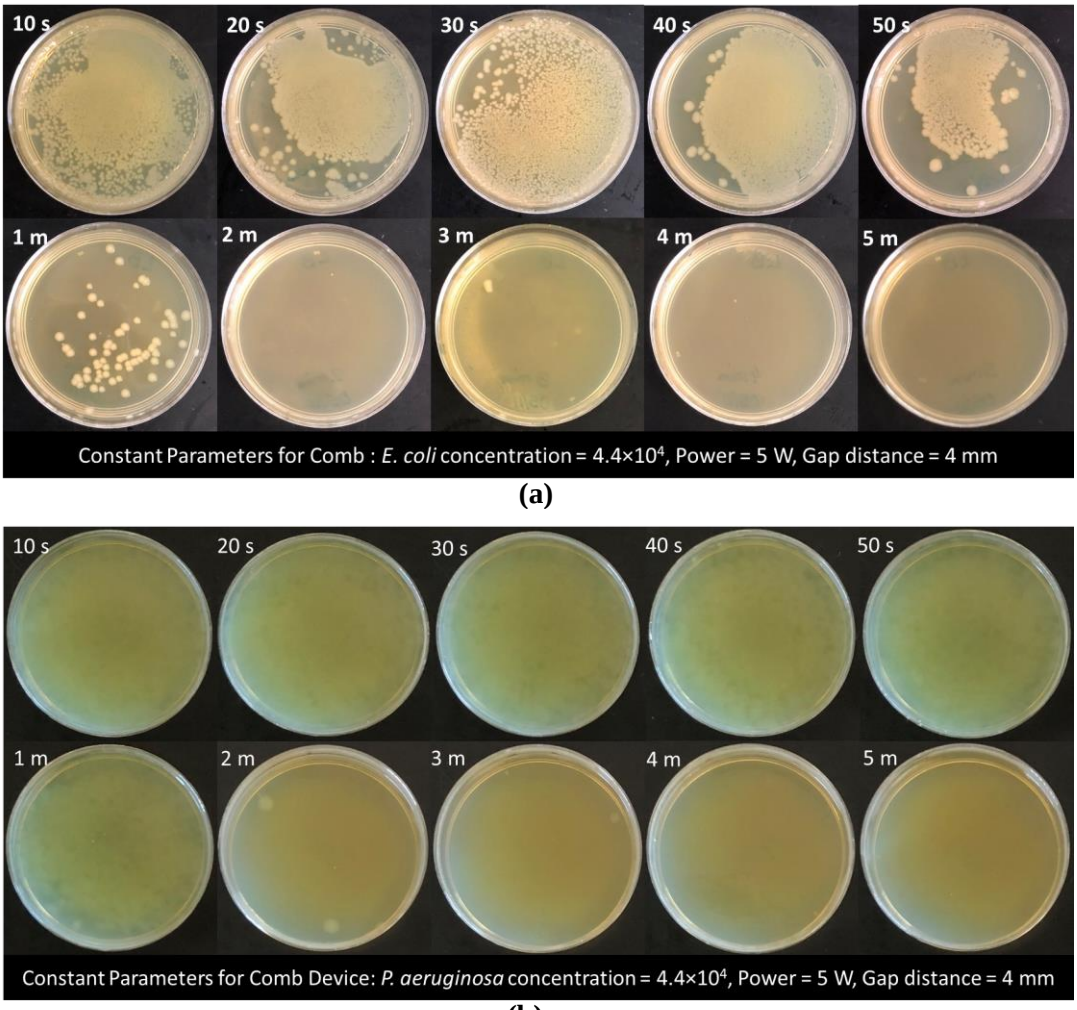

Figure 4.10: Results for varying treatment time (a) *E. coli* and (b) *P. aeruginosa* on LB solid media for comb device.

ambient air. For the honeycomb MDD, a 4 $\log_{10}$ reduction was achieved for *E. coli* and *P. aeruginosa* irrespective of the gap distance between the MDD and the biofilm.

The results for varying treatment times to inactivate *E. coli* and *P. aeruginosa* are shown in Fig. 4.10 and Fig. 4.11 for comb and honeycomb structured MDDs, respectively. The efficacy of the comb and honeycomb structured MDDs was investigated by varying treatment times ranging

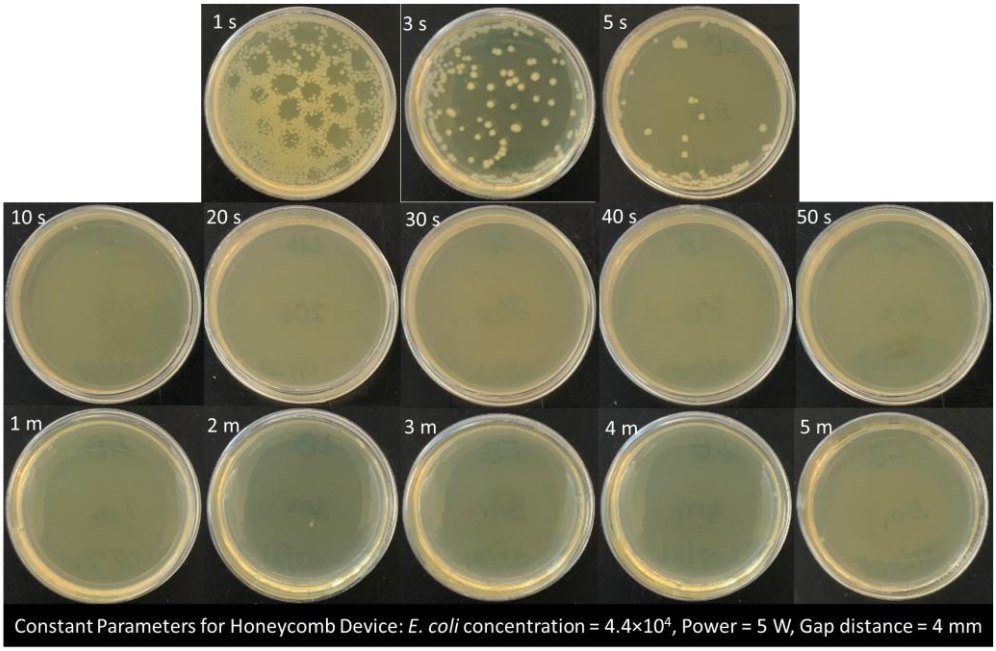

(a)

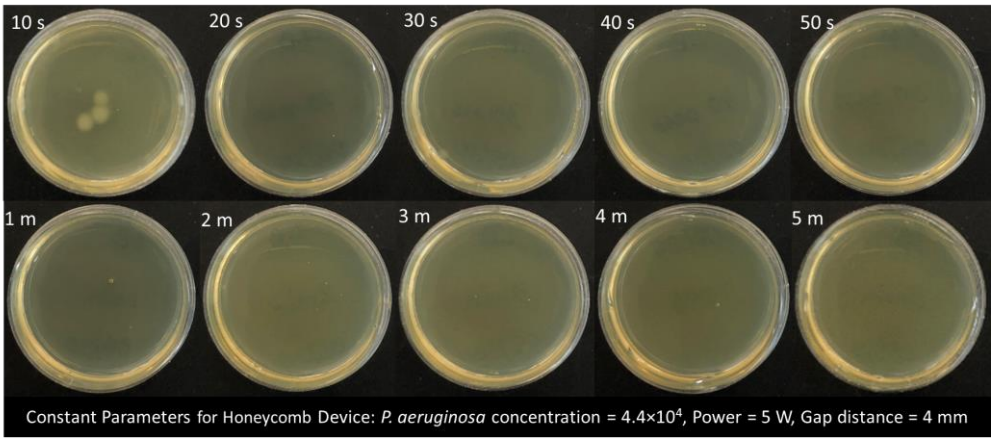

(b)

Figure 4.11: Results for varying treatment time (a) *E. coli* and (b) *P. aeruginosa* on LB solid media for honeycomb device.

from 10 to 50 seconds and 60 to 300 seconds, with a step size of 10 seconds and 60 seconds, respectively. The total power of the devices was 5 W and the distance between the MDD and the bacterial colonies was kept constant at 4 mm. The number of bacteria used for this experiment was 4.4×10^4 bacteria cells. After treatment, the plates were incubated for 24 hours. For the comb structured MDD it was observed that the inactivation of bacteria was effective from 10 seconds to 1 minute of device activation. However, complete eradication of *E. coli* was observed at 2 minutes resulting in a 4 $\log_{10}$ reduction. Similarly, utilizing the comb structured MDD, *P. aeruginosa* cells were also inactivated. It was observed that only two colonies grew on the agar surface after 2 minutes of treatment. As the exposure time was increased to 3 minutes, complete eradication of *P. aeruginosa* cells was observed, resulting in a 4 $\log_{10}$ reduction. The above experimental protocol was repeated with the honeycomb structured MDD. It was observed that the device is effective starting from one second of treatment time and complete eradication of bacteria was observed at 10 seconds resulting in a 4 $\log_{10}$ reduction. Similarly, utilizing the honeycomb structured MDD, most of the *P. aeruginosa* cells were also eradicated. It was observed that only three colonies grew on the agar medium after 10 seconds of treatment. As the exposure time was increased to 20 seconds, complete eradication of *P. aeruginosa* was observed resulting in a 4 $\log_{10}$ reduction. The honeycomb MDD was much more effective due to the uniform voltage distribution across the electrode when compared to the comb structured MDD.

E. coli and *P. aeruginosa* cells were treated with varying input voltages, ranging from 4 V to 8 V with a step size of 1 V. The results are shown in Fig. 4.12 and Fig. 4.13. Bacterial cell concentrations of 4.4×10^4 were used. The gap distance between the device and the agar surface was kept constant at 4 mm and a treatment time of one minute was used in the experiment. After treatment, the plates were incubated for 24 hours. For the comb structured MDD, no reduction in

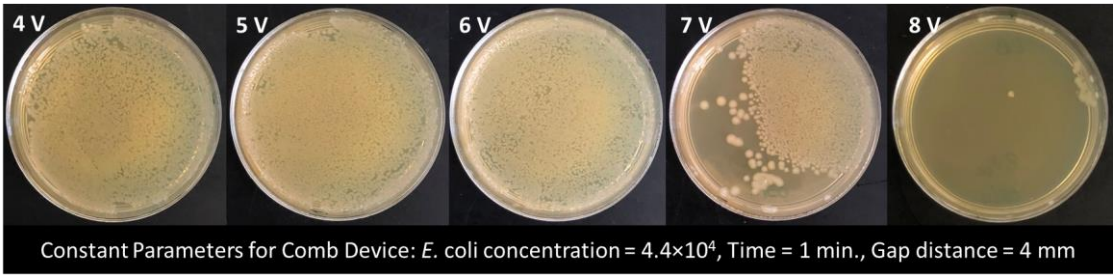

(a)

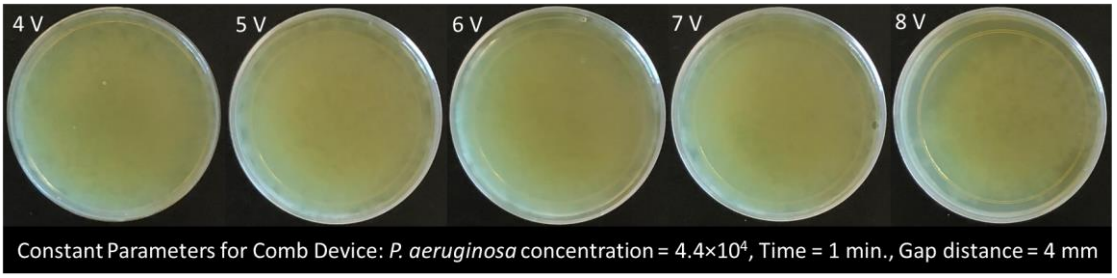

(b)

Figure 4.12: Results for varying input voltage (a) *E. coli* and (b) *P. aeruginosa* on LB solid media for comb device.

E. coli CFUs was observed for 4 V, 5 V and 6 V input voltage. Effective reduction in cell numbers was observed starting from 7 V. At 8 V of input voltage, only a few surviving *E. coli* CFUs were observed. The comb structured MDD was also used to treat *P. aeruginosa* cells. No reduction in

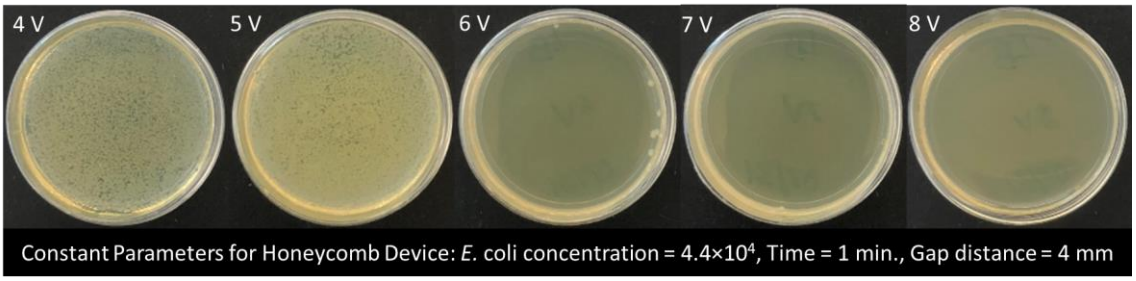

(a)

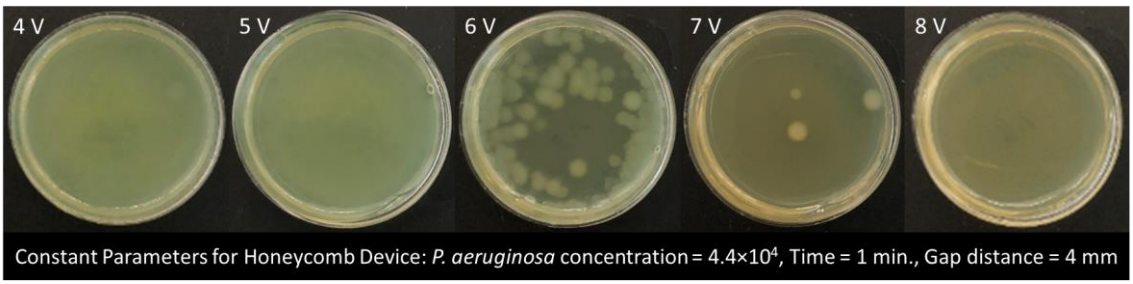

(b)

Figure 4.13: Results for varying input voltage (a) *E. coli* and (b) *P. aeruginosa* on LB solid media for honeycomb device.

CFUs was observed for input voltages ranging from 4 V to 7 V. There was some reduction in CFUs for an input voltage of 8 V but it would require longer exposure time to fully eradicate *P. aeruginosa*. Nevertheless, for the honeycomb structured MDD, no reduction in CFUs was observed for an input voltage of 4 V and 5 V. When the input voltage was increased to 6 V, effective reduction in numbers was observed, resulting in only six surviving CFUs on the agar surface. No colonies were observed at 7 V, thereby resulting in a 4 $\log_{10}$ reduction of *E. coli*. Similarly, when *P. aeruginosa* cells were treated with the honeycomb MDD, no change in bacterial viability was observed for an input voltage of 4 V and 5 V. Effective reduction in numbers was observed at 6 V and only three CFUs were observed when the input voltage increased to 7 V. Nevertheless, when the input voltage increased beyond to 8 V, no colonies were observed, thereby resulting in a 4 $\log_{10}$ reduction of *P. aeruginosa*. The comb structured MDD required higher input voltage to compensate for the non-uniform voltage distribution, whereas the honeycomb structured MDD achieved almost complete eradication of bacteria at a lower input voltage. This demonstrates how voltage distribution and electrode design are critical for uniform microplasma discharge and effective eradication of bacteria.

E. coli and *P. aeruginosa* with a density of 4.4×10^8 bacterial cells were plated on LB agar plates and treated for 300 seconds at a total power consumption of 5 W for the comb and honeycomb structured MDD, shown in Fig. 4.14. The gap between the sample bacteria on LB agar

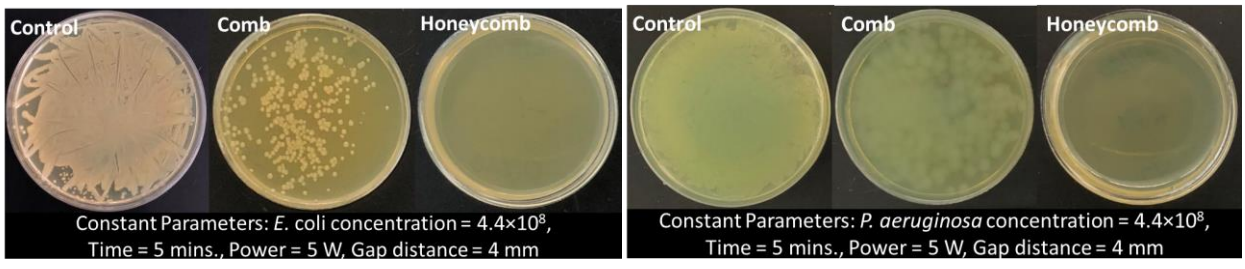

(a) **(b)**

Figure 4.14: Comb and honeycomb MDD performance on higher concentration of (a) *E. coli* and (b) *P. aeruginosa* on LB solid media

media and MDD was also kept constant at 4 mm. After treatment, the plates were incubated for 24 hours. Partial eradication was achieved utilizing the comb structured MDD on *E. coli* and *P. aeruginosa* (Fig. 4.14(a)). However, at the density of 4.4×10^8 bacterial cells of *E. coli* and *P. aeruginosa*, the honeycomb structured MDD was more efficient when compared to the comb device in sterilizing, resulting in an 8 $\log_{10}$ reduction (Fig. 4.14 (b)). The results validate the importance of having a MDD with uniform voltage distribution for achieving maximum sterilization efficacy.

4.2.3.4 Experimental Results for *B. subtilis*

The honeycomb-structured MDD is more effective as compared to the comb MDD as shown when treating Gram-negative bacteria with microplasma. For treating Gram-positive spore forming *B. subtilis* bacteria, the honeycomb MDD was utilized to showcase it effectiveness. *B. subtilis* cells from one- and seven-day old cultures were spread on top of BHI agar media and exposed to microplasma radiation for varying treatment times ranging from one to sixty seconds. A control of 4.4×10^4 number of bacterial cells were used for this experiment. The distance

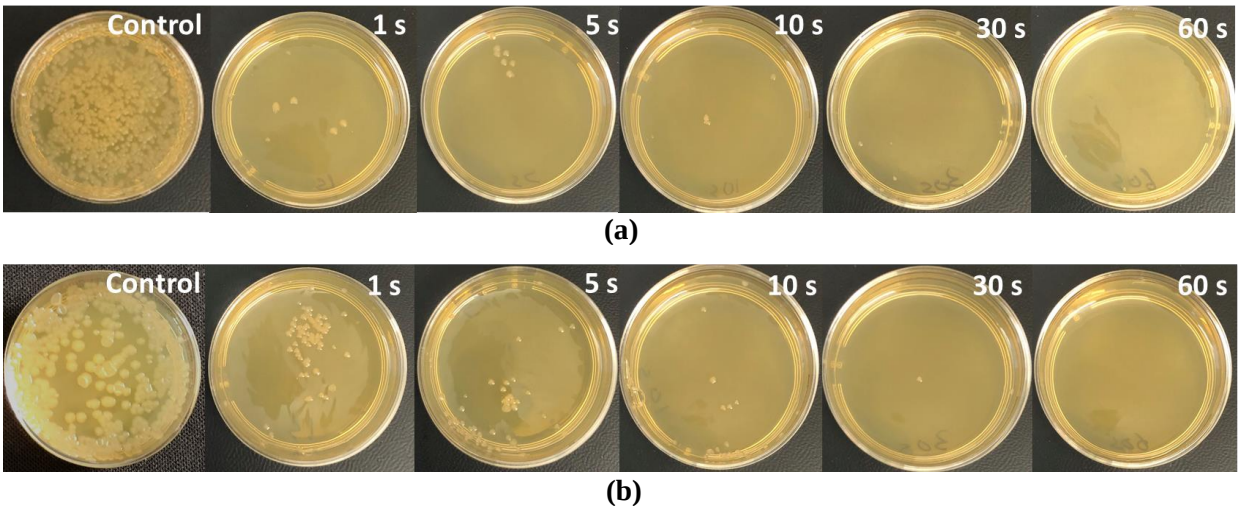

Figure 4.15: Results of varying treatment time for *B. subtilis* on LB solid media using honeycomb MDD on (a) one-day, and (b) seven-day culture.

between the MDD and agar surface containing the bacterial cells was 4 mm. A constant input voltage of 10 V from the DC power supply was maintained for the experiment. After treatment, the agar plates were incubated at 28°C for 16 hours to observe the inhibition capability of the MDD. The results for the efficacy of the device on one and seven-day old cultures of *B. subtilis* are shown in Fig. 4.15 (a) and Fig. 4.15 (b), respectively. It was observed that the MDD was effective from only one second of exposure time. Seven-day old cultures of *B. subtilis* have more sporulated cells as compared to one-day old cultures of *B. subtilis*, which consist of vegetative cells. Sporulated cells of *B. subtilis* are also more resistant to plasma generated species and UV radiation. [36,37]. As evident from Fig. 4.15, the number of CFUs in seven-day old culture was more than in the one-day old culture *B. subtilis* for similar range of treatment time. However, when the agar surface was treated for sixty seconds, a $4Log_{10}$ reduction was observed for both cultures, demonstrating the capability of the MDD to inactivate sporulated *B. subtilis* cells. The results for one- and seven-days cultured *B. subtilis* cells are shown in Fig. 4.16 (a) and Fig. 4.16 (b), respectively. Similarly, by pouring different volumes of agar medium into the petri dish, the distance between the surface of the agar to the honeycomb MDD was varied ranging from 1 to

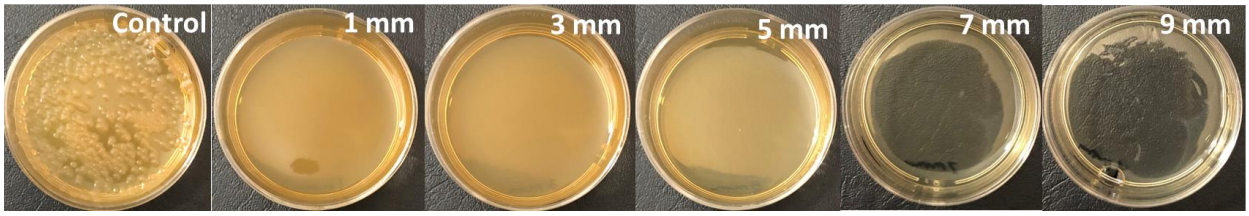

(a)

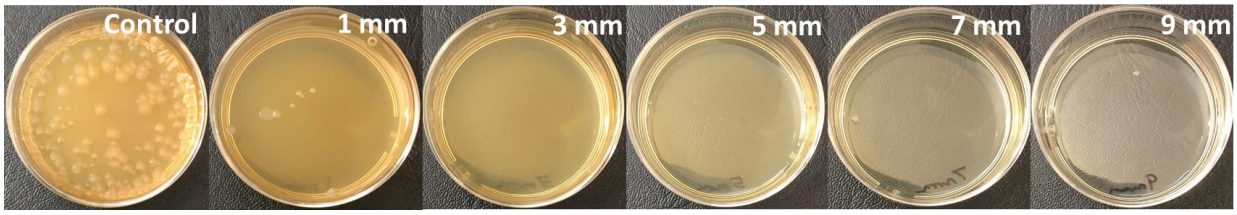

(b)

Figure 4.16: Results of varying gap distance for *B. subtilis* on LB solid media using honeycomb MDD on (a) one-day, and (b) seven-day culture.

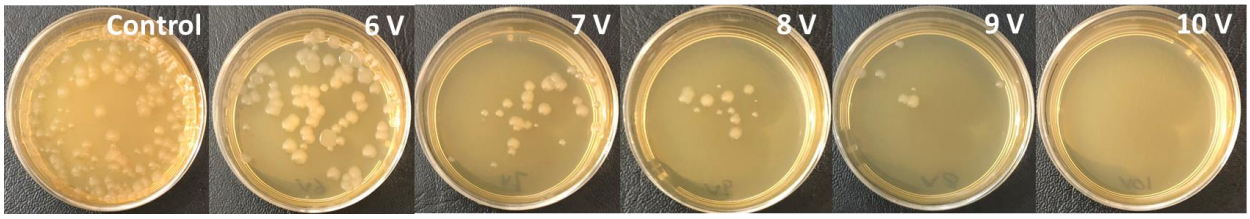

(a)

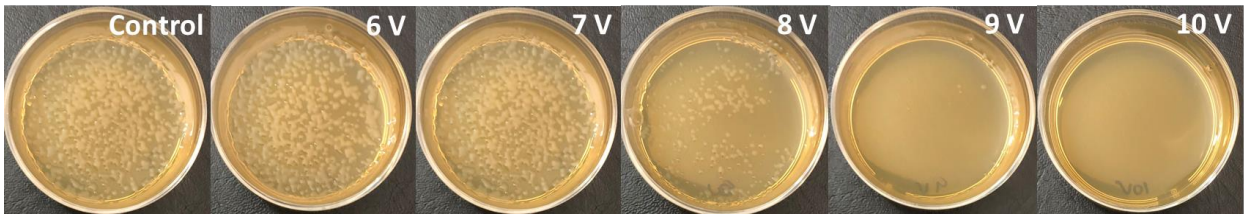

(b)

Figure 4.17: Results of varying input voltage for *B. subtilis* on LB solid media using honeycomb MDD on (a) one-day, and (b) seven-day culture.

9 mm, with a step size of 2 mm. *B. subtilis* cells cultured for one day or seven- days were treated at an input voltage of 10V at the DC power supply, for 60 seconds and a control of 4.4×10^4 cells were used to compare to the treated samples. The treated and control plates were also incubated for 24 hours to observe any growth of colonies after the treatment. It was observed that for one-day culture the MDD was able to inactivate the *B. subtilis* cells irrespective of the gap distance achieving a 4log10 reduction. However, for the seven-day old culture, 3mm and 5mm gap distance was the optimum gap distance for inactivating the cells. *B. subtilis* spores occurring in the seven-day old culture have a thicker peptidoglycan layer and the presence of a thicker cell wall and other mechanisms (special proteins, absence of water) protect the DNA from irradiation [529, 530].

B. subtilis cells were treated with varying input voltages, ranging from 4 V to 8 V with a step size of 1 V. The gap distance between the device and the agar surface was kept constant at 4 mm and a treatment time of one minute was used in the experiment. The results for one- and seven-day old cultures of *B. subtilis* are shown in Fig. 4.17 (a) and Fig. 4.17 (b), respectively. The

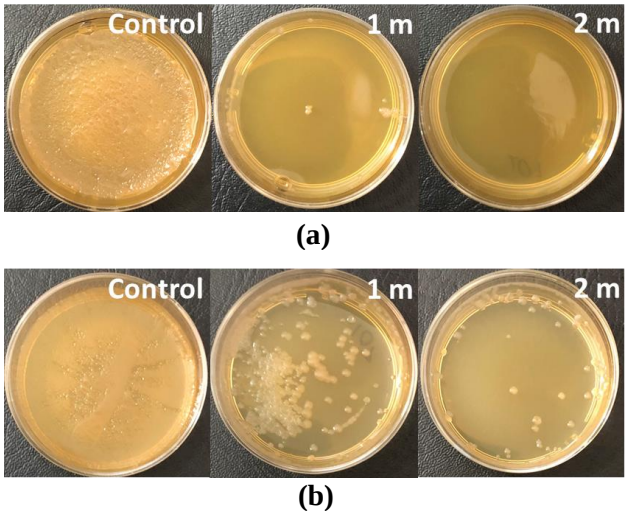

Figure 4.18: Results of treatment for higher concentration of *B. subtilis* on LB solid media for honeycomb MDD on (a) one-day, and (b) seven-day culture.

results indicate that a $4\log_{10}$ reduction required 10V input voltage at the DC power supply to destroy one- and seven-day old cultures of *B. subtilis*. It was also observed that at lower input voltage seven-day-old cultures of *B. subtilis* which contained sporulated cells are more resistant as compared to the one-day-old cultures of *B. subtilis* cells as they contain mostly vegetative cells (non-sporulated cells). Higher cell concentrations in the one- and seven-day-old cultures of *B. subtilis* were also inactivated. The gap distance between the device and the agar surface was kept constant at 4 mm, the input DC voltage was 10V and 2.5×10^7 cells were used in this experiment. The treatment time was varied from one to three minutes. At three minutes, no bacterial colonies were observed. The results for one- and seven-day-old cultures of *B. subtilis* are shown in Fig. 4.18 (a) and Fig. 4.18 (b), respectively. For one-day cultures, some *B. subtilis* colonies were observed after one minute of treatment after 24hours of incubation. However, a $7\log_{10}$ reduction was observed for one-day-old culture of *B. subtilis* when treated for two minutes. When seven-day-old cultures of *B. subtilis* were treated, they were more resistant to microplasma due to the presence of sporulated cells which have thicker peptidoglycan layer and the presence of a thicker cell wall also protects the DNA from irradiation [529, 530]. Although colonies were observed for

one and two minute treatment times, a 7$\log_{10}$ reduction was observed when the treatment time was increased to three minutes.

4.3 Protocol 2: Inactivating Bacteria Suspended in ***Liquid Media***

4.3.1 Materials

The materials used for making the MDD was the same as used in the protocol 1. In addition, polystyrene sheets from polymer shapes were used as a platform to attach the MDD on the top side of the petri dishes. Bacterial cultures were grown in sterile 50 mL conical-bottom centrifuge tubes (UX-06336-91, Cole-Parmer). Sterile 15 mL centrifuge tubes (VWR®) were used to aliquot 3 mL of the bacterial cultures. Bacteria res-supended in phosphate buffered saline (PBS: 0.01 M phosphate buffer, 0.0027 M KCL, and 0.137 M NaCl; pH 7.4) were transferred to 35 × 10 mm sterile petri dishes (351008, Corning™ Falcon™) for this experiment.

4.3.2 Preparation of Bacteria

The bacteria were prepared as per the standard batch culture method [531]. Initially, a single colony of *E. coli* (ATCC 25922), *P. aeruginosa* (strain PAO1, ATCC 87110), *S. aureus* (ATCC 6538) or *B. subtilis* (ATCC 6051) was inoculated in separate 50 mL Brain Heart Fusion (BHI) broth batch cultures. The cultures were then placed on an orbital shaker (EW-51700-14, Cole-Palmer) and incubated at 37 °C for 16 hours for *E. coli, P. aeruginosa, S. aureus*. For *B. subtilis*, an ideal growth temperature of 28 °C was maintained for a time period of 24 hours for vegetative *B. subtilis cells*, and to induce sporulation of *B. subtilis* cells, the culture was incubated for 7 days on the orbital shaker. The optical density (OD) of the cultures was measured by a Pharmacia GeneQuant Pro Spectrophotometer at a wavelength of 600 nm. The OD_{600} was adjusted using BHI broth to achieve a cell density in the range of 10^6-10^8. For cultures of *E. coli* and *P. aeruginosa*,

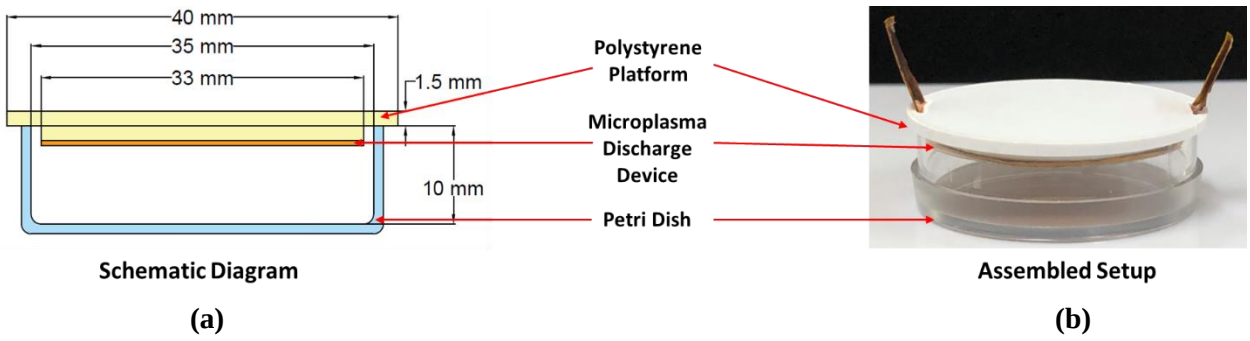

Figure 4.19: (a) Schematic of the MDD device setup (b) Photograph of the MDD device setup.

an OD_{600} of 0.627 ± 0.007 was obtained to achieve ~10^8 colony forming units (CFU) per milliliter. Similarly, for cultures of *S. aureus*, an OD_{600} of 1.025 ± 0.016 was obtained to achieve ~10^6 CFU per milliliter. The optical absorbance was limited from zero to one, which is the linear range of the spectrophotometer and therefore ~10^6 was utilized as the control for *S. aureus*. Finally, for cultures of *B. subtilis*, an OD_{600} of 0.241 ± 0.006 was obtained representing ~10^7 CFU per milliliter. Three milliliter aliquots of the culture were then pipetted into 15 mL centrifuge tubes and centrifuged (Sorvall Legend RT+ centrifuge, Thermo Scientific) at 3,500 rpm for 10 minutes resulting in pellets. These bacterial pellets were re-suspended in 3 mL of PBS and vortexed (Genie 2, Thermo Scientific) until the bacteria were homogenous in the solution. The bacteria suspended in PBS were transferred into the petri dish and treated with microplasma radiation.

4.3.3 MDD Fabrication

The fabrication steps of the MDD is same as in protocol 1. In addition, polystyrene sheets were also laser ablated in circular shapes with an overall diameter of 40 mm and 33 mm and attached to the MDD so that it could be placed on top of the petri dish. The schematic and the fully assembled setup including the MDD attached to the polystyrene platform on top of the 35 mm circular petri dish are shown in Fig. 4.19 (a) and (b), respectively. The parameters for the laser to cut the polystyrene sheets using a 10.6 µ 75 W CO_2 cartridge were 3 % power, 10 % speed and 500 pulses

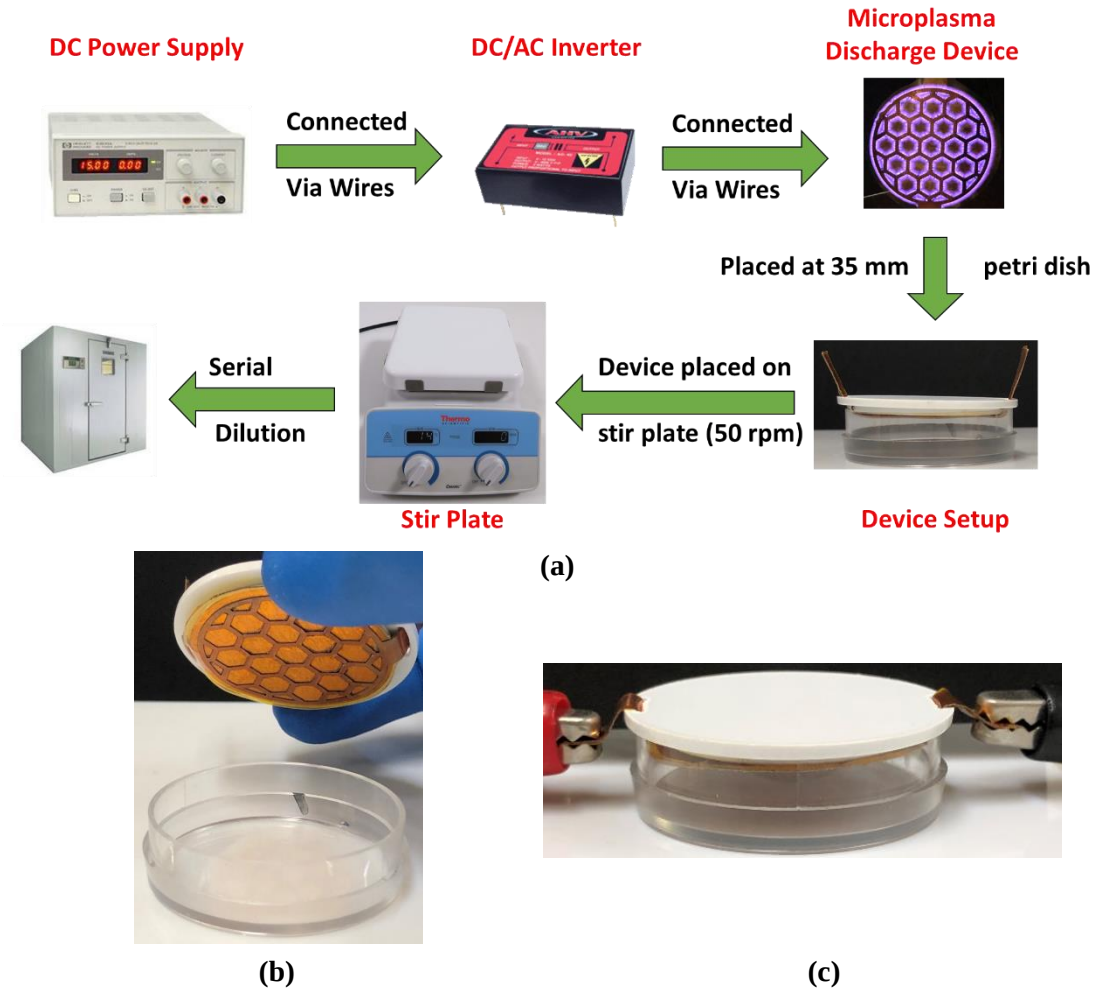

Figure 4.20: (a) Experiment setup, (b) Photograph of the MDD attached to the polystyrene platform, and (c) setup on the stir plate with the power supply connected to the terminal and ground electrodes.

per inch (PPI) using 2.0" lens. Only two passes were required to fully cut the ~1.5 mm thick polystyrene sheets.

4.3.4 Experimental Setup

The experimental setup is shown in Fig. 4.20 (a). A variable DC input power supply (Agilent E3610A) was connected to a step-up DC/AC inverter (American High Voltage 5 W) which was connected to the MDD. The DC input voltages of 6 V, 7 V, 8 V, 9 V and 10 V applied in this experiment correspond to AC output voltages of 505 V, 607 V, 679 V, 765 V and 828 V,

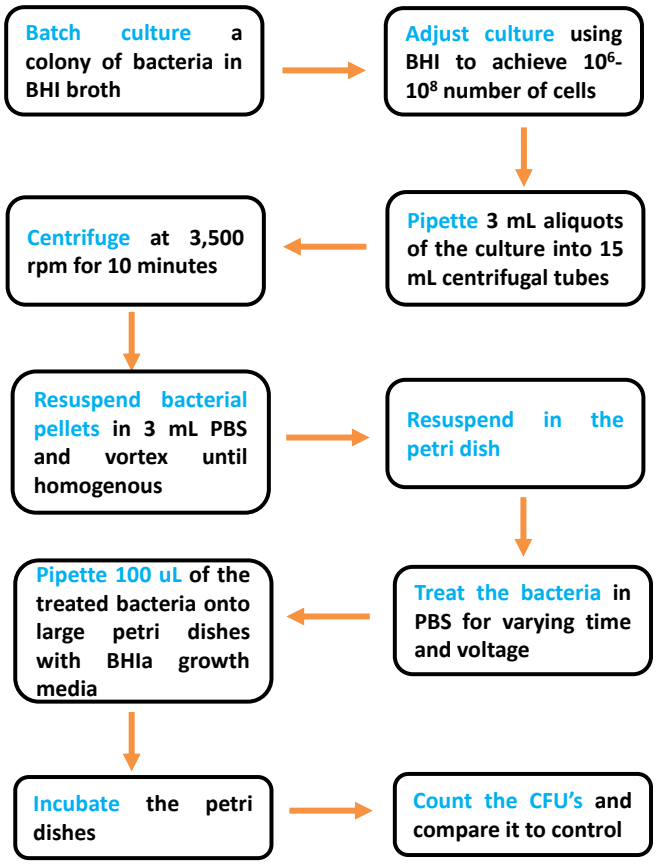

Figure 4.21: Summary of the experiment protocol.

respectively. The MDD attached to the polystyrene platform and connected to the terminal (red) and the ground (black) alligator clips is shown in Fig. 4.20 (b) and (c), respectively. A 10 mm × 3 mm magnetic stir bar was placed inside the petri dish that was filled with the bacterial suspension in PBS solution. The petri dish was then placed on top of the stir plate (stir rate: ~50 rpm) at ambient temperature. The MDD with the polystyrene platform was placed over the petri dish and the distance between the surface of the PBS solution to the MDD was kept constant at ~4 mm. The efficacy of MDD disinfection for varying parameters such as treatment time (1 to 10 minutes) and input voltage (6 to 10 V) were tested. Then, 100 µL of the treated bacterial suspension was pipetted and serially diluted from 10^{-1} to 10^{-8} to determine the surviving CFU on Luria Bertani (LB) agar in petri dishes with a size of 85 mm × 15 mm. The petri dishes were then

incubated at 37ºC for 16 hours and the surviving CFUs were counted to determine the efficacy of the MDD. A flowchart summary of the experimental protocol is shown in Fig. 4.21.

4.3.5 Results and Discussions

4.3.5.1 Varying Treatment Time

E. coli, *P. aeruginosa*, *S. aureus*, and *B. subtilis*, suspended in PBS solution, were initially subjected to varying treatment times ranging from 1 to 20 minutes at constant input voltage of 10 V from the DC power supply. The results for *E. coli*, *P. aeruginosa*, *S. aureus*, and *B. subtilis* are shown in Fig. 4.22 (a), (b), (c) and (d), respectively. Each experiment was performed in triplicate, and the error bars indicate the standard deviation. The control for the experiment was represented as "time-zero" along the x-axis. Photographs of the bacteria on BHI agar growth media

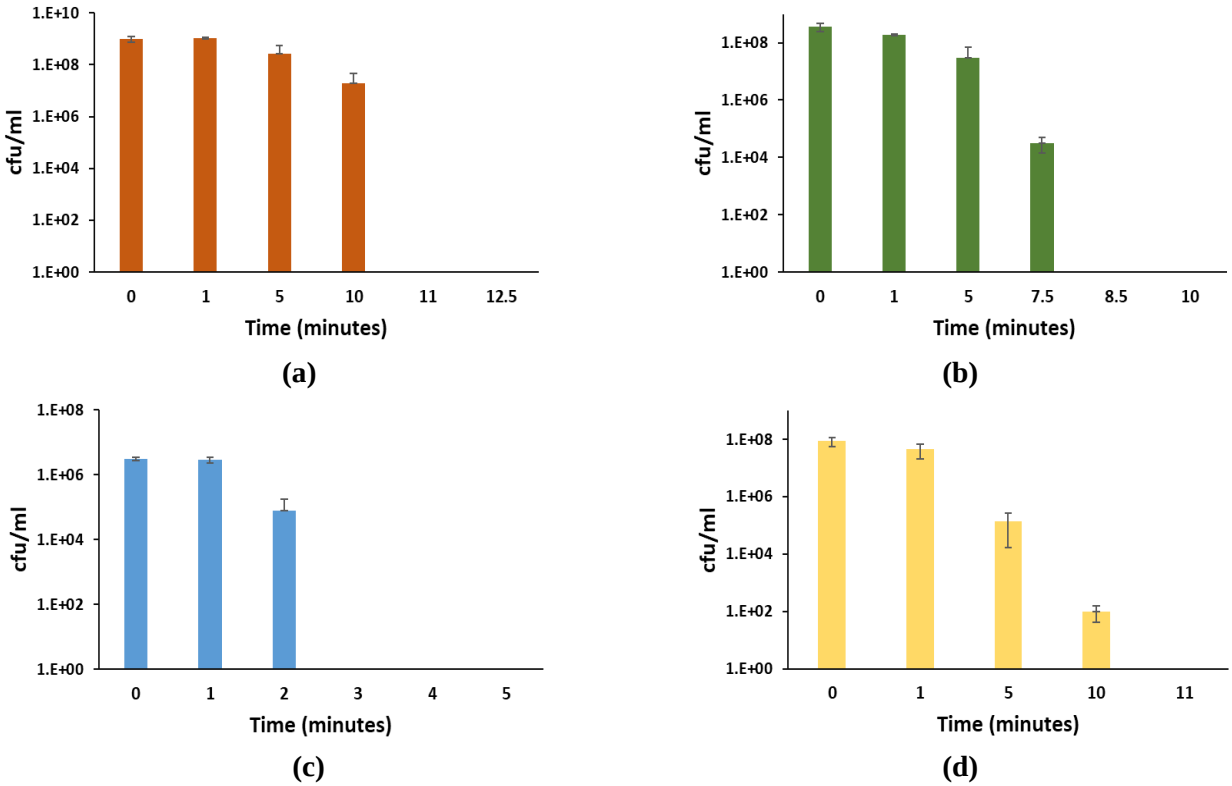

Figure 4.22: Efficacy of the MDD for varying treatment time on (a) *E. coli*, (b) *P. aeruginosa* (c) *S. aureus* (d) *B. subtilis*.

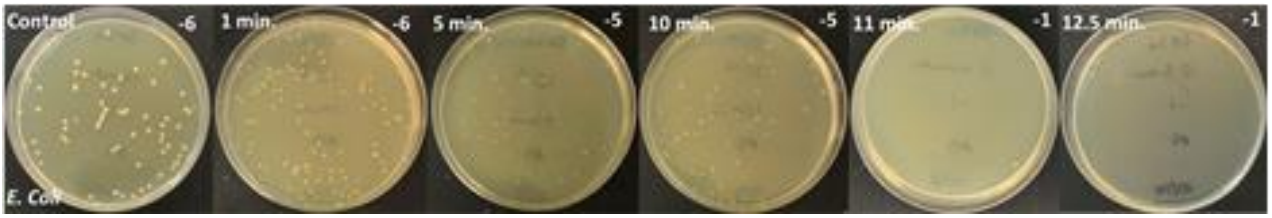

(a)

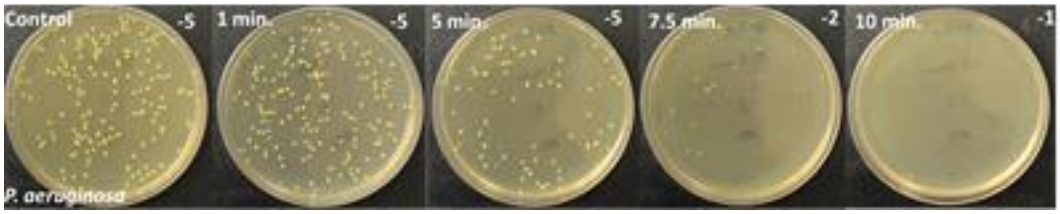

(b)

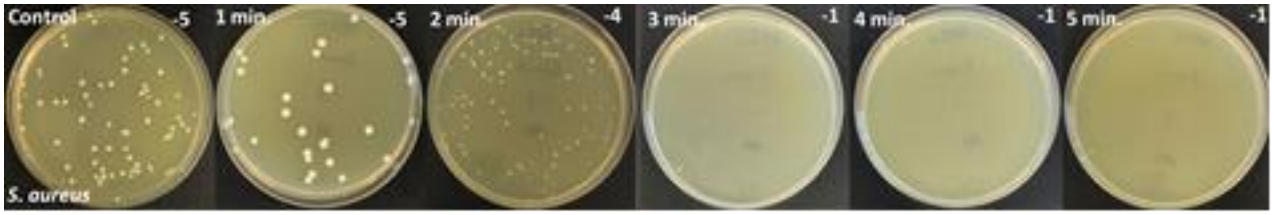

(c)

(d)

Figure 4.23: Photographs of the bacteria cultures (a) *E. coli*, (b) *P. aeruginosa* (c) *S. aureus* (d) *B. subtilis*.

indicating the countable plate and serial dilution number are also shown for *E. coli*, *P. aeruginosa*, *S. aureus*, and *B. subtilis* in Fig. 4.23 (a), (b), (c), and (d), respectively. As shown in Fig. 4.22 (a) and Fig. 4.23 (a), when *E. coli* was treated with the MDD, there was no reduction in total cell viability for an exposure time of 1 minute. When the exposure time was increased, a reduction in viable cell count was observed. A 1 Log_{10} reduction was observed at around 10 minutes of exposure time. Finally, as the treatment time was increased further to 11 minutes, an 8 log_{10} reduction of CFUs was observed resulting in complete eradication of *E. coli*. Similarly, *P. aeruginosa* was treated with the MDD (Fig. 4.22 (b) and Fig. 4.23 (b)). No reduction in colonies

was observed for 1 minute of exposure time. However, when the exposure to MDD was increased to 5 minutes, a partial reduction in CFUs was observed. Furthermore, at 7.5 minutes of exposure time, a 3 $\log_{10}$ reduction was observed when compared to the control. An 8 $\log_{10}$ reduction of CFU was observed from a treatment time of 8.5 minutes and onwards. The results indicated that 8.5 minutes at 10 V of input voltage is sufficient to eradicate the bacteria suspended in liquid media. Gram-negative bacteria such as *E. coli* and *P. aeruginosa* have a thin layer of peptidoglycan layer in the cell wall and the entire cell is encapsulated in a lipopolysaccharide membrane which protects them from harmful substances in the environment [390]. The peptidoglycan layer in *E. coli* and *P. aeruginosa* is ~6.4 nm and ~2.4 nm, respectively [532, 533]. It is hypothesized that due to the relatively thicker peptidoglycan layer in *E. coli*, it is more resistant to microplasma discharge and required higher treatment time when compared to *P. aeruginosa* [391].

The Gram-positive bacterium *S. aureus* was similarly treated with the MDD, and the results are shown in Fig. 4.22 (c) and Fig. 4.23 (c). For one minute of exposure time there was no reduction in cell viability. However, when the treatment time was increased to two minutes, ~1 Log_{10} reduction was observed, and then, a 6 Log_{10} reduction when treated for three minutes. The device showed a higher efficacy against *S. aureus* when compared to Gram-negative bacteria such as *E. coli* and *P. aeruginosa*. Similarly, Gram-positive bacteria such as *B. subtilis* were also exposed to the MDD. The performance of the device was evaluated and is as shown in Fig. 4.22 (d) and Fig. 4.23 (d). It was observed that when *B subtilis* cells were exposed to the MDD for one minute, almost no change in bacterial cell viability was observed. When the treatment time was increased to five and ten minutes, a 3 Log_{10} and 6 Log_{10} reduction was observed, respectively. The treatment time was increased further to 11 minutes, which resulted in more than a 7 Log_{10}

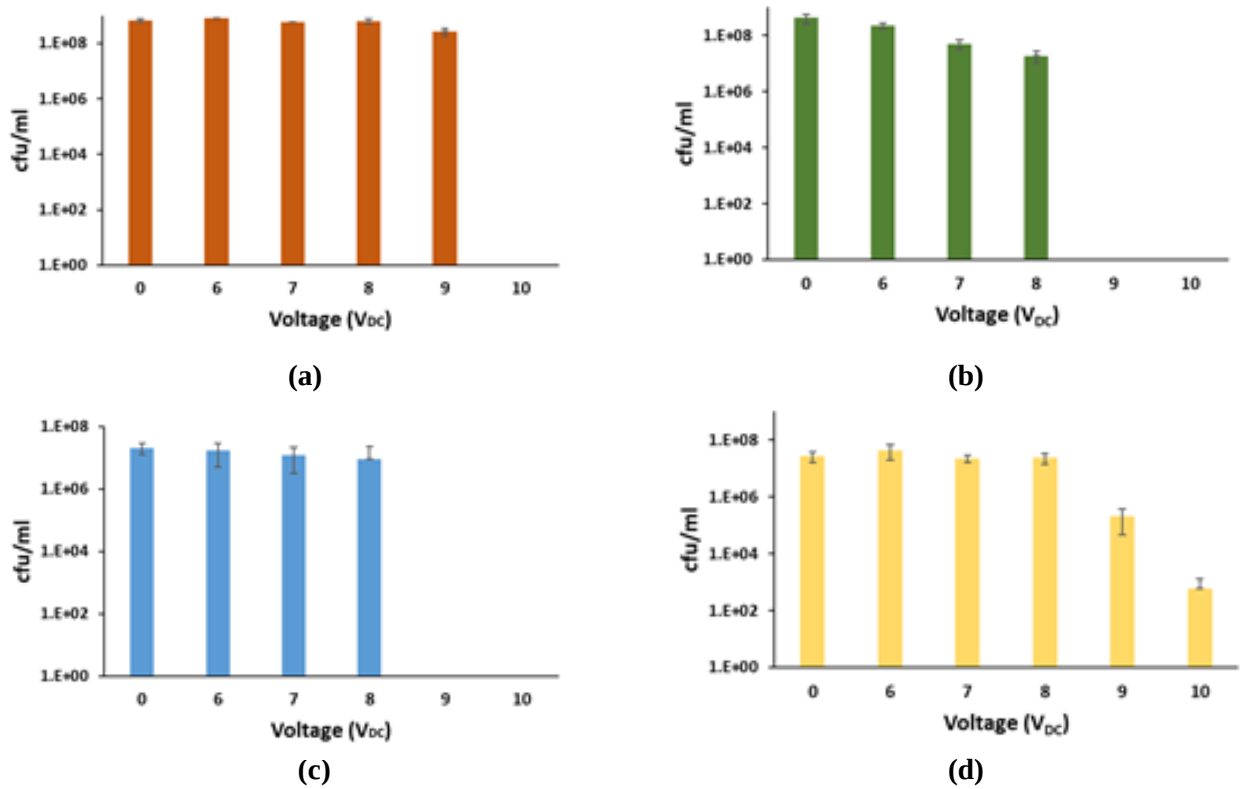

Figure 4.24: Efficacy of the MDD for varying input voltage on (a) *E. coli*, (b) *P. aeruginosa* (c) *S. aureus* (d) *B. subtilis*.

reduction in cell viability. Gram-positive bacteria have a much thicker peptidoglycan layer in their cell walls [390]. Moreover, unlike the Gram-negative bacteria, Gram-positive bacteria do not have an outer lipopolysaccharide membrane, which makes them more susceptible to harmful substances in the environment [390]. *S. aureus* has a peptidoglycan layer thickness ranging from 20-40 nm [534], whereas the peptidoglycan layer thickness of *B. subtilis* ranges from 50-70 nm [391, 535].

4.3.5.2 Varying Input Voltage

E. coli, *P. aeruginosa*, *S. aureus*, and *B. subtilis* suspended in PBS solution were initially subjected to varying input voltage ranging from 6 to 10 V from the DC power supply, at constant treatment time of 10 minutes. The efficacy results for *E. coli*, *P. aeruginosa*, *S. aureus*, and *B. subtilis* are shown in Fig. 4.24 (a), (b), (c), and (d), respectively. The control for the experiment is represented as "time-zero" along the x-axis. *E. coli* suspended in PBS solution was treated with

the MDD. No reduction in bacterial viability was observed from 6 to 8 V of input voltage. Partial reduction in CFU was observed at 9 V, however, when the voltage was increased to 10 V, an 8 Log_{10} reduction was observed. Similarly, the other Gram-negative bacterium, *P. aeruginosa*, was exposed to MDD. The results indicated no reduction in colonies for an input voltage of 6 V. Nevertheless, partial reduction was observed for an input voltage of 7 V and 8 V. Finally, an 8 log_{10} reduction was observed when the voltage was increased to 9 V and 10 V. The results indicate that a 10 minute of exposure time at 9 V of input voltage is sufficient to inactivate *P. aeruginosa* suspended in liquid media.

The Gram-positive bacterium *S. aureus* was similarly treated with the MDD for varying input voltage. For input voltage of 6 to 8 V, no significant changes in the bacterial viability was observed. However, when the input voltage was increased to 9 and 10 V, an over 6 Log_{10} reduction in CFUs was observed. The experiment was repeated for cultures of *B. subtilis*. For *B. subtilis*, no change in CFUs was observed for input voltages ranging from 6-8 V. As the voltage was increased to 9 and 10 V, an over 2 Log_{10} and 4 Log_{10} reduction in CFUs was observed, respectively.

4.3.5.3 Decimal Reduction Time

Decimal reduction time or D-value is a log-linear model and is defined as the duration of time required to reduce the number of living bacteria by 90% (one log factor) [536-538]. The D-value is highly dependent on the type of microorganisms, the operating temperature/input voltage to the microplasma device and the growth medium of the microorganisms [538]. The D-value simply provides a measure to evaluate the resistance of microorganisms towards experimental results of a particular sterilization process and is not based on any biological mechanism of cell death [538]. In this experiment, the D-value for each microorganism was calculated for varying

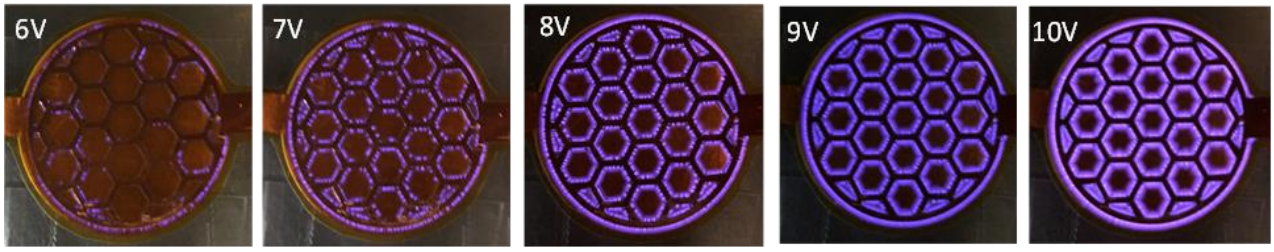

Figure 4.25: Microplasma discharge distribution for input voltage ranging from 6-10 V.

treatment times when the MDD was operated at an input voltage of 10 V. *E. coli* was the most resistant organism towards radiation from the MDD and the estimated D-value was calculated as ~5 minutes. Similarly, for *S. aureus*, *P. aeruginosa* and *B. subtilis*, the D-values were estimated as 1.3, 1.9 and 1.8 minutes, respectively.

4.4.5.4 Power Density

The power density of the MDD was also obtained for a flat surface. Photographs of the microplasma discharge at input voltage ranging from 6-10 V are shown in Fig. 4.25. Initially, the current was measured for every input voltage ranging from 6-10 V. Triplicate measurements from three different MDD samples were used. The input voltage of 6 V, 7 V, 8 V, 9 V and 10 V resulted in an operational current of 0.092 ± 0.001 A, 0.172 ± 0.002 A, 0.241 ± 0.001 A, 0.302 ± 0.003 A and 0.368 ± 0.010 A, respectively. The power of the device was then calculated as the product of the input voltage and the current. The corresponding power for input voltage of 6 V, 7 V, 8 V, 9 V and 10 V were 0.553 ± 0.008 W, 1.202 ± 0.017 W, 1.928 ± 0.011 W, 2.719 ± 0.023 W and 3.677 ± 0.102 W, respectively. The spread of the microplasma on the surface of the device was approximately 1 mm and the area of the microplasma discharge was calculated as 4.34 cm^2. Since there was partial discharge of microplasma across the MDD at 6 V and 7 V voltage, the microplasma area was assumed to be 4.34 cm^2 for power density calculations. The power density of a device is given as the total power of the device over the total area of the microplasma discharge

Table 4.2. Summary of the current, power and power density of the device for varying input voltages from the DC power supply.

Voltage (V)	Current (A)		
	Flat	25 mm	50 mm
6	0.092 ± 0.001	0.092 ± 0.002	0.097 ± 0.002
7	0.172 ± 0.002	0.173 ± 0.004	0.178 ± 0.003
8	0.241 ± 0.001	0.243 ± 0.001	0.247 ± 0.001
9	0.302 ± 0.003	0.304 ± 0.002	0.309 ± 0.002
10	0.368 ± 0.010	0.369 ± 0.009	0.373 ± 0.009

Voltage (V)	Power (W)		
	Flat	25 mm	50 mm
6	0.553 ± 0.008	0.550 ± 0.010	0.581 ± 0.012
7	1.202 ± 0.017	1.212 ± 0.025	1.245 ± 0.022
8	1.928 ± 0.011	1.941 ± 0.007	1.975 ± 0.011
9	2.719 ± 0.023	2.734 ± 0.020	2.781 ± 0.015
10	3.677 ± 0.102	3.689 ± 0.093	3.731 ± 0.095

Voltage (V)	Power Density (W/cm^2)		
	Flat	25 mm	50 mm
6	0.127 ± 0.002	0.126 ± 0.002	0.133 ± 0.003
7	0.276 ± 0.004	0.279 ± 0.006	0.286 ± 0.005
8	0.443 ± 0.003	0.446 ± 0.002	0.454 ± 0.003
9	0.625 ± 0.005	0.629 ± 0.004	0.639 ± 0.003
10	0.845 ± 0.024	0.848 ± 0.021	0.858 ± 0.022

[539]. The corresponding power densities for the input voltages of 6 V, 7 V, 8 V, 9 V and 10 V were 0.127 ± 0.002 W/cm^2, 0.276 ± 0.004 W/cm^2, 0.443 ± 0.003 W/cm^2, 0.629 ± 0.004 W/cm^2 and $0.845 \pm 0.0.024$ W/cm^2, respectively. The summary of the current measured, and the calculations for power and power density for the input voltage ranging from 6 V to 10 V are given Table 4.2.

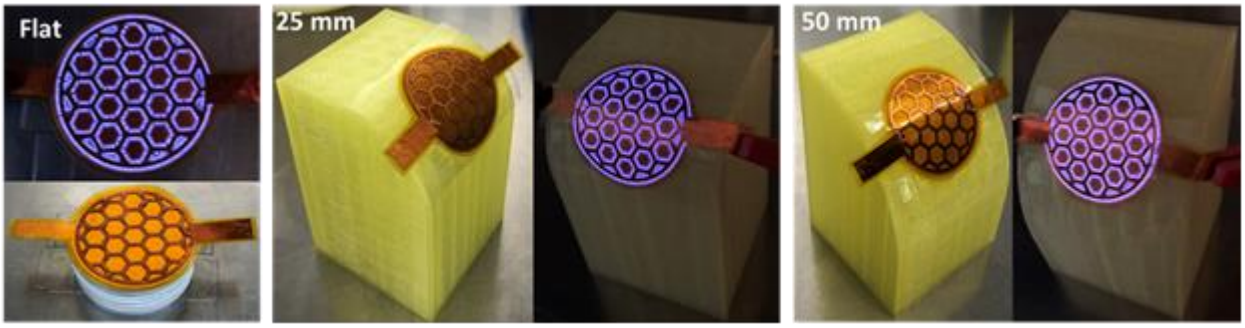

Figure 4.26: MDD on surfaces with different radius of curvature of zero (Flat), 25 mm, 50 mm.

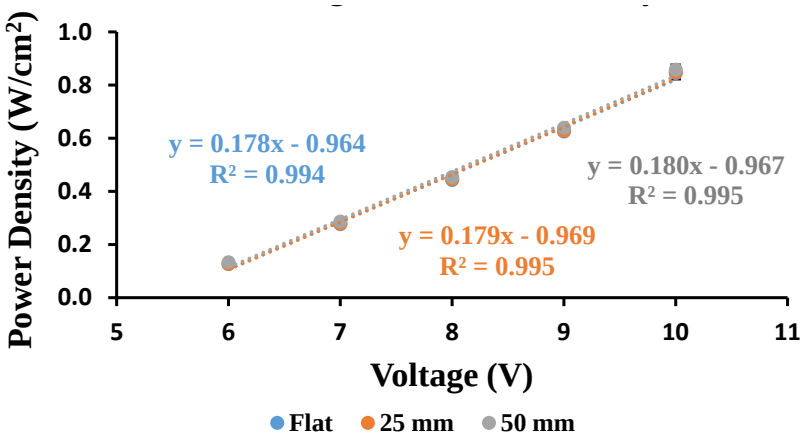

Figure 4.27: Power density of the MDD in relation to the input voltage.

4.3.5.5 Flexibility Test

Polylactic acid (PLA) filaments were used for printing three-dimensional (3D) blocks with one of its side having a radius of curvature (ROC) of 25 mm and 50 mm, utilizing a da Vinci mini (XYZ Printing Inc.) 3D printer. The MDD was attached to the curved surface of the block by double-sided tape as shown in Fig. 4.26. The flexibility of the MDD was investigated by activating it on the curved surfaces (Fig. 4.26) and by measuring the current during activation of the MDD for voltages ranging from 6 to 10 V. The power and power density were calculated for corresponding input voltages of MDD for ROC surfaces of 25 mm and 50 mm and compared with the MDD performance in its flat position. Triplicate measurements from three different MDD samples were considered for calculating error bars. It was observed that the results were very similar when the MDD was bent on a ROC of 25 mm and 50 mm, when compared to its flat position. The slopes of the linear fit for flat, 25 mm and 50 mm were 0.178, 0.179 and 0.180, respectively, as shown in Fig. 4.27. The corresponding correlation coefficients for the linear fit for the power density of the MDD for flat, 25 mm and 50 mm position were 0.994, 0.995 and 0.995, respectively. The results indicate that there is a minimal change in power density of the device

when the MDD is bent and this clearly shows that the fabricated MDDs are flexible. The full summary of the results with their standard deviations is provided in Table 4.1.

4.4 Summary

Flexible microplasma discharge devices of comb and honeycomb pattern were fabricated to eradicate Gram-negative bacteria of biosafety level 1 and 2 such as *E. coli* and *P. aeruginosa*, respectively. The voltage distribution across the devices were first simulated with the FEA software. The results indicated that the honeycomb-structured devices had a uniform voltage distribution across the terminal electrode, whereas the comb-structured device had a voltage drop towards the tips by ~15%. The effectiveness of the honeycomb-structured MDD versus the comb-structured MDD was investigated by using the devices to eradicate bacteria. *E. coli* and *P. aeruginosa* bacteria were plated on agar medium and exposed to the microplasma generated from the MDDs. The sterilizing efficacy of the MDDs was investigated by testing the effect of varying parameters including gap distance (1 to 9 mm), treatment time (10 to 300 seconds), input DC voltage (4 to 8 V) and bacterial concentrations. An efficacy of a 4 $\log_{10}$ reduction was achieved for a gap distance of 9 mm, when compared to the untreated control for both the devices. In addition, efficacy of a 4 $\log_{10}$ reduction was achieved with a treatment time of 10 seconds for the honeycomb-structured MDD while it was 2 minutes for the comb-structured MDD. A 4 $\log_{10}$ reduction in bacterial cells was also observed at an input voltage of 8 V for the honeycomb MDD with *E. coli* and *P. aeruginosa*. Furthermore, an 8 $\log_{10}$ reduction was observed when the honeycomb MDD was used to inactivate 10^8 *E. coli* and *P. aeruginosa* cells. The results also demonstrate the effectiveness of the honeycomb MDD when compared to the comb MDD. Moreover, the honeycomb-structured MDD was also utilized to inactivate spore-forming *B. subtilis* cells. The MDD was effective from just one second of treatment time as compared to the

control. A $4\log_{10}$ of bacterial numbers was observed when *B. subtilis* cells from one- and seven-day-old cultures were treated for sixty seconds. The honeycomb MDD was also effective in inactivating one-day-old cultures of *B. subtilis* cells with using varying gap distance of 1-9 mm and it was effective at an optimum gap distance of 3mm or 5mm for seven-day-old cultures of *B. subtilis*. When one- or seven-day-old cultures of *B. subtilis* were inactivated for varying input DC voltages ranging from 6-10V, it was observed that 10V was optimal for achieving a $4\log_{10}$ reduction. A higher concentration of *B. subtilis* cells (2.5×10^7 cells) was utilized as control and the sterilizing efficacy of the honeycomb MDD was also observed. The MDD was effective in inactivating one-day-old cultures of *B. subtilis* and a $7\log_{10}$ was observed at two minutes of treatment time. For the seven-day-old culture of *B. subtilis* cells, three minutes of treatment were required to achieve a $7\log_{10}$ reduction as sporulated cells have thicker peptidoglycan layers and thicker cell walls, protecting the DNA against the effects of microplasma. The uniform voltage distribution of the honeycomb-structured MDD over the comb MDD, facilitates the formation of reactive species and UV radiation throughout the surface of the MDD in ambient air conditions. Such reactive species of oxygen and nitrogen (ROS and RNS), and UV radiation will affect the integrity of the microbial cell walls and membranes. Such plasma induced stress will not only degrade the integrity of the cellular structure but also inhibits bacterial growth by damaging its DNA [188, 183, 401].

A flexible MDD was successfully fabricated for the inactivation of Gram-negative (*E. coli*, *P. aeruginosa*) and Gram-positive bacteria (*S. aureus* and *B. subtilis*) suspended in liquid media under ambient environmental conditions. The MDD was fabricated by sandwiching a flexible PET film, as the dielectric layer, between two layers of flexible copper tape. The copper tape was patterned in a honeycomb and circular design for making the top and bottom electrodes,

respectively, using laser ablation. A polystyrene-based platform was custom fabricated using laser ablation and attached to the MDD, and suspended over the liquid medium containing the bacteria. The capability of the MDD to inactivate bacteria was investigated by testing the effect of varying parameters including treatment time and input voltage from the DC power supply. An 8 $\log_{10}$ reduction was observed for *E. coli* and *P. aeruginosa* when treated for 11 and 8.5 minutes, respectively. A 6 $\log_{10}$ reduction was observed for *S. aureus* when treated for 3 minutes. When *B. subtilis* was treated with microplasma discharge, an 8 $\log_{10}$ reduction was observed. The power density of the MDD was also calculated which ranged from ~0.127 to ~0.845 W/cm^2 for DC input voltage ranging from 6 to 10 V. In addition, the MDD exhibited similar power density when bent at a ROC of 25 mm and 50 mm when compared to the power density of MDD in a flat state, indicating that the MDD is flexible. A maximum surface temperature of ~ 48 °C was obtained for the MDD at 10 V input voltage, indicating that the surface temperature of the microplasma is not a factor in inactivating the bacteria. Concurrently, a copper film was used as electrode material in the fabrication of MDD due to its abundant availability and low cost compared to many other metals.

CHAPTER V

SCREEN-PRINTED STRAIN GAUGE FOR MICRO-STRAIN DETECTION APPLICATIONS

5.1 Introduction

Strain gauges, which are one of the most fundamental sensing devices, can be utilized as transducers for monitoring load, pressure, strain and torque [540-544]. There has been a recent surge in the varied use of strain gauges, in different configurations, to monitor strain and analyze the stress and deformation on civil structures, robots and automobiles [545-548]. Strain gauges have also been implemented in biomedical applications for monitoring body vitals including heartbeat, respiration rate and motion sensing [549-551]. However, one of the growing interests for application of strain gauges is in structural health monitoring (SHM) of civil structures, wind turbines, aircraft structure and components [541-553]. It is essential to detect micro-strain ($\mu\mathcal{E}$) on such structures to detect crack propagation that could lead to structural failures [541, 543]. The strain gauges must adhere to high degree of civil and aviation safety standards required to maintain the aircrafts and prevent failures of components that can lead to fatal calamities. Therefore, it is important that such strain gauges, employed for SHM of aircrafts, are sensitive to μƐ and can detect severe strains before it leads to failure.

Conventional strain gauges are typically manufactured using MEMS based technology [160, 162, 433, 555, 554], involving manufacturing processes, that have slow developmental cycles, multiple fabrication platforms and high costs of research and development. Such fabrication processes also require controlled environments, thus significantly increasing the complexity of fabrication and cost of manufacturing [161, 556-567]. In addition, processing silicon wafers involves the use of toxic chemicals that are harmful to the environment and need specialized

training and equipment. Strain gauges designed and fabricated based on lithography-based techniques also utilize expensive metals that increases the production cost [163, 164, 561]. Further, the silicon-based substrates used for MEMS based devices are brittle and not flexible. The devices also include rigid housing and are not conformal enough to be used on three-dimensional (3-D) surfaces and remain relatively limited in form factor.

Printed electronics (PE) has emerged as one of the forms of manufacturing methods that can alleviate the limitations associated with conventional MEMS based fabrications methods [568-631]. Traditional additive printing processes such as screen, inkjet, flexography, aerosol and gravure are utilized for fabricating electronic circuits and transducers [632-653]. Such additive print manufacturing processes are more advantageous as compared to MEMS-based manufacturing methods since they involve less manufacturing steps, roll-to-roll (R2R) fabrication capabilities and low operating temperatures during fabrication. This significantly improves production throughput and thus lowers the cost of fabrication [168, 654, 655]. PE also enables the use of diverse substrates, deposition materials, and fabrication methods that are relatively easier to integrate with conventional manufacturing processes and systems [131, 656]. Among traditional additive print manufacturing methods, screen-printing is one of the simplest and cost-effective printing methods that enables mass production [657]. In this printing method, a viscous ink can be deposited on different substrates, by pushing the ink through a patterned screen mesh by a squeegee. Parameters such as screen mesh, ink, squeegee pressure and speed can be optimized for precision printing [657]. Screen printing has been extensively utilized to fabricate sensors [591-662], transistors [596], solar cells [663], organic light emitting diodes [664] and printed circuit

Table 5.1. Summary of recently published composite strain gauges.

Strain Gauge Material	Substrate	Fabrication Method	Gauge Factor	Reference
CNT yarns	-	Capstan rod system	0.15	[665]
PEDOT/PSS ink.	3D printed resin	Inkjet Printing	0.3/0.98	[666, 667]
Silver nanowires / ecoflex composite	PDMS	Screen Printing	0.7	[668]
PANI/PVDF nanofibrous membrane	PDMS	Electrospinning	0.045-0.840	[669]
MWCNT on polystyrene microspheres	PDMS	Solvent evaporation	1.35	[670]
OTFT sensor	Polyimide	Molecular beam deposition	1.51	[671]
Resin reinforced MWCNT	Epoxy blend	Incorporated by ultrasonication	0.43	[672]
Silver ink	CNT sheet	Aerosol Printing	0.49	[544]
Commercial Foil type	Polyimide	Etching Lithography	~ 2.1	[673]
Ag/C ink on polyimide	Polyimide	Screen Printing	2.39	This work

boards [131].

Commercially available strain gauges have been fabricated on flexible polyimide or glass-fiber reinforced epoxy-phenolic substrates using lithography-based fabrication process [163, 164]. The most common gauge resistance values of commercial linear strain gauges are 120 Ω, 350 Ω, and 1,000 Ω [163, 164]. Typical sensing layers are Constantan (copper-nickel) and Karma alloy (nickel-chromium) lithographically fabricated with metallic foils in a meandering pattern. These devices are not printed and this involves relatively expensive fabrication processes when compared to additive print manufactured devices. Typically, strain gauges have been fabricated by blending conductive inks and particles with polymer composites [674-678]. However, this increases the complexity of fabrication, thereby potentially increasing the costs of the device. Moreover, the conductive and polymer composites do not necessarily increase the sensitivity of the device. A summary of various composites utilized for strain gauge fabrication and their gauge factors is

given in Table 5.1. It is envisioned that direct printing of conductive composites on thin films will not only reduce fabrication costs but also be used to selectively attach on to civil structures and vehicles for optimum monitoring and testing [678]. Silver ink-based devices have low absolute resistance and low strain sensitivity but show higher stability at high temperatures [679]. However, carbon black based inks have higher absolute resistance and provides higher sensitivity but have very high temperature dependence on deformation sensitivity [679]. Blending silver and carbon ink in the desired ratio can result in custom gauge resistances of the sensor, compared with standard commercial linear strain gauges and also be integrated into existing sensing systems [680]. In this paper, a strain gauge was screen printed on a flexible polyimide substrate. The sensing layer was prepared by blending a commercially available silver and carbon ink to achieve a comparable gauge resistance to a commercially available strain gauge. The electromechanical response of the strain gauge towards varying tensile and compressive loads was investigated and is presented in this paper.

5.2. Methods

5.2.1. Materials

A Kapton film (HN500) from DuPont de Nemours, Inc. was used as the substrate for depositing the silver/carbon (Ag/C) composite ink as the sensing layer. Silver ink (Ag800) and carbon ink (C200) from Applied Ink Solutions was blended in a centrifugal mixer (AR-100, Thinky) at 1500 rpm for 4 minutes. Encapsulant ink (UV2510) from Applied Ink Solutions as the passivation layer was used to protect the sensor from environmental effects of humidity. Silver conductive epoxy adhesive (8331-14G) from MG Chemicals was used for soldering the wires to the sensor.

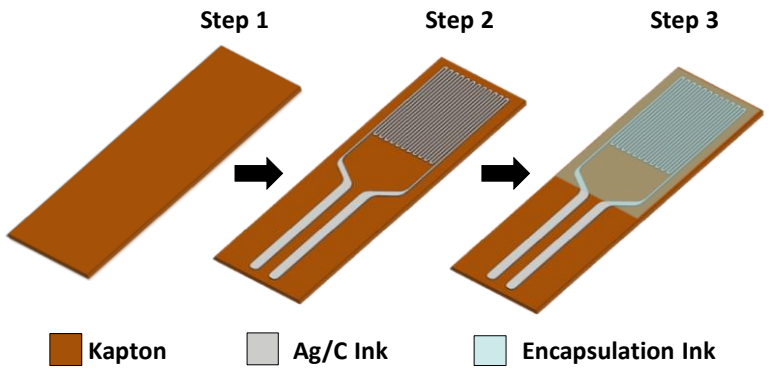

Figure 5.1: Strain gauge fabrication steps.

5.2.2. Preparation of Beam

An aluminum flat beam (1/8" × 1") from Hillman Group was used as the platform for bonding the strain gauge. A surface application kit (BAK-200) from the Vishay Precision Group was utilized for surface preparation of the aluminum beam. Initially, the surface of the beam was degreased with isopropyl alcohol (91%, Equate). The aluminum surface was then dry abraded using a 320-grit silicon carbide paper wetted with M-Prep Conditioner A, after which it was rigorously cleaned using a cotton gauge. Then, the aluminum surface was abraded again using a 400-grit silicon carbide paper wetted with M-Prep Neutralizer 5A followed by cleaning the surface using cotton gauge. The surface of the beam was further cleaned with cotton tips wetted by the M-Prep Neutralizer 5A until no residue can be seen left on the cotton tips.

5.2.3. Strain Gauge Fabrication

The layers and the steps of fabrication are shown in Fig. 5.1. The strain gauge has an overall dimension of 9 mm by 30 mm was consisted of three layers: Kapton substrate, Ag/C composite ink as the sensing layer and an encapsulant for passivation against environmental effects. The sensor consists of a meandering trace line of 200 μm width and spacing. Stainless steel screens with mesh count of 325, wire diameter of 28 microns, mesh angle of 22.5 degree and emulsion

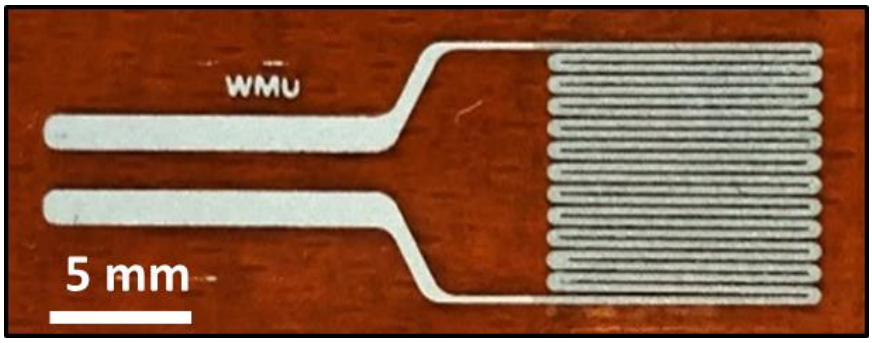

Figure 5.2: Screen printed strain gauge.

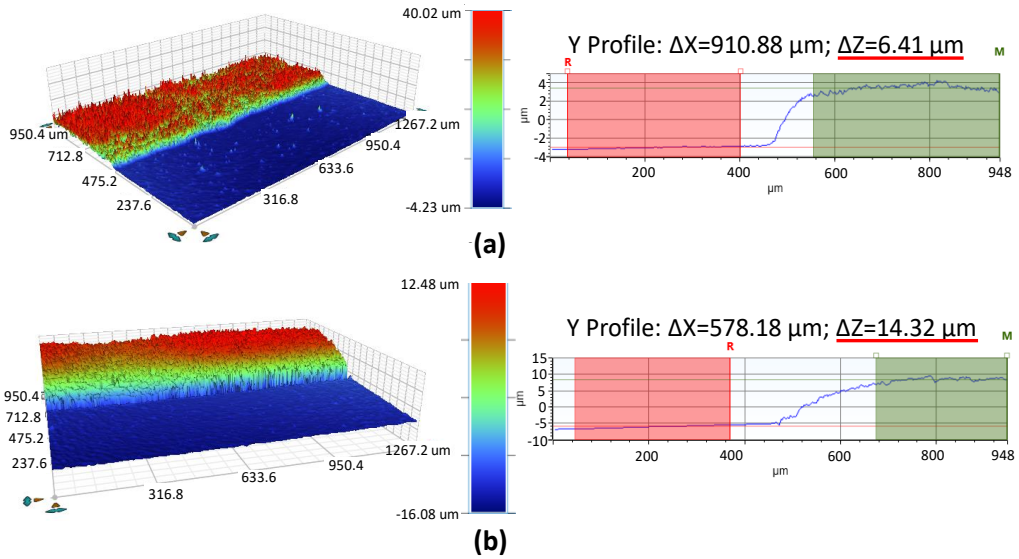

Figure 5.3: (a) Ag/C composite ink (b) Encapsulation ink thickness.

thickness of 12.7 microns were used for screen printing the inks on to the substrate. The strain gauge was screen printed on a flexible Kapton substrate by depositing Ag/C composite ink using MSP 485 screen printer (Affiliated Manufacturing Inc.). The ink was then cured in a thermal oven (VWR® 1320) at 110 °C for 8 minutes. The encapsulant ink was then screen printed and UV cured (LC6B Benchtop Conveyor Fusion UV Systems Inc.) at 17 feet/min. with a 300 W/inch UV lamp for 2 passes. The fully fabricated strain gauge is shown in Fig. 5.2. The morphology of the printed Ag/C composite layer and encapsulant layer including thickness and roughness was investigated using a Bruker Contour GT-K profilometer. The thickness and roughness of the printed Ag/C composite layer and encapsulant layer is shown in Fig. 5.3 and Fig. 5.4, respectively. An average

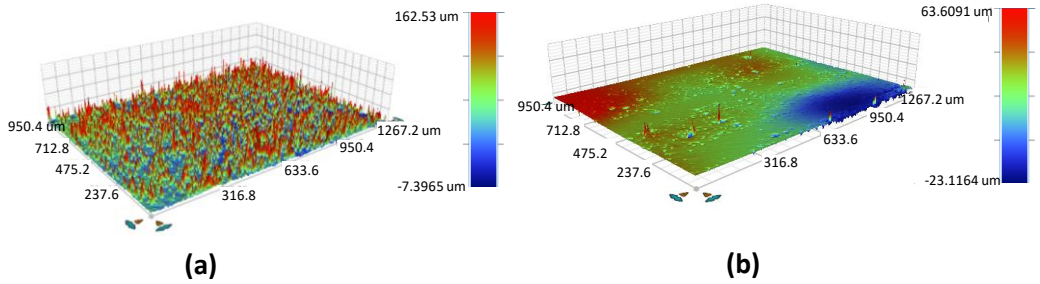

Figure 5.4: (a) Ag/C composite ink (b) Encapsulation ink roughness.

thickness of 6.4 ± 0.08 µm (Fig. 5.3 (a)) and 14.22 ± 0.09 µm (Fig. 5.3 (b)) was measured for the printed Ag/C composite and encapsulation layers, respectively. Similarly, an average roughness of 3.43 ± 0.14 µm (Fig. 5.4 (a)) and 1.82 ± 0.14 µm (Fig. 5.4 (b)) was measured for the printed Ag/C composite and encapsulant layers, respectively.

5.2.4. Experiment Setup

A flat aluminum beam of 305 mm in length was fixed on one end to represent a cantilever structure. A strain gauge was then attached to the top and bottom of the aluminum beams to

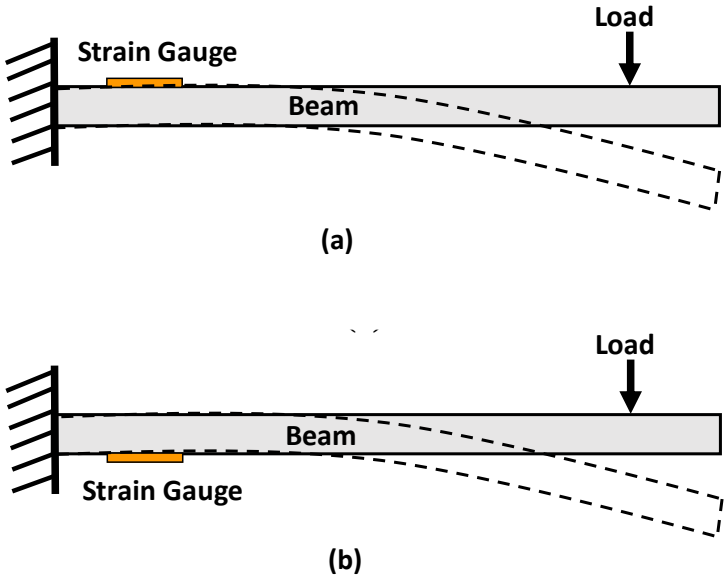

Figure 5.5: Schematic representation of the strain gauge placed on (a) top of the beam to simulate tensile strain and (b) bottom of the beam to simulate compressive strain.

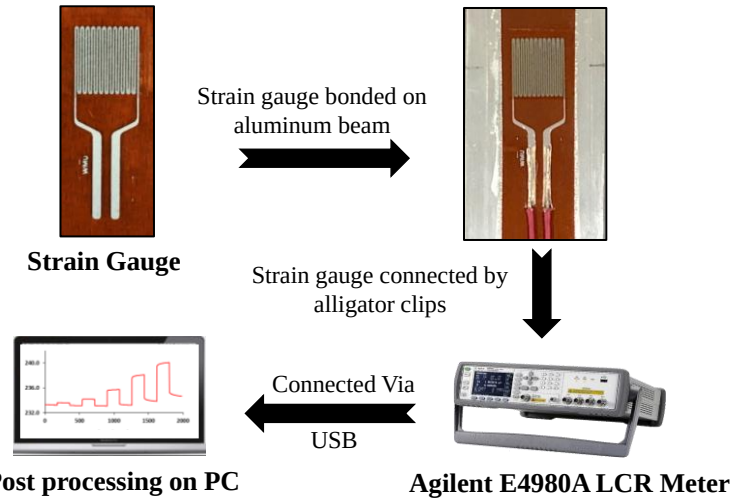

Figure 5.6: Experiment setup for micro-strain detection.

simulate tensile (Fig. 5.5 (a)) and compressive (Fig. 5.5 (b)) strain. The experimental setup for measuring the electromechanical response from the strain gauge is shown in Fig. 5.6. The printed strain gauge was bonded on to the flat aluminum bar 25 mm from the fixed end using M-Bond 200 Adhesive from Vishay Precision Group. The distance between the center of the sensor to the load was maintained at 220 mm. Then, loads varying from 0.2 kg to 1.8 kg was placed at the end of the beam. Connecting wires were used for connecting the strain gauge to a precision LCR meter (Agilent E4980A) using silver conductive epoxy paste and alligator clips. The LCR meter was connected to a PC via USB for post-processing and data analysis. The experimental setup for

measuring the temperature coefficient resistance (TCR) is shown in Fig. 5.7. The electrical connections for the printed strain gauge were made using a flat flexible connector (Amphenol ICC 65801-002LF). Multiple strain gauges were placed in a programable Thermotron® SE - 3000 Environmental Chamber and was subjected to varying relative humidity (RH), at a different temperature. Sensors were multiplexed to an Instek 6100 precision LCR meter by using a Keithley 7700 multiplexer, integrated in a Keithley 2700 main frame. The Instek 6100 was used to record the resistance response of the sensors sequentially at an operating frequency of 1 kHz and an applied voltage of 1 V. A custom-built MATLAB program on a PC was used to control Keithley 2700 and Instek 6100.The MATLAB program sequentially switch Keithley 2700 main frame channels, followed by measuring the resistance using Instek 6100 and write in excel file simultaneously.

5.3. Results and Discussion

5.3.1. Gauge Factor

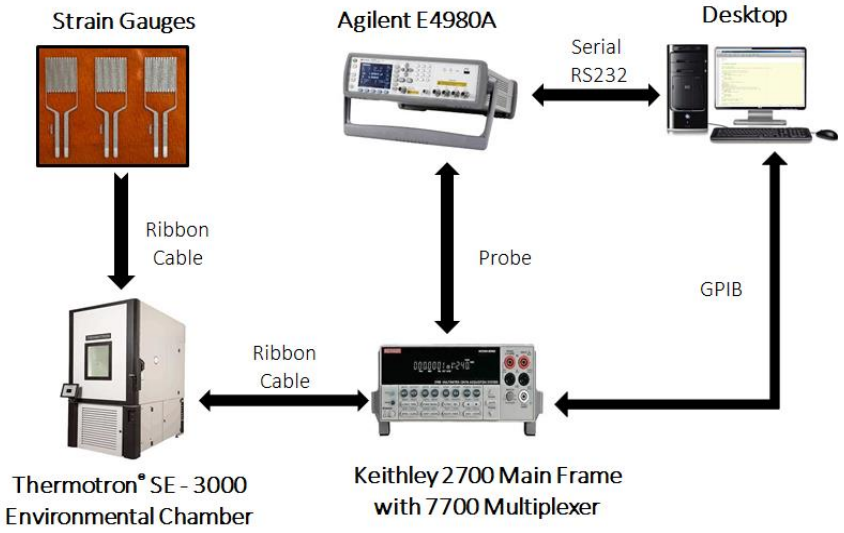

Figure 5.7: Experiment setup for measuring TCR of the strain gauge.

The calculated gauge factor (GF) of the strain gauge for varying loads applied to the beam is determined using Eq. (1):

$$GF = \frac{\frac{\Delta R}{R}}{\varepsilon} \tag{1}$$

where, ΔR is the change in resistance, R is the base resistance of the sensor and $\mathcal{E}$ is the strain on the beam due to load. The strain was calculated using Eq. (2):

$$\varepsilon = \frac{M \times C}{E \times I} \tag{2}$$

where, M is the bending moment, C is the centroid, E is the Young's Modulus of the aluminum beam (69 GPa) and I is the moment of inertia. M and I were calculated using Eq. (3) and Eq. (4),

$$M = m \times g \times x \tag{3}$$

$$I = \frac{b \times h^3}{12} \tag{4}$$

where, m is the mass of the load, g is the acceleration due to gravity, x is the distance between the center of the strain gauge and the load, b and h is the width and thickness of the of the cantilever respectively.

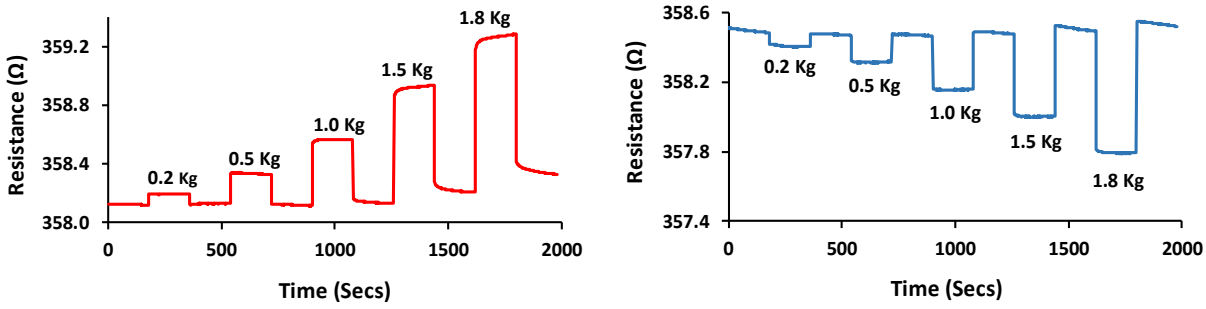

Figure 5.8: Sensor response towards varying (a) tensile and (b) compressive loads.

5.3.2. Strain Gauge Linear Sensitivity

The electromechanical response of the printed strain gauge towards varying tensile and compressive loads ranging from 0.2 kg to 1.8 kg is shown in Fig. 5.8 (a) and (b), respectively. The loads of 0.2 kg, 0.5 kg, 1.0 kg, 1.5 kg and 1.8 kg generates a calculated microstrain ($\mu\mathcal{E}$) of ~141, ~352, ~704, ~1056 and ~1267, respectively, which corresponds to 0.01 %, 0.04 %, 0.07 %, 0.11 % and 0.13 % of strain respectively. The loads were placed on the beam with a dwell time of 180 seconds for both under-load and rest conditions. The experiment was repeated for three different strain gauges, with three runs for each strain gauge [681]. It was observed that the resistance increased from its base resistance of ~358 Ω, resulting in a resistance change of 0.071 ± 0.002 Ω, 0.205 ± 0.011 Ω, 0.443 ± 0.012, 0.779 ± 0.009 and 1.038 ± 0.008 when tensile

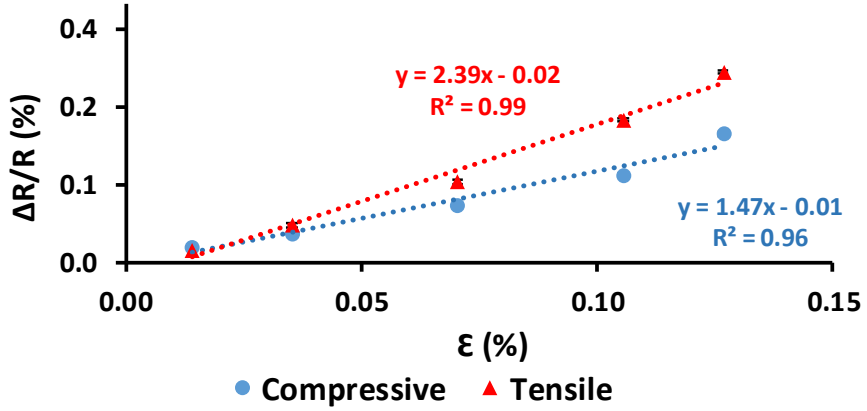

Figure 5.9: Relative resistive change for varying linear tensile and compressive loads.

strain of 0.01 %, 0.04 %, 0.07 %, 0.11 % and 0.13 %, were applied on the beam, respectively. As shown in Fig. 5.9, these results correspond to resistance changes of 0.020 ± 0.001 %, 0.058 ± 0.003 %, 0.125 ± 0.003 %, 0.220 ± 0.003 % and 0.293 ± 0.002 % when tensile strain of 0.01 %, 0.04 %, 0.07 %, 0.11 % and 0.13 %, were applied on the beam, respectively. A tensile gauge factor of 2.39, with a correlation coefficient of 0.99, was calculated.

Similarly, when compressive strain of 0.01 %, 0.04 %, 0.07 %, 0.11 % and 0.13 %were applied on the beam it was observed that the resistance decreased from its base resistance of ~358 Ω, resulting in a resistance change of 0.089 ± 0.009 Ω, 0.160 ± 0.004 Ω, 0.315 ± 0.003 Ω, 0.482 ± 0.006 Ω and 0.713 ± 0.011 Ω. These results correspond to resistance changes of 0.025 ± 0.003 %, 0.045 ± 0.001 %, 0.088 ± 0.001 %, 0.135 ± 0.002 % and 0.199 ± 0.003 % when compressive strain of 0.01 %, 0.04 %, 0.07 %, 0.11 % and 0.13 %, were applied on the beam, respectively (Fig. 5.9). A compressive gauge factor of 1.47, with a correlation coefficient of 0.96,

Table 5.2. Summarized results of the screen-printed Ag/C strain gauge.

Load (Kg)	Strain (με)	Strain (%)	Linear Sensitivity ΔR/R (%)		Transverse Sensitivity ΔR/R (%)	
			Tensile	Compressive	Tensile	Compressive
0.2	140.76	0.01	0.020 ± 0.001	0.025 ± 0.003	0.006 ± 0.001	0.011 ± 0.002
0.5	351.90	0.04	0.058 ± 0.003	0.045 ± 0.001	0.017 ± 0.001	0.020 ± 0.002
1.0	703.81	0.07	0.125 ± 0.003	0.088 ± 0.001	0.050 ± 0.001	0.035 ± 0.001
1.5	1055.71	0.11	0.220 ± 0.003	0.135 ± 0.002	0.102 ± 0.002	0.048 ± 0.002
1.8	1266.85	0.13	0.293 ± 0.002	0.199 ± 0.003	0.139 ± 0.002	0.060 ± 0.001

Table 5.3. Comparison of Ag/C composite and commercial strain gauge factor in linear and transverse direction of load.

	Ag/C		Commercial	
	Tensile	Compressive	Tensile	Compressive
Linear Gauge Factor	2.39	1.47	2.21	2.27
Transverse Gauge Factor	1.18	0.43	0.76	0.78

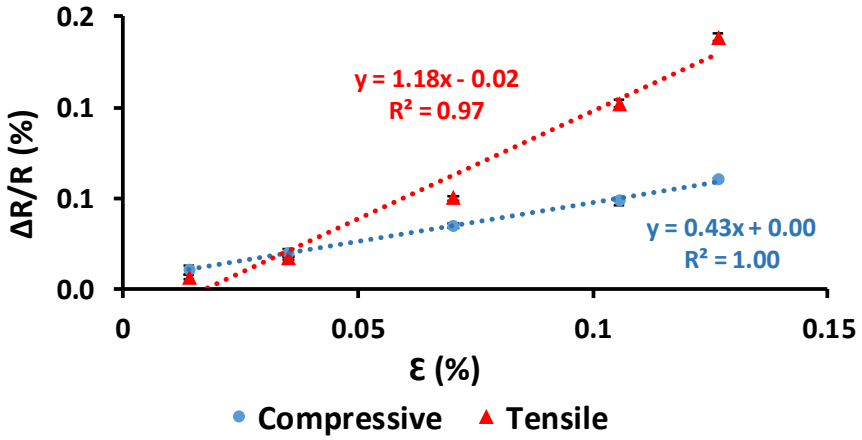

Figure 5.10: Relative resistive change for varying transverse tensile and compressive loads.

was calculated for the printed strain gauge. A summary of the results of the Ag/C composite strain gauge towards tensile and compressive strain is given Table 5.2. The results demonstrate the capability of the printed Ag/C composite strain gauge to detect tensile and compressive loads.

The performance of the screen-printed Ag/C strain gauge was compared to a linear patterned commercial strain gauge (CEA-13-250UN-350, Vishay Precision Group) with a gauge resistance of 350 Ω. The commercial sensor was also attached to the aluminum beam and the experiment was performed in a similar manner. Linear gauge factor for tensile and compressive loads were calculated as 2.21 and 2.27 respectively. A comparison of the tensile and compressive gauge factor between the Ag/C and commercial strain gauge is shown in Table 5.3. It was observed that the tensile response of the Ag/C composite strain gauge is greater than the commercial sensor. However, the compressive gauge factor for the Ag/C composite strain gauge is lower than the commercial strain gauge. According to the theory of tunneling effect, the resistance of the strain gauge is directly dependent on the particle separation distance [675]. Therefore, such non-linear piezoresistive response to tensile and compressive loads can be attributed to the dependence of piezo resistance on bandgap of the inter- atomic spacing [676, 677].

5.3.3. Strain Gauge Transverse Sensitivity

Transverse sensitivity is the response of the strain gauge to loads that are perpendicular to the primary sensing axis. Ideally, it is desirable to have transverse sensitivity of the strain gauge much smaller when compared to the response of the strain gauge to the linear sensing axis [682]. This is because, the directional sensitivity of the strain is an important parameter that needs to be measured to determine at which direction the strain is being applied. The strain gauge is attached on the surface of the aluminum beam transaxially to the application of the load.

Tensile and compressive loads ranging from 0.2 kg to 1.8 kg, corresponding to $\mu\mathcal{E}$ ranging from ~141 to ~1267 were applied on the cantilever beam. The transverse electromechanical response of the sensor was measured, and the results are shown in Fig. 5.10. When tensile strain of 0.01 %, 0.04 %, 0.07 %, 0.11 % and 0.13 %, were applied on the cantilever beam, resistance changes of approximately 0.006 %, 0.017 %, 0.050 %, 0.102 % and 0.139 % were observed, respectively. A transverse tensile gauge factor of 1.18, with a correlation coefficient of 0.97, was calculated.

Similarly, when compressive strain of 0.01 %, 0.04 %, 0.07 %, 0.11 % and 0.13 %, were applied on the beam, resistance changes of approximately 0.011 %, 0.020 %, 0.035 %, 0.048 % and 0.060 % were observed, respectively. A transverse compressive gauge factor of 0.43, with a correlation coefficient of 1.00 was calculated. Finally, the transverse gauge factor for the commercial sensor was also calculated as 0.76 and 0.78 for tensile and compressive loads respectively.

The comparison of the transverse sensitivity for Ag/C composite and commercial strain gauge is tabulated in Table 5.3. The results indicate that the transverse tensile and compressive

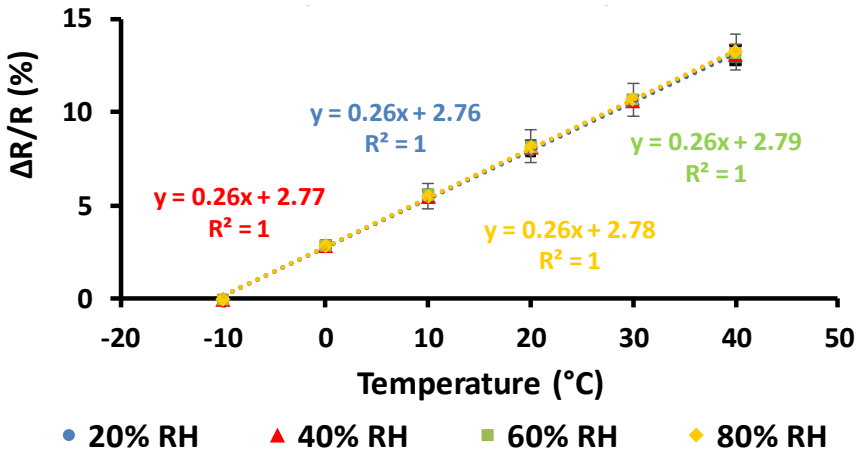

Figure 5.11: Temperature coefficient of the strain gauge at varying ambient temperature and humidity conditions.

sensitivity of the Ag/C strain gauge is lower than its linear tensile and compressive sensitivity by ~50% and ~30% respectively as compared to ~34% for both the instances of the commercial strain gauge.

5.3.4. Temperature Coefficient Resistance

The measured resistance changes for evaluating the TCR of the strain gauge are shown in Fig. 5.11. The temperature of the chamber was increased in steps of 10 °C, starting from -10 °C to 40 °C at 20 % RH. The temperature was similarly incremented for 40 %, 60 % and 80 % RH as well. It was observed that resistance increased by approximately 0.9 Ω for every 1 °C increase in ambient temperature resulting in a temperature coefficient of 0.26 %/°C with a correlation coefficient of one. It was observed that humidity had almost no effect on the base resistance of the strain gauge. The temperature coefficient was constant even when the humidity was varied from 20 % to 80 % RH. Such minimal change can be attributed to the encapsulation layer that was screen printed on top of the sensing layer to protect the strain gauge it from the humidity in ambient conditions.

The temperature sensitivity of the screen-printed strain gauge must be investigated in order to predict the sensor performance in a temperature-varying environment. The temperature sensitivity of the Ag/C ink is a material-related property. Therefore, the thermal effect on the strain gauge response can be mitigated using a dummy gauge compensation technique or calculating the apparent strain using measured temperature data and material properties. One of the methods to alleviate the effect of temperature on strain measurements, the dummy gauge compensation technique in the adjacent arm of the Wheatstone bridge can be utilized [683-687]. The dummy gauge must be identical to the strain gauge under test which is unstrained and placed under the same ambient conditions. Since the active and dummy gauge are in the adjacent arm of the Wheatstone bridge circuit, the thermal effects will cancel, registering only the stress-induced strain [686, 687]. Some of the factors contributing to the thermal output are resistivity change as a function of temperature, thermal stress due to the sensor-substrate thermal expansion coefficient, thermal expansion of the material the strain gauge it is attached to and the transverse sensitivity of the strain gauge. Therefore, the apparent thermal strain (ε_a) can be described by Eq. (5) [688],

$$\varepsilon_a = [\frac{\beta_G}{GF} + \frac{1 + S_t}{1 - v_o S_t}(\alpha_S - \alpha_i)]\Delta T \tag{5}$$

where, β_G and v_o is the linear thermal expansion and Poisson's ratio of material the strain gauge is attached to, respectively. S_t is the transverse sensitivity, ΔT is the ambient change in temperature, α_s and α_i are the linear coefficients of thermal expansion of substrate and ink, respectively.

5.4. Summary

A screen-printed strain gauge based on metal/non-metal composite was successfully fabricated and tested for micro-strain ($\mu\mathcal{E}$) detection. A silver ink was blended with a carbon ink

to achieve a silver-carbon (Ag/C) composite ink to get the desired resistance of ~350 Ω which was printed on a polyimide substrate in a meandering pattern. The strain gauge was then bonded on to a flat aluminum beam and fixed on one end to represent a cantilever structure. The capability of the printed strain gauge to detect linear and transverse strain was investigated by applying varying tensile and compressive loads on the aluminum beam, to simulate $\mu\mathcal{E}$. The performance of the Ag/C composite ink-based strain gauge was benchmarked to a commercial strain gauge with similar gauge resistance. A linear gauge factor of 2.39 and 1.47 for tensile and compressive loads was calculated for the Ag/C composite strain gauge as compared to 2.21 and 2.27 for the commercial foil type strain gauge respectively. Similarly, a transverse gauge factor of 1.18 and 0.43 for tensile and compressive loads was calculated for the Ag/C composite strain gauge as compared to 0.76 and 0.78 for the commercial strain gauge respectively. The results indicate that the linear sensitivity of the screen-printed Ag/C composite strain gauges is more sensitive than standard foil gauge for tensile loads. However, for compressive loads, the linear sensitivity of standard commercial strain gauges is higher than Ag/C composite strain gauges. The temperature coefficient resistance of 0.26 %/°C was also measured in an environmental chamber to analyze the effect of temperature on the Ag/C composite strain gauge. Temperature has a significant effect on the base resistance of the Ag/C strain gauge, however, with proper compensation techniques the effects can be alleviated. It was also observed that humidity has a minimal effect on the base resistance of the strain gauge response, since the sensing layer was enveloped with a screen-printed encapsulation layer. The results demonstrate that a strain gauge with screen-printed Ag/C ink on a polyimide substrate can be utilized for με detection. for structural health monitoring applications. Further research is underway to fabricate strain gauges on different substrates such as thermoplastic polyurethane (TPU) and thin film polyimide that are stretchable and more flexible.

It is in our scope of future research to develop self-temperature compensation (STC) printed strain gauges, utilizing constantan ink-based sensing layer.

CHAPTER VI

CONCLUSION AND FUTURE WORK

6.1 Conclusion

In the course of this dissertation work, the author successfully demonstrated that flexible hybrid electronics can be utilized in applications to fabricating sterilization devices and strain gauges. Flexible microplasma discharge devices were fabricated by laser ablation process to eradicate pathogenic bacteria on surface and liquid media. In addition, silver and carbon composite ink-based strain gauge screen printed on polyimide substrate were fabricated to demonstrate their capability to detect linear and transverse micro-strain for structural health monitoring applications. The results obtained through the research work of all the three projects are listed below:

In the first research project, the voltage distribution and surface DBD of a MDD were modelled in two-dimensional domains using FEA. Initially, the voltage distribution across comb, H-tree and honeycomb-structured MDD was analyzed. Then, the cross-section of an MDD consisting of a polyimide-based dielectric sandwiched between two copper electrodes was used for modelling the microplasma discharge characteristics in an argon environment. A sinusoidal voltage was applied to one of the copper electrodes while the other electrode was grounded. The spatial distribution of electron temperature across the electrodes for varying input voltages was simulated to demonstrate the importance of breakdown voltage. A detailed analysis on the effect of varying electrode and dielectric barrier thicknesses on the electron density and electron temperature was also performed to understand the importance of optimizing device configurations for microplasma discharge. Moreover, the MDD was also simulated at varying ambient temperature and pressure conditions to evaluate their effects on electron temperature and density

across the electrodes. The results from these simulations provide a better understanding of the parameters such as varying input voltage, electrode and dielectric thickness on electron temperature and electron density. This will enable to optimize design parameters for fabricating MDDs for sterilization applications.

In the second project, flexible MDDs were successfully developed for inactivation of Gram-negative bacteria such as *E. coli* and *P. aeruginosa*, using ambient air as the sterilizing agent. The design of the electrodes influences the voltage distribution across the device and is an important contributor to the overall sterilization efficacy. Therefore, the voltage distribution across the top electrode of two different MDDs (designed in comb- and honeycomb-patterns) were analyzed initially using COMSOL Multiphysics® simulation software. The honeycomb-patterned MDD resulted in a uniform distribution of the applied voltage as compared to the comb-structured MDD. The fabrication of MDD was realized by laser patterning flexible copper tape as electrodes and sandwiching PET film as a dielectric layer between electrodes. The efficacy of the MDDs was analyzed by varying parameters such as gap distance between MDD surface and bacteria (1 mm to 9 mm), treatment time (10 seconds to 300 seconds), input DC voltage (4 V to 8 V) and bacterial cell concentrations. Surface temperatures ranging from ~26 °C to ~33 °C were observed as the input voltage was increased from 4 V to 8 V, respectively, for both MDDs. It was observed that the honeycomb-patterned MDD inactivated ~4Log_{10} of *E. coli* and *P. aeruginosa* cells in less than 20 seconds as compared to two minutes for the comb-structured MDD for an input voltage of 10 V. Bacterial viability against varying parameters using comb- and honeycomb-patterned MDDs was analyzed and presented in this project.

Following this, the honeycomb-patterned MDD was employed for inactivating multi-drug resistant Gram-negative (*E coli, P aeruginosa*) and Gram-positive (*S aureus, B. subtilis*) bacteria,

under ambient operating conditions in liquid medium. The efficacy of the MDD to inactivate bacterial cells in phosphate buffer saline (PBS) was investigated by testing the effects of varying treatment times and input voltages, ranging from 1 to 10 minutes and 6 to 10 V, respectively. Around $8\log_{10}$ reduction of bacterial viability was achieved when the MDD was activated for less than 11 minutes at an input voltage of 10 V. The corresponding decimal reduction time was calculated, and it was observed that *E. coli* and *P. aeruginosa* were most resistant to radiation from microplasma with a D-value of around 5 and 1.9, respectively. The flexibility of the device was also tested by bending the MDD on surfaces with a radius of curvature of 25 mm and 50 mm. The calculated power density of the MDD in bent condition and flat state was same, clearly indicating that the MDD is flexible. The optical spectra of the microplasma radiation and surface temperature of the MDD were also characterized in the project.

In the fourth project, a printed strain gauge based on metal/non-metal composite was successfully fabricated and tested for micro-strain (με) detection. A silver ink was blended with a carbon ink to achieve a silver-carbon (Ag/C) composite ink. The composite ink was then screen printed on a polyimide substrate in a meandering pattern to achieve a desired resistance of ~350 Ω. The printed strain gauge was bonded onto a flat aluminum beam. The capability of the printed strain gauge to detect linear strain was investigated by applying varying tensile and compressive loads on the aluminum beam, to simulate με. Corresponding linear gauge factors for tensile and compressive loads were calculated as 2.26 and 1.47, respectively. In addition, transverse gauge factors for tensile and compressive loads were calculated as 1.18 and 0.43, respectively. The strain gauge had a temperature coefficient resistance of 0.26 %/°C. The screen-printed Ag/C composite strain gauge was also compared to a commercial strain gauge of similar gauge resistance. The results demonstrate that a strain gauge with screen-printed Ag/C and encapsulation ink on a

polyimide substrate can be utilized for μƐ detection. The electromechanical response of the fabricated strain gauge as a function of resistance was investigated and presented in this project.

6.2 Future Work

Based on the experience gained during the course of the doctoral studies, the author believes that the current three projects can be optimized or further improved by implementing some of the following suggestions.

Fabrication of the Flexible Microplasma Device

- Optimizing fabrication of the flexible microplasma discharge device and evaluate alternate fabrication methods
    - Laser patterning the top electrode on PET substrate causes sometimes perforation on the PET substrate. Heat resistant flexible substrates such as polyimide can be utilized that may reduce/ eliminate the risk of perforation during fabricating the top electrode.
    - Additive print manufacturing process such as screen printing can be utilized to print the conductive electrodes on a flexible dielectric substrate and the plasma generation and sterilization efficacy rate for different pathogens should be compared.
- For real-world application, the top and bottom electrodes can be encapsulated to prevent any potential shock to the user without compromising the sterilization efficacy of the current microplasma discharge device.

Sterilize Various Other Microorganisms and Explore Other Applications

- Sterilize other types of microorganisms such as fungi, which include yeasts and molds, and develop the device for healthcare applications.

- Current research was focused on developing and proving the efficacy of devices for surface sterilization. *In-vivo* tests on animals can be investigated for further developing the device for applications such as skin treatment.
- Currently, the microplasma discharge device has proven its effectiveness against opportunistic and drug-resistant pathogens such as *E. coli*, *P. aeruginosa*, *S. aureus* and spore forming bacteria such as *B. subtilis*. Sterilizing fungi, which include yeasts and molds, can further expand the application of the device in food and refrigeration industry.

- There are limited articles available on the effect of microplasma for inactivating viruses. Further research will provide significant knowledge on the efficacy of microplasma devices to inactivate viruses.

Screen Printed Strain Gauge Design and Application

- Various other strain gauge designs such as tee and rectangular rosettes can be fabricated by screen printing. Such printed rosettes can be used to detect strain and loads at 0º, 45º and 90º angles, simultaneously.
- Current printed strain gauges were used in measuring linear and transverse strain. Screen printed strain gauges can be used to investigate its capability to detect shear strain and torque.

REFERENCES

[1] J. W. Judy, "Microelectromechanical systems (MEMS): fabrication, design and applications," Smart materials and Structures, vol. 10, no. 6, p. 1115, 2001.

[2] J. Hafner, M. Teuschel, J. Schrattenholzer, M. Schneider and U. Schmid, "Optimized batch process for organic MEMS devices," Multidisciplinary Digital Publishing Institute Proceedings, vol. 2, no. 13, p. 904, 2018.

[3] A. K. Basu, S. Tatiya, G. Bhatt and S. Bhattacharya, "Fabrication processes for sensors for automotive applications: A review," Sensors for automotive and aerospace applications, pp. 123-142, 2019.

[4] S. E. Lyshevski, "MEMS and NEMS: systems, devices, and structures," CRC Press, 2018.

[5] H. Qu, "CMOS MEMS fabrication technologies and devices," Micromachines, vol. 7, no. 1, p. 14, 2016.

[6] K. Totsu, M. Moriyama and M. Esashi, "MEMS research is better together.," Nature Electronics, vol. 2, no. 4, pp. 134-136, 2019.

[7] J. Zhu, X. Liu, Q. Shi, T. He, Z. Sun, X. Guo, W. Liu, O. Sulaiman, B. Dong and C. Lee, "Development trends and perspectives of future sensors and MEMS/NEMS.," Micromachines, vol. 11, no. 1, p. 7, 2020.

[8] S. Masihi, M. Panahi, S. Hajian, D. Maddipatla, S. Ali, X. Zhang, A. K. Bose, B. B. Narakathu, B. J. Bazuin and M. Z. Atashbar, "A highly sensitive capacitive based dual-axis accelerometer for wearable applications," In 2020 IEEE International Conference on Electro Information Technology (EIT), pp. 557-561, 2020, doi: 10.1109/EIT48999.2020.9208236.

[9] B. B. Narakathu, B. E. Bejcek and M. Z. Atashbar, "Impedance based electrochemical biosensors," In 2009 IEEE Sensors, 2009, doi: 10.1109/ICSENS.2009.5398365.

[10] M. Z. Atashbar, S. Krishnamurthy and G. Korotcenkov, "Basic principles of chemical sensor operation," Chemical Sensors: Fundamentals of Sensing Materials, vol. 1, pp. 1-62, 2010.

[11] Z. Qiu and W. Piyawattanamatha, "New endoscopic imaging technology based on MEMS sensors and actuators.," Micromachines, vol. 8, no. 7, p. 210, 2017.

[12] A. Nastro, M. Ferrari and V. Ferrari, "Double-actuator position-feedback mechanism for adjustable sensitivity in electrostatic-capacitive MEMS force sensors.," Sensors and Actuators A: Physical, vol. 312, p. 112127, 2020.

[13] S. Iqbal and A. Malik, "A review on MEMS based micro displacement amplification mechanisms.," Sensors and Actuators A: Physical, vol. 300, p. 111666, 2019.

[14] C. Baratto, M. Z. Atashbar, G. Faglia and G. Sberveglieri, "Functionalized single-wall carbon nanotube-based gas sensor," Proceedings of the Institution of Mechanical Engineers, Part N: Journal of Nanoengineering and Nanosystems, vol. 1, pp. 17-21, 2007. doi: 10.1243/17403499JNN98

[15] C. Baratto, G. Faglia, M. Ferroni, G. Sberveglieri, M. Z. Atashbar and E. Hrehorova, "Investigation on novel poly (3-hexylthiophene)-ZnO nanocomposite thin films gas sensor," In 2006 IEEE Sensors, pp. 452-455, 2006, doi: 10.1109/ICSENS.2007.355503.

[16] B. B. Narakathu, M. Z. Atashbar, F. A. Abebe, C. S. Eribal and E. Sinn, "Detection of Zn2+ Ions Using a Novel Chemosensor Based on Coumarin Schiff-base Derivatives by Electrochemical and Fluorescence Spectroscopy," Tagungsband, pp. 690-693, 2012, doi 10.5162/IMCS2012/8.2.5.

[17] K. Haisch, M. Z. Atashbar and B. J. Bazuin, "Identification of acoustic wave modes in piezoelectric substrates," In IEEE International Conference on Electro Information Technology (EIT), pp. 5-pp., 2005, doi: 10.1109/EIT.2005.1626993.

[18] S. Gangadaran, V. V. Varadan, V. K. Varadan, K. A. Jose and M. Z. Atashbar, "Love-wave-based ice sensor," In Smart Structures and Materials 1999: Smart Electronics and MEMS, vol. 3673, pp. 287-293, 1999 doi: /10.1117/12.354279.

[19] John Manyala and M. Z. Atashbar, "Electromagnetic actuator dynamic response prediction for an automated mechanical transmission," SAE International Journal of Commercial Vehicles, vol. 6, pp. 1-9, 2013, doi: 10.4271/2012-01-2260.

[20] M. Z. Atashbar, "Nano-sized TiO2 thin film for alcohol sensing application," In IEEE-NANO, 2001.

[21] S. Krishnamurthy, B. J. Bazuin and M. Z. Atashbar, "Wireless SAW sensors reader: architecture and design," in In IEEE International Conference on Electro Information Technology, pp. 6-pp., 2005, doi: 10.1109/EIT.2005.1626992.

[22] C. J. Cheng, C. T. Feng, M. Z. Atashbar, W. Wlodarski and K. Kantar-Zadeh, "Guided SH-SAW Sensing System for Liquid Viscosity Sensing Applications," Sensor Letters, vol. 9, pp. 605 - 608, doi: 10.1166/sl.2011.1572

[23] M. Z. Atashbar, K. Kalantar-Zadeh, S. J. Ippolitto and W. Wlodarski, "Palladium nanowire hydrogen sensor based on a SAW transducer," In 2005 IEEE Sensors, pp. 3-pp., 2005, doi: 10.1109/ICSENS.2005.1597961.

[24] E. Comini, G. Faglia, G. Sberveglieri, M. Z. Atashbar and W. Wlodarski, "Alcohol and organic vapours sensor based on nano-sized TiO/sub 2/thin film," In Conference on Optoelectronic and Microelectronic Materials and Devices. Proceedings, pp. 302-305, 1998, doi: 10.1109/COMMAD.1998.791647.

[25] Z. Ramshani, M. J. Johnson, M. Z. Atashbar and D. B. Go, "A broad area electrospray generated by a piezoelectric transformer," Applied Physics Letters, vol. 109, no. 4, p. 044103, 2016, doi: 10.1063/1.4960153.

[26] J. Manyala and M. Atashbar, "On-Line Lubricants Health Condition Monitoring in Gearbox Application," SAE International Journal of Fuels and Lubricants, vol. 6, no. 3, pp. 907-914, 2013, doi: 10.4271/2013-01-9074.

[27] B. J. Bazuin, M. Z. Atashbar and S. Krishnamurthy, "A prototype burst transceiver for SAW sensors interrogation," In Proceedings of International Conference on Intelligent Sensing and Information Processing, pp. 190-195, 2004, doi: 10.1109/ICISIP.2004.1287650.

[28] P. Wang, Q. Lu and Z. Fan, "Evolutionary design optimization of MEMS: a review of its history and state-of-the-art.," Cluster Computing, vol. 22, no. 4, pp. 9105-9111, 2019.

[29] W. H. Ko, "Early history and challenges of implantable electronics," ACM Journal on Emerging Technologies in Computing Systems (JETC), vol. 8, no. 2, pp. 1-9, 2012.

[30] M. Z. Atashbar and S. Singamaneni, "Room temperature gas sensor based on metallic nanowires," Sensors and Actuators B: Chemical, vol. 111, pp. 13-21, 2005, doi: 10.1016/j.snb.2005.07.034.

[31] M. Z. Atashbar, D. Banerji and S. Singamaneni, "Room-temperature hydrogen sensor based on palladium nanowires," IEEE Sensors Journal, vol. 5, no. 5, pp. 792-797, 2005, 10.1109/JSEN.2004.840837.

[32] A. Eshkeiti, B. B. Narakathu, A. S. G. Reddy, A. Moorthi, M. Z. Atashbar, E. Rebrosova, M. Rebros and M. Joyce, "Detection of heavy metal compounds using a novel inkjet printed surface enhanced Raman spectroscopy (SERS) substrate," Sensors and Actuators B: Chemical, vol. 171, pp. 705-711, 2012, doi: 10.1016/j.snb.2012.05.060.

[33] B. B. Narakathu, M. Z. Atashbar and B. E. Bejcek, "Improved detection limits of toxic biochemical species based on impedance measurements in electrochemical biosensors," Biosensors and Bioelectronics, vol. 26, no. 2, pp. 923-928, 2010, doi: 10.1016/j.bios.2010.06.051.

[34] C. Cantalini, M. Z. Atashbar, Y. Li, M. K. Ghantasala, S. Santucci, W. Wlodarski and M. Passacantando, "Characterization of sol-gel prepared WO3 thin films as a gas sensor," Journal of Vacuum Science & Technology A: Vacuum, Surfaces, vol. 17, no. 4, pp. 1873-1879, 1999, doi: 10.1116/1.581698.

[35] E. E. Aktakka, H. Kim, M. Z. Atashbar and K. Najafi, "Mechanical energy scavenging from flying insects," in Solid-State Sensors, Actuators, and Microsystems Workshop, 2008.

[36] J. O. Manyala, T. Fritz and M. Z. Atashbar, "Gearbox speed sensor design and performance optimization," IEEE Sensors Journal, vol. 13, no. 2, pp. 629-636, 2012, doi: 10.1109/JSEN.2012.2224862.

[37] B. B. Narakathu, M. Z. Atashbar and B. Bejcek, "Pico-mole level detection of toxic bio/chemical species using impedance based electrochemical biosensors," Sensor Letters, vol. 9, no. 2, pp. 872-875, 2011, doi: 10.1166/sl.2011.1634.

[38] I. E. Obuh, V. Doychinov, D. P. Steenson, P. Akkaraekthalin, I. D. Robertson and N. Somjit, "Low-cost microfabrication for MEMS switches and varactors," IEEE Transactions on Components, Packaging and Manufacturing Technology , vol. 8, no. 9, pp. 1702-1710, 2018.

[39] A. A. Chlaihawi, B. B. Narakathu, S. Emamian, A. Eshkeiti, S. G. A. Reddy, B. J. Bazuin and M. Z. Atashbar, "Development of flexible dry ECG electrodes based on MWCNT/PDMS composite," In 2015 IEEE sensors, pp. 1-4, 2015, doi: 10.1109/ICSENS.2015.7370218.

[40] V. Palaniappan, S. Masihi, M. Panahi, D. Maddipatla, A. K. Bose, X. Zhang, B. B. Narakathu, B. J. Bazuin and M. Z. Atashbar, "Laser-assisted fabrication of flexible micro-structured pressure sensor for low pressure applications," In 2019 IEEE International Conference on Flexible and Printable Sensors and Systems (FLEPS), pp. 1-3, 2019, doi: 10.1109/FLEPS.2019.8792235.

[41] X. Zhang, D. He, D. Maddipatla, Q. Yang and M. Z. Atashbar, "A Novel Integrated MWCNTs/PDMS based Flexible Triboelectric Nanogenerator," In 2021 IEEE International Flexible Electronics Technology Conference (IFETC), pp. 0029-0031, 2021, doi: 10.1109/IFETC49530.2021.9580508.

[42] T. S. Saeed, D. Maddipatla, B. B. Narakathu, S. S. Albalawi, S. O. Obare and M. Z. Atashbar, "Synthesis of a novel hexaazatriphenylene derivative for the selective detection of copper ions in aqueous solution," RSC Advances, vol. 9, no. 68, pp. 39824-39833, 2019, doi: 10.1039/C9RA08825C.

[43] S. Hajian, S. M. Tabatabaei, B. B. Narakathu, D. Maddipatla, S. Masihi, M. Panahi, P. D. Fleming, B. J. Bazuin and M. Z. Atashbar, "Chlorine-terminated Titanium Carbide MXene as Nitrogen Oxide Gas Sensor: A First-Principles Study," in IEEE International Conference on Flexible and

Printable Sensors and Systems (FLEPS), pp. 1-4, 2021, doi: https://doi.org/10.1109/FLEPS51544.2021.9469784.

[44] H. Li, Y. Ma and Y. Huang, "Material innovation and mechanics design for substrates and encapsulation of flexible electronics: a review," Materials Horizons, vol. 8, no. 2, pp. 383-400, 2021.

[45] R. Saleh, M. Barth, W. Eberhardt and A. Zimmermann, "Bending setups for reliability investigation of flexible electronics," Micromachines , vol. 12, no. 1, p. 78, 2021.

[46] S. Masihi, M. Panahi, D. Maddipatla, A. K. Bose, X. Zhang, A. J. Hanson, B. B. Narakathu, B. J. Bazuin and M. Z. Atashbar, "Development of a flexible tunable and compact microstrip antenna via laser assisted patterning of copper film," IEEE Sensors Journal , vol. 20, no. 14, pp. 7579-7587, 2020, doi: 10.1109/JSEN.2020.2987318.

[47] A. K. Bose, D. Maddipatla, X. Zhang, M. Panahi, S. Masihi, B. B. Narakathu, B. J. Bazuin and M. Z. Atashbar, "Screen printed silver/carbon composite strain gauge on a TPU platform for wearable applications," in In 2020 IEEE International Conference on Flexible and Printable Sensors and Systems (FLEPS), pp. 1-4, 2020, doi: 10.1109/FLEPS49123.2020.9239547.

[48] X. Zhang, D. Maddipatla, A. K. Bose, B. B. Narakathu and M. Z. Atashbar, "A printed MWCNTs/PDMS based flexible resistive temperature detector," in In 2020 IEEE International Conference on Electro Information Technology (EIT), pp. 509-513, 2020, doi: 10.1109/EIT48999.2020.9208334.

[49] A. K. Bose, D. Maddipatla, B. B. Narakathu, B. J. Bazuin and M. Z. Atashbar, "Laser-assisted patterning of a flexible microplasma discharge device for heavy metal and salt detection in ambient air," in In 2019 IEEE International Conference on Flexible and Printable Sensors and Systems (FLEPS), pp. 1-4, 2019, doi: 10.1109/FLEPS.2019.8792243.

[50] X. Zhang, D. Maddipatla, A. K. Bose, B. B. Narakathu, J. D. Williams, M. F. Mitchell and M. Z. Atashbar, "Effect of excitation signal frequency on the electrical response of a MWCNT/HEC composite based humidity sensor," In 2020 IEEE Sensors, pp. 1-4, 2020, 10.1109/SENSORS47125.2020.9278817.

[51] M. M. Ali, D. Maddipatla, B. B. Narakathu, A. A. Chlaihawi, S. Emamian, F. Janabi, B. J. Bazuin and M. Z. Atashbar, "Printed strain sensor based on silver nanowire/silver flake composite on flexible and stretchable TPU substrate," Sensors and Actuators A: Physical, vol. 274, pp. 109-115, 2018, doi: 10.1016/j.sna.2018.03.003.

[52] M. Z. Atashbar, B. Bejcek, S. Singamaneni and S. Santucci, "Carbon nanotube based biosensors," In IEEE Sensors, pp. 1048-1051, 2004, doi: 10.1109/ICSENS.2004.1426354.

[53] V. Palaniappan, S. Masihi, M. Panahi, D. Maddipatla, A. K. Bose, X. Zhang, B. B. Narakathu, B. J. Bazuin and M. Z. Atashbar, "Laser-assisted fabrication of a highly sensitive and flexible micro pyramid-structured pressure sensor for E-skin applications," IEEE Sensors Journal, vol. 20, no. 14, pp. 7605-7613, 2020, doi: 10.1109/JSEN.2020.2989146.

[54] M. Hosseini, M. Javad and R. A. Nawrocki, "A Review of the Progress of Thin-Film Transistors and Their Technologies for Flexible Electronics," Micromachines , vol. 12, no. 6, p. 655, 2021.

[55] Y. Ni, Y. Wang and W. Xu, "Recent process of flexible transistor-structured memory," Small, vol. 17, no. 9, p. 1905332, 2021.

[56] M. Panahi, S. Masihi, D. Maddipatla, A. K. Bose, S. Hajian, A. J. Hanson, V. Palaniappan, B. B. Narakathu, B. J. Bazuin and M. Z. Atashbar, "Investigation of temperature effect on the porosity

of a fabric based porous capacitive pressure sensor," in In 2020 IEEE International Conference on Flexible and Printable Sensors and Systems (FLEPS), pp. 1-4, 2020, doi: 10.1109/FLEPS49123.2020.9239439.

[57] X. Zhang, A. K. Bose, D. Maddipatla, S. Masihi, V. Palaniappan, M. Panahi, B. B. Narakathu and M. Z. Atashbar, "Development of a novel and flexible MWCNT/PDMS based resistive force sensor," in In 2020 IEEE International Conference on Flexible and Printable Sensors and Systems (FLEPS), pp. 1-4, 2020, doi: 10.1109/FLEPS49123.2020.9239548.

[58] S. Masihi, M. Panahi, D. Maddipatla, S. Hajian, A. Bose, V. Palaniappan, B. B. Narakathu and B. J. B. M. Z. A. , "Cohesion Failure Analysis in a Bi-layered Copper/Kapton Structure for Flexible Hybrid Electronic Sensing Applications," in 2021 IEEE International Conference on Electro Information Technology (EIT), pp. 409-412, 2021, doi: 10.1109/EIT51626.2021.9491906.

[59] A. S. G. Reddy, A. Eshkeiti, B. B. Narakathu, M. Rebros, E. Rebrosova, M. Joyce and M. Z. Atashbar, "Fully printed wireless LC sensor for heavy metal detection," In Proceedings IMCS 2012, pp.1191-1194, 2012, doi: 10.5162/IMCS2012/P1.9.12.

[60] S. Hajian, P. Khakbaz, B. B. Narakathu, S. Masihi, M. Panahi, D. Maddipatla, V. Palaniappan, R. G. Blair, B. J. Bazuin and M. Z. Atashbar, "Humidity sensing properties of halogenated graphene: A comparison of fluorinated graphene and chlorinated graphene," in 2020 IEEE International Conference on Flexible and Printable Sensors and Systems (FLEPS), pp. 1-4, 2020 doi: 10.1109/FLEPS49123.2020.9239564 .

[61] C. D. Do, A. Erbes, J. Yan, K. Soga and A. A. Seshia, "Vacuum packaged low-power resonant MEMS strain sensor," Journal of Microelectromechanical Systems, vol. 25, no. 5, pp. 851-858, 2016.

[62] A. C. Fischer, F. Forsberg, M. Lapisa, S. J. Bleiker, G. Stemme, N. Roxhed and F. Niklaus, "Integrating mems and ics," Microsystems & Nanoengineering, vol. 1, no. 1, pp. 1-16, 2015.

[63] M. Esashi, "MEMS development focusing on collaboration using common facilities: a retrospective view and future directions," Microsystems & Nanoengineering, vol. 7, no. 1, pp. 1-9, 2021.

[64] P. Khakbaz, M. Moshayedi, S. Hajian, M. Soleimani, B. B. Narakathu, B. J. Bazuin, M. Pourfath and M. Z. Atashbar, "Titanium Carbide MXene as NH3 Sensor: Realistic First-Principles Study," The Journal of Physical Chemistry C, vol. 123, no. 49, pp. 29794-29803, 2019, doi: 10.1021/acs.jpcc.9b09823.

[65] H. Lim, H. S. Kim, R. Qazi, Y. Kwon, J. Jeong and W. Yeo, "Advanced soft materials, sensor integrations, and applications of wearable flexible hybrid electronics in healthcare, energy, and environment," Advanced Materials, vol. 32, no. 15, p. 1901924, 2020.

[66] Y. Ma, Y. Zhang, S. Cai, Z. Han, X. Liu, F. Wang, Y. Cao, H. L. Y. C. Z. Wang and X. Feng, "Flexible hybrid electronics for digital healthcare," Advanced Materials, vol. 32, no. 15, p. 1902062, 2020.

[67] Y. Khan, A. Thielens, S. Muin, J. Ting, C. Baumbauer and A. C. Arias, "A new frontier of printed electronics: flexible hybrid electronics," Advanced Materials, vol. 32, no. 15, p. 1905279, 2020.

[68] "Future Trends and Business Size and Share with Revenue Forecast to 2026," MarketWatch, 1st February 2022. [Online]. Available: https://www.marketwatch.com/press-release/flexible-hybrid-electronics-fhe-market-2022-with-growth-opportunities-top-countries-data-future-trends-and-

business-size-and-share-with-revenue-forecast-to-2026-2022-02-01#:~:text=Electronics%20(FHE)%20Market-,The. [Accessed 26th February 2022].

[69] D. M. Dyson, "Printed and Flexible Sensors 2022-2032: Technologies, Players, Markets," IDTechEX, [Online]. Available: https://www.idtechex.com/en/research-report/printed-and-flexible-sensors-2022-2032-technologies-players-markets/838. [Accessed 26th February 2022].

[70] R. Dar and D. X. He, "Flexible, Printed and Organic Electronics 2020-2030: Forecasts, Technologies, Markets," IDTechEX, [Online]. Available: https://www.idtechex.com/en/research-report/flexible-printed-and-organic-electronics-2020-2030-forecasts-technologies-markets/687. [Accessed 26th February 2022].

[71] T. H. Phung, A. N. Gafurov, I. Kim, S. Y. Kim, K. M. Kim and T.-M. Lee, "IoT device fabrication using roll-to-roll printing process," Scientific Reports, vol. 11, no. 1, pp. 1-11, 2021.

[72] R. Pirmagomedov and Y. Koucheryavy, "IoT technologies for Augmented Human: A survey," Internet of Things, vol. 14, p. 100120, 2021.

[73] "Flexible Hybrid Electronics (FHE) Market - Growth, Trends, COVID-19 Impact, and Forecasts (2022 - 2027)," Mordor Intelligence, [Online]. Available: https://www.mordorintelligence.com/industry-reports/flexible-hybrid-electronics-market#. [Accessed 12 2 2022].

[74] D. M. Dyson, IDTechEX, [Online]. Available: https://www.idtechex.com/en/research-article/flexible-hybrid-electronics-future-of-flexible-printed-circuit-boards/20603. [Accessed 12 2 2022].

[75] Y. Huang, H. Wu, C. Zhu, W. Xiong, F. Chen, L. Xiao, J. Liu, K. Wang, H. Li, D. Ye and Y. Duan, "Programmable robotized ‘transfer-and-jet’printing for large, 3D curved electronics on complex surfaces," International Journal of Extreme Manufacturing, vol. 3, no. 4, p. 045101, 2021.

[76] R. Nolden, K. Zöll and A. Schwarz-Pfeiffer, "Development of flexible and functional sequins using subtractive technology and 3d printing for embroidered wearable textile applications," Materials, vol. 14, no. 10, p. 2633, 2021.

[77] E. R. Griffiths and S. J. Leigh, "Hybrid additive manufacture: Surface finishing methods for improving conductivity of inkjet printed tracks on non-planar substrates fabricated using fused deposition modeling," Sensors and Actuators A: Physical , vol. 333, p. 113235, 2022.

[78] D. Maddipatla, X. Zhang, A. K. Bose, S. Masihi, M. Panahi, V. Palaniappan, B. B. Narakathu, B. J. Bazuin and M. Z. Atashbar, "Development of a flexible force sensor using additive print manufacturing process," In 2019 IEEE International Conference on Flexible and Printable Sensors and Systems, pp. 1-3, 2019, doi: 10.1109/FLEPS.2019.8792307.

[79] V. Palaniappan, D. M. M. Panahi, S. Masihi, A. K. Bose, X. Zhang, S. Hajian, B. B. Narakathu, B. J. Bazuin and M. Z. A. , "Highly sensitive and flexible M-tooth based hybrid micro-structured capacitive pressure sensor," In 2020 IEEE International Conference on Flexible and Printable Sensors and Systems (FLEPS), pp. 1-3, 2020, doi: 10.1109/FLEPS49123.2020.9239447.

[80] S. Masihi, M. Panahi, A. K. Bose, D. Maddipatla, A. J. Hanson, B. B. Narakathu, B. J. Bazuin and M. Z. Atashbar, "Rapid prototyping of a tunable and compact microstrip antenna by laser machining flexible copper tape," in In 2019 IEEE International Conference on Flexible and Printable Sensors and Systems (FLEPS), 2019.

[81] A. J. Hanson, D. Maddipatla, A. K. Bose, C. J. Kosik, S. Hajian, M. Panahi, S. Masihi, B. B. Narakathu, B. J. Bazuin and M. Z. Atashbar, "Flexible and Portable Electrochemical System for

the Detection of Analytes," in 2021 IEEE International Conference on Flexible and Printable Sensors and Systems (FLEPS), pp. 1-3, 2021, doi: 10.1109/FLEPS.2019.8792295.

[82] A. S. G. Reddy, B. B. Narakathu, M. Z. Atashbar, M. Rebros and M. J. E Hrehorova, "Printed electrochemical based biosensors on flexible substrates," In 2010 IEEE Sensors, pp. 1596-1600, 2010, doi: 10.1109/ICSENS.2010.5690281.

[83] S. Masihi, M. Panahi, D. Maddipatla, A. K. Bose, X. Zhang, A. J. Hanson, V. Palaniappan, B. B. Narakathu, B. J. Bazuin and M. Z. A. , "A novel printed fabric based porous capacitive pressure sensor for flexible electronic applications," In 2019 IEEE sensors, pp. 1-4, 2019, doi: 10.1109/SENSORS43011.2019.8956672.

[84] V. S. Turkani, B. B. Narakathu, D. Maddipatla, B. N. Altay, P. D. Fleming, B. J. Bazuin and M. Z. Atashbar, "Nickel based printed resistance temperature detector on flexible polyimide substrate," In 2018 IEEE Sensors, pp. 1-4, 2018, doi: 10.1109/ICSENS.2018.8589549.

[85] J. Shin, J. Ko, S. Jeong, P. Won, Y. Lee, J. Kim, S. Hong, N. L. Jeon and S. H. Ko, "Monolithic digital patterning of polydimethylsiloxane with successive laser pyrolysis," Nature Materials, vol. 20, no. 1, pp. 100-107, 2021.

[86] J. Lim, S. Park, H. Cho, Y. Lee, I. Ha, Y. Kim, E. Hwang, H. Lee, J. Shin, J. Kwon and S. H. Ko, "Monolithic digital patterning of polyimide by laser-induced pyrolytic jetting," Chemical Engineering Journal, vol. 428, p. 131050, 2022.

[87] A. J. Hanson, D. Maddipatla, A. K. Bose, C. J. Kosik, S. Hajian, M. Panahi, S. Masihi, B. B. Narakathu, B. J. Bazuin and M. Z. Atashbar, "Designing and development of a handheld portable electrochemical analyzer for flexible hybrid electronics," In 2021 IEEE International Conference on Electro Information Technology (EIT), pp. 1-4; 2021, doi: 10.1109/EIT51626.2021.9491877.

[88] D. Maddipatla, B. B. Narakathu, V. S. Turkani, S. Hajian, B. J. Bazuin and M. Z. Atashbar, "A flexible copper based electrochemical sensor using laser-assisted patterning process," In 2018 IEEE Sensors, pp. 1-4, 2018, doi: 10.1109/ICSENS.2018.8589754.

[89] V. B. Nam and D. Lee, "Evaluation of Ni-Based Flexible Resistance Temperature Detectors Fabricated by Laser Digital Pattering," Nanomaterials , vol. 11, no. 3, p. 576, 2021.

[90] Y. Wang, Y. Gao, Y. Liu, Z. Gao, Y. Su and Q. Zhang, "Optimal aperture and digital speckle optimization in digital image correlation," Experimental Mechanics, vol. 61, no. 4, pp. 677-684, 2021.

[91] M. Wang, Y. Yang and W. Gao, "Laser-engraved graphene for flexible and wearable electronics," Trends in Chemistry, vol. 3, no. 11, pp. 969-981, 2021.

[92] D. Maddipatla, B. B. Narakathu and M. Atashbar, "Recent progress in manufacturing techniques of printed and flexible sensors: a review," Biosensors, vol. 10, no. 12, p. 199, 2020, doi: 10.3390/bios10120199.

[93] A. Das, E. L. Gilmer, S. Biria and M. J. Bortner, "Importance of polymer rheology on material extrusion additive manufacturing: Correlating process physics to print properties," ACS Applied Polymer Materials, vol. 3, no. 3, pp. 1218-1249, 2021.

[94] M. Joyce, P. D. F. III, S. G. Avuthu, S. Emamian, A. Eshkeiti, M. Atashbar and T. Donato, "Contribution of flexo process variables to fine line Ag electrode performance," International Journal of Engineering Research & Technology, vol. 3, no. 8, pp. 1645-1656, 2014.

[95] H. Kipphan, Handbook of Print Media: Technologies and Production Methods, New York: Springer, 2001.

[96] J. P. Metters, R. O. Kadara and C. E. Banks, "New directions in screen printed electroanalytical sensors: An overview," Analyst, vol. 136, pp. 1067-1076, 2011.

[97] S. Emamian, B. B. Narakathu, A. A. Chlaihawi, B. J. Bazuin and M. Z. Atashbar, "Screen printing of flexible piezoelectric based device on polyethylene terephthalate (PET) and paper for touch and force sensing applications," Sensors and Actuators A: Physical, vol. 263, pp. 639-647, 2017, doi: 10.1016/j.sna.2017.07.045.

[98] A. Moorthi, B. B. Narakathu, A. S. G. Reddy, A. Eshkeiti, H. Bohra and M. Z. Atashbar, "A novel flexible strain gauge sensor fabricated using screen printing," In 2012 Sixth International Conference on Sensing Technology (ICST), pp. 765-768, 2012, doi: 10.1109/ICSensT.2012.6461780.

[99] A. A. Chlaihawi, S. Emamian, B. B. Narakathu, B. J. Bazuin and M. Z. Atashbar, "Novel screen printed and flexible low frequency magneto-electric energy harvester," In 2016 IEEE Sensors, pp. 1-3, 2016, doi: 10.1109/ICSENS.2016.7808947 .

[100] N. Zavanelli and W.-H. Yeo, "Advances in screen printing of conductive nanomaterials for stretchable electronics," ACS Omega, vol. 6, no. 14, pp. 9344-9351, 2021.

[101] T. M. Eggenhuisen, Y. Galagan, A. F. K. V. Biezemans, T. M. W. L. Slaats, W. P. Voorthuijzen, S. Kommeren, S. Shanmugam, J. P. Teunissen, A. Hadipour, W. J. H. Verhees and S. C. Veenstra, "High efficiency, fully inkjet printed organic solar cells with freedom of design," Journal of Materials Chemistry A, vol. 3, no. 14, pp. 7255-7262, 2015.

[102] D. Corzo, K. Almasabi, E. Bihar, S. Macphee, D. Rosas-Villalva, N. Gasparini, S. Inal and D. Baran, "Digital inkjet printing of high-efficiency large-area nonfullerene organic solar cells," Advanced Materials Technologies, vol. 4, no. 7, p. 1900040, 2019.

[103] A. Eshkeiti, B. B. Narakathu, A. S. G. Reddy, A. Moorthi and M. Z. Atashbar, "A novel inkjet printed surface enhanced Raman spectroscopy (SERS) substrate for the detection of toxic heavy metals," Procedia Engineering, vol. 25, pp. 338-341, 2011, doi: 10.1016/j.proeng.2011.12.083.

[104] S. Lim, M. Joyce, P. D. Fleming, A. T. Aijazi and M. Z. Atashbar, "Inkjet printing and sintering of nano-copper ink," Journal of Imaging Science and Technology, vol. 57, no. 5, pp. 50506-1-50506-7, 2013.

[105] M. Singh, H. M. Haverinen, P. Dhagat and G. E. Jabbour, "Inkjet printing—process and its applications," Advanced materials, vol. 22, no. 6, pp. 673-685, 2010.

[106] S. Shrestha, R. Yerramilli and N. C. Karmakar, "Microwave performance of flexo-printed chipless RFID tags," Flexible and Printed Electronics, vol. 4, no. 4, p. 045003, 2019.

[107] M. Joyce, P. D. F. III, S. G. Avuthu, S. Emamian, A. Eshkeiti, M. Atashbar and T. Donato, "Contribution of flexo process variables to fine line Ag electrode performance," International Journal of Engineering Research & Technology, vol. 3, no. 8, pp. 1645-1656, 2014.

[108] A. Lorenz, A. S. J. Rohde, S. Kroh, M. Wittenberg, K. Krüger, F. Clement and D. Biro, "Evaluation of flexographic printing technology for multi-busbar solar cells," Energy Procedia, vol. 67, pp. 126-137, 2015.

[109] H. Kang, H. Park, Y. Park, M. Jung, B. C. Kim, G. Wallace and G. Cho, "Fully roll-to-roll gravure printable wireless (13.56 MHz) sensor-signage tags for smart packaging," Scientific reports, vol. 4, no. 1, pp. 1-7, 2014.

[110] H. Zhu, B. B. Narakathu, Z. Fang, A. T. Aijazi, M. Joyce, M. Atashbar and L. Hu, "A gravure printed antenna on shape-stable transparent nanopaper," Nanoscale, vol. 6, no. 15, pp. 9110-9115, 2014, doi: https://doi.org/10.1039/C4NR02036G.

[111] S. Emamian, A. Eshkeiti, B. B. Narakathu, S. G. R. Avuthu and M. Z. Atashbar, "Gravure printed flexible surface enhanced Raman spectroscopy (SERS) substrate for detection of 2, 4-dinitrotoluene (DNT) vapor," Sensors and Actuators B: Chemical, vol. 217, pp. 129-135, 2015, doi: 10.1016/j.snb.2014.10.069.

[112] A. Eshkeiti, M. Rezaei, B. B. Narakathu, A. S. G. Reddy, S. Emamian and M. Z. Atashbar, "Gravure printed paper based substrate for detection of heavy metals using surface enhanced Raman spectroscopy (SERS)," In 2013 IEEE Sensors, pp. 1-4, 2013, doi: 10.1109/ICSENS.2013.6688292.

[113] E. B. Secor, S. Lim, H. Zhang, C. D. Frisbie, L. F. Francis and M. C. Hersam, "Gravure printing of graphene for large-area flexible electronics," Advanced materials, vol. 26, no. 26, pp. 4533-4538, 2014.

[114] G. L. Goh, H. Zhang, T. H. Chong and W. Y. Yeong, "3D printing of multilayered and multimaterial electronics: A review," Advanced Electronic Materials, vol. 7, no. 10, p. 2100445, 2021.

[115] J. Li, C. Wu, P. K. Chu and M. Gelinsky, "3D printing of hydrogels: Rational design strategies and emerging biomedical applications," Materials Science and Engineering R: Reports, vol. 140, p. 100543, 2020.

[116] A. Dawood, B. M. Marti, V. Sauret-Jackson and A. Darwood, "3D printing in dentistry," British dental journal, vol. 219, no. 11, pp. 521-529, 2015.

[117] B. Liu, A. K. Bose, X. Zhang and Z. Zhang, "CB/PDMS based strain gauge using 3D Printed mold," in In 2021 IEEE International Conference on Electro Information Technology (EIT), 2021.

[118] Y. Zhang, Y. Zhu, S. Zheng, L. Zhang, X. Shi, J. He, X. Chou and Z.-S. Wu, "Ink formulation, scalable applications and challenging perspectives of screen printing for emerging printed microelectronics," Journal of Energy Chemistry, 2021.

[119] B. F. Gonçalves, A. P. LaGrow, S. Pyrlin, B. Owens-Baird, G. Botelho, L. S. Marques, M. Ramos, K. Kovnir, S. Lanceros-Mendez and Y. V. Kolen'ko, "Large-Scale Synthesis of Semiconducting Cu (In, Ga) Se2 Nanoparticles for Screen Printing Application," Nanomaterials , vol. 11, no. 5, p. 1148, 2021.

[120] S. Emamian, A. A. Chlaihawi, B. B. Narakathu, B. J. Bazuin and M. Z. Atashbar, "A piezoelectric based vibration energy harvester fabricated using screen printing technique," In 2016 IEEE Sensors, pp. 1-3, 2016, doi: 10.1109/ICSENS.2016.7808560.

[121] B. Huang, E. Chen, L. Sun and T. Guo, "Quantum-dot color conversion film patterned by screen printing and overprinting process for display backlights," Optics & Laser Technology, vol. 145, p. 107486, 2022.

[122] A. R. B. Salman, M. M. Ismail and J. A. Razak, "State of Art Printing Technique for Wearable Communication Antenna," in In Proceedings of the 11th International Conference on Robotics, Vision, Signal Processing and Power Applications, Singapore, 2022.

[123] A. K. Bose, X. Zhang, D. Maddipatla, S. Masihi, M. Panahi, B. B. Narakathu, B. J. Bazuin, J. D. Williams, M. F. Mitchell and M. Z. Atashbar, "Screen-Printed Strain Gauge for Micro-Strain Detection Applications.",," IEEE Sensors Journal, vol. 20, no. 21, pp. 12652-12660, 2020, doi: 10.1109/JSEN.2020.3002388.

[124] D. Maddipatla, X. Zhang, A. K. Bose, S. Masihi, B. B. Narakathu, B. J. Bazuin, J. D. Williams, M. F. Mitchell and M. Z. Atashbar, "A Polyimide Based Force Sensor Fabricated Using Additive Screen-Printing Process for Flexible Electronics," IEEE Access, vol. 8, pp. 207813-207821, 2020, doi: 10.1109/ACCESS.2020.3037703.

[125] X. Zhang, D. Maddipatla, A. K. Bose, S. Hajian, B. B. Narakathu, J. D. Williams, M. F. Mitchell and M. Z. Atashbar, "Printed Carbon Nanotubes-Based Flexible Resistive Humidity Sensor," IEEE Sensors Journal, vol. 20, no. 21, pp. 12592-12601, 2020, doi: 10.1109/JSEN.2020.3002951.

[126] B. B. Narakathu, M. S. Devadas, A. S. G. Reddy, A. Eshkeiti, A. Moorthi, I. R. Fernando, B. P. Miller, G. Ramakrishna, E. Sinn, M. Joyce, M. Rebros, E. Rebrosova, G. Mezei and M. Z. Atashbar, "Novel fully screen printed flexible electrochemical sensor for the investigation of electron transfer between thiol functionalized viologen and gold clusters," Sensors and Actuators B: Chemical, vol. 176, pp. 768-774, 2013, doi: 10.1016/j.snb.2012.10.069.

[127] V. S. Turkani, D. Maddipatla, B. B. Narakathu, B. N. Altay, D. Fleming, B. J. Bazuin and M. Z. Atashbar, "A Screen-Printed Nickel Based Resistance Temperature Detector (RTD) on Thin Ceramic Substrate," In IEEE EIT Conference, pp. 577-580, 2020, doi: 10.1109/EIT48999.2020.9208252.

[128] K. Bhatt, S. Kumar and C. C. Tripathi, "High-performance ultra-low leakage current graphene-based screen-printed field-effect transistor on paper substrate," Pramana, vol. 94, no. 1, pp. 1-4, 2020.

[129] A. Descoeudres, J. Horzel, B. Paviet-Salomon, L. Senaud, G. Christmann, J. Geissbühler, P. Wyss, N. Badel, J. W. Schüttauf, J. Zhao and C. Allebé, "The versatility of passivating carrier-selective silicon thin films for diverse high-efficiency screen-printed heterojunction-based solar cells," Progress in Photovoltaics: Research and Applications, vol. 28, no. 6, pp. 569-577, 2020.

[130] D. Han, Y. Khan, K. Gopalan, A. Pierre and A. C. Arias, "Emission Area Patterning of Organic Light-Emitting Diodes (OLEDs) via Printed Dielectrics," Advanced Functional Materials , vol. 28, no. 37, p. 1802986, 2018.

[131] A. Eshkeiti, A. S. Reddy, S. Emamian, B. B. Narakathu, M. Joyce, M. Joyce, P. D. Fleming, B. J. Bazuin and M. Z. Atashbar., "Screen printing of multilayered hybrid printed circuit boards on different substrates.," IEEE transactions on components, packaging and manufacturing technology, vol. 5, no. 3, pp. 415-421, 2015, doi: 10.1109/TCPMT.2015.2391012.

[132] A. A. Gabriel, M. C. C. F. Ugay, M. A. T. Siringan, L. M. D. Rosario, R. B. Tumlos and H. J. Ramos, "Atmospheric pressure plasma jet inactivation of Pseudomonas aeruginosa biofilms on stainless steel surfaces," Innovative Food Science & Emerging Technologies, vol. 36, pp. 311-319, 2016.

[133] J. Szulc, W. Urbaniak-Domagała, W. Machnowski, H. Wrzosek, K. Łącka and B. Gutarowska, "Low temperature plasma for textiles disinfection," International Biodeterioration & Biodegradation, vol. 131, pp. 97-106, 2018.

[134] J. G. Birmingham, "Mechanisms of bacterial spore deactivation using ambient pressure nonthermal discharges," IEEE Transactions on Plasma Science, vol. 32, no. 4, pp. 1526-1531, 2004.

[135] A. K. Bose, C. L. Beaver, D. Maddipatla, S. Rossbach and M. Z. Atashbar, "In-vitro Analysis of Thin-Film Microplasma Discharge Devices for Surface Sterilization," IEEE Transactions on Radiation and Plasma Medical Sciences, 2022, doi: 10.1109/TRPMS.2022.3147468.

[136] A. K. Bose, C. L. Beaver, D. Maddipatla, S. Rossbach and M. Z. Atashbar, "Inactivation of B. subtilis Spores Using Flexible Microplasma Discharge Device," In 2021 IEEE International Flexible Electronics Technology Conference (IFETC), pp. pp. 0038-0040, 2021, 10.1109/IFETC49530.2021.9580519.

[137] R. Foest, M. Schmidt and K. Becker, "Microplasmas as an Emerging Field of Low-Temperature Plasma Science and Technology," International Journal of Mass Spectrometry, vol. 248, no. 3, pp. 87-102, 2006.

[138] A. P. Papadakis, S. Rossides and A. C. Metaxas, "Microplasmas: A review.," The Open Applied Physics Journal, vol. 4, no. 1, 2011.

[139] A. K. Bose, C. L. Beaver, D. Maddipatla, S. Rossbach and M. Z. Atashbar, "A Novel and Flexible Microplasma Discharge Device for Inactivating Pathogens Suspended in Fluids," In 2021 IEEE International Conference on Flexible and Printable Sensors and Systems (FLEPS), pp. 1-3, 2021, doi: 10.1109/FLEPS51544.2021.9469733.

[140] V. Palaniappan, S. Masihi, M. Panahi, D. Maddipatla, X. Zhang, B. B. Narakathu, B. J. Bazuin and M. Z. Atashbar, "A porous microstructured dielectric layer based pressure sensor for wearable applications," In 2021 IEEE International Conference on Flexible and Printable Sensors and Systems (FLEPS), pp. 1-3, 2021, doi: 10.1109/FLEPS51544.2021.9469706.

[141] V. Palaniappan, M. Panahi, D. Maddipatla, X. Zhang, S. Masihi, H. R. K. M. Emani, B. B. Narakathu, B. J. Bazuin and M. Z. Atashbar, "Flexible M-Tooth Hybrid Micro-Structure-Based Capacitive Pressure Sensor With High Sensitivity and Wide Sensing Range," IEEE Sensors Journal, vol. 21, no. 23, pp. 26261-26268, 2021, doi: 10.1109/JSEN.2021.3064451.

[142] U. Kogelschatz, B. Eliasson and W. Egli, "Dielectric-Barrier Discharges. Principle and Applications," Journal de Physique IV, vol. 7, no. C4, pp. C4-47, 1997.

[143] U. Kogelschatz, "Dielectric-barrier discharges: their history, discharge physics, and industrial applications," Plasma Chemistry and Plasma Processing, vol. 23, no. 1, pp. 1-46, 2003.

[144] A. Bose, B. Narakathu, B. Bazuin and M. Atashbar, "Modelling and simulation of microplasma discharge device for sterilization applications," In Multidisciplinary Digital Publishing Institute Proceedings, vol. 2, no. 13, p. 948, 2018, doi: 10.3390/proceedings2130948.

[145] J. F. Kolb, A.-A. H. Mohamed, R. O. Price, R. J. Swanson, A. Bowman, R. L. Chiavarini, M. Stacey and K. H. Schoenbach, "Cold atmospheric pressure air plasma jet for medical applications," Applied Physics Letters, vol. 92, no. 24, p. 241501, 2008.

[146] M. Laroussi, "Low-temperature plasma jet for biomedical applications: a review," IEEE transactions on plasma science, vol. 43, no. 3, pp. 703-712, 2015.

[147] H. S. Uhm, E. H. Choi, G. S. Cho and Y. C. Hong, "Sterilization of microbes by using various plasma jets," Journal of the Korean Physical Society, vol. 60, no. 6, pp. 897-902, 2012.

[148] H. S. Uhm and Y. C. Hong, "Various microplasma jets and their sterilization of microbes," Thin Solid Films , vol. 519, no. 20, pp. 6974-6980, 2011.

[149] S. Ma, K. Kim, S. Lee, S. Moon and Y. Hong, "Effects of a porous dielectric in atmospheric-pressure plasma jets submerged in water," Physics of Plasmas, vol. 25, no. 8, p. 083519, 2018.

[150] Y. Yang, J. Guo, X. Zhou, Z. Liu, C. Wang, K. Wang, J. Zhang and Z. Wang, "A novel cold atmospheric pressure air plasma jet for peri-implantitis treatment: An in vitro study," Dental Materials Journal , vol. 37, no. 1, pp. 157-166, 2018.

[151] P. Guo, Y. Liu, J. Li, N. Zhang, M. Zhou, Y. Li, G. Zhao, N. Wang, A. Wang, Y. Wang and F. Wang, " A novel atmospheric-pressure air plasma jet for wound healing," International Wound Journal, 2021.

[152] S. Ma, Y. Kumaresan, A. S. Dahiya and R. Dahiya, "Ultra-Thin Chips with Printed Interconnects on Flexible Foils," Advanced Electronic Materials, p. 2101029, 2021.

[153] V. Palaniappan, S. Masihi, X. Zhang, S. Emamian, A. K. Bose, D. Maddipatla, S. Hajian, M. Panahi, B. B. Narakathu, B. J. Bazuin and M. Z. Atashbar, "A flexible triboelectric nanogenerator fabricated using laser-assisted patterning process," In 2019 IEEE SENSORS, pp. 1-4, 2019, doi: 10.1109/SENSORS43011.2019.8956682 .

[154] J. Xie, Q. Chen, P. Suresh, S. Roy, J. F. White and A. D. Mazzeo, "Paper based plasma sanitizers," Proceedings of the National Academy of Sciences, vol. 114, no. 20, pp. 5119-5124, 2017.

[155] A. K. Bose, C. L. Beaver, D. Maddipatla, S. Rossbach and M. Z. Atashbar, "Laser Ablated Microplasma Discharge Device for Inactivating Bacteria Suspended in Liquid Media," IEEE Sensors Journal, 2021, doi: 10.1109/JSEN.2021.3133507.

[156] J. D. Reis, C. O. Costa and J. S. d. Costa, "Strain gauges debonding fault detection for structural health monitoring," Structural Control and Health Monitoring, vol. 25, no. 12, p. e2264, 2018.

[157] M. Okayasu and T. Yamasaki, "Structural health monitoring system for remote inspection of material failure," Journal of Nondestructive Evaluation, vol. 38, no. 2, pp. 1-6, 2019.

[158] A. K. Bose, X. Zhang, D. Maddipatla, S. Masihi, M. Panahi, B. B. Narakathu, B. J. Bazuin and M. Z. Atashbar, "Highly sensitive screen printed strain gauge for micro-strain detection," in In 2019 IEEE International Conference on Flexible and Printable Sensors and Systems (FLEPS), pp. 1-3, 2019, doi: 10.1109/FLEPS.2019.8792282.

[159] A. K. Sawhney and P. Sawhney, A course in Electrical and Electronic Measurements and Instrumentation, Dhanpat Rai & Company, 2016.

[160] M. Vutukuru, J. Christopher, Z. Chen, D. Bishop and A. Swan, "Generating strain in 2D materials using microelectromechanical systems," in In APS March Meeting Abstracts, 2019.

[161] L. Belsito, M. Ferri, F. Mancarella, L. Masini, J. Yan, A. A. Seshia, K. Soga and A. Roncaglia, "Fabrication of high-resolution strain sensors based on wafer-level vacuum packaged MEMS resonators," Sensors and Actuators A: Physical, vol. 239, pp. 90-101, 2016.

[162] S. Boettger, J. Bonitz, M. Kini, S. E. Schulz and S. Hermann, "Adding CNT-based functionality to MEMS: A technology demonstration for strain and IR sensors on wafer scale." In Micro-Nano-Integration," in In Micro-Nano-Integration; 7th GMM-Workshop, 2018.

[163] "Omega Strain Gauges Product Catalog," Omega Engineering Inc., [Online]. Available: https://www.omega.com/guides/straingages.html. [Accessed 22nd 4 2020].

[164] "Micro-Measurements Strain Gauges Product Catalog," Micro-Measurements, [Online]. Available: https://www.micro- 502. [Accessed 22nd 4 2020].

[165] M. Ahmad, S. Malik, S. Dewan, A. K. Bose, D. Maddipatla, B. B. Narakathu, M. Z. Atashbar and M. S. Baghini, "An auto-calibrated resistive measurement system with low noise instrumentation

ASIC," IEEE Journal of Solid-State Circuits, vol. 55, no. 11, pp. 3036-3050, 2020, doi: 10.1109/JSSC.2020.3017639.

[166] S. Khan, L. Lorenzelli and R. S. Dahiya, "Technologies for printing sensors and electronics over large flexible substrates: a review," IEEE Sensors Journal, vol. 15, no. 6, pp. 3164-3185, 2015.

[167] X. Cao, H. Chen, X. Gu, B. Liu, W. Wang, Y. Cao, F. Wu and C. Zhou, "Screen printing as a scalable and low-cost approach for rigid and flexible thin-film transistors using separated carbon nanotubes," ACS nano , vol. 8, no. 12, pp. 12769-12776, 2014.

[168] A. Sandström and L. Edman, "Towards High-Throughput Coating and Printing of Light-Emitting Electrochemical Cells: A Review and Cost Analysis of Current and Future Methods," Energy Technology, vol. 3, no. 4, pp. 329-339, 2015.

[169] Y. Ma, C. Wang, Y. Li, J. Li, Q. Wan, J. Chen, F. R. Tay and L. Niu, "Considerations and caveats in combating ESKAPE pathogens against nosocomial infections," Advanced Science, vol. 7, no. 1, p. 1901872, 2020.

[170] H. D. Nelson, "Chronic Wounds Affect 6.5 Million in U.S.," Intermountain Healthcare, 25th April 2017. [Online]. Available: https://intermountainhealthcare.org/blogs/topics/live-well/2017/04/chronic-wounds-affect-65-million-in%20us/#:~:text=Known%20as%20the%20silent%20epidemic,U.S.%20National%20Institutes%20of%20Health. [Accessed 20 February 2022].

[171] M. S. Mulani, E. E. Kamble, S. N. Kumkar, M. S. Tawre and K. R. Pardesi, "Emerging strategies to combat ESKAPE pathogens in the era of antimicrobial resistance: a review," Frontiers in microbiology, vol. 10, p. 539, 2019.

[172] "Antibiotic Resistance Threats in The United States," Centers for Disease Control and Prevention, United States Department of Health and Human Services, [Online]. Available: https://www.cdc.gov/drugresistance/pdf/threats-report/2019-ar-threats-report-508.pdf. [Accessed 20 February 2022].

[173] "Antimicrobial resistance," World Health Organization, 17th November 2021. [Online]. Available: https://www.who.int/news-room/fact-sheets/detail/antimicrobial-resistance. [Accessed 20 February 2022].

[174] "How Drug-Resistant E. coli Succeeds as a Public Health Menace," American Society for Microbiology, 23rd April 2019. [Online]. Available: https://asm.org/Press-Releases/2019/April/How-Drug-resistant-E-coli-Succeeds-as-a-Public-Hea. [Accessed 20 February 2022].

[175] "Multi-Drug Resistant Organisms (MDROs)," Provincial Health Services Authority, 2016. [Online]. Available: http://policyandorders.cw.bc.ca/resource-gallery/Documents/Infection%20Control/MDROs_Information_Sheet_for_Patient_and_Families.pdf. [Accessed 20th February 2022].

[176] J. Kwon and P. G. William, "The post-antibiotic era is here," Science, vol. 373, no. 6554, pp. 471-471, 2021.

[177] "Lack of new antibiotics threatens global efforts to contain drug-resistant infections," World Health Organization, 17th January 2020. [Online]. Available: https://www.who.int/news/item/17-01-2020-lack-of-new-antibiotics-threatens-global-efforts-to-contain-drug-resistant-infections. [Accessed 20 Februaury 2022].

[178] "Noscomial Infections & Hospital-Acquired Illnesse - Overview," EHA Consulting Group Inc., [Online]. Available: https://www.ehagroup.com/epidemiology/nosocomial-infections/. [Accessed 20 Februaury 2022].

[179] S. Subramanian, "The Mechanism of DNA Damage by UV Radiation," News Medical Life Sciences, [Online]. Available: https://www.news-medical.net/life-sciences/The-Mechanism-of-DNA-Damage-by-UV-Radiation.aspx. [Accessed 20 February 2022].

[180] D. L. Sai, J. Lee, D. L. Nguyen and Y. P. Kim, "Tailoring photosensitive ROS for advanced photodynamic therapy," Experimental & Molecular Medicine, vol. 53, no. 4, pp. 495-504, 2021.

[181] J. R. A. Cosme, D. C. Gagui, N. H. Green, H. E. Bryant and F. Claeyssens, "In Vitro Low-Fluence Photodynamic Therapy Parameter Screening Using 3D Tumor Spheroids Shows that Fractionated Light Treatments Enhance Phototoxicity," ACS Biomaterials Science & Engineering, vol. 7, no. 11, pp. 5078-5089, 2021.

[182] O. J. Lee, H. W. Ju, G. Khang, P. P. Sun, J. Rivera, J. H. Cho, S.-J. Park, J. G. Eden and C. H. Park, "An experimental burn wound-healing study of non-thermal atmospheric pressure microplasma jet arrays," Journal of Tissue Engineering and Regenerative Medicine, vol. 10, no. 4, pp. 348-357, 2016.

[183] S. Rattanakul and K. Oguma, "Inactivation kinetics and efficiencies of UV-LEDs against Pseudomonas aeruginosa, Legionella pneumophila, and surrogate microorganisms," Water Research, vol. 130, pp. 31-37, 2018.

[184] M. Raeiszadeh and F. Taghipour, "Microplasma UV lamp as a new source for UV-induced water treatment: Protocols for characterization and kinetic study," Water Research, vol. 164, p. 114959, 2019.

[185] S. Dorevitch, K. Anderson, A. Shrestha, D. Wright, A. Odhiambo, J. Oremo and I. Heimler, "Solar Powered Microplasma-Generated Ozone: Assessment of a Novel Point-of-Use Drinking Water Treatment Method," International journal of environmental research and public health, vol. 17, no. 6, p. 1858, 2020.

[186] W. Chiang, D. Mariotti, R. M. Sankaran, J. G. Eden and K. Ostrikov, "Microplasmas for advanced materials and devices," Advanced Materials, vol. 32, no. 18, p. 1905508, 2020.

[187] C. Herring, Cyrus and S.-J. Park, "Large scale, Low Temperature, Microplasma UV Lighting Tiles for Water Purification and Sterilization," Eden Park Illumination, 2019.

[188] R. P. Rastogi, A. Kumar, M. B. Tyagi and R. P. Sinha, "Molecular mechanisms of ultraviolet radiation-induced DNA damage and repair," Journal of nucleic acids, 2010.

[189] S. Pizzimenti, C. Toaldo, P. Pettazzoni, M. U. Dianzani and G. Barrera, "The" two-faced" effects of reactive oxygen species and the lipid peroxidation product 4-hydroxynonenal in," Cancers, vol. 2, no. 2, pp. 338-363, 2010.

[190] K. Lofty, "The impact of the carrier gas composition of non-thermal atmospheric pressure plasma jet for bacteria sterilization.," American Institute of Physics (AIP) Advances, vol. 10, no. 1, p. 015303, 2020.

[191] J. A. Rogers, X. Chen and X. Feng, "Flexible hybrid electronics," Advanced Materials, vol. 32, no. 15, p. e1905590, 2020.

[192] D. Maddipatla, B. B. Narakathu, M. Ochoa, R. Rahimi, J. Zhou, C. K. Yoon, H. Jiang, H. Al-Zubaidi, S. O. Obare, M. A. Zieger, B. Ziaie and M. Z. Atashbar, "Rapid prototyping of a novel

and flexible paper based oxygen sensing patch via additive inkjet printing process," Royal Society of Chemistry Advances, vol. 3, no. 39, pp. 22695-22704, 2019, doi: 10.1039/C9RA02883H.

[193] M. M. Ali, B. B. Narakathu, S. Emamian, A. A. Chlaihawi, F. Aljanabi, D. Maddipatla, B. J. Bazuin and M. Z. Atashbar, "Eutectic Ga-In liquid metal based flexible capacitive pressure sensor," In 2016 IEEE Sensors, pp. 1-4, 2016, doi: 10.1109/ICSENS.2016.7808515.

[194] X. Zhang, V. S. Turkani, S. Hajian, A. K. Bose, D. Maddipatla, A. J. Hanson, B. B. Narakathu and M. Z. Atashbar, "Novel printed carbon nanotubes based resistive humidity sensors," In 2019 IEEE International Conference on Flexible and Printable Sensors and Systems (FLEPS), pp. 1-4 2019, doi: 10.1109/FLEPS.2019.8792298 .

[195] S. Emamian, B. B. Narakathu, A. A. Chlaihawi and M. Z. Atashbar, "Fabrication and characterization of piezoelectric paper based device for touch and force sensing applications," In Procedia engineering, vol. 168, pp.688-6912016, doi: 10.1016/j.proeng.2016.11.248.

[196] D. Birchfield, X. Jackson, T. Pasternak, A. Hanson and M. Atashbar, "Strain sensor fabrication by means of laser carbonization," In 2019 IEEE International Conference on Flexible and Printable Sensors and Systems (FLEPS), pp. 1-3, 2019, doi: 10.1109/FLEPS.2019.8792290.

[197] S. Masihi, M. Panahi, D. Maddipatla, A. J. Hanson, A. K. Bose, S. Hajian, V. Palaniappan, B. B. Narakathu, B. J. Bazuin and M. Z. Atashbar, "Highly Sensitive Porous PDMS-Based Capacitive Pressure Sensors Fabricated on Fabric Platform for Wearable Applications," ACS Sensors, vol. 6, no. 3, pp. 938-949, 2021, doi: 10.1021/acssensors.0c02122.

[198] L. Bonek, S. Fenech, N. Sapoznik, A. J. Hanson, S. Masihi, D. Maddipatla, M. Panahi and M. Z. Atashbar, "Development of a flexible and wireless ECG monitoring device," In 2020 IEEE Sensors, pp. 1-3, 2020, doi: 10.1109/SENSORS47125.2020.9278904 .

[199] X. Zhang, D. He, Q. Yang and M. Z. Atashbar, "Rapid, highly sensitive, and highly repeatable printed porous paper humidity sensor," Chemical Engineering Journal , vol. 433, p. 133751, 2022, doi: 10.1016/j.cej.2021.133751.

[200] J. O. Crosby, H. R. K. M. Emani, X. Zhang, D. Maddipatla, S. Ahmadi, Q. Wu, B. Bazuin, M. Stoops and M. Z. Atashbar, "Development of a Zn/MnO2 Based Flexible Battery," in In 2021 IEEE International Flexible Electronics Technology Conference (IFETC), pp. 0035-0037, 2021, doi: 10.1109/IFETC49530.2021.9580507.

[201] H. R. K. M. Emani, X. Zhang, G. Wang, D. Maddipatla, T. Saeed, Q. Wu, W. Lu and M. Z. Atashbar, "Development of a screen-printed flexible porous graphite electrode for Li-Ion battery," in In 2021 IEEE International Conference on Flexible and Printable Sensors and Systems (FLEPS),pp. 1-4, 2021, doi: 10.1109/FLEPS51544.2021.9469794.

[202] S. Hajian, Binu B. Narakathu, Dinesh Maddipatla, Simin Masihi, Masoud Panahi, R. G. Blair, Bradley J. Bazuin, and Massood Z. Atashbar, "Flexible Temperature Sensor based on Fluorinated Graphene," in In IEEE EIT Confrence, pp. 597-600, 2020, doi: 10.1109/EIT48999.2020.9208256.

[203] R. Qin, M. Hu, N. Zhang, Z. Guo, Z. Yan, J. Li, J. Liu, G. Shan and J. Yang, "Flexible fabrication of flexible electronics: a general laser ablation strategy for robust large-area copper-based electronics," Advanced Electronic Materials, vol. 5, no. 10, p. 1900365, 2019.

[204] V. Palaniappan, M. Panahi, D. Maddipatla, X. Zhang, S. Masihi, H. Emani, B. Narakathu, B. Bazuin and M. Atashbar, "Flexible M-tooth hybrid micro-structure based capacitive pressure sensor with high sensitivity and wide sensing range," IEEE Sensors, vol. 21, no. 23, pp. 26261-26268, 2021, doi: 10.1109/JSEN.2021.3064451.

[205] M. Ochoa, R. Rahimi, J. Zhou, H. Jiang, C. K. Yoon, D. Maddipatla, B. B. Narakathu, V. Jain, M. Oscai, T. J. Morken and R. H. Oliveira, "Integrated sensing and delivery of oxygen for next-generation smart wound dressings," Microsystems & nanoengineering, vol. 6, no. 1, pp. 1-16, 2020, doi: 10.1038/s41378-020-0141-7.

[206] R. Rahimi, U. Brener, S. Chittiboyina, T. Soleimani, D. A. Detwiler, S. A. Lelievre and B. Ziaie, "Laser-enabled fabrication of flexible and transparent pH sensor with near-field communication for in-situ monitoring of wound infection," Sensors and Actuators B: Chemical, vol. 267, pp. 198-207, 2018, doi: 10.1016/j.snb.2018.04.004.

[207] R. Rahimi, M. Ochoa and B. Ziaie, "Direct laser writing of porous-carbon/silver nanocomposite for flexible electronics," ACS applied materials & interfaces, vol. 8, no. 26, pp. 16907-16913, 2016.

[208] R. Rahimi, M. Ochoa, A. Tamayol, S. Khalili, A. Khademhosseini and B. Ziaie, "Highly stretchable potentiometric pH sensor fabricated via laser carbonization and machining of Carbon− Polyaniline composite," ACS applied materials & interfaces, vol. 9, no. 10, pp. 9015-9023, 2017.

[209] D. Maddipatla, F. Janabi, B. B. Narakathu, S. Ali, V. S. Turkani, B. J. Bazuin, P. D. Fleming and M. Z. Atashbar, "Development of a novel wrinkle-structure based SERS substrate for drug detection applications," Sensing and Bio-Sensing Research, vol. 24, p. 100281, 2019, doi: 10.1016/j.sbsr.2019.100281.

[210] X. Zhang, D. He, V. Palaniappan, D. Maddipatla, Q. Yang and M. Z. Atashbar, "A Novel graphite/PDMS based flexible triboelectric nanogenerator," in 2021 IEEE International Conference on Flexible and Printable Sensors and Systems (FLEPS), pp. 1-4, 2021, doi: 10.1109/FLEPS51544.2021.9469812.

[211] E. Klarmann and V. A. Shternov, "Bactericidal value of coal-tar disinfectants," Industrial & Engineering Chemistry Analytical Edition, vol. 8, no. 5, pp. 369-372, 1938.

[212] A. Taj and R. Baqai, "Antimicrobial effects of alum and sulphur on bacteria isolated from mineral and hospital water," Infectious Disease Journal, vol. 16, no. 10, p. 13, 2007.

[213] M. Tijare, D. Smitha, S. Kasetty, S. Kallianpur, S. Gupta and H. V. Amith, "Vinegar as a disinfectant of extracted human teeth for dental educational use," Journal of Oral and Maxillofacial Pathology: JOMFP, vol. 18, no. 1, p. 14, 2014.

[214] E. Mantlo, T. Rhodes, J. Boutros, L. Patterson-Fortin, A. Evans and S. Paessler, "In vitro efficacy of a copper iodine complex PPE disinfectant for SARS-CoV-2 inactivation," F1000Research, vol. 9, 2020.

[215] W. B. Hugo, "A brief history of heat and chemical preservation and disinfection," Journal of applied bacteriology. Oxford , vol. 71, no. 1, pp. 9-18, 1991.

[216] J. Blancou, "History of disinfection from early times until the end of the 18th century," Revue scientifique et technique (International Office of Epizootics), vol. 14, no. 1, pp. 21-39, 1995.

[217] W. B. Hugo, "A brief history of heat, chemical and radiation preservation and disinfection," International biodeterioration & biodegradation, vol. 36, no. 3-4, pp. 197-217, 1995.

[218] W. A. Rutala and D. J. Weber, "Disinfection and sterilization in health care facilities: what clinicians need to know," Clinical infectious diseases, vol. 39, no. 5, pp. 702-709, 2004.

[219] "Infection Control," Centers for Disease Control and Prevention, U.S. Department of Health & Human Services, [Online]. Available:

https://www.cdc.gov/infectioncontrol/guidelines/disinfection/tables/index.html. [Accessed 5th May 2021].

[220] W. A. Rutala and D. J. Weber, "Disinfection and Sterilization in Health Care Facilities: An Overview and Current Issues," Infectious Disease Clinics, vol. 35, no. 3, pp. 575-607, 2021.

[221] W. A. Rutala and D. J. Weber, "Guideline for Disinfection and Sterilization in Healthcare Facilities, 2008," the Healthcare Infection Control Practices Advisory Committee (HICPAC), Department of Health & Human Services USA, Last updated Feb. 15, 2017, 2008.

[222] L. McKeen, "The Effect of Sterilization on Plastics and Elastomers," in Introduction to food irradiation and medical sterilization, William Andrew Publishing, 2012.

[223] G. Panta, A. K. Richardson and I. C. Shaw, "Effectiveness of autoclaving in sterilizing reusable medical devices in healthcare facilities," The Journal of Infection in Developing Countries, vol. 13, no. 10, pp. 858-864, 2019.

[224] A. Götz, A. Wani, H.-C. Langowski and J. Wunderlich, "Food Technologies: Aseptic Packaging," Encyclopedia of Food Safety, vol. 3, pp. 124-134, 2014.

[225] F. Schottroff, T. Pyatkovskyy, K. Reineke, P. Setlow, S. K. Sastry and H. Jaeger, "Mechanisms of enhanced bacterial endospore inactivation during sterilization by ohmic heating," Bioelectrochemistry, vol. 130, p. 107338, 2019.

[226] E. M. Darmady, K. E. A. Hughes, J. D. Jones, D. Prince and W. Tuke, "Sterilization by dry heat," Journal of clinical pathology, vol. 14, no. 1, pp. 38-44, 1961.

[227] P. Phothilangka, M. A. Schoen, M. Huber, P. Luchetta, T. Winkler and B. Wett, "Prediction of thermal hydrolysis pretreatment on anaerobic digestion of waste activated sludge," Water Science and Technology, vol. 58, no. 7, pp. 1467-1473, 2008.

[228] S. Lerouge, "Sterilisation and cleaning of metallic biomaterials," in Metals for Biomedical Devices, Boca Raton, CRC Press, 2010, p. 320.

[229] J. Hoslett, T. M. Massara, S. Malamis, D. Ahmad, I. v. d. Boogaert, E. Katsou, B. Ahmad, H. Ghazal, S. Simons, L. Wrobel and H. Jouhara, "Surface water filtration using granular media and membranes: A review," Science of the Total Environment, vol. 639, pp. 1268-1282, 2018.

[230] V. L. Dhadge, C. R. Medhi, M. Changmai and M. K. Purkait, "House hold unit for the treatment of fluoride, iron, arsenic and microorganism contaminated drinking water," Chemosphere, vol. 199, pp. 728-736, 2018.

[231] A. Ding, J. Wang, D. Lin, X. Tang, X. Cheng, H. Wang, L. Bai, G. Li and H. Liang, "low pressure gravity-driven membrane filtration (GDM) system for rainwater recycling: Flux stabilization and removal performance," Chemosphere, vol. 172, pp. 21-28, 2017.

[232] S. Jain, G. Bhanjana, S. Heydarifard, N. Dilbaghi, M. M. Nazhad, V. Kumar, K.-H. Kim and S. Kumar, "Enhanced antibacterial profile of nanoparticle impregnated cellulose foam filter paper for drinking water filtration," Carbohydrate polymers, vol. 202, pp. 219-226, 2018.

[233] L. Manukyan, P. Li, S. Gustafsson and A. Mihranyan, "Growth media filtration using nanocellulose-based virus removal filter for upstream biopharmaceutical processing," Journal of membrane science, vol. 572, pp. 464-474, 2019.

[234] A. Ottenhall, J. Henschen, J. Illergård and M. Ek, "Cellulose-based water purification using paper filters modified with polyelectrolyte multilayers to remove bacteria from water through

electrostatic interactions," Environmental Science: Water Research & Technology, vol. 4, no. 12, pp. 2070-2079, 2018.

[235] A. Onur, A. Ng, W. Batchelor and G. Garnier, "Multi-layer filters: adsorption and filtration mechanisms for improved separation," Frontiers in chemistry, vol. 6, p. 417, 2018.

[236] J. G. Solon and S. Killeen, "Decontamination and sterilization," Surgery (Oxford), vol. 37, no. 1, pp. 51-57, 2019.

[237] "Chemical Disinfectants," Centers for Disease Control and Prevention, United States Department of Health and Human Services, [Online]. Available: https://www.cdc.gov/infectioncontrol/guidelines/disinfection/disinfection-methods/chemical.html. [Accessed 20th February 2022].

[238] A.-J. T.-T.-A. Razzaq, D. Shnan and A.-B. M. Ali, "Sterilization of Surgical Tools: Removing Bacterial Endospores with a Combination of Povidone-iodine, Chlorhexidine Gluconate, Ethanol, and Methanol," Journal of Pure and Applied Microbiology, vol. 13, no. 4, pp. 2499-2506, 2019.

[239] R. E. Harrington, T. Guda, B. Lambert and J. Martin, "Sterilization and Disinfection of Biomaterials for Medical Devices," In Biomaterials Science, pp. 1431-1446, 2020.

[240] M. Mikhail and T. Young, "Sterilization of flexible endoscopes," In Decontamination in Hospitals and Healthcare, pp. 519-529, 2020.

[241] D. M. Mattox, "Cleaning,," in Handbook of Physical Vapor Deposition (PVD) Processing (Second Edition), William Andrew Publishing, 2010, pp. 475-527.

[242] X. Li and M. Farid, "A review on recent development in non-conventional food sterilization technologies," Journal of Food Engineering, vol. 182, pp. 33-45, 2016.

[243] C. M. Charoux, K. S. Ojha, C. P. O'Donnell, A. Cardoni and B. K. Tiwari, "Applications of airborne ultrasonic technology in the food industry," Journal of Food Engineering, vol. 208, pp. 28-36, 2017.

[244] J. Feng, Y. Fu, X. Liu, S. Tian, S. Lan and Y. Xiong, "Significant improvement and mechanism of ultrasonic inactivation to escherichia coli with piezoelectric effect of hydrothermally synthesized t-BaTiO3," ACS Sustainable Chemistry & Engineering, vol. 6, no. 5, pp. 6032-6041, 2018.

[245] L. Liu, Z. Lu, L. Li, B. Li, X. Zhang, X. Zhang and Z. Xu, "Physical relation and mechanism of ultrasonic bactericidal activity on pathogenic E. coli with WPI," Microbial pathogenesis, vol. 117, pp. 73-79, 2018.

[246] A. Sarkinas, K. Sakalauskiene, R. Raisutis, J. Zeime, A. Salaseviciene, E. Puidaite, E. Mockus and D. Cernauskas, "Inactivation of some pathogenic bacteria and phytoviruses by ultrasonic treatment," Microbial pathogenesis, vol. 123, pp. 144-148, 2018.

[247] Z.-M. Zhao, L. Wang and H.-Z. Chen, "A novel steam explosion sterilization improving solid-state fermentation performance," Bioresource technology, vol. 192, pp. 547-555, 2015.

[248] N. Girard-Perier, S. Dorey, S. R. Marque and N. Dupuy, "Mapping the scientific research on the gamma irradiated polymers degradation (1975–2018)," Radiation Physics and Chemistry, vol. 1688, p. 108577, 2020.

[249] S. Lerouge, "Sterilization and cleaning of metallic biomaterials," In Metals for Biomedical Devices, pp. 405-428, 2019.

[250] K. Dey, S. Agnelli and L. Sartore, "Effects of gamma sterilization on the physicomechanical and thermal properties of gelatin-based novel hydrogels," Polymer Engineering & Science, vol. 59, no. 12, pp. 2533-2540, 2019.

[251] D. d. Cassan, A. L. Hoheisel, B. Glasmacher and H. Menzel, "Impact of sterilization by electron beam, gamma radiation and X-rays on electrospun poly-(ε-caprolactone) fiber mats," Journal of Materials Science: Materials in Medicine, vol. 30, no. 4, pp. 1-11, 2019.

[252] M. Silindir and A. Y. Özer, "Sterilization methods and the comparison of E-beam sterilization with gamma radiation sterilization," Fabad Journal of Pharmaceutical Sciences, vol. 34, no. 1, p. 43, 2009.

[253] J. T. Rodrigues, F. N. d. S. Neto, M. F. Ferreira, P. L. F. Naves and L. R. Guilherme, "Application of Gamma Radiation on Hard Gelatin Capsules as Sterilization Technique and Its Consequences on the Chemical Structure of the Material," Aaps Pharmscitech, vol. 20, no. 5, pp. 1-8, 2019.

[254] P. O. Maksimchuk, S. L. Yefimova, V. V. Omielaieva, K. O. Hubenko, V. K. Klochkov, O. D. Opolonin and Y. V. Malyukin, "X-ray Induced Hydroxyl Radical Generation by GdYVO4: Eu3+ Nanoparticles in Aqueous Solution: Main Mechanisms," Crystals, vol. 10, no. 5, p. 370, 2020.

[255] A. Cramer, E. Tian, H. Y. Sherryl, M. Galanek, E. Lamere, J. Li, R. Gupta and M. P. Short, "Disposable N95 masks pass qualitative fit-test but have decreased filtration efficiency after cobalt-60 gamma irradiation," MedRxiv, 2020.

[256] A. Soni, J. Smith, A. Thompson and G. Brightwell, "Microwave-induced thermal sterilization-A review on history, technical progress, advantages and challenges as compared to the conventional methods," Trends in Food Science & Technology, vol. 97, pp. 433-442, 2020.

[257] "Point-to-Point Microwave," Federal Communications Commission, [Online]. Available: https://www.fcc.gov/wireless/bureau-divisions/broadband-division/point-point-microwave. [Accessed 20th February 2022].

[258] R. MacDonald and C. Reitmeier, "Food Processing," in Understanding Food Systems, Academic Press, 2017, pp. 179-225.

[259] Food and Drug Administration, "Kinetics of microbial inactivation for alternative food processing technologies–microwave and radio frequency processing," Government Services Administration, Washington, DC, 2000.

[260] Y. Wang, Z. Li, D. Yang, X. Qiu, Y. Xie and X. Zhang, "Microwave-mediated fabrication of silver nanoparticles incorporated lignin-based composites with enhanced antibacterial activity via electrostatic capture effect," Journal of Colloid and Interface Science, vol. 583, pp. 80-88, 2021.

[261] M. Huang, M. Zhang and B. Bhandari, "Recent development in the application of alternative sterilization technologies to prepared dishes: A review," Critical reviews in food science and nutrition, vol. 59, no. 7, pp. 1188-1196, 2019.

[262] "Radiation: Ultraviolet (UV) radiation," World Health Organization, 6th March 2016. [Online]. Available: https://www.who.int/news-room/questions-and-answers/item/radiation-ultraviolet-(uv)#:~:text=The%20UV%20region%20covers%20the,(100%2D280%20nm). [Accessed 20th February 2022].

[263] M. Heßling, K. Hönes, P. Vatter and C. Lingenfelder, "Ultraviolet irradiation doses for coronavirus inactivation–review and analysis of coronavirus photoinactivation studies," GMS hygiene and infection control, vol. 15, 2020.

[264] "Chloride in drinking-water: Background document for development of WHO guidelines for drinking-water quality," World Health Organization, [Online]. Available: https://www.who.int/water_sanitation_health/publications/chloride/en/. [Accessed 20th February 2022].

[265] M. Diana, M. Felipe-Sotelo and T. Bond, "Disinfection byproducts potentially responsible for the association between chlorinated drinking water and bladder cancer: A review," Water Research, vol. 162, pp. 492-504, 2019.

[266] Q. Tan, W. Li, J. Zhang, W. Zhou, J. Chen, Y. Li and J. Ma, "Presence, dissemination and removal of antibiotic resistant bacteria and antibiotic resistance genes in urban drinking water system: A review," Frontiers of Environmental Science & Engineering, vol. 13, no. 3, pp. 1-15, 2019.

[267] A. R. Kadam, G. B. Nair and S. J. Dhoble, "nsights into the extraction of mercury from fluorescent lamps: A review," Journal of Environmental Chemical Engineering, vol. 7, no. 4, p. 103279, 20199.

[268] J. Chen, S. Loeb and J.-H. Kim, "LED revolution: fundamentals and prospects for UV disinfection applications," Environmental Science: Water Research & Technology, vol. 3, no. 2, pp. 188-202, 2017.

[269] K. Song, M. Mohseni and F. Taghipour, "Application of ultraviolet light-emitting diodes (UV-LEDs) for water disinfection: A review," Water Research, vol. 94, pp. 341-349, 2016.

[270] D. Amodeo, L. Pallecchi, C. Nagaia, G. Spataro, R. Cardaci and G. Messina, "Tuning a UV-C device to challenge new threats in the sanitization setting of healthcare facilities," European Journal of Public Health, vol. 30, no. 5, pp. 165-171, 2020.

[271] B. T. Gemici, F. B. Karel, F. Karaer and A. S. Koparal, "Water disinfection with advanced methods: Successive and hybrid application of antibacterial column with silver, ultrasound and UV radiation," Applied Ecology and Environmental Research, vol. 16, no. 4, pp. 4667-4680, 2018.

[272] World Health Organization, "Water quality and health-review of turbidity: information for regulators and water suppliers," 2017.

[273] F. F. Chen, "Introduction to Plasma Physics and Controlled Fusion Volume 1: Plasma Physics," Physics Today, vol. 38, p. 87, 1985.

[274] Z. Zhang, Z. Xu, C. Cheng, J. Wei, Y. Lan, G. Ni, Q. Sun, S. Qian, H. Zhang, W. Xia and J. Shen, "Bactericidal effects of plasma induced reactive species in dielectric barrier gas–liquid discharge," Plasma Chemistry and Plasma Processing, vol. 37, no. 2, pp. 415-431, 2017.

[275] A. Dascalu, V. Pohoata, K. Shimizu and L. Sirghi, "Molecular species generated by surface dielectric barrier discharge micro-plasma in small chambers enclosing atmospheric air and water samples," Plasma Chemistry and Plasma Processing, vol. 4, no. 1, pp. 389-408, 2021.

[276] L. Invernizzi, C. Muja, F. P. Sainct and P. Guillot, "Investigation of RONS production and complex molecules degradation induced by an APPJ generated by two different sources," IEEE Transactions on Radiation and Plasma Medical Sciences, vol. 4, no. 1, pp. 121-129, 2019.

[277] S. Bekeschus, R. Clemen, L. Haralambiev, F. Niessner, P. Grabarczyk, K.-D. Weltmann, J. Menz, M. Stope, T. v. Woedtke, R. Gandhirajan and A. Schmidt, "The plasma-induced leukemia cell death is dictated by the ROS chemistry and the HO-1/CXCL8 axis," IEEE Transactions on Radiation and Plasma Medical Sciences, vol. 5, no. 3, pp. 398-411, 2020.

[278] Y.-M. Kim, H.-S. Yun, S.-H. Eom, B.-J. Sung, S.-H. Lee, S.-M. Jeon, S.-W. Chin and M.-S. Lee, "Bactericidal action mechanism of nonthermal plasma: denaturation of membrane proteins," IEEE Transactions on Radiation and Plasma Medical Sciences, vol. 2, no. 1, pp. 77-83, 2018.

[279] "Ethylene Oxide "Gas" Sterilization," Centers for Disease Control and Prevention, United States Department of Health and Human Services, [Online]. Available: https://www.cdc.gov/infectioncontrol/guidelines/disinfection/sterilization/ethylene-oxide.html. [Accessed 20th February 2022].

[280] "Hydrogen Peroxide Gas Plasma," Centers for Disease Control and Prevention, United States Department of Health and Human Services, [Online]. Available: https://www.cdc.gov/infectioncontrol/guidelines/disinfection/sterilization/hydrogen-peroxide-gas.html. [Accessed 20th February 2022].

[281] "IARC Monographs on the Identification of Carcinogenic Hazards to Humans," International Agency for Research on Cancer, World Health Organization, [Online]. Available: https://monographs.iarc.who.int/agents-classified-by-the-iarc/. [Accessed 20th February 2022].

[282] "Hydrogen peroxide (Hydrogen dioxide) (000595) Fact Sheet," United States Environmental Protection Agency, [Online]. Available: https://www3.epa.gov/pesticides/chem_search/reg_actions/registration/fs_PC-000595_30-Jan-02.pdf. [Accessed 20th February 2022].

[283] S. Lerouge, "Non-traditional sterilization techniques for biomaterials and medical devices," in Sterilisation of Biomaterials and Medical Devices, Woodhead Publishing, 2012, pp. 97-116.

[284] W. A. Rutala and D. J. Weber, "Disinfection, Sterilization, and Control of Hospital Waste," in Mandell, Douglas, and Bennett's Principles and Practice of Infectious Diseases (Eighth Edition), 2015, pp. 3294-3309.

[285] M. Kong and G. Shama, "Cold Atmospheric Gas Plasmas," in Encyclopedia of Food Microbiology (Second Edition), Academic Press, 2014, pp. 493-496.

[286] M. Moisan, J. Barbeau, S. Morea, J. P. M. Tabrizian and L. H. Yahia, "Low-temperature sterilization using gas plasmas: a review of the experiments and an analysis of the inactivation mechanisms," International Journal of Pharmaceutics, vol. 226, no. 1-2, pp. 1-21, 2001.

[287] K. Reineke, K. Langer, C. Hertwig, J. Ehlbeck and O. Schlüter, "The impact of different process gas compositions on the inactivation effect of an atmospheric pressure plasma jet on Bacillus spores," Innovative Food Science & Emerging Technologies, vol. 30, pp. 112-118, 2015.

[288] M. Cooper, N. Vaze, S. Anderson, G. Fridman, V. N. Vasilets, A. Gutsol, A. Tsapin and A. Fridman, "Spacecraft sterilization using non-equilibrium atmospheric pressure plasma," in 18th International Symposium on Plasma Chemistry, Kyoto, 2007.

[289] K. G. Kostov, V. Rocha, C. Y. Koga-Ito, B. M. Matos, M. A. Algatti, R. Y. Honda, M. E. Kayama and R. P. Mota, "Bacterial sterilization by a dielectric barrier discharge (DBD) in air," Surface and Coatings Technology, vol. 204, no. 18-19, pp. 2954-2959, 2010.

[290] K. Wiesemann, "A short introduction to plasma physics," arXiv preprint arXiv, vol. 1404.0509, 2014.

[291] A. Fridman, Plasma chemistry, Cambridge university press, 2008.

[292] D. Wu, S. Tashiro, X. Hua and M. Tanaka, "Analysis of the energy propagation in the keyhole plasma arc welding using a novel fully coupled plasma arc-keyhole-weld pool model," International Journal of Heat and Mass Transfer, vol. 141, pp. 604-614, 2019.

[293] M. Fiebrandt, J. Lackmann and K. Stapelmann, "From patent to product? 50 years of low-pressure plasma sterilization," Plasma Processes and Polymers, vol. 15, no. 12, p. 1800139, 2018.

[294] C. G. Lee, K. J. Kanarik and R. A. Gottscho, "The grand challenges of plasma etching: a manufacturing perspective," Journal of Physics D: Applied Physics, vol. 47, no. 27, p. 273001, 2014.

[295] A. Tsuchida, T. Shimamura, S. Sawada, S. Sato, N. Serpone and S. Horikoshi, "In-liquid plasma. A stable light source for advanced oxidation processes in environmental remediation," Radiation Physics and Chemistry, vol. 147, pp. 53-58, 2018.

[296] A. M. Alrashidi, N. M. Adam, A. A. Hairuddin and L. C. Abdullah, "A review on plasma combustion of fuel in internal combustion engines," International Journal of Energy Research, vol. 42, no. 5, pp. 1813-1833, 2018.

[297] Franklin R. Chang-Díaz, "Plasma propulsion for interplanetary flight," Thin Solid Films, vol. 506, pp. 449-453, 2006.

[298] P. J. Cullen, J. Lalor, L. Scally, D. Boehm, V. Milosavljević, P. Bourke and K. Keener, "Translation of plasma technology from the lab to the food industry," Plasma Processes and Polymers, vol. 15, no. 2, p. 1700085, 2018.

[299] P. A. Martens, V. Galliani, G. Graham and R. A. Caputo, "Sterilization of medical products using gas plasma technology," in In Sterilization of Drugs and Devices, CRC Press, 2018, pp. 157-195.

[300] Y. Zhao, R. Chen, E. Tian, D. Liu, J. Niu, W. Wang, Z. Qi, Y. Xia, Y. Song and Z. Zhao, "Plasma-activated water treatment of fresh beef: Bacterial inactivation and effects on quality attributes," IEEE Transactions on Radiation and Plasma Medical Sciences, vol. 4, no. 1, pp. 113-120, 2018.

[301] Z. Chen, L. Lin, E. Gjika, X. Cheng, J. Canady and M. Keidar, "Selective treatment of pancreatic cancer cells by plasma-activated saline solutions," IEEE Transactions on Radiation and Plasma Medical Sciences, vol. 2, no. 2, pp. 116-120, 2017.

[302] M. E. Shaer, A. Zaki, A. M. Reda, M. Adel, M. Mobasher and S. Ali, "Effect of plasma activated mist on breast cancer cells," IEEE Transactions on Radiation and Plasma Medical Sciences, vol. 2, no. 2, pp. 103-108, 2017.

[303] C. Duchesne, S. Banzet, J. Lataillade, A. Rousseau and N. Frescaline, "Cold atmospheric plasma modulates endothelial nitric oxide synthase signalling and enhances burn wound neovascularisation," The Journal of pathology, vol. 249, no. 3, pp. 368-380, 2019.

[304] H. H. Kurt and E. Tanrıverdi, "Estimation of Minimal Breakdown Point in a GaP Plasma Structure and Discharge Features in Air and Argon Media," Journal of Electronic Materials, vol. 45, no. 8, pp. 3872-3881, 2016.

[305] C. Torres, P. G. Reyes, F. Castillo and H. Martínez, "Paschen law for argon glow discharge," In Journal of Physics: Conference Series, vol. 370, no. 1, p. 012067, 2012.

[306] A. Dominguez, "Derivation of the Paschen curve law ALPhA Laboratory Immersion," 2014.

[307] L. F. Berzak, S. E. Dorfman and S. P. Smith, "Paschen's Law in Air and Noble Gases," Lawrence Berkeley National Laboratory, 2006.

[308] "Paschen's Law," WolframAlpha, [Online]. Available: https://www.wolframalpha.com/input/?i=paschen%27s+law. [Accessed 20th February 2022].

[309] S. Samal, "Thermal Plasma Technology: The Prospective Future in Material Processing," Journal of Cleaner Production, vol. 142, pp. 3131-3150, 2017.

[310] P. R. Taylor and S. A. Pirzada, "Thermal plasma processing of materials: A review," Advanced Performance Materials, vol. 1, no. 1, pp. 35-50, 1994.

[311] S. Samal, P. S. Mukherjee and T. K. Mukherjee, "Thermal plasma processing of ilmenite: a review," Mineral Processing and Extractive Metallurgy, vol. 119, no. 2, pp. 116-123, 2010.

[312] V. Nehra, A. Kumar and H. Dwivedi, "Atmospheric non-thermal plasma sources," International Journal of Engineering, vol. 2, no. 1, pp. 53-68, 2008.

[313] D. Mariotti and R. M. Sankaran, "Microplasma for Nanomaterials Synthesis," Journal of Physics D, vol. 43, no. 32, p. 323001, 2010.

[314] X. Cai, X. Wei and C. Du, "Thermal plasma treatment and co-processing of sludge for utilization of energy and material," Energy & Fuels, vol. 34, no. 7, pp. 7775-7805, 2020.

[315] E. H. Choi, H. S. Uhm and N. K. Kaushik, "Plasma bioscience and its application to medicine," AAPPS Bulletin, vol. 31, no. 1, pp. 1-38, 2021.

[316] J. G. Eden, S.-J. Park, J. H. Cho, M. H. Kim, T. J. H. Jr., B. Li, E. S. Kim, T. L. Kim, S. K. Lee, K. S. Kim, J. K. Yoon, S. H. Sung, P. Sun, C. M. Herring and C. J. Wagner, "Plasma Science and Technology in the Limit of the Small: Microcavity Plasmas and Emerging Applications," IEEE Transactions on Plasma Science, vol. 41, no. 4, pp. 661-675, 2013.

[317] N. Zhang, C. Huang, J. Li, L. Kang, H. Zheng, Y. He, Z. Wang, X. Zhou and J. Zhang, "Control and Patterning of Various Hydrophobic Surfaces: In-situ Modification Realized by Flexible Atmospheric Plasma Stamp Technique," Journal of Bionic Engineering, vol. 17, pp. 436-447, 2020.

[318] A. K. Bose, D. Maddipatla, B. B. Narakathu, V. S. Turkani, B. J. Bazuin and M. Z. Atashbar, "Flexible microplasma discharge device for the detection of biochemicals," In Proceedings IMCS, pp.419-420, 2018, doi: 10.5162/IMCS2018/ME.4.

[319] K. S. Joshy, S. Snigdha and S. Thomas, "Plasma modified polymeric materials for scaffolding of bone tissue engineering," Non-Thermal Plasma Technology for Polymeric Materials, pp. 439-458, 2019.

[320] D. F. Zheng and B. Wang, "Utilization of nonthermal plasma in pulse detonation engine ignition," Journal of Propulsion and Power, vol. 34, no. 2, pp. 539-549, 2018.

[321] R. Foest, M. Schmidt and K. Becker, "Microplasmas as an Emerging Field of Low-Temperature Plasma Science and Technology," International Journal of Mass Spectrometry, vol. 248, no. 3, pp. 87-102, 2006.

[322] K. Tachibana, "Current status of microplasma research," IEEJ Transactions on Electrical and Electronic Engineering, vol. 1, no. 2, pp. 145-155, 2006.

[323] J. Han, "Review of major directions in non-equilibrium atmospheric plasma treatments in medical, biological, and bioengineering applications," Plasma Medicine, vol. 3, no. 3, 2013.

[324] S. Kawano, K. Wada, T. Kakuta, K. Takaki, N. Satta and K. Takahashi, "Influence of pulse width on decolorization efficiency of organic dye by discharge inside bubble in water," In Journal of Physics: Conference Series, vol. 441, no. 1, p. 012007, 2013.

[325] I. Shorstkii, "Application of cold filamentary microplasma pretreatment assisted by thermionic emission for potato drying," Innovative Food Science & Emerging Technologies, vol. 66, p. 102540, 2020.

[326] K. H. Becker, K. H. Schoenbach and J. G. Eden, "Microplasmas and Applications," Journal of Physics D, vol. 39, no. 3, p. R55, 2006.

[327] O. Nguon, S. Huang, M. Gauthier and V. Karanassios, "Microplasmas: from applications to fundamentals," In Next-Generation Spectroscopic Technologies VII, vol. 9101, p. 910106, 2014.

[328] "Plasma Science: Enabling Technology, Sustainability, Security, and Exploration," The National Academies Press, Washington, DC, 2020.

[329] P. Mathew, J. George, S. M. T and P. J. Kurian, "Experimental verification of modified Paschen's law in DC glow discharge argon plasma," AIP Advances, vol. 9, no. 2, p. 025215, 2019.

[330] D. B. Go and D. A. Pohlman, "A mathematical model of the modified Paschen's curve for breakdown in microscale gaps," Journal of Applied physics, vol. 107, no. 10, p. 103303, 2010.

[331] W. Hartmann, V. Dominic, G. F. Kirkman and M. A. Gundersen, "An analysis of the anomalous high-current cathode emission in pseudospark and back-of-the-cathode lighted thyratron switches," Journal of applied physics, vol. 65, no. 11, pp. 4388-4395, 1989.

[332] J. S. Chang, P. A. Lawless and T. Yamamoto, "Corona discharge processes," IEEE Transactions on plasma science, vol. 19, no. 6, pp. 1152-1166, 1991.

[333] J. Greenan, C. M. O. Mahony, D. Mariotti and P. D. Maguire, "Characterization of hollow cathode and parallel plate microplasmas: scaling and breakdown," Plasma Sources Science and Technology, vol. 20, no. 2, p. 025011, 2011.

[334] K. H. Becker, H. Kersten, J. Hopwood and J. L. Lopez, "Microplasmas: scientific challenges & technological opportunities," The European Physical Journal D, vol. 60, no. 3, pp. 437-439, 2010.

[335] D. B. Go and A. Venkattraman, "Microscale gas breakdown: ion-enhanced field emission and the modified Paschen's curve," Journal of Physics D: Applied Physics, vol. 47, no. 50, p. 503001, 2014.

[336] James L. Walsh, F. Iza, N. B. Janson, V. J. Law and M. G. Kong, "Three distinct modes in a cold atmospheric pressure plasma jet," Journal of Physics D: Applied Physics, vol. 43, no. 7, p. 075201, 2010.

[337] P. J. Bruggeman, F. Iza and R. Brandenburg, "Foundations of atmospheric pressure non-equilibrium plasmas," Plasma Sources Science and Technology, vol. 26, no. 12, p. 123002, 2017.

[338] X. Xu, "Dielectric barrier discharge—properties and applications," Thin solid films, vol. 390, no. 1-2, pp. 237-242, 2001.

[339] D. Z. Pai, G. D. Stancu, D. A. Lacoste and C. O. Laux, "Nanosecond repetitively pulsed discharges in air at atmospheric pressure—the glow regime," Plasma Sources Science and Technology, vol. 18, no. 4, p. 045030, 2009.

[340] H. S. Nalwa, Handbook of low and high dielectric constant materials and their applications, Elsevier, 1999.

[341] R. Brandenburg, "Dielectric barrier discharges: progress on plasma sources and on the understanding of regimes and single filaments," Plasma Sources Science and Technology, vol. 26, no. 5, p. 053001, 2017.

[342] A. El-Zein, M. Talaat, G. El-Aragi and A. El-Amawy, "The Characteristics of Dielectric Barrier Discharge Plasma Under the Effect of Parallel Magnetic Field," IEEE Transactions on Plasma Science, vol. 48, no. 4, pp. 1022-1029, 2020.

[343] D. Pappas, "Status and potential of atmospheric plasma processing of materials," Journal of Vacuum Science & Technology A: Vacuum, Surfaces, and Films, vol. 29, no. 2, p. 020801, 2011.

[344] J. R. Roberts, "Vacuum Ultraviolet Spectroscopy," in Glow Discharges and Wall Stabilized, Academic Press, 2000, pp. 37-63.

[345] K. Matra and S. Wongkuan, "Non-thermal dielectric barrier discharge generator," Procedia Computer Science, vol. 86, pp. 313-316, 2016.

[346] T. Ishida, K. Hirasawa, M. Dozen and Y. Tada, "Appearance of DC dielectric barrier discharge," in In Proceedings of 2011 International Symposium on Electrical Insulating Materials, 2011.

[347] H. Luo, K. Liu, J. Ran, Y. Yue, X. Wang, S. Yap and C. S. Wong, "Study of dielectric barrier Townsend discharge in 3-mm air gap at atmospheric pressure," IEEE Transactions on Plasma Science, vol. 42, no. 5, pp. 1211-1215, 2014.

[348] H. S. Uhm and Y. C. Hong, "Various microplasma jets and their sterilization of microbes," Thin Solid Films, vol. 519, no. 20, pp. 6974-6980, 2011.

[349] S. Song, J. Lane and C. Jiang, "Comparison study of spatiotemporally resolved emissions of nanosecond pulsed microplasma jets," IEEE Transactions on Plasma Science, vol. 46, no. 3, pp. 587-593, 2018.

[350] J. Y. Kim, S.-O. Kim, Y. Wei and J. Li, "A flexible cold microplasma jet using biocompatible dielectric tubes for cancer therapy," Applied physics letters, vol. 96, no. 20, p. 203701, 2010.

[351] P. P. Sun, E. M. Araud, C. Huang, Y. Shen, G. L. Monroy, S. Zhong, Z. Tong, S. A. Boppart, J. G. Eden and T. H. Nguyen, "Disintegration of simulated drinking water biofilms with arrays of microchannel plasma jets," npj Biofilms and Microbiomes, vol. 4, no. 1, pp. 1-10, 2018.

[352] A. Khlyustova, C. Labay, Z. Machala, M.-P. Ginebra and C. Canal, "Important parameters in plasma jets for the production of RONS in liquids for plasma medicine: A brief review," Frontiers of Chemical Science and Engineering, vol. 13, no. 2, pp. 238-252, 2019.

[353] K. Barman, D. Behmani, M. Mudgal, S. Bhattacharjee, R. Rane and S. K. Nema, "Characteristics of atmospheric pressure micro-plasma jets in two different modes of excitation depending upon wave amplitude and frequency," Plasma Research Express, vol. 2, no. 2, p. 025007, 2020.

[354] S. Wilczek, J. Schulze, R. P. Brinkmann, Z. Donkó, J. Trieschmann and T. Mussenbrock, "Electron dynamics in low pressure capacitively coupled radio frequency discharges," Journal of Applied Physics, vol. 127, no. 18, p. 181101, 2020.

[355] P. Chabert, T. V. Tsankov and U. Czarnetzki, "Foundations of capacitive and inductive radio-frequency discharges," Plasma Sources Science and Technology, vol. 30, no. 2, p. 024001, 2021.

[356] A. G. Yahaya, T. Okuyama, J. Kristof, M. G. Blajan and K. Shimizu, "Direct and Indirect Bactericidal Effects of Cold Atmospheric-Pressure Microplasma and Plasma Jet," Molecules, vol. 26, no. 9, p. 2523, 2021.

[357] H. M. Abourayana and D. P. Dowling, "Plasma processing for tailoring the surface properties of polymers," in Surface Energy, vol. 123, IntechOpen, 2015, p. 123.

[358] I. C. Gerber, I. Mihaila, D. Hein, A. V. Nastuta, R. Jijie, V. Pohoata and I. Topala, "Time behaviour of helium atmospheric pressure plasma jet electrical and optical parameters," Applied Sciences, vol. 7, no. 8, p. 812, 2017.

[359] S. J. Kim, T. H. Chung, S. H. Bae and S. H. Leem, "Characterization of atmospheric pressure microplasma jet source and its application to bacterial inactivation," Plasma Processes and Polymers, vol. 6, no. 10, pp. 676-685, 2009.

[360] L. Wu, W. Zhang, Z. Liu, J. Yu, J. Tao, Y. Yang and K. Huang, "Discharge properties of a coaxial plasma jet at different microwave frequencies," Physics of Plasmas, vol. 27, no. 12, p. 123508, 2020.

[361] P. P. Sun, J. H. Cho, S.-J. Park and J. G. Eden, "Influence of multiple electrode configurations on atmospheric pressure microplasma jet arrays in flexible polymer," in In 2012 Abstracts IEEE International Conference on Plasma Science, 2012.

[362] X. Pei, J. Kredl, X. Lu and J. F. Kolb, "Discharge modes of atmospheric pressure DC plasma jets operated with air or nitrogen," Journal of Physics D: Applied Physics, vol. 51, no. 38, p. 384001, 2018.

[363] A. H. Basher and A.-A. H. Mohamed, "Laminar and turbulent flow modes of cold atmospheric pressure argon plasma jet," Journal of Applied Physics, vol. 123, no. 19, p. 193302, 2018.

[364] H. Jung, B. Gweon, D. B. Kim and W. Choe, "A simple approach to surface modification using polytetrafluoroethylene (PTFE) with laminar and turbulent flows of micro plasma jets at atmospheric pressure," Plasma Processes and Polymers, vol. 8, no. 6, pp. 535-541, 2011.

[365] A.-A. Mohamed, J. F. Kolb and K. H. Schoenbach, "Low temperature, atmospheric pressure, direct current microplasma jet operated in air, nitrogen and oxygen," The European Physical Journal D, vol. 60, no. 3, pp. 517-522, 2010.

[366] X. L. Deng, A. Y. Nikiforov, P. Vanraes and C. Leys, "Direct current plasma jet at atmospheric pressure operating in nitrogen and air," Journal of Applied Physics, vol. 113, no. 2, p. 023305, 2013.

[367] S. Nijdam, J. Teunissen and U. Ebert, "The physics of streamer discharge phenomena," Plasma Sources Science and Technology, vol. 29, no. 10, p. 103001, 2020.

[368] H. J. Park, S. H. Kim, H. W. Ju, H. Lee, Y. Lee, S. Park, H. Yang, S. J. Park, J. G. Eden, J. Yang and C. H. Park, "Microplasma jet arrays as a therapeutic choice for fungal keratitis," Scientific reports, vol. 8, no. 1, pp. 1-11, 2018.

[369] N. Y. Babaeva and M. J. Kushner, "Interaction of multiple atmospheric-pressure micro-plasma jets in small arrays: He/O2 into humid air," Plasma Sources Science and Technology, vol. 23, no. 1, p. 015007, 2014.

[370] B. Despax, O. Pascal, N. Gherardi, N. Naude, A. Belinger and L. C. Pitchford, "Influence of electromagnetic radiation on the power balance in a radiofrequency microdischarge with a hollow needle electrode," Applied Physics Letters, vol. 101, no. 14, p. 144104, 2012.

[371] K. H. Schoenbach, M. MOSelhy, W. Shi and R. Bentley, "Microhollow cathode discharges," Journal of Vacuum Science & Technology A: Vacuum, Surfaces, and Films, vol. 21, no. 4, pp. 1260-1265, 2003.

[372] K. H. Schoenbach, R. Verhappen, T. Tessnow, F. E. Peterkin and W. W. Byszewski, "Microhollow cathode discharges," Applied Physics Letters, vol. 68, no. 1, pp. 13-15, 1996.

[373] W. Shi, R. H. Stark and K. H. Schoenbach, "Parallel operation of microhollow cathode discharges," IEEE transactions on plasma science, vol. 27, no. 1, pp. 16-17, 1999.

[374] P. Chabert, C. Lazzaroni and A. Rousseau, "A model for the self-pulsing regime of microhollow cathode discharges," Journal of Applied Physics, vol. 108, no. 11, p. 113307, 2010.

[375] K. Kunze, "Miniaturized discharges," PhD dissertation, Department of Physics, University of Dortmund, 2004.

[376] O. Taylan and H. Berberoglu, "Dissociation of carbon dioxide using a microhollow cathode discharge plasma reactor: effects of applied voltage, flow rate and concentration," Plasma Sources Science and Technology, vol. 24, no. 1, p. 015006, 2014.

[377] M. Miclea, K. Kunze, U. Heitmann, S. Florek, J. Franzke and K. Niemax, "Diagnostics and application of the microhollow cathode discharge as an analytical plasma," Journal of Physics D: Applied Physics, vol. 38, no. 11, p. 1709, 2005.

[378] A. I. Saifutdinov and S. S. Sysoev, "Diagnostics and comparative analyzes of plasma parameters in micro hollow cathode discharges with an open and covered external surface of cathode in helium using an additional electrode," Plasma Sources Science and Technology, vol. 30, no. 1, p. 017001, 2021.

[379] X. Wang, Q. Huang, S. Ding, W. Liu, J. Mei, J. Luo, L. Lei and F. He, "Micro hollow cathode excited dielectric barrier discharge (DBD) plasma bubble and the application in organic wastewater treatment," Separation and Purification Technology, vol. 240, p. 116659, 2020.

[380] O. O. Baranov, S. Xu, L. Xu, S. Huang, J. W. M. Lim, U. Cvelbar, I. Levchenko and K. Bazaka, "Miniaturized plasma sources: Can technological solutions help electric micropropulsion?," IEEE Transactions on Plasma Science, vol. 46, no. 2, pp. 230-238, 2017.

[381] T.-S. Cho, S.-H. Park, K. H. Becker and E. E. Kunhardt, "Investigation of discharge phenomena in microscale capillary plasma electrode discharges," IEEE Transactions on Plasma Science, vol. 39, no. 6, pp. 1496-1499, 2011.

[382] S.-H. Park, T.-S. Cho, K. H. Becker and E. E. Kunhardt, "Capillary plasma electrode discharge as an intense and efficient source of vacuum ultraviolet radiation for plasma display," IEEE transactions on plasma science, vol. 37, no. 8, pp. 1611-1614, 2009.

[383] A. D. Koutsospyros, S.-M. Yin, C. Christodoulatos and K. Becker, "Plasmochemical degradation of volatile organic compounds (VOC) in a capillary discharge plasma reactor," IEEE transactions on plasma science, vol. 33, no. 1, pp. 42-49, 2005.

[384] A. Fridman, A. Gutsol and Y. I. Cho, "Non-thermal atmospheric pressure plasma," Advances in Heat Transfer, vol. 40, pp. 1-142, 2007.

[385] S. Okazaki and M. Kogoma, "Development OP atmospheric pressure glow discharge plasma and its application on a surface with curvature," Journal of Photopolymer Science and Technology, vol. 6, no. 3, pp. 339-342, 1993.

[386] Y. C. Hong, H. W. Jeon, B. J. Lee and H. S. Uhm, "Generation of plasma using capillary discharge in water," IEEE Transactions on Plasma Science, vol. 38, no. 12, pp. 3464-3466, 2010.

[387] Y. Lu, S. F. Xu, X. X. Zhong, K. Ostrikov, U. Cvelbar and D. Mariotti, "Characterization of a DC-driven microplasma between a capillary tube and water surface," Europhysics Letters, vol. 102, no. 1, p. 15002, 2013.

[388] F. D. Baerdemaeker, M. Šimek, J. Schmidt and C. Leys, "Characteristics of ac capillary discharge produced in electrically conductive water solution," Plasma Sources Science and Technology, vol. 16, no. 2, p. 341, 2007.

[389] T. J. Silhavy, D. Kahne and S. Walker, "The Bacterial Cell Envelope," Cold Spring Harb Perspective Biology, vol. 2, no. 5, p. a000414, 2010.

[390] T. J. Silhavy, D. Kahne and S. Walker, "The bacterial cell envelope," Cold Spring Harbor Perspectives in Biology, vol. 2, no. 5, p. a000414, 2010.

[391] A. Mai-Prochnow, M. Clauson, J. Hong and A. B. Murphy, "Gram positive and Gram negative bacteria differ in their sensitivity to cold plasma," Science Reports, vol. 6, no. 1, pp. 1-11, 2016.

[392] I. Golding and E. C. Cox, "Physical nature of bacterial cytoplasm," Physical review letters, vol. 96, no. 9, p. 098102, 2006.

[393] A. Al-Abduly and P. Christensen, "An in situ and downstream study of non-thermal plasma chemistry in an air fed dielectric barrier discharge (DBD)," Plasma Sources Science and Technology, vol. 24, no. 6, p. 065006, 2015.

[394] M. K. Boudam, M. Moisan, B. Saoudi, C. Popovici, N. Gherardi and F. Massines, "Bacterial spore inactivation by atmospheric-pressure plasmas in the presence or absence of UV photons as obtained with the same gas mixture," Journal of Physics D: Applied Physics, vol. 39, no. 16, p. 3494, 2006.

[395] G. Gogniat, M. Thyssen, M. Denis, C. Pulgarin and S. Dukan, "The bactericidal effect of TiO2 photocatalysis involves adsorption onto catalyst and the loss of membrane integrity," FEMS microbiology letters, vol. 258, no. 1, pp. 18-24, 2006.

[396] M. Krewing, B. Schubert and J. E. Bandow, "A Dielectric Barrier Discharge Plasma Degrades Proteins to Peptides by Cleaving the Peptide Bond," Plasma Chemistry and Plasma Processing, vol. 40, no. 3, pp. 685-696, 2020.

[397] S. Fiedler and R. Wirth, "Transformation of bacteria with plasmid DNA by electroporation," Analytical Biochemistry, vol. 170, no. 1, pp. 38-44, 1988.

[398] Z. Fang, T. Shao, R. Wang, J. Yang and C. Zhang, "Influences of oxygen content on characteristics of atmospheric pressure dielectric barrier discharge in argon/oxygen mixtures," European Physical Journal D, vol. 70, no. 4, pp. 1-9, 2016.

[399] S. K. Sharma and A. Sharma, "Sterilization of microorganisms contaminated surfaces and its treatment with dielectric barrier discharge plasma," Transactions of the Indian National Academy of Engineeringhttps://academic-accelerator.com › Tr...· Translate this page, vol. 5, no. 2, pp. 321-326, 2020.

[400] J. H. Lozano-Parada, F. M. Martínez and D. S. Díaz, "Producción eficiente de ozono en un microplasma en aire a presión atmosférica," Cienc en Desarro, vol. 8, no. 1, pp. 169-178, 2017.

[401] A. L. Santos, V. Oliveira, I. Baptista, I. Henriques, N. C. Gomes, A. Almeida, A. Correia and A. Cunha, "Effects of UV-B radiation on the structural and physiological diversity of bacterioneuston and bacterioplankton," Applied and environmental microbiology, vol. 78, no. 6, pp. 2066-2069, 2012.

[402] Y. Yue, X. Pei and X. Lu, "OH density optimization in atmospheric-pressure plasma jet by using multiple ring electrodes," International Journal of Applied Physics, vol. 119, no. 3, p. 033301, 2016.

[403] I. A. f. R. o. Cancer, "IARC Monographs on the Evaluation of Carcinogenic Risks to Humans, No. 100D," IARC Working Group on the Evaluation of Carcinogenic Risks to Humans, 2012.

[404] A. L. Santos, V. Oliveira, I. Baptista, I. Henriques, N. C. Gomes, A. Almeida, A. Correia and Â. Cunha, "Wavelength dependence of biological damage induced by UV radiation on bacteria," Archives of microbiology, vol. 195, no. 1, pp. 63-74, 2013.

[405] S. Mukhopadhyay, D. O. Ukuku, V. Juneja and X. J. F. C. Fan, "Effects of UV-C treatment on inactivation of Salmonella enterica and Escherichia coli O157: H7 on grape tomato surface and stem scars, microbial loads, and quality," Food Control, vol. 44, pp. 110-117, 2014.

[406] S. E. Beck, H. Ryu, L. A. Boczek, J. L. Cashdollar, K. M. Jeanis, J. S. Rosenblum, O. R. Lawal and K. G. Linden, "Evaluating UV-C LED disinfection performance and investigating potential dual-wavelength synergy," Water research, vol. 109, pp. 207-216, 2017.

[407] C. Oh, P. P. Sun, E. Araud and T. H. Nguyen, "Mechanism and efficacy of virus inactivation by a microplasma UV lamp generating monochromatic UV irradiation at 222 nm," Water Research, vol. 186, p. 116386, 2020.

[408] J. Zheng, C. Su, J. Zhou, L. Xu, Y. Qian and H. Chen, "Effects and mechanisms of ultraviolet, chlorination, and ozone disinfection on antibiotic resistance genes in secondary effluents of municipal wastewater treatment plants," Chemical Engineering Journal, vol. 317, pp. 309-316, 2017.

[409] J. B. Mitchell, L. Y. Sifuentes, A. Wissler, S. Abd-Elmaksoud, G. U. Lopez and C. P. Gerba, "Modelling of ultraviolet light inactivation kinetics of methicillin-resistant Staphylococcus aureus, vancomycin-resistant Enterococcus, Clostridium difficile spores and murine norovirus on fomite surfaces," Journal of applied microbiology, vol. 126, no. 1, pp. 58-67, 2019.

[410] J. B. Gillespie, M. Maclean, M. J. Given, M. P. Wilson, M. D. Judd, I. V. Timoshkin and S. J. MacGregor, "Efficacy of pulsed 405-nm light-emitting diodes for antimicrobial photodynamic inactivation: effects of intensity, frequency, and duty cycle," Photomedicine and laser surgery, vol. 35, no. 3, pp. 150-156, 2017.

[411] L. Urban, F. Charles, M. R. A. d. Miranda and J. Aarrouf, "Understanding the physiological effects of UV-C light and exploiting its agronomic potential before and after harvest," Plant Physiology and Biochemistry, vol. 105, pp. 1-11, 2016.

[412] M. Gentile, L. Latonen and M. Laiho, "ell cycle arrest and apoptosis provoked by UV radiation-induced DNA damage are transcriptionally highly divergent responses," Nucleic acids research, vol. 31, no. 16, pp. 4779-4790, 2003.

[413] S. Dong, J. Li, M.-H. Kim, S.-J. Park, J. G. Eden, J. S. Guest and T. H. Nguyen, "Human health trade-offs in the disinfection of wastewater for landscape irrigation: microplasma ozonation vs. chlorination," Environmental Science: Water Research & Technology, vol. 3, no. 1, pp. 106-118, 2017.

[414] W. Chiang, D. Mariotti, R. M. Sankaran, J. G. Eden and K. Ostrikov, "Microplasmas for advanced materials and devices," Advanced Materials, vol. 32, no. 18, p. 1905508, 2020.

[415] F. Iza, G. J. Kim, S. M. Lee, J. K. Lee, J. L. Walsh, Y. T. Zhang and M. G. Kong, "Microplasmas: sources, particle kinetics, and biomedical applications.," Plasma Processes and Polymers, vol. 5, no. 4, pp. 322-344, 2008.

[416] P. Bourke, D. Ziuzina, L. Han, P. J. Cullen and B. F. Gilmore, "Microbiological interactions with cold plasma," Journal of Applied Microbiology, vol. 123, no. 2, pp. 308-324, 2017.

[417] X. Hao, A. M. Mattson, C. M. Edelblute, M. A. Malik, L. C. Heller and J. F. Kolb, "Nitric Oxide Generation with an Air Operated Non-Thermal Plasma Jet and Associated Microbial Inactivation Mechanisms," Plasma Processes and Polymers, vol. 11, no. 11, pp. 1044-1056, 2014.

[418] K. Pai, C. Timmons, K. D. Roehm, A. Ngo, S. S. Narayanan, A. Ramachandran, J. D. Jacob, L. M. Ma and S. V. Madihally, "Investigation of the roles of plasma species generated by surface dielectric barrier discharge," Science Reports, vol. 8, no. 1, pp. 1-13, 2018.

[419] R. Radjef, K. Jarvis, B. L. Fox and S. L. McArthur, "Design and characterization of a plasma chamber for improved radial and axial film uniformity," Plasma Processes and Polymers, vol. 17, no. 8, p. 2000017, 2020.

[420] J. Han, P. Pribyl, W. Gekelman, A. Paterson, S. J. Lanham, C. Qu and M. J. Kushner, "Three-dimensional measurements of plasma parameters in an inductively coupled plasma processing chamber," Physics of Plasmas, vol. 26, no. 10, p. 103503, 2019.

[421] E. C. B. B. Aragão, J. C. Nascimento, A. D. Fernandes, F. T. F. Barbosa, D. C. Sousa, C. Oliveira, G. J. P. Abreu, V. W. Ribas and B. N. Sismanoglu, "Low temperature microplasma jet at atmospheric pressure for inducing surface modification on polyethylene substrates," American Journal of Condensed Matter Physics, vol. 4, no. 3A, pp. 1-7, 2014.

[422] P. Bruggeman and R. Brandenburg, "Atmospheric pressure discharge filaments and microplasmas: physics, chemistry and diagnostics," Journal of Physics D, vol. 46, no. 46, p. 464001, 2013.

[423] Y. Song, D. Liu, Q. Lu, Y. Xia, R. Zhou, D. Yang, L. Ji and W. Wang, "An atmospheric-pressure large-area diffuse surface dielectric barrier discharge used for disinfection application," IEEE Transactions on Plasma Science, vol. 43, no. 3, pp. 821-827, 2015.

[424] S. B. Karki, E. Yildirim-Ayan, K. M. Eisenmann and H. Ayan, "Miniature dielectric barrier discharge nonthermal plasma induces apoptosis in lung cancer cells and inhibits cell migration," BioMed Research International, vol. 2017, 2017.

[425] H. Yamazaki, T. Ohshima, Y. Tsubota, H. Yamaguchi, J. A. Jayawardena and Y. Nishimura, "Microbicidal activities of low frequency atmospheric pressure plasma jets on oral pathogens," Dental Materials Journal, vol. 30, no. 3, pp. 384-391, 2011.

[426] A. Rahman, A. P. Yalin, V. Surla, O. Stan, K. Hoshimiya, Z. Yu, E. Littlefield and G. J. Collins, "Absolute UV and VUV emission in the 110–400 nm region from 13.56 MHz driven hollow slot microplasmas operating in open air," Plasma Sources Science and Technology, vol. 13, no. 3, p. 537, 2004.

[427] C. Lazzaroni and P. Chabert, "A comparison between micro hollow cathode discharges and atmospheric pressure plasma jets in Ar/O2 gas mixtures.," Plasma Sources Science and Technology, vol. 25, no. 6, p. 065015, 2016.

[428] Y. C. Hong, H. J. Park, B. J. Lee, W.-S. Kang and H. S. Uhm, "Plasma formation using a capillary discharge in water and its application to the sterilization of E. coli," Physics of Plasmas, vol. 17, no. 5, p. 053502, 2010.

[429] T.-S. Cho, S.-H. Park, K. H. Becker and E. E. Kunhardt, "Investigation of discharge phenomena in microscale capillary plasma electrode discharges," IEEE Transactions on Plasma Science, vol. 39, no. 6, pp. 1496-1499, 2011.

[430] N. A. Huynh, T. Li, M. Kovalenko, R. D. Robinson, A. A. Fridman, A. Rabinovich and G. Fridman, "Nonequilibrium plasma decontamination of corn steep liquor for ethanol production: SO2 removal and disinfection," Plasma Medicine, vol. 6, no. 3-4, 2016.

[431] A. Sakudo, Y. Yagyu and T. Onodera, "Disinfection and Sterilization Using Plasma Technology: Fundamentals and Future Perspectives for Biological Applications.," International Journal of Molecular Sciences, vol. 20, no. 20, p. 5216, 2019.

[432] J. Winter, R. Brandenburg and K. D. Weltmann, "Atmospheric pressure plasma jets: an overview of devices and new directions.," Plasma Sources Science and Technology, vol. 24, no. 6, p. 064001, 2015.

[433] X. Zhang, A. Bose, D. Maddipatla, B. Narakathu, V. Turkani and M. Z. Atashbar, "Design, simulation and fabrication of a novel MEMS based pulsometer," In Multidisciplinary Digital Publishing Institute Proceedings, vol. 2, no. 3, p. 951, 2018, doi: 10.3390/proceedings2130951.

[434] M. E. Moses, S. Forrest, A. L. Davis, M. A. Lodder and J. H. Brown, "Scaling theory for information networks," Journal of the Royal Society Interface, vol. 5, no. 29, pp. 1469-1480, 2008.

[435] H. Kim and S. Lee, "Characterization of electrical heating of graphene/PLA honeycomb structure composite manufactured by CFDM 3D printer," Fashion and Textiles, vol. 7, no. 1, pp. 1-18, 2020.

[436] G. McNeill and S. A. Hale, "Generating tile maps," In Computer Graphics Forum, vol. 36, no. 3, pp. 435-445, 2017.

[437] S. Garg and R. B. Patel, "Review of different deployment schemes in wireless sensor networks," in In 2017 3rd International Conference on Computational Intelligence & Communication Technology (CICT), 2017.

[438] J. Choi, F. Iza, J. K. Lee and C.-M. Ryu, "Electron and ion kinetics in a DC microplasma at atmospheric pressure," IEEE Transactions on Plasma Science, vol. 35, no. 5, pp. 1274-1278, 2007.

[439] Y. J. Hong, S. M. Lee, G. C. Kim and J. K. Lee, "Modeling High-Pressure Microplasmas: Comparison of Fluid Modeling and Particle-in-Cell Monte Carlo Collision Modeling," Plasma Processes and Polymers, vol. 5, no. 6, pp. 583-592, 2008.

[440] M. U. Lee, S. Y. Jeong, I. H. Won, S. K. Sung, G. S. Yun and J. K. Lee, "Non-Maxwellian to Maxwellian transitions of atmospheric microplasmas at microwave frequencies," Physics of Plasmas, vol. 23, no. 7, p. 070704, 2016.

[441] H. Y. Kim, M. Gołkowski, C. Gołkowski, P. Stoltz, M. B. Cohen and M. Walker, "PIC simulations of post-pulse field reversal and secondary ionization in nanosecond argon discharges," Plasma Sources Science and Technology, vol. 27, no. 5, p. 055011, 2018.

[442] L.-G. Meng, J.-P. Xing, Y.-J. Lv, Z.-H. Liang and C.-L. Liu, "Simulations of Breakdown Voltage of Coplanar Electrodes Microplasma Devices," IEEE Transactions on Plasma Science, vol. 41, no. 1, pp. 12-16, 2012.

[443] M. Z. Atashbar, B. J. Bazuin, M. Simpeh and S. Krishnamurthy, "3D FE simulation of H2 SAW gas sensor.," Sensors and Actuators B: Chemical, vol. 111, pp. 213-218, 2005, doi: 10.1016/j.snb.2005.06.054.

[444] A. Bose, B. Narakathu, B. Bazuin and M. Atashbar, "Modelling and simulation of microplasma discharge device for sterilization applications," In Multidisciplinary Digital Publishing Institute Proceedings, vol. 2, no. 13, p. 948, 2018, doi: 10.3390/proceedings2130948.

[445] M. Z. Atashbar, B. J. Bazuin and S. Krishnamurthy, "Design and simulation of SAW sensors for wireless sensing," In IEEE Sensors, pp. 1-4, 2003, doi: 10.1109/ICSENS.2003.1279005.

[446] M. Z. Atashbar and W. Wlodarski, "Design, simulation and fabrication of doped TiO2-coated surface acoustic wave oxygen sensor," Journal of Intelligent Material Systems and Structures, vol. 8, no. 11, pp. 953-959, 1997, doi: 10.1177/1045389X9700801104.

[447] S. Krishnamurthy, M. Z. Atashbar and K. Kalantar-zadeh, "3D modeling and simulation of SH-SAW devices using the finite element method," In IEEE Sensors, pp. 1-4, 2007, doi: 10.1109/ICSENS.2007.4388409.

[448] C.-J. Cheng and M. Z. Atashbar, "Finite element simulation of SMFBAR based sensor.," In 2009 IEEE International Conference on Electro/Information Technology, pp. 190-195, 2009, doi: https://doi.org/10.1109/EIT.2009.5189609.

[449] C. J. Cheng and M. Z. Atashbar, "Three dimensional finite element modeling and simulation of quasi-shear mode resonator based on c-axis-titled ZnO film," In IEEE Sensors, pp. 1-4, 2009, doi: 10.1109/ICSENS.2009.5398562.

[450] M. Z. Atashbar, B. J. Bazuin and .. Krishnamurthy, "Performance evaluation of SAW devices by simulation," International Journal of Modelling and Simulation, vol. 24, no. 4, pp. 250-262, 2004, doi: 10.1080/02286203.2004.11442310.

[451] T. Deconinck, S. Mahadevan and L. L. Raja, "Computational simulation of coupled nonequilibrium discharge and compressible flow phenomena in a microplasma thruster," Journal of Applied Physics, vol. 106, no. 6, p. 063305, 2009.

[452] T. Takahashi, Y. Takao, K. Eriguchi and K. Ono, "Numerical and experimental study of microwave-excited microplasma and micronozzle flow for a microplasma thruster," Physics of Plasmas, vol. 16, no. 8, p. 083505, 2009.

[453] M. S. Sawant, N. K. Jain and S. H. Nikam, "Theoretical modeling and finite element simulation of dilution in micro-plasma transferred arc additive manufacturing of metallic materials," International Journal of Mechanical Sciences, vol. 164, p. 105166, 2019.

[454] Y. Dai, L. Wen, J. Liu and H. Wang, "Simulation and experiment of inverted pyramid DBD micro-plasma devices array for maskless nanoscale etching," in In IEEE Nano/Micro Engineered and Molecular Systems (NEMS), 2016.

[455] J. Mizeraczyk, B. Hrycak, M. Jasiński and M. Dors, "Low-temperature microwave microplasma for bio-decontamination," Przegląd Elektrotechniczny, vol. 88, no. 9b, pp. 38-241, 2012.

[456] T. Martens, A. Bogaerts, W. Brok and J. v. Dijk, "Computer simulations of a dielectric barrier discharge used for analytical spectrometry," Analytical and Bioanalytical Chemistry, vol. 388, no. 8, pp. 1583-1594, 2007.

[457] K. Shimizu, M. Yoshinori, I. Akihiko and B. Marius, "Microplasma actuator for active flow control: Experiment and simulation," in Procceedings of The Japan Society of Applied Physics, 2015.

[458] J. H. Seo and J. G. Eden, "Two-dimensional simulation of ac-driven microplasmas confined to 100–300 μ m diameter cylindrical microcavities in dielectric barrier devices," Journal of Applied Physics, vol. 100, no. 12, p. 123302, 2006.

[459] K. H. Schoenbach and K. Becker, "20 Years of Microplasma Research: A Status Report," European Physical Journal D, vol. 70, no. 2, p. 29, 2016.

[460] C.-C. Hsu, J.-H. Tsai, Y.-J. Yang, Y.-C. Liao and Y. W. Lu, "Foldable Microplasma Generation Device on a Paper Substrate," Journal of Microelectromechanical Systems, vol. 21, no. 5, pp. 1013-1015, 2012.

[461] A. Schmidt-Bleker, J. Winter, A. Bösel, S. Reuter and K.-D. Weltmann, "On the plasma chemistry of a cold atmospheric argon plasma jet with shielding gas device," Plasma Sources Science and Technology, vol. 25, no. 1, p. 015005, 2015.

[462] R. Massarczyk, P. Chu, C. Dugger, S. R. Elliott, K. Rielage and W. Xu, "Paschen's law studies in cold gases," Journal of Instrumentation, vol. 12, no. 6, p. P06019, 2017.

[463] Y. Fu, P. Zhang, J. P. Verboncoeur and X. Wang, "Electrical breakdown from macro to micro/nano scales: a tutorial and a review of the state of the art," Plasma Research Express, vol. 2, no. 1, p. 013001, 2020.

[464] C. Canali, C. Jacoboni, F. Nava, G. Ottaviani and A. Alberigi-Quaranta, "Electron drift velocity in silicon," Physical Review B: Condensed Matter, vol. 12, no. 6, p. 2265, 1975.

[465] G. A. Haas, T. P. Jr and F. H. Harris, "Temperature dependence of electron drift velocity in silicon.," Journal of Applied Physics, vol. 44, no. 5, pp. 2433-2434, 1973.

[466] S. T. Surzhikov and J. S. Shang, "Two-component plasma model for two-dimensional glow discharge in magnetic field," Journal of Computational Physics, vol. 199, no. 2, pp. 437-464, 2004.

[467] V. A. Lisovsky, "Electron temperature dependence on electrode layer characteristics in low-pressure RF discharge," in In IEEE International Conference on Plasma Science, 1995.

[468] "Dielectric Barrier Discharge," Comsol, [Online]. Available: https://www.comsol.com/model/dielectric-barrier-discharge-8637. [Accessed 22nd February 2020].

[469] A. F. Borghesani and P. Lamp, "Electron mobility in dense argon gas at several temperatures," IEEE Transactions on Dielectrics and Electrical Insulation, vol. 10, no. 6, pp. 977-984, 2003.

[470] A. Laugier and J. Garai, "Derivation of the ideal gas law," Journal of Chemical Education, vol. 84, no. 11, p. 1832, 2007.

[471] G. Isbary, J. L. Zimmermann, T. Shimizu, G. E. Morfill, A. Mitra, H. Thomas, T. G. Klampfl, J. Koeritzer, V. Boxhammer, J. Schlegel and W. Stolz, "Reasons Why We Need Cold Atmospheric Plasmas in Bacteria-Related Diseases in Medicine," Plasma Medicine, vol. 2, no. 1-3, pp. 85-96, 2012.

[472] H. Eto, Y. Ono, A. Ogino and M. Nagatsu, "Low-Temperature Sterilization of Wrapped Materials Using Flexible Sheet-Type Dielectric Barrier Discharge," Applied Physics Letters, vol. 93, no. 22, p. 221502, 2008.

[473] K. D. Weltmann, R. Brandenburg, T. v. Woedtke, J. Ehlbeck, R. Foest, M. Stieber and E. Kindel, "Antimicrobial Treatment of Heat Sensitive Products by Miniaturized Atmospheric Pressure Plasma Jets (APPJs)," Journal of Physics D, vol. 41, p. 194008, 2008.

[474] Z. S. Rad and F. A. Davani, "Non-thermal Atmospheric Pressure Dielectric Barrier Discharge Plasma Source Construction and Investigation on the Effect of Grid on Wound Healing Application," Clinical Plasma Medicine, vol. 4, pp. 56-64, 2016.

[475] C. V. Suschek and C. Opländer, "The Application of Cold Atmospheric Plasma in Medicine: The Potential Role of Nitric Oxide in Plasma-induced Effects," Clinical Plasma Medicine, vol. 4, pp. 1-8, 2016.

[476] R. López-Callejas, R. Peña-Eguiluz, R. Valencia-Alvarado, A. Mercado-Cabrera, B. G. Rodríguez-Méndez, J. H. Serment-Guerrero, A. Cabral-Prieto, A. C. González-Garduño, N. A. Domínguez-Cadena, J. Muñoz-Infante and M. Betancourt-Ángeles, "Alternative method for healing the diabetic foot by means of a plasma needle," Clinical Plasma Medicine, vol. 9, pp. 19-23, 2018.

[477] X. Liao, D. Liu, Q. Xiang, J. Ahn, S. Chen, X. Ye and T. Ding, "Inactivation Mechanisms of Non-thermal Plasma on Microbes: A Review," Food Control, vol. 75, pp. 83-91, 2017.

[478] N. Y. Babaeva and G. V. Naidis, "Modeling of plasmas for biomedicine," Trends in Biotechnology, vol. 36, no. 6, pp. 603-614, 2018.

[479] X. Su, Y. Tian, H. Zhou, Y. Li, Z. Zhang, B. Jiang, B. Yang, J. Zhang and J. Fang, "Inactivation efficacy of nonthermal plasma-activated solutions against Newcastle disease virus," Applied and Environmental Microbiology, vol. 84, no. 9, pp. e02896-17, 2018.

[480] F. Su, W. Wang, A. G. Burns, X. Yue and F. Zhu, "The correlation between electron temperature and density in the topside ionosphere during 2006–2009.," Journal of Geophysical Research: Space Physics, vol. 120, no. 12, pp. 10-724, 2015.

[481] A. P. Rao, M. Gragston, A. K. Patnaik, P. S. Hsu and M. B. Shattan, "Measurement of electron density and temperature from laser-induced nitrogen plasma at elevated pressure (1–6 bar)," Optics Express, vol. 27, no. 23, pp. 33779-33788, 2019.

[482] S. C. Schaub, J. S. Hummelt, W. C. Guss, M. A. Shapiro and R. J. Temkin., "Electron density and gas density measurements in a millimeter-wave discharge," Physics of Plasmas, vol. 23, no. 8, p. 083512, 2016.

[483] K. W. McDermott, W. J. Freeman and A. Elixhauser, "Overview of operating room procedures during inpatient stays in US hospitals, 2014: statistical brief# 233," Agency for Healthcare Research and Quality, Rockville, 2017.

[484] "Global guidelines on the prevention of surgical site infection," World Health Organization, [Online]. Available: https://www.who.int/gpsc/ssi-prevention-guidelines/en/. [Accessed 5 5 2021].

[485] S. S. Magill, J. R. Edwards, W. Bamberg, Z. G. Beldavs, G. Dumyati, M. A. Kainer, R. Lynfield, M. Maloney, L. McAllister-Hollod, J. Nadle and S. M. Ray, "Multistate point-prevalence survey of health care–associated infections," The New England Journal of Medicine, vol. 370, no. 13, pp. 1198-1208, 2014.

[486] G. D. Lissovoy, K. Fraeman, V. Hutchins, D. Murphy, D. Song and B. B. Vaughn, "Surgical site infection: incidence and impact on hospital utilization and treatment costs," American journal of infection control, vol. 37, no. 5, pp. 387-397, 2009.

[487] "Drinking water," World Health Organization, [Online]. Available: https://www.who.int/news-room/fact-sheets/detail/drinking-water. [Accessed 6th June 2020].

[488] N. Pichel, M. Vivar and M. Fuentes, "The problem of drinking water access: A review of disinfection technologies with an emphasis on solar treatment methods," Chemosphere , vol. 218, pp. 1014-1030, 2019.

[489] "Chloride in drinking-water: Background document for development of WHO guidelines for drinking-water quality.," World health Organization, [Online]. Available: https://www.who.int/water_sanitation_health/publications/chloride/en/. [Accessed 6 June 2020].

[490] K. Song, M. Mohseni and F. Taghipour, "Application of ultraviolet light-emitting diodes (UV-LEDs) for water disinfection: A review," Water research, vol. 94, pp. 341-349, 2016.

[491] Q. Tan, W. Li, J. Zhang, W. Zhou, J. Chen, Y. Li and J. Ma, "Presence, dissemination and removal of antibiotic resistant bacteria and antibiotic resistance genes in urban drinking water system: A review," Frontiers of Environmental Science & Engineering , vol. 13, no. 3, pp. 1-15, 2019.

[492] M. Raeiszadeh and F. Taghipour, "Microplasma UV lamp as a new source for UV-induced water treatment: Protocols for characterization and kinetic study," Water research, vol. 164, p. 114959, 2019.

[493] A. El-Saed, H. H. Balkhy, M. M. Alshamrani, S. Aljohani, A. Alsaedi, W. A. Nasser, A. E. Gammal, S. A. Almohrij, Z. Alyousef, S. Almunif and M. Alzahrani, "High contribution and impact of resistant gram negative pathogens causing surgical site infections at a multi-hospital healthcare system in Saudi Arabia, 2007–2016," BMC Infectious Diseases, vol. 20, pp. 1-9, 2020.

[494] "E. coli (Escherichia coli)," Centers for Disease Control and Prevention, U.S. Department of Health & Human Services, [Online]. Available: https://www.cdc.gov/ecoli/general/index.html. [Accessed 14th September 2020].

[495] S. Yin, P. Chen, B. You, Y. Zhang, B. Jiang, G. Huang, Z. Yang, Y. Chen, J. Chen, Z. Yuan and Y. Zhao, "Molecular typing and carbapenem resistance mechanisms of Pseudomonas aeruginosa isolated from a Chinese burn center from 2011 to 2016," Frontiers in microbiology, vol. 9, p. 1135, 2018.

[496] "Healthcare-Associated Infections (HAIs)," Centers for Disease Control and Prevention, U.S. Department of Health & Human Services, [Online]. Available: https://www.cdc.gov/hai/organisms/pseudomonas.html. [Accessed 14th September 2020].

[497] "Antibiotic / Antimicrobial Resistance (AR / AMR)," Centers for Disease Control and Prevention, U.S. Department of Health & Human Services, [Online]. Available: https://www.cdc.gov/drugresistance/biggest-threats.html#pse. [Accessed 14 September 2020].

[498] "Multidrug-Resistant Pseudomonas aeruginosa," Centers for Disease Control and Prevention, U.S. Department of Health & Human Services, [Online]. Available: https://www.cdc.gov/drugresistance/pdf/threats-report/pseudomonas-aeruginosa-508.pdf. [Accessed 14th September 2020].

[499] "Staphylococcus aureus," Centers for Disease Control and Prevention, U.S. Department of Health & Human Services, [Online]. Available: https://www.cdc.gov/hai/organisms/staph.html.

[500] T. A. Taylor and C. G. Unakal, "Staphylococcus aureus," Treasure Island, FL, StatPearls Publishing, 2017.

[501] "Final risk assessment of Bacillus subtilis," United States Environmental Protection Agency, [Online]. Available: https://www.epa.gov/sites/production/files/2015-09/documents/fra009.pdf. [Accessed 9th April 2021].

[502] B. J. Jacobsen, N. K. Zidack and B. J. Larson, "The role of Bacillus-based biological control agents in integrated pest management systems: plant diseases," Phytopathology, vol. 94, no. 11, pp. 1272-1275, 2004.

[503] X. Q. Wang, D. L. Zhao, L. L. Shen, C. L. Jing and C. S. Zhang, "Application and mechanisms of Bacillus subtilis in biological control of plant disease," in In Role of rhizospheric microbes in soil, Singapore, Springer, 2018, pp. 225-250.

[504] E. Bédard, M. Prévost and E. Déziel, "Pseudomonas aeruginosa in premise plumbing of large buildings," Microbiologyopen, vol. 5, no. 6, pp. 937-956, 2016.

[505] R. Shrivastava, R. K. Upreti, S. R. Jain, K. N. Prasad, P. K. Seth and U. C. Chaturvedi, "Suboptimal chlorine treatment of drinking water leads to selection of multidrug-resistant Pseudomonas aeruginosa," Ecotoxicology and Environmental Safety, vol. 58, no. 2, pp. 277-283, 2004.

[506] B. B. Narakathu, S. G. R. Avuthu, A. Eshkeiti, S. Emamian and M. Z. Atashbar, "Development of a Microfluidic Sensing Platform by Integrating PCB Technology and Inkjet Printing Process," IEEE Sensors Journal, vol. 15, no. 11, pp. 6374-6380, 2015, doi: 10.1109/JSEN.2015.2457239.

[507] L. He, Z. Chen, S. Wang, M. Wu, P. Setlow and Y. Li, "Germination, outgrowth, and vegetative-growth kinetics of dry-heat-treated individual spores of Bacillus species," Applied and Environmental Microbiology, vol. 84, no. 7, pp. e02618-17, 2018.

[508] A. Han, J. K. Tsoi, J. P. Matinlinna, Y. Zhang and Z. Chen, "Effects of different sterilization methods on surface characteristics and biofilm formation on zirconia in vitro.," Dental Materials, vol. 34, no. 2, pp. 272-281, 2018.

[509] J.-H. Yoo, "Review of disinfection and sterilization–back to the basics," Infection & Chemotherapy, vol. 50, no. 2, p. 101, 2018.

[510] A. Soni, J. Smith, A. Thompson and G. Brightwell, "Microwave-induced thermal sterilization-A review on history, technical progress, advantages and challenges as compared to the conventional methods," Trends in Food Science and Technology, vol. 97, pp. 433-442, 2020.

[511] N. Pichel, M. Vivar and M. Fuentes, "The problem of drinking water access: A review of disinfection technologies with an emphasis on solar treatment methods," Chemosphere, vol. 218, pp. 1014-1030, 2019.

[512] "Chloride in drinking-water: Background document for development of WHO guidelines for drinking-water quality," World health Organization, [Online]. Available: https://www.who.int/water_sanitation_health/publications/chloride/en/. [Accessed 6th June 2020].

[513] B. Sera and M. Sery, "Non-thermal plasma treatment as a new biotechnology in relation to seeds, dry fruits, and grains," Plasma Science and Technology, vol. 20, p. 044012, 2018.

[514] A. K. Bose, D. Maddipatla and M. Z. Atashbar, "2-D Finite-Element Modeling of Surface Dielectric Barrier Plasma Discharge Devices to Understand the Influence of Design Parameters on Sterilization Applications," IEEE Transactions on Plasma Science, vol. 50, no. 4, pp. 841-852, 2022, doi: 10.1109/TPS.2022.3156031.

[515] W. M. Arnold, "Microplasma Disinfection of Meat," Australian Meat Processor Corporation, 2018.

[516] B. G. Dasan, T. Yildirim and I. H. Boyaci, "Surface Decontamination of Eggshells by Using Non-Thermal Atmospheric Plasma," International Journal of Food Microbiology, vol. 266, pp. 267-273, 2018.

[517] K. Shimizu, H. Fukunaga and M. Blajan, "Biomedical Applications of Atmospheric Microplasma," Current Applied Physics, vol. 14, pp. 154-161, 2014.

[518] R. Olsen, E. Kudirkiene, I. Thøfner, S. Pors, P. Karlskov-Mortensen, L. Li, S. Papasolomontos, C. Angastiniotou and J. Christensen, "Impact of Egg Disinfection of Hatching Eggs on the Eggshell Microbiome and Bacterial Load," Poultry Science, vol. 96, pp. 3900-3911, 2017.

[519] D. Santo, A. Graca, C. Nunes and C. Quintas, "Escherichia coli and Cronobacter sakazakii in 'Tommy Atkins' Minimally Processed Mangos: Survival, Growth and Effect of UV-C and Electrolyzed Water," Food microbiology, vol. 70, pp. 49-54, 2018.

[520] B. S. Nagoba, S. P. Selkar, B. J. Wadher and R. C. Gandhi, "Acetic Acid Treatment of Pseudomonal Wound Infections – A Review," Journal of Infection and Public Health, vol. 6, pp. 410-415, 2013.

[521] P. F. Ambrico, M. Šimek, C. Rotolo, M. Morano, A. Minafra, M. Ambrico, S. Pollastro, D. Gerin, F. Faretra and R. M. D. M. Angelini, "Surface Dielectric Barrier Discharge plasma: a suitable measure against fungal plant pathogens," Science Reports, vol. 10, no. 1, pp. 1-17, 2020.

[522] Y. Rao, W. Shang, Y. Yang, R. Zhou and X. Rao, "mixed-species microbial biofilms with cold atmospheric plasma," Frontiers in Microbiology, vol. 11, p. 1000, 2020.

[523] E. R. Sanders, "Aseptic laboratory techniques: plating methods," Journal of Visualized Experiments, vol. 63, p. e3064, 2012.

[524] T. E. Kimkes and M. Heinemann, "How bacteria recognise and respond to surface contact," FEMS Microbiology Reviews, vol. 44, no. 1, pp. 106-122, 2020.

[525] A. Choudhary, "Pharmaceutical Guidelines," [Online]. Available: https://www.pharmaguideline.com/2015/09/incubation-of-petri-dishes-in-inverted-position.html. [Accessed 17th September 2021].

[526] M. Krewing, B. Schubert and J. E. Bandow, "Dielectric Barrier Discharge Plasma Degrades Proteins to Peptides by Cleaving the Peptide Bond," Plasma Chemistry and Plasma Processing, vol. 40, no. 3, pp. 685-696, 2020.

[527] J. Hopwood, F. Iza, S. Coy and D. B. Fenner, "A microfabricated atmospheric-pressure microplasma source operating in air," Journal of Physics D: Applied Physics, vol. 38, no. 11, p. 1698, 2005.

[528] H. J. Ahn, K. I. Kim, N. N. Hoan, C. H. Kim, E. Moon, K. S. Choi, S. S. Yang and J.-S. Lee, "Targeting cancer cells with reactive oxygen and nitrogen species generated by atmospheric-pressure air plasma," Public Library of Science (PLOS) One, vol. 9, no. 1, p. e86173, 2014.

[529] D. L. P. Jennifer Meador-Parton, "Structural analysis of Bacillus subtilis spore peptidoglycan during sporulation," Journal of bacteriology, vol. 182, no. 16, pp. 4491-4499, 2000.

[530] D.-J. S. Danae Morales Angeles, "The cell wall of Bacillus subtilis," Current Issues in Molecular Biology, vol. 41, no. 1, pp. 539-596, 2021.

[531] Y. Liu, Q.-S. Liu and J.-H. Tay, "Initial conditions-dependent growth kinetics in microbial batch culture," Process Biochemistry, vol. 40, no. 1, pp. 155-160, 2005.

[532] S. Dhar, H. Kumari, D. Balasubramanian and K. Mathee, "Cell-wall recycling and synthesis in Escherichia coli and Pseudomonas aeruginosa–their role in the development of resistance," Journal of Medical Microbiology, vol. 67, no. 1, pp. 1-21, 2018.

[533] W. Vollmer, D. Blanot and M. A. D. Pedro, "Peptidoglycan structure and architecture," FEMS Microbiology Reviews, vol. 32, no. 2, pp. 149-167, 2008.

[534] P. Giesbrecht, T. Kersten, H. Maidhof and J. Wecke, "Staphylococcal cell wall: morphogenesis and fatal variations in the presence of penicillin," Microbiology and Molecular Biology Reviews, vol. 62, no. 4, pp. 1371-1414, 1998.

[535] E. I. Tocheva, J. López-Garrido, H. V. Hughes, J. Fredlund, E. Kuru, M. S. VanNieuwenhze, Y. V. Brun, K. Pogliano and G. J. Jensen, "Peptidoglycan transformations during B acillus subtilis sporulation," Molecular microbiology, vol. 88, no. 4, pp. 673-686, 2013.

[536] H. I. Yong, H.-J. Kim, S. Park, K. Kim, W. Choe, S. J. Yoo and C. Jo, "Pathogen inactivation and quality changes in sliced cheddar cheese treated using flexible thin-layer dielectric barrier discharge plasma," Food Research International, vol. 69, pp. 57-63, 2015.

[537] J. Y. Kim, E. B. Jeon, M.-S. Choi, E. H. Choi, J. S. Lim, J. Choi and S. Y. Park, "The efficiency of atmospheric dielectric barrier discharge plasma against Escherichia coli and Bacillus cereus on dried laver (Porphyra tenera)," Foods, vol. 9, no. 8, p. 1013, 2020.

[538] Z. Berk, Food process engineering and technology, Academic press, 2018.

[539] R. Prakash, "Dielectric Barrier Discharge based Mercury-free plasma UV-lamp for efficient water disinfection," Science Reports, vol. 7, no. 1, pp. 1-8, 2017.

[540] A. Menciassi, A. Eisinberg, M. C. Carrozza and P. Dario, "Force sensing microinstrument for measuring tissue properties and pulse in microsurgery," IEEE/ASME transactions on mechatronics, vol. 8, no. 1, pp. 10-17, 2003.

[541] Y. Zhang, N. Anderson, S. Bland, S. Nutt, G. Jursich and S. Joshi, "All-printed strain sensors: Building blocks of the aircraft structural health monitoring system," Sensors and Actuators A: Physical, vol. 253, pp. 165-172, 2017.

[542] G.-Y. Lee, M.-S. Kim, H.-S. Yoon, J. Yang, J.-B. Ihn and S.-H. Ahn, "Direct printing of strain sensors via nanoparticle printer for the applications to composite structural health monitoring," Procedia CIRP, vol. 66, pp. 238-242, 2017.

[543] X. Liao, Q. Liao, X. Yan, Q. Liang, H. Si, M. Li, H. Wu, S. Cao and Y. Zhang, "Flexible and highly sensitive strain sensors fabricated by pencil drawn for wearable monitor," Advanced Functional Materials, vol. 25, no. 16, pp. 2395-2401, 2015.

[544] S. Siddique, J. G. Park, P. Andrei and R. Liang, "M3D aerosol jet printed buckypaper multifunctional sensors for composite structural health monitoring," Results in physics, vol. 13, p. 102094, 2019.

[545] H.-N. Li, L. Ren, Z.-G. Jia, T.-H. Yi and D.-S. Li, "State-of-the-art in structural health monitoring of large and complex civil infrastructures," Journal of Civil Structural Health Monitoring, vol. 6, no. 1, pp. 3-16, 2016.

[546] D. Agdas, J. A. Rice, J. R. Martinez and I. R. Lasa, "Comparison of visual inspection and structural-health monitoring as bridge condition assessment methods," Journal of Performance of Constructed Facilities, vol. 30, no. 3, p. 04015049, 2016.

[547] L. P. J. C. a. K. W. Mikolaj Miskiewicz, "Structural health monitoring of composite shell footbridge for its design validation," in In 2016 Baltic Geodetic Congress (BGC Geomatics), 2016.

[548] A. R. Burton, J. P. Lynch, M. Kurata and K. H. Law, "Fully integrated carbon nanotube composite thin film strain sensors on flexible substrates for structural health monitoring," Smart Materials and Structures, vol. 26, no. 9, p. 095052, 2017.

[549] H. Jin, Y. S. Abu-Raya and H. Haick, "Advanced materials for health monitoring with skin-based wearable devices," Advanced healthcare materials, vol. 6, no. 11, p. 1700024, 2017.

[550] Y. Yamamoto, S. Harada, D. Yamamoto, W. Honda, T. Arie, S. Akita and K. Takei, "Printed multifunctional flexible device with an integrated motion sensor for health care monitoring," Science advances, vol. 2, no. 11, p. e1601473, 2016.

[551] T. Augustin, J. Karsten, B. Kötter and B. Fiedler, "Health monitoring of scarfed CFRP joints under cyclic loading via electrical resistance measurements using carbon nanotube modified adhesive films," Composites Part A: Applied Science and Manufacturing, vol. 105, pp. 150-155, 2018.

[552] M. L. Wymore, J. E. V. Dam, H. Ceylan and D. Qiao, "A survey of health monitoring systems for wind turbines," Renewable and Sustainable Energy Reviews, vol. 52, pp. 976-990, 2015.

[553] M. Martinez-Luengo, A. Kolios and L. Wang, "Structural health monitoring of offshore wind turbines: A review through the Statistical Pattern Recognition Paradigm," Renewable and Sustainable Energy Reviews, vol. 64, pp. 91-105, 2016.

[554] S. Gupta and O. N. Pierron, "MEMS based nanomechanical testing method with independent electronic sensing of stress and strain," Extreme Mechanics Letters, vol. 8, pp. 167-176, 2016.

[555] H. Saboonchi, D. Ozevin and M. Kabir, "MEMS sensor fusion: Acoustic emission and strain," Sensors and Actuators A: Physical, vol. 247, pp. 566-578, 2016.

[556] C. D. Do, A. Erbes, J. Yan, K. Soga and A. A. Seshia, "Vacuum packaged low-power resonant MEMS strain sensor," Journal of Microelectromechanical Systems, vol. 25, no. 5, pp. 851-858, 2016.

[557] A. C. Fischer, F. Forsberg, M. Lapisa, S. J. Bleiker, G. Stemme, N. Roxhed and F. Niklaus, "Integrating mems and ics," Microsystems & Nanoengineering, vol. 1, no. 1, pp. 1-16, 2015.

[558] S. Masihi, P. Rezaei and M. Panahi, "Compact chip-resistor loaded active integrated patch antenna for ISM band applications," Wireless Personal Communications, vol. 97, no. 4, pp. 5733-5746, 2017.

[559] B. G. Rius, A. Baldi, B. Ziaie and M. Z. Atashbar, "Introduction to micro-/nanofabrication," in Handbook of Nanotechnology, Berlin, Springer, 2017, pp. 51-86.

[560] M. Z. Atashbar, B. E. Bejcek and S. Singamaneni, "Carbon nanotube network-based biomolecule detection," IEEE Sensors Journal, vol. 6, no. 3, pp. 524-528, 2006, doi: 10.1109/JSEN.2006.874491.

[561] H. P. Phan, D.-V. Dao and N.-T. Nguyen, "Silicon micro-/nanomachining and applications.," in Micro and Nanomanufacturing Volume II, Springer, 2018, pp. 225-261.

[562] M. Z. Atashbar, H. T. Sun, B. Gong, W. Wlodarski and R. Lamb, "XPS study of Nb-doped oxygen sensing TiO2 thin films prepared by sol-gel method," Thin Solid Films, vol. 326, no. 1-2, pp. 238-244, 1998, doi: 10.1016/S0040-6090(98)00534-3.

[563] G. Sberveglieri, E. Comini, G. Faglia, M. Z. Atashbar and W. Wlodarski, "Titanium dioxide thin films prepared for alcohol microsensor applications," Sensors and Actuators B: Chemical, vol. 66, no. 1-3, pp. 139-141, 2000.

[564] M. Z. Atashbar, B. Gong, H. T. Sun, W. Wlodarski and R. Lamb, "Investigation on ozone-sensitive In2O3 thin films," Thin Solid Films, vol. 354, no. 1-2, pp. 222-226, 1999, doi: 10.1016/S0040-6090(99)00405-8.

[565] S. G. R. Avuthu, B. B. Narakathu, A. Eshkeiti, S. Emamian, B. J. Bazuin, M. Joyce and M. Z. Atashbar, "Detection of heavy metals using fully printed three electrode electrochemical sensor," In 2014 IEEE Sensors, pp. 1-4, 2014, doi: 10.1109/ICSENS.2014.6985087.

[566] S. Krishnamurthy, M. Z. Atashbar and B. J. Bazuin, "Burst transceiver unit for wireless passive SAW sensing system," IEEE transactions on instrumentation and measurement, vol. 58, no. 10, pp. 3746-3753, 2009, doi: 10.1109/TIM.2009.2019707.

[567] C. Cantalini, W. Wlodarski, H. T. Sun, M. Z. Atashbar, M. Passacantando, A. R. Phani and S. Santucci, "Investigation on the cross sensitivity of NO2 sensors based on In2O3 thin films prepared by sol-gel and vacuum thermal evaporation," Thin Solid Films, vol. 350, no. 1-2, pp. 276-282, 1999, doi: 10.1016/S0040-6090(99)00269-2.

[568] Z. Ramshani, A. S. G. Reddy, B. B. Narakathu, J. T. Wabeke, S. O. Obare and M. Z. Atashbar, "SH-SAW sensor based microfluidic system for the detection of heavy metal compounds in liquid environments," Sensors and Actuators B: Chemical, vol. 217, pp. 72-77, 2015, doi: 10.1016/j.snb.2014.12.026.

[569] S. Hajian, P. Khakbaz, M. Moshayedi, D. Maddipatla, B. B. Narakathu, V. S. Turkani, B. J. Bazuin, M. Pourfath and M. Z. Atashbar, "Impact of Different Ratios of Fluorine, Oxygen, and Hydroxyl Surface Terminations on Ti3C2TxMXene as Ammonia Sensor: A First-Principles Study," In 2018 IEEE Sensors, pp. 1-3, 2018, doi: 10.1109/ICSENS.2018.8589699.

[570] K. Kalanatar-zadeh, A. Trinchi, W. Wlodarski, A. Holland and M. Z. Atashbar, "A novel SAW love mode device with nanocrystalline ZnO film for gas sensing applications," In IEEE-NANO, pp. 556-561, 2001, doi: 10.1109/NANO.2001.966484.

[571] B. R. Young, T. L. Young, M. K. Joyce, S. I. Kennedy and M. Z. Atashbar , "Future opportunities for advancing glucose test device electronics," Journal of Diabetes Science and Technology , vol. 5, no. 5, pp. 1077-1086, 2011, doi: 10.1177/193229681100500508.

[572] M. Z. Atashbar and S. Singamaneni, "Template-based fabrication of metal nanostructures," in Proceedings of the Institution of Mechanical Engineers, Part N: Journal of Nanoengineering and Nanosystems, vol. 218, no. 2, pp. 83-89, 2004, doi: 10.1243/174034905X42308.

[573] M. Z. Atashbar, V. N. Bliznyuk and S. Singamaneni, "Manipulation of Nickel Nanoparticles Deposited on HOPG," In MRS Online Proceedings Library, vol. 853, pp. 81-86, 2004, doi: 10.1557/PROC-853-I5.9.

[574] M. Z. Atashbar, B. Bejcek, A. Vijh and S. Singamaneni, "Sensitivity enhancement of a QCM biosensor using polymer treatment," In IEEE Ultrasonics Symposium, vol. 1, pp. 329-332, 2004, doi: https://doi.org/10.1109/ULTSYM.2004.1417732.

[575] M. Z. Atashbar, V. Bliznyuk, D. Banerji and S. Singamaneni, "Deposition and manipulation of nickel nanoparticles," Proceedings of International Conference on Intelligent Sensing and Information Processing, pp. 258-261, 2004, doi: 10.1109/ICISIP.2004.1287663.

[576] M. Z. Atashbar, D. Banerji and S. Singamaneni, "Hydrogen sensor based on palladium nanowire array," In International Conference on Intelligent Sensing and Information Processing, pp. 185-189, 2004, doi: https://doi.org/10.1109/ICISIP.2004.1287649.

[577] M. Z. Atashbar, B. Bejcek and S. Singamaneni, "SWNT network for biomolecule detection," In MRS Online Proceedings Library (OPL), vol. 858, 2004, doi: 10.1557/PROC-858-HH14.8.

[578] D. B. Go, M. Z. Atashbar, Z. Ramshani and H. C. Chang, "Surface acoustic wave devices for chemical sensing and microfluidics: a review and perspective," Analytical methods, vol. 9, no. 28, pp. 4112-4134, 2017, doi: 10.1039/C7AY00690J.

[579] M. F. Yu, M. Z. Atashbar and X. Chen, "Mechanical and Electrical Characterization of/spl beta/-Ga/sub 2/O/sub 3/Nanostructures for Sensing Applications," IEEE Sensors Journal 5 (1), , vol. 5, no. 1, pp. 20-25, 2005, doi: 10.1109/JSEN.2004.838669.

[580] M. Z. Atashbar and S. Singamaneni, "Comparative studies of temperature dependence of G-band peak in single walled carbon nanotube and highly oriented pyrolytic graphite," Applied physics Letters, vol. 86, no. 12, p. 123112, 2005, doi: 10.1063/1.1884260.

[581] N. Ghafouri, H. Kim, M. Z. Atashbar and K. Najafi, "A micro thermoelectric energy scavenger for a hybrid insect," In 2008 IEEE Sensors, pp. 1249-1252, 2008, doi: 10.1109/ICSENS.2008.4716670 .

[582] V. S. Turkani, D. Maddipatla, B. B. Narakathu, T. S. Saeed, S. O. Obare, B. J. Bazuin and M. Z. Atashbar, "A highly sensitive printed humidity sensor based on a functionalized MWCNT/HEC composite for flexible electronics application," Nanoscale Advances, vol. 1, no. 6, pp. 2311-2322, 2019, doi: 10.1039/C9NA00179D.

[583] S. G. R. Avuthu, J. T. Wabeke, B. B. Narakathu, D. Maddipatla, J. S. Arachchilage, S. O. Obare and M. Z. Atashbar, "A screen printed phenanthroline-based flexible electrochemical sensor for selective detection of toxic heavy metal ions," IEEE Sensors Journal, vol. 16, no. 24, pp. 8678-8684, 2016, doi: 10.1109/JSEN.2016.2572184.

[584] S. Emamian, S. G. R. Avuthu, B. B. Narakathu, A. Eshkeiti, A. A. Chlaihawi, B. J. Bazuin, M. K. Joyce and M. Z. Atashbar, "Fully printed and flexible piezoelectric based touch sensitive skin," In 2015 IEEE Sensors, pp. 1-4, 2015, doi: 10.1109/ICSENS.2015.7370651.

[585] M. Ochoa, R. Rahimi, J. Zhou, H. Jiang, C. K. Yoon, M. Oscai, V. Jain, T. Morken, R. H. Oliveira, D. Maddipatla and B. B. Narakathu, "A Manufacturable Smart Dressing With Oxygen Delivery And Sensing Capability For Chronic Wound Management," in In Micro-and Nanotechnology Sensors, Systems, and Applications X, vol. 10639, p. 106391C, 2018, doi: 10.1117/12.2306083.

[586] S. Hajian, X. Zhang, P. Khakbaz, S.-M. Tabatabaei, D. Maddipatla, B. B. Narakathu, R. G. Blair and M. Z. Atashbar, "Development of a Fluorinated Graphene-Based Resistive Humidity Sensor," IEEE Sensors Journal, vol. 20, no. 14, pp. 7517-7524, 2020, doi: 10.1109/JSEN.2020.2985055.

[587] A. Eshkeiti, M. Joyce, B. B. Narakathu, S. Emamian, S. G. R. Avuthu and M. Z. A. M. Joyce, "A novel self-supported printed flexible strain sensor for monitoring body movement and temperature," In 2014 IEEE Sensors, pp. 1-4, 2014, doi: 10.1109/ICSENS.2014.6985328.

[588] V. S. Turkani, B. B. Narakathu, D. Maddipatla, B. J. Bazuin and M. Z. Atashbar, "P1FW. 5-A Fully Printed CNT Based Humidity Sensor on Flexible PET Substrate," In Proceedings IMCS 2018, pp.519-520, 2018, doi: 10.5162/IMCS2018/P1FW.5.

[589] A. Eshkeiti, S. Emamian, S. G. R. Avathu, B. B. Narakathu, M. J. Joyce, M. K. Joyce, B. J. Bazuin and M. Z. Atashbar, "Screen printed flexible capacitive pressure sensor," In 2014 IEEE Sensors, pp. 1-4, 2014, doi: 10.1109/ICSENS.2014.6985222.

[590] D. Maddipatla, B. B. Narakathu, B. J. Bazuin and M. Z. Atashbar, "Development of a printed impedance based electrochemical sensor on paper substrate," In 2016 IEEE Sensors, pp. 1-4, 2016, doi: 10.1109/ICSENS.2016.7808785.

[591] V. S. Turkani, D. Maddipatla, B. B. Narakathu and M. Z. A. B. J. Bazuin, "A carbon nanotube based NTC thermistor using additive print manufacturing processes," Sensors and Actuators A: Physical, vol. 279, pp. 1-9, 2018, doi: 10.1016/j.sna.2018.05.042.

[592] D. Maddipatla, B. B. Narakathu, M. M. Ali, A. A. Chlaihawi and M. Z. Atashbar, "Development of a novel carbon nanotube based printed and flexible pressure sensor," In 2017 IEEE Sensors Applications Symposium (SAS), pp. 1-4, 2017, doi: 10.1109/SAS.2017.7894034.

[593] B. B. Narakathu, A. Eshkeiti, A. S. G. Reddy, M. Rebros, E. Rebrosova, M. K. Joyce, B. J. Bazuin and M. Z. Atashbar, "A novel fully printed and flexible capacitive pressure sensor," In 2012 IEEE Sensors, pp. 1-4, , 2012, doi: 10.1109/ICSENS.2012.6411354.

[594] A. S. G. Reddy, B. B. Narakathu, M. Z. Atashbar, M. Rebros, E. Rebrosova and M. K. Joyce, "Gravure printed electrochemical biosensor," Procedia Engineering, vol. 25, pp. 956-959, 2011, doi: 10.1016/j.proeng.2011.12.235.

[595] A. S. G. Reddy, B. B. Narakathu, M. Z. Atashbar, M. Rebros, E. Rebrosova, B. J. Bazuin, M. K. Joyce, P. D. Fleming and A. Pekarovicova, "Printed capacitive based humidity sensors on flexible substrates," Sensor Letters, vol. 9, no. 2, pp. 869-871, 2011, doi: 10.1166/sl.2011.1633.

[596] A. S. G. Reddy, B. B. Narakathu, A. Eshkeiti, B. J. Bazuin, M. Joyce and M. Z. Atashbar, "Fully printed organic thin film transistors (OTFT) based flexible humidity sensors," In 2013 IEEE Sensors, pp. 1-4, 2013,doi: 10.1109/ICSENS.2013.6688309 .

[597] A. K. Bose, C. L. Beaver, B. B. Narakathu, S. Rossbach, B. J. Bazuin and M. Z. Atashbar, "Development of flexible microplasma discharge device for sterilization applications," In 2018 IEEE Sensors, pp. 1-4, 2018, doi: 10.1109/ICSENS.2018.8589816.

[598] V. S. Turkani, B. B. Narakathu, D. Maddipatla, B. J. Bazuin and M. Z. Atashbar, "A Fully Printed CNT Based Humidity Sensor on Flexible PET Substrate," In Proceedings IMCS 2018, pp. 519-520, 2018, doi: 10.5162/IMCS2018/P1FW.5.

[599] V. S. Turkani, D. Maddipatla, B. B. Narakathu, B. J. Bazuin and M. Z. Atashbar, "A Fully Printed CNT Based Humidity Sensor on Flexible PET Substrate," In 17th International Meeting on Chemical Sensors (IMCS), pp.519-520, 2018, doi: 10.5162/IMCS2018/P1FW.5 .

[600] A. Eshkeiti, M. Joyce, B. B. Narakathu, S. Emamian, S. G. R. Avuthu, M. Joyce and M. Z. Atashbar, "A novel self-supported printed flexible strain sensor for monitoring body movement and temperature," in In 2014 IEEE Sensors, pp. 1615-1618, 2014, doi: 10.1109/ICSENS.2014.6985328.

[601] V. S. Turkani, D. Maddipatla, B. B. Narakathu, B. N. Altay, P. D. Fleming, B. J. Bazuin and M. Z. Atashbar, "Nickel based RTD fabricated via additive screen printing process for flexible electronics," IEEE Access, vol. 7, pp. 37518-37527, 2019, doi: 10.1109/ACCESS.2019.2904970.

[602] S. G. R. Avuthu, J. T. Wabeke, B. B. Narakathu, D. Maddipatla, A. Eshkeiti, S. Emamian, A. A. Chlaihawi, M. Joyce, S. O. Obare and M. Z. Atashbar, "Development of screen printed electrochemical sensors for selective detection of heavy metals," In 2015 IEEE Sensors, pp. 1-4, 2015 doi: 10.1109/ICSENS.2015.7370297.

[603] B. B. Narakathu, B. E. Bejcek and M. Z. Atashbar, "Impedance based electrochemical biosensors," In 2009 IEEE Sensors, pp. 1-4, 2009.

[604] S. Hajian, X. Zhang, D. Maddipatla, B. Baby Narakathu, J. I. Rodriguez-Labra, R. G. Blair and M. Z. Atashbar, "Flexible capacitive humidity sensor based on fluorinated graphene," In 2019 IEEE Sensors, pp. 1-4, 2019, doi: 10.1109/SENSORS43011.2019.8956564.

[605] M. Z. Atashbar, C. Baratto, G. Faglia and G. Sberveglieri, "Functionalized single wall carbon nanotubes based gas sensor," In 2006 IEEE Sensors, pp. 247-250, 2006, doi: 10.1109/ICSENS.2007.355758.

[606] D. Maddipatla, B. B. Narakathu and M. Atashbar, "Recent Progress in Manufacturing Techniques of Printed and Flexible Sensors: A Review," Biosensors, vol. 10, no. 199, pp. 1-24, 2020, doi: 10.3390/bios10120199.

[607] X. Zhang, D. Maddipatla, B. B. Narakathu, B. J. Bazuin and M. Z. Atashbar, "Development of a Novel Wireless Multi-Channel Stethograph System for Monitoring Cardiovascular and Cardiopulmonary Diseases," IEEE Access, vol. 9, pp. 128951-128964, 2021, doi: 10.1109/ACCESS.2021.3111778.

[608] X. Zhang, B. B. Narakathu, D. Maddipatla, V. S. Turkani, B. J. Bazuin and M. Z. Atashbar, "Digital signal processing and analysis of cardiopulmonary audio using a multi-channel stethograph system," In 2018 IEEE Sensors, pp. 1-4, 2018, doi: 10.1109/ICSENS.2018.8589512.

[609] J. I. Rodriguez-Labra, C. Kosik, D. Maddipatla, B. B. Narakathu and M. Z. Atashbar, "Development of a PPG Sensor Array as a Wearable Device for Monitoring Cardiovascular Metrics," IEEE Sensors Journal, vol. 21, no. 23, pp. 26320-26327, 2021, doi: 10.1109/JSEN.2021.3064219.

[610] M. Z. Atashbar, B. J. Bazuin, M. Simpeh and S. Krishnamurthy, "3-D finite-element simulation model of SAW palladium thin film hydrogen sensor," In Proceedings of the 2004 IEEE International Frequency Control Symposium and Exposition, pp. 549-553, 2004, doi: 10.1109/FREQ.2004.1418517.

[611] B. B. Narakathu, W. Guo, S. O. Obare and M. Z. Atashbar, "Novel approach for detection of toxic organophosphorus compounds," Sensors and Actuators B: Chemical, vol. 158, no. 1, pp. 69-74, 2011, doi: 10.1016/j.snb.2011.05.040.

[612] M. Z. Atashbar, D. Banerji, S. Singamaneni and V. Bliznyuk, "Deposition of parallel arrays of palladium nanowires and electrical characterization using microelectrode contacts," Nanotechnology, vol. 15, no. 3, p. 374, 2004.

[613] V. Bliznyuk, S. Singamaneni, R. Kattumenu and M. Atashbar, "Surface electrical conductivity in ultrathin single-wall carbon nanotube/polymer nanocomposite films," Applied physics letters, vol. 88, no. 16, p. 164101, 2006, doi: 10.1063/1.2193812.

[614] J. O. Manyala, T. Fritz and M. Z. Atashbar, "Integration of triaxial Hall-effect sensor technology for gear position sensing in commercial vehicle transmissions," IEEE Transactions on Instrumentation and Measurement, vol. 61, no. 3, pp. 664-672, 2011, doi: 10.1109/TIM.2011.2170376.

[615] A. Eshkeiti, Z. Ramshani, S. Emamian, B. B. Narakathu, S. G. R. Avuthu, M. M. Ali, A. Chlaihawi, M. K. Joyce and M. Z. Atashbar, "A stretchable and wearable printed sensor for human body motion monitoring," In 2015 IEEE Sensors, pp. 1-4, 2015, doi: 10.1109/ICSENS.2015.7370412.

[616] A. Eshkeiti, Z. Ramshani, S. Emamian, B. B. Narakathu, S. G. R. Avuthu, M. M. Ali, A. Chlaihawi, M. K. Joyce and M. Z. Atashbar, "A stretchable and wearable printed sensor for human body motion monitoring," In 2015 IEEE Sensors, pp. 1-4, 2015, doi: 10.1109/ICSENS.2015.7370412.

[617] S. Hajian, X. Zhang, D. Maddipatla, B. B. Narakathu, A. J. Hanson, R. G. Blair and M. Z. Atashbar, "Development of a fluorinated graphene-based flexible humidity sensor," in In 2019 IEEE

International Conference on Flexible and Printable Sensors and Systems (FLEPS), pp. 1-4, 2019, doi: 10.1109/FLEPS.2019.8792254.

[618] M. Z. Atashbar, V. Bliznyuk, D. Banerji and S. Singamaneni, "Deposition of parallel arrays of palladium nanowires on highly oriented pyrolytic graphite," Journal of alloys and compounds, vol. 372, no. 1-2, pp. 107-110, 2004, doi: 10.1016/j.jallcom.2003.10.014.

[619] J. I. Rodriguez-Labra, B. B. Narakathu and M. Z. Atashbar, "Development of a wireless robotic arm control system using piezoelectric sensors and neural networks," In 2019 IEEE Sensors, pp.1-4, 2019, doi: 10.1109/SENSORS43011.2019.8956669.

[620] X. Zhang, B. B. Narakathu, D. Maddipatla, B. J. Bazuin and M. Z. Atashbar, "Development of a Novel Wireless Multi-Channel Stethograph System for Diagnosing Pulmonary and Cardiovascular Diseases," In 17th International Meeting on Chemical Sensors (IMCS), pp. 673-674, 2018, doi: 10.5162/IMCS2018/P1DH.10.

[621] M. Z. Atashbar, D. Banerji, S. Singamaneni and V. Bliznyuk, "Polystyrene palladium nanocomposite for hydrogen sensing," In 5th International Conference Electronic Processes in Organic Materials, pp. 201-202, 2004, doi: 10.1080/15421400590892299.

[622] B. B. Narakathu, W. Guo, S. O. Obare and M. Z. Atashbar, "Detection of picomolar levels of toxic organophosphorus compounds by electrochemical and fluorescence spectroscopy," Sensor Letters, vol. 9, no. 2, pp. 907-909, 2011, doi: 10.1166/sl.2011.1641.

[623] B. B. Narakathu, A. S. G. Reddy, A. Eshkeiti, B. J. Bazuin and M. Z. Atashbar, "Opto-electrochemical based dual detection of heavy metal compounds using a novel flow cell," In 2013 IEEE Sensors, pp. 1-4, 2013, doi: 10.1109/ICSENS.2013.6688337.

[624] Z. Ramshani, B. B. Narakathu, A. S. G. Reddy, M. Z. Atashbar, J. T. Wabeke and S. O. Obare, "SH-SAW-based sensor for heavy metal ion detection," In 2015 Joint Conference of the IEEE International Frequency Control Symposium & the European Frequency and Time Forum, pp. 536-540, 2015, doi: 10.1109/FCS.2015.7138901.

[625] Z. Ramshani, B. B. Narakathu, S. Emamian, A. S. G. Reddy and M. Z. Atashbar, "Investigation of SH-SAW sensors for toxic heavy metal detection," In 2013 IEEE Sensors, pp. 1-4, 2013, doi: 10.1109/ICSENS.2013.6688510.

[626] B. B. Narakathu, W. Guo, S. O. Obare and M. Z. Atashbar, "Electrochemical impedance spectroscopy sensing of toxic organophosphorus compounds," In 2010 IEEE Sensors, pp. 1518-1521, 2010, doi: 10.1109/ICSENS.2010.5690337.

[627] C. J. Cheng, C. T. Feng and M. Z. Atashbar, "The analysis of IgG-protein a binding effect by quartz crystal microbalance biosensor," In 2010 IEEE Sensors, pp. 228-231, 2010, doi: 10.1109/ICSENS.2010.5690442.

[628] V. K. Varadan, P. Xavier, V. V. Varadan, D. Suh, M. Z. Atashbar and K. A. Jose, "MEMS-IDT-based accelerometers and gyroscopes," In Smart Structures and Materials 1999: Smart Electronics and MEMS, vol. 3673, pp. 182-189, 1999, doi: 10.1117/12.354267.

[629] M. Z. Atashbar and W. Wlodarski, "Design and fabrication of doped TiO2-coated surface acoustic wave oxygen sensor," Smart Materials, Structures, and Integrated Systems , vol. 3241, pp. 486-492, 1997, doi: 10.1117/12.293523.

[630] M. Z. Atashbar, A. Z. Sadek, W. Wlodarski, S. Sriram, M. Bhaskaran, C. J. Cheng, R. B. Kaner and K. Kalantar-Zadeh, "Layered SAW gas sensor based on CSA synthesized polyaniline nanofiber

on AlN on 64 YX LiNbO3 for H2 sensing," Sensors and Actuators B: Chemical, vol. 138, no. 1, pp. 85-89, 2009, doi: 10.1016/j.snb.2009.01.072.

[631] M. Z. Atashabr, J. O. Manyala, "Development of particle contaminants monitor system for gearbox lubricant prognostics," In 2016 IEEE Sensors, pp. 1-4, 2016, doi: 10.1109/ICSENS.2016.7808900.

[632] X. Zhang, D. Maddipatla, A. K. Bose, S. Hajian, B. B. Narakathu, J. D. Williams, M. F. Mitchell and M. Z. Atashbar, "Printed carbon nanotubes-based flexible resistive humidity sensor," IEEE Sensors Journal, vol. 20, no. 21, pp. 12592-12601, 2020, doi: 10.1109/JSEN.2020.3002951.

[633] V. S. Turkani, D. Maddipatla, B. B. Narakathu, B. J. Bazuin and M. Z. Atashbar, "A carbon nanotube based NTC thermistor using additive print manufacturing processes," Sensors and Actuators A: Physical, vol. 279, pp. 1-9, 2018, doi: 10.1016/j.sna.2018.05.042.

[634] H. Zhu, B. B. Narakathu, Z. Fang, A. T. Aijazi, M. Joyce, M. Atashbar and L. Hu, "A gravure printed antenna on shape-stable transparent nanopaper," Nanoscale, vol. 6, no. 15, pp. 9110-9115, 2014, doi: 10.1039/C4NR02036G.

[635] D. A. Alsaid, E. Rebrosova, M. Joyce, M. Rebros, M. Z. Atashbar and B. J. Bazuin, "Gravure printing of ITO transparent electrodes for applications in flexible electronics," Journal of Display Technology, vol. 8, no. 7, pp. 391-396, 2012.

[636] D. Maddipatla, B. B. Narakathu, S. G. R. Avuthu, S. Emamian, A. Eshkeiti, A. A. Chlaihawi, B. J. Bazuin, M. K. Joyce, C. W. Barrett and M. Z. Atashbar, "A novel flexographic printed strain gauge on paper platform," In 2015 IEEE Sensors, pp. 1-4, 2015, doi: 10.1109/ICSENS.2015.7370606.

[637] B. B. Narakathu, S. G. A. Reddy, M. Z. Atashbar, E. Rebrosova, M. Rebros and M. K. Joyce, "A novel gravure printed impedance based flexible electrochemical sensor," In 2011 IEEE Sensors, pp. 577-580, 2011, doi: 10.1109/ICSENS.2011.6127225.

[638] B. B. Narakathu, S. G. R. Avuthu, A. Eshkeiti, S. Emamian and M. Z. Atashbar, "Development of a novel printed flexible microfluidic sensing platform based on PCB technology," In 2014 IEEE Sensors, pp. 1-4, 2014, doi: 10.1109/ICSENS.2014.6985086.

[639] F. Aljanabi, B. B. Narakathu, S. Emamian, M. M. Ali, B. J. Bazuin, P. D. Fleming and M. Z. Atashbar, "Detection of cocaine using gravure printed silver nanoparticle based SERS substrate," In 2016 IEEE Sensors, pp. 1-4, 2016, doi: 10.1109/ICSENS.2016.7808639.

[640] S. Emamian, A. Eshkeiti, B. B. Narakathu, S. G. R. Avuthu and M. Z. Atashbar, "Detection of 2, 4-dinitrotoluene (DNT) using gravure printed surface enhancement Raman spectroscopy (SERS) flexible substrate," In 2014 IEEE Sensors,pp. 1-4, 2014, doi: 10.1109/ICSENS.2014.6985189.

[641] V. S. Turkani, D. Maddipatla, B. B. Narakathu, B. J. Bazuin and M. Z. Atashbar, "A carbon nanotube based NTC thermistor using additive print manufacturing processes," Sensors and Actuators A: Physical, vol. 279, pp. 1-9, 2018, doi: 10.1016/j.sna.2018.05.042.

[642] D. Maddipatla, B. B. Narakathu, V. S. Turkani, B. J. Bazuin and M. Z. Atashbar, "Development of a Gravure Printed Flexible Electrochemical Sensor," in 17th International Meeting on Chemical Sensors (IMCS), pp. 734-735, 2018, doi: 10.5162/IMCS2018/P2EC.19.

[643] S. G. R. Avuthu, J. T. Wabeke, B. B. Narakathu, D. Maddipatla, S. Emamian, A. Eshkeiti, A. A. Chlaihawi, B. J. Bazuin, S. O. Obare and M. Z. Atashbar, "Detection of heavy metal ions using screen printed wireless LC sensor," In 2015 IEEE Sensors, pp. 1-4, 2015, doi: 10.1109/ICSENS.2015.7370298.

[644] A. S. G. Reddy, B. B. Narakathu, M. Z. Atashbar, M. Rebros, E. Rebrosova and M. K. Joyce, "Fully printed flexible humidity sensor," Procedia Engineering, vol. 25, pp. 120-123, 2011, doi: 10.1016/j.proeng.2011.12.030.

[645] M. Z. Atashbar, B. Bejcek, A. Vijh and S. Singamaneni, "QCM biosensor with ultra thin polymer film," Sensors and Actuators B: Chemical, vol. 107, no. 2, pp. 945-951, 2005, doi: 10.1016/j.snb.2004.12.047.

[646] J. Crosby, D. Maddipatla, Q. Wu, B. Bazuin, M. Stoops and M. Atashbar, "Development Of A Flexible Printed Battery," In 2021 IEEE International Conference on Electro Information Technology (EIT), pp. 401-404, 2021, doi: 10.1109/EIT51626.2021.9491880.

[647] H. R. K. M. Emani, X. Zhang, G. Wang, D. Maddipatla, T. Saeed, Q. Wu, W. Lu and M. Z. Atashbar, "Development of a screen-printed flexible porous graphite electrode for Li-Ion battery," in 2021 IEEE International Conference on Flexible and Printable Sensors and Systems (FLEPS), pp. 1-4, 2021, doi: 10.1109/FLEPS51544.2021.9469794.

[648] B. N. Altay, B. Aksoy, D. Banerjee, D. Maddipatla, P. D. Fleming, M. Bolduc, S. G. Cloutier, M. Z. Atashbar, R. B. Gupta and M. Demir, "Lignin-derived carbon-coated functional paper for printed electronics," ACS Applied Electronic Materials, vol. 3, no. 9, pp. 3904-3914, 2021, doi: 10.1021/acsaelm.1c00502.

[649] S. Masihi, M. Panahi, D. Maddipatla, A. J. Hanson, S. Fenech, L. Bonek, N. Sapoznik, P. D. Fleming, B. J. Bazuin and M. Z. Atashbar, "Development of a Flexible Wireless ECG Monitoring Device with Dry Fabric Electrodes for Wearable Applications," IEEE Sensors Journal, 2021, doi: 10.1109/JSEN.2021.3116215.

[650] B. N. Altay, V. S. Turkani, A. Pekarovicova, P. D. Fleming, M. Z. Atashbar, M. Bolduc and S. G. Cloutier, "One-step photonic curing of screen-printed conductive Ni flake electrodes for use in flexible electronics," Scientific Reports, vol. 11, no. 1, pp. 1-12, 2021, doi: 10.1038/s41598-021-82961-3.

[651] D. Maddipatla, B. Narakathu, V. Turkani, B. Bazuin and M. Atashbar, "A gravure printed flexible electrochemical sensor for the detection of heavy metal compounds," In Multidisciplinary Digital Publishing Institute Proceedings,, vol. 2, no. 13, pp. 950, 2018, doi: 10.3390/proceedings2130950.

[652] B. B. Narakathu, S. G. A. Reddy, D. Maddipatla, S. Emamian, A. Eshkeiti, A. A. Chlaihawi, B. J. Bazuin and M. Z. Atashbar, "Rapid prototyping of a flexible microfluidic sensing system using inkjet and screen printing processes," In 2015 IEEE Sensor, pp. 1-4, 2015, doi: 10.1109/ICSENS.2015.7370340.

[653] D. Maddipatla, B. B. Narakathu, V. S. Turkani, B. J. Bazuin and M. Z. Atashbar, "Development of a Gravure Printed Flexible Electrochemical Sensor," In 17th International Meeting on Chemical Sensors (IMCS), pp.734-735, 2018, doi: 10.5162/IMCS2018/P2EC.19.

[654] S. Khan, L. Lorenzelli and R. S. Dahiya, "Technologies for printing sensors and electronics over large flexible substrates: a review," IEEE Sensors Journal, vol. 15, no. 6, pp. 3164-3185, 2014.

[655] X. Cao, H. Chen, X. Gu, B. Liu, W. Wang, Y. Cao, F. Wu and C. Zhou, "Screen printing as a scalable and low-cost approach for rigid and flexible thin-film transistors using separated carbon nanotubes," ACS nano, vol. 8, no. 12, pp. 12769-12776, 2014.

[656] S. Ahmadi, G. Wang, D. Maddipatla, Q. Wu, W. Lu and M. Z. Atashbar, "Investigating the Impact of Thickness, Calendering and Channel Structures of Printed Electrodes on the Energy Density of

LIBs-3D Simulation and Validation," In IEEE International Flexible Electronics Technology Conference (IFETC), pp. 1-3, 2021, doi: 10.1109/IFETC49530.2021.9580515.

[657] G. Manjunath, P. Pujar, B. Gupta, D. Gupta and S. Mandal, "Low-temperature reducible particle-free screen-printable silver ink for the fabrication of high conductive electrodes," Journal of Materials Science: Materials in Electronics, vol. 30, no. 20, pp. 18647-18658, 2019.

[658] A. A. Chlaihawi, S. Emamian, B. B. Narakathu, M. M. Ali, D. Maddipatla, B. J. Bazuin, and M. Z. Atashbar, "Novel screen printed flexible magnetoelectric thin film sensor," Procedia Engineering, vol. 168, pp. 684-687, 2016, doi: 10.1016/j.proeng.2016.11.247.

[659] A. A. Chlaihawi, S. Emamian, B. B. Narakathu, M. M. Ali, D. Maddipatla, B. J. Bazuin and M. Z. Atashbar, "A screen printed and flexible piezoelectric-based AC magnetic field sensor," Sensors and Actuators A: Physical, vol. 268, pp. 1-8, 2017, doi: 10.1016/j.sna.2017.10.030.

[660] B. N. Altay, J. Jourdan, V. S. Turkani, H. Dietsch, D. Maddipatla, A. Pekarovicova, P. D. Fleming and M. Atashbar, "Impact of substrate and process on the electrical performance of screen-printed nickel electrodes: fundamental mechanism of ink film roughness," ACS Applied Energy Materials, vol. 1, no. 12, pp. 7164-7173, 2018, doi: 10.1021/acsaem.8b01618.

[661] A. A. Chlaihawi, B. B. Narakathu, A. Eshkeiti, S. Emamian, S. G. R. Avuthu and M. Z. Atashbar, "Screen printed MWCNT/PDMS based dry electrode sensor for electrocardiogram (ECG) measurements," In 2015 IEEE International Conference on Electro/Information Technology (EIT), pp. 526-529, 2015, doi: 10.1109/EIT.2015.7293392.

[662] D. Maddipatla, T. S. Saeed, B. B. Narakathu, S. O. Obare and M. Z. Atashbar, "Incorporating a novel hexaazatriphenylene derivative to a flexible screen-printed electrochemical sensor for copper ion detection in water samples," IEEE Sensors Journal, vol. 20, no. 21, pp. 12582-12591, 2020, doi: 10.1109/JSEN.2020.3002811.

[663] Z.-W. Peng, T. Buck, L. J. Koduvelikulathu, V. D. Mihailetchi and R. Kopecek, "Industrial screen-printed n-PERT-RJ solar cells: Efficiencies beyond 22% and open-circuit voltages approaching 700 mV," IEEE Journal of Photovoltaics, vol. 9, no. 5, pp. 1166-1174, 2019.

[664] S. C. Lim, "Organic thin-film transistor using high-resolution screen-printed electrodes," Japanese Journal of Applied Physics, vol. 48, no. 8R, 2009.

[665] T.-K. Nguyen, T. Dinh, H.-P. Phan, C.-D. Tran, A. R. M. Foisal, Y. Zhu and D. V. Dao, "Electrically stable carbon nanotube yarn under tensile strain," IEEE Electron Device Letters, vol. 38, no. 9, pp. 1331-1334, 2017.

[666] M. Liu, Y. Zhao, Y. Shao, Q. Zhang and C. Liu, "3D printed force sensor with inkjet printed piezoresistive based strain gauge," in In 2018 IEEE SENSORS, 2018.

[667] M. Liu, Q. Zhang, Y. Shao, C. Liu and Y. Zhao., "Research of a novel 3D printed strain gauge type force sensor," Micromachines , vol. 10, no. 1, p. 20, 2019.

[668] S. Yao and Y. Zhu, "Wearable multifunctional sensors using printed stretchable conductors made of silver nanowires," Nanoscale , vol. 6, no. 4, pp. 2345-2352, 2014.

[669] G.-F. Tu, X. Yan, M. Yu, M.-Y. Jia, W. Pan, X.-X. He, W.-P. Han, Z.-M. Zhang, L.-M. Yu and Y.-Z. Long, "Patterned, highly stretchable and conductive nanofibrous PANI/PVDF strain sensors based on electrospinning and in situ polymerization," Nanoscale, vol. 8, no. 5, pp. 2944-2950, 2016.

[670] Z. Su, H. Chen, Y. Song, X. Cheng, X. Chen, H. Guo, L. Miao and H. Zhang, "Microsphere-assisted robust epidermal strain gauge for static and dynamic gesture recognition," Small, vol. 13, no. 47, p. 1702108, 2017.

[671] Y. Cho, P. J. Jeon, J. S. Kim and S. Im, "Organic strain sensor comprised of heptazole-based thin film transistor and Schottky diode," Organic Electronics, vol. 40, pp. 24-29, 2017.

[672] L. Vertuccio, L. Guadagno, G. Spinelli, P. Lamberti, V. Tucci and S. Russo, "Piezoresistive properties of resin reinforced with carbon nanotubes for health-monitoring of aircraft primary structures," Composites Part B: Engineering, vol. 107, pp. 192-202, 2016.

[673] A. S. Fiorillo, C. D. Critello and S. A. Pullano, "Theory, technology and applications of piezoresistive sensors: A review," Sensors and Actuators A: Physical, vol. 281, pp. 156-175, 2018.

[674] K. Takei, Z. Yu, M. Zheng, H. Ota, T. Takahashi and A. Javey, "Highly sensitive electronic whiskers based on patterned carbon nanotube and silver nanoparticle composite films," Proceedings of the National Academy of Sciences, vol. 111, no. 5, pp. 1703-1707, 2014.

[675] S. Zhang, H. Zhang, G. Yao, F. Liao, M. Gao, Z. Huang, K. Li and Y. Lin, "Highly stretchable, sensitive, and flexible strain sensors based on silver nanoparticles/carbon nanotubes composites," Journal of Alloys and compounds, vol. 652, pp. 48-54, 2015.

[676] S. Shengbo, L. Lihua, J. Aoqun, D. Qianqian, J. Jianlong, Z. Qiang and Z. Wendong, "Highly sensitive wearable strain sensor based on silver nanowires and nanoparticles," Nanotechnology , vol. 29, no. 5, p. 255202, 2018.

[677] M. G. Saborio, S. Cai, J. Tang, M. B. Ghasemian, M. Mayyas, J. Han, M. J. Christoe, S. Peng, P. Koshy, D. Esrafilzadeh and R. Jalili, "Liquid Metal Droplet and Graphene Co-Fillers for Electrically Conductive Flexible Composites," Small, vol. 16, no. 12, p. 1903753, 2020.

[678] K. Zhou and Z. Y. Wu, "Strain gauge placement optimization for structural performance assessment," Engineering Structures, vol. 141, pp. 184-197, 2017.

[679] P. Kulha, H. Enser, J. K. Sell, B. Strauß, M. Schatzl-Linder, B. Jakoby and W. Hilber, "Temperature dependence of gauge factor of printed piezoresistive layers embedded in organic coatings," in In Multidisciplinary Digital Publishing Institute Proceedings, 2017.

[680] M. J. Christoe, J. Hn and K. Kalantar-Zadeh, "Telecommunications and data processing in flexible electronic systems," Advanced Materials Technologies, vol. 5, no. 1, p. 1900733, 2020.

[681] M. Z. Atashbar and S. Krishnamurthy, Sensing and sampling strategies, Momentum Press, 2011.

[682] S. A. Dyer, Wiley Survey of Instrumentation and Measurement, New Jersey: Wiley, 2004.

[683] "Measuring With Strain Gauges: How to Prevent Unwanted Temperature Effects on Your Measurement Result," HBK Inc., [Online]. Available: https://www.hbm.com/en/6725/article-temperature-compensation-of-strain-gauges/. [Accessed 22nd 4 2020].

[684] "Strain Gage Thermal Output and Gage Factor Variation With Temperature," Micro-measurements, [Online]. Available: http://www.vishaypg.com/docs/11054/tn504.pdf. [Accessed 22nd 4 2020].

[685] N. Purwasih, N. Kasai, S. Okazaki, H. Kihira and Y. Kuriyama, "Atmospheric corrosion sensor based on strain measurement with an active dummy circuit method in experiment with corrosion products," Metals, vol. 9, no. 5, p. 579, 2019.

[686] J. L. Ramirez and F. Fruett, "Integrated octagonal mechanical stress sensor with temperature compensation," IEEE Sensors Journal, vol. 18, no. 14, pp. 5707-5714, 2018.

[687] H. F. Castro, V. Correia, N. Pereira, P. Costab, J. Oliveiraa and S. Lanceros-Méndez, "Printed wheatstone bridge with embedded polymer based piezoresistive sensors for strain sensing applications," Additive Manufacturing, vol. 20, pp. 119-125, 2018.

[688] A. Ajovalasit, "Advances in strain gauge measurement on composite materials," Strain, vol. 47, no. 4, pp. 313-325, 2011.

APPENDIX

PUBLICATIONS

Journals:

1. **A. Bose**, C. Beaver, D. Maddipatla, S. Rossbach, M. Atashbar, “Laser Ablated Microplasma Discharge Device for Inactivating Bacteria Suspended in Liquid Media”, IEEE Sensors, In Press.
2. **A. Bose**, C. Beaver, D. Maddipatla, S. Rossbach, M. Atashbar, “In-Vitro Analysis Of Thin-Film Microplasma Discharge Devices For Surface Sterilization” IEEE Transactions On Radiation And Plasma Medical Sciences, In Press
3. **A. Bose**, D. Maddipatla, M. Z. Atashbar, “2d Finite Element Modeling Of Surface Dielectric Barrier Plasma Discharge Devices To Understand The Influence Of Design Parameters On Sterilization Applications”, IEEE Transactions on Plasma Science, In Press
4. **A. Bose**, X. Zhang, D. Maddipatla, S. Masihi, M. Panahi, B. Narakathu, B. Bazuin, J. Williams, M. Mitchell, M. Atashbar, " Screen-Printed Strain Gauge for Micro-Strain Detection Applications", IEEE Sensors Journal, vol. 20, no. 21, pp. 12652-12660, 2020.
5. X. Zhang, D. Maddipatla, **A. Bose**, S. Hajian, B. Narakathu, J. D. Williams, M. Mitchell, M. Atashbar, " Printed Carbon Nanotubes-Based Flexible Resistive Humidity Sensor", IEEE Sensors Journal, vol. 20, no. 21, pp. 12592-12601, 2020.
6. D. Maddipatla, X. Zhang, **A. Bose**, S. Masihi, B. Narakathu, B. Bazuin, M. Atashbar, “A Polyimide Based Force Sensor Fabricated using Additive Screen-Printing Process for Flexible Electronics”, IEEE Access, vol. 8, pp. 207813-207821, 2020.
7. S. Masihi, M. Panahi, **A. Bose**, D. Maddipatla, X. Zhang, A. Hanson, B. Narakathu, B. Bazuin, M. Atashbar, "Development of a Flexible Tunable and Compact Microstrip Antenna via Laser

Assisted Patterning of Copper Film", IEEE Sensors Journal, vol. 20, no. 14, pp. 7579 - 7587, 2020.

8. M. Ahmad, S. Malik, S. Dewan, **A. Bose**, D. Maddipatla, B. Narakathu, M. Atashbar, M. Baghini, "An Auto-Calibrated Resistive Measurement System With Low Noise Instrumentation ASIC", IEEE Journal of Solid State Circuits, vol. 55, no. 11, pp. 3036-3050, 2020.
9. V. Palaniappan, M. Panahi, S. Masihi, D. Maddipatla, **A. Bose**, X. Zhang, B. Narakathu,B. Bazuin, M. Atashbar, "Laser-Assisted Fabrication of a Highly Sensitive and FlexibleMicro Pyramid-Structured Pressure Sensor for E-Skin Applications ", IEEE Sensors Journal, vol. 20, no. 14, pp. 7605 - 7613, 2020.
10. S. Masihi, M. Panahi, D. Maddipatla, A. Hanson, **A. Bose**, S. Hajian, V. Palaniappan, B. Narakathu, B. Bazuin, M. Atashbar, "A Highly Sensitive Porous PDMS Based Capacitive Pressure Sensor Fabricated on Fabric Platform for Wearable Applications", ACS Sensors, vol. 6 (3), pp. 938-949, 2021.

Conferences:

1. **A. Bose**, C. L. Beaver, D. Maddipatla, S. Rossbach, and M. Z. Atashbar. "Inactivation of B. subtilis Spores Using Flexible Microplasma Discharge Device.", In 2021 IEEE International Flexible Electronics Technology Conference (IFETC), pp. 0038-0040, 2021.
2. **A. Bose**, C. L. Beaver, D. Maddipatla, S. Rossbach, and M. Z. Atashbar. "A Novel and Flexible Microplasma Discharge Device for Inactivating Pathogens Suspended in Fluids.", In 2021 IEEE International Conference on Flexible and Printable Sensors and Systems (FLEPS), pp. 1-4, 2021.

3. B. Liu, **A. Bose**, X. Zhang and Z. Zhang. "CB/PDMS based strain gauge using 3D Printed mold." In 2021 IEEE International Conference on Electro Information Technology (EIT), pp. 197-201, 2021.
4. A. Hanson, D. Maddipatla, **A. Bose**, C. J. Kosik, S. Hajian, M. Panahi, S. Masihi, B. B. Narakathu, B. J. Bazuin, and M. Z. Atashbar. "Designing and development of a handheld portable electrochemical analyzer for flexible hybrid electronics." In 2021 IEEE International Conference on Electro Information Technology (EIT), pp. 1-4, 2021.
5. A. Hanson, D. Maddipatla, **A. Bose**, C. J. Kosik, S. Hajian, M. Panahi, S. Masihi, B. B. Narakathu, B. J. Bazuin, and M. Z. Atashbar. "Flexible and Portable Electrochemical System for the Detection of Analytes." In 2021 IEEE International Conference on Flexible and Printable Sensors and Systems (FLEPS), pp. 1-4, 2021.
6. S. Masihi, M. Panahi, D. Maddipatla, S. Hajian, **A. Bose**, V. Palaniappan, B. B. Narakathu, B. J. Bazuin, and M. Z. Atashbar. "Cohesion Failure Analysis in a Bi-layered Copper/Kapton Structure for Flexible Hybrid Electronic Sensing Applications." In 2021 IEEE International Conference on Electro Information Technology (EIT), pp. 409-412, 2021.
7. **A. Bose**, D. Madipatla, X. Zhang, M. Panahi, S. Masihi, B. B. Narakathu, B. J. Bazuin, and M. Z. Atashbar, “Screen Printed Silver/Carbon Composite Strain Gauge on a TPU Platform for Wearable Applications”, In 2020 IEEE International Conference on Flexible and Printable Sensors and Systems (FLEPS), pp. 1-5, 2020.
8. X. Zhang, **A. Bose**, D. Maddipatla, B. Narakathu, M. Atashbar, “Development of a Novel and Flexible MWCNT/PDMS Based Resistive Force Sensor”, In 2020 IEEE International Conference on Flexible and Printable Sensors and Systems (FLEPS), pp. 1-4, 2020.

9. X. Zhang, D. Maddipatla, **A. Bose**, B. B. Narakathu, J. D. Williams, M. F. Mitchell, and M. Z. Atashbar. "Effect of Excitation Signal Frequency on the Electrical Response of a MWCNT/HEC Composite Based Humidity Sensor.", In 2020 IEEE Sensors Conference, pp. 1-4, 2020.
10. V. Palaniappan, S. Masihi, M. Panahi, D. Maddipatla, **A. Bose**, X. Zhang, B. Narakathu, B. Bazuin, and M. Atashbar, "Highly Sensitive and Flexible M-Tooth Based Hybrid Micro-Structured Capacitive Pressure Sensor", In 2020 IEEE International Conference on Flexible and Printable Sensors and Systems (FLEPS), pp. 1-4, 2020.
11. M. Panahi, S. Masihi, D. Maddipatla, **A. Bose**, V. Palaniappan, S. Hajian, A. Hanson, B. Narakathu, B. Bazuin, and M. Atashbar, "Investigation of Temperature Effect on the Porosity of a Fabric Based Porous Capacitive Pressure Sensor", In 2020 IEEE International Conference on Flexible and Printable Sensors and Systems (FLEPS), pp. 1-4, 2020.
12. X. Zhang, D. Maddipatla, **A. Bose**, B. Narakathu, M. Atashbar, "A Printed MWCNTs/PDMS Based Flexible Resistive Temperature Detector", In 2020 IEEE International Conference on Electro/Information Technology (EIT), pp. 509-513, 2020.
13. S. Masihi, M. Panahi, S. Hajian, D. Maddipatla, S. Ali, X. Zhang, **A. Bose**, B. B. Narakathu, B. J. Bazuin, M. Z. Atashbar, "A Highly Sensitive Capacitive Based Dual-Axis Accelerometer for Wearable Applications", In 2020 IEEE International Conference on Electro/Information Technology (EIT), pp. 557-561, 2020.
14. **A. Bose**, D. Maddipatla, B. Narakathu, B. Bazuin, and M. Atashbar. "Laser-Assisted Patterning of a Flexible Microplasma Discharge Device for Heavy Metal and Salt Detection in Ambient Air." In 2019 IEEE International Conference on Flexible and Printable Sensors and Systems (FLEPS), pp. 1-3. IEEE, 2019.

15. **A. Bose**, X. Zhang, D. Maddipatla, S. Masihi, M. Panahi, B. Narakathu, B. Bazuin, and M. Atashbar. "Highly Sensitive Screen Printed Strain Gauge for Micro-Strain Detection." In 2019 IEEE International Conference on Flexible and Printable Sensors and Systems (FLEPS), pp. 1-3. IEEE, 2019.
16. X. Zhang, V. Turkani, S. Hajian, **A. Bose**, D. Maddipatla, A. J. Hanson, B. Narakathu, and M. Atashbar. "Novel Printed Carbon Nanotubes Based Resistive Humidity Sensors." In 2019 IEEE International Conference on Flexible and Printable Sensors and Systems (FLEPS), pp. 1-3. IEEE, 2019.
17. D. Maddipatla, X. Zhang, **A. Bose**, S. Masihi, M. Panahi, V. Palaniappan, B. Narakathu, B. Bazuin, M. Atashbar "Development of a flexible force sensor using additive print manufacturing process", IEEE International Conference on Flexible and Printable Sensors and Systems (FLEPS), July 7-10, Glasgow, UK, pp. 31, 2019.
18. S. Masihi, M. Panahi, **A. Bose**, D. Maddipatla, A. Hanson, B. Narakathu, B. Bazuin, and M. Atashbar. "Rapid Prototyping of a Tunable and Compact Microstrip Antenna by Laser Machining Flexible Copper Tape." In 2019 IEEE International Conference on Flexible and Printable Sensors and Systems (FLEPS), pp. 1-3. IEEE, 2019.
19. V. Palaniappan, S. Masihi, M. Panahi, D. Maddipatla, **A. Bose**, X. Zhang, B. Narakathu, B. Bazuin, and M. Atashbar. "Laser-Assisted Fabrication of Flexible Micro-Structured Pressure Sensor for Low Pressure Applications." In 2019 IEEE International Conference on Flexible and Printable Sensors and Systems (FLEPS), pp. 1-3. IEEE, 2019.
20. S. Masihi, M. Panahi, D. Maddipatla, **A. Bose**, X. Zhang, A.J. Hanson, V. Palaniappan, B. Narakathu, B. Bazuin, M. Atashbar, "A novel and printed fabric based porous capacitive

pressure sensor for flexible electronic applications", IEEE Sensors Conference, October 27-30, Montreal, Canada, 2019.

21. V. Palaniappan, S. Masihi, X. Zhang, S. Emamian, **A. Bose**, D. Maddipatla, S. Hajian, M. Panahi, B. Narakathu, B. Bazuin, M. Atashbar, "A flexible triboelectric Nanogenerator fabricated using laser-assisted patterning process", IEEE Sensors Conference, October 27-30, Montreal, Canada, 2019.
22. **A. Bose**, C. Beaver, D. Madipatla, B. Narakathu, S. Rossbach, B. Bazuin, M. Atashbar, "Laser-Assisted Patterning of Flexible Microplasma Discharge Device for Sterilization Applications", Flexible and Printed Electronics Conference (FlexTech), February 12-15, Monterey, California, USA, 2019.
23. **A. Bose**, C. L. Beaver, B. Narakathu, S. Rossbach, B. Bazuin, M. Atashbar, "Development of Flexible Microplasma Discharge Device for Sterilization Applications", IEEE Sensors conference, October 28-31, 2018, New Delhi, India.
24. X. Zhang, **A. Bose**, D. Maddipatla, B. Narakathu, V. Turkani, M. Atashbar, "Design, Simulation and Fabrication of a Novel MEMS Based Pulsometer", Eurosensors conference. September 9-12, 2018, Graz, Austria.
25. **A. Bose**, B. Narakathu, B. Bazuin M. Atashbar, "Modelling and Simulation of Microplasma Discharge Device for Sterilization Applications", Eurosensors conference. September 9-12, 2018, Graz, Austria.
26. **A. Bose**, D. Maddipatla, B. Narakathu, V. Turkani, B. Bazuin, M. Atashbar, "Flexible Microplasma Discharge Device for the Detection of Biochemicals", 17th International Meeting on Chemical Sensors, July 15-19, 2018, University of Vienna, Austria.

27. D. Maddipatla, B. Narakathu, **A. Bose**, V. Turkani, B. Bazuin, M. Atashbar, “Development of a gravure printed flexible electrochemical sensor”, 17th International Meeting on Chemical Sensors (IMCS), July 15-19, Austria, 2018.
28. **A. Bose**, X. Zhang, B. Narakathu, B. Bazuin and M. Atashbar, “A novel and flexible atmospheric pressure microplasma discharge device for sterilization applications”, 28th Anniversary World Congress on Biosensors, June 12-15, Florida, USA, 2018.
29. D. Maddipatla, B. Narakathu, V.S. Tukarni, **A. Bose**, B. Bazuin, M. Atashbar, “A novel and flexible screen printed electrochemical sensor on paper substrate”, Flexible and Printed Electronics Conference (FlexTech), February 12-15, Monterey, California, USA, 2018.
30. **A. Bose**, B. Narakathu, X. Zhang, D. Maddipatla, B. Bazuin and M. Atashbar, “Analysis of Microplasma Discharge on a Flexible Platform for Sterilization Applications”, Flexible and Printed Electronics Conference (FlexTech), February 12-15, Monterey, California, USA, 2018.